University of Alberta

Shear-Induced Growth of Asphaltene Aggregates

by

Nazmul Haq Gazi Rahmani ©

A thesis submitted to the Faculty of Graduate Studies and Research in partial fulfillment of the requirements for the degree of Doctor of Philosophy in Chemical Engineering

Department of Chemical and Materials Engineering

Edmonton, Alberta
Spring, 2004

Library and
Archives Canada

Published Heritage
Branch

395 Wellington Street
Ottawa ON K1A 0N4
Canada

Bibliothèque et
Archives Canada

Direction du
Patrimoine de l'édition

395, rue Wellington
Ottawa ON K1A 0N4
Canada

Your file Votre référence
ISBN: 0-612-96315-2
Our file Notre référence
ISBN: 0-612-96315-2

The author has granted a non-exclusive license allowing the Library and Archives Canada to reproduce, loan, distribute or sell copies of this thesis in microform, paper or electronic formats.

L'auteur a accordé une licence non exclusive permettant à la Bibliothèque et Archives Canada de reproduire, prêter, distribuer ou vendre des copies de cette thèse sous la forme de microfiche/film, de reproduction sur papier ou sur format électronique.

The author retains ownership of the copyright in this thesis. Neither the thesis nor substantial extracts from it may be printed or otherwise reproduced without the author's permission.

L'auteur conserve la propriété du droit d'auteur qui protège cette thèse. Ni la thèse ni des extraits substantiels de celle-ci ne doivent être imprimés ou aturement reproduits sans son autorisation.

In compliance with the Canadian Privacy Act some supporting forms may have been removed from this thesis.

Conformément à la loi canadienne sur la protection de la vie privée, quelques formulaires secondaires ont été enlevés de cette thèse.

While these forms may be included in the document page count, their removal does not represent any loss of content from the thesis.

Bien que ces formulaires aient inclus dans la pagination, il n'y aura aucun contenu manquant.

Canada

Reproduced with permission of the copyright owner. Further reproduction prohibited without permission.

Abstract

A model system was studied to investigate asphaltenes coagulation in toluene-heptane solvent mixtures. The effects of shear rate (*G*), solids volume fraction (φ), and toluene-to-heptane ratio (T:H) in solvent mixtures can be identified as the theme of the first part of the dissertation. The evolution of aggregates size distribution in an aggregating and fragmenting suspension of asphaltene particles is studied experimentally in a Couette device and theoretically using a population balance approach. Initially, aggregation rapidly depletes the primary particles, forming larger aggregates. The larger aggregates become more susceptible to breakage and the primary particles diminish until aggregation and fragmentation balance each other and a steady state is attained. Raising the shear rate, *G*, contributes to higher collision rate, but, eventually, fragmentation mode also increases. As a result, higher *G* gives smaller steady-state average aggregate sizes and reduces time before the steady state is reached. Higher φ and lower T:H produces aggregates with larger average size.

The second part of the thesis work involves experiments that were performed in a bench scale stirred tank using a photometric dispersion analyzer (PDA) to examine asphaltenes aggregation. It was shown that the presence of maltenes in the bitumen solution retards the aggregation kinetics significantly, though the steady-state aggregate size reaches the same size as found with asphaltenes alone. Aggregates formed at a certain shear rate are broken at a higher shear rate, and can reform (re-grow) if a lower shear rate is applied. But, the aggregates do not attain the previous size. Asphaltenes flocculation in toluene-heptane mixture is *not fully reversible* and the final, steady-state

floc size depends on the shear history. Cyclic- and tapered-shear flocculation appear more advantageous than constant-shear flocculation for production of denser, and more compact particles beneficial for faster settling.

Free settling test results show that the asphaltene aggregates are highly porous, higher shear rate produces more compact and denser aggregates, and porosity increases with aggregate size. Larger aggregates with smaller effective density exhibited higher settling velocities due to their fractal structure and flow through effect. The dynamic evolution of boundary fractal dimension exhibits the presence of shear-induced breakage/ restructuring. The lower values of 3-D fractal dimension ($D<2$) indicate tenuous aggregate structure with very low space-filling capacity.

Acknowledgments

I am truly thankful to my supervisors, Drs. Jacob H. Masliyah and Tadeusz Dabros, for their support, encouragement and guidance during this work. Their combined knowledge, enthusiasm, and attention to minute details are reflected throughout the thesis. Initially, the ordeal to lay the foundation of this doctoral project was intricate. Without Dr. Masliyah's active participation in the lab work for first few weeks, this work would have been nearly impossible.

I would like to express my sincere thanks to my peers and colleagues at the University of Alberta, who provided an enjoyable environment for research and learning. In particular, Drs. Tony Yeung, Yadollah Maham, Joe Zhou, Weixing Wang, Guoxing Gu, Mahbub-ur Razzaque, Liyan Zhang, Mr. Manoj Luthra, Robert Lopetinsky, Wei Li, and Alejandro Magual had been a great help. Ms. Leanne Swekla was ever smiling with her continual help to the students.

This work was conducted under the auspices of the NSERC Industrial Research Chair in Oil Sands Research Engineering with financial support from Alberta Energy, University of Alberta, and Albian Sands Energy Corporation.

I am grateful to my parents and sisters for their understanding, unconditional love and support from miles and miles away. Finally, I am grateful to my wife, Samina, for sacrificing a part of her career to be with me throughout this thesis.

Table of Contents

List of Tables

List of Figures

Chapter 1

Introduction

1.1 Background

Oil and gas have powered the world economy for the past century and will likely continue to do so for at least the coming century. With the rapid depletion of conventional oil reservoirs, increased oil production from technologically challenging sources, such as heavy oil and the oil sands has become the norm. In the case of oil sands, the asphaltene content of the bitumen is high, up to 22% (Strausz, 1989). Asphaltenes are known to stabilize water-in-oil emulsions that are carried in the bitumen froth (Yarranton, 1997). The water in the diluted bitumen is in the form of water droplets approximately 2 micrometers in diameter. The chloride content in the droplets is similar to that of the process water. The water-in-oil emulsion travels through the downstream upgrading process and eventually brings the chlorides in contact with the hot metal equipment. The chlorides form complexes with the iron from the equipment and corrode the metal. Moreover, asphaltenes are converted to coke in upgrading of heavy oil whereby lowering the final yield.

In order to eliminate these potential problems, the oil sand industry has a growing interest in asphaltenes precipitation from bitumen, which is a recently commercialized technology of froth treatment (Firmin, 2000). The technology relies on addition of a paraffinic solvent above the inception point of asphaltene precipitation. The precipitated asphaltenes act as flocculent to the emulsified water droplets and fine solids in the diluted froth. Clusters of precipitated asphaltenes, water droplets and solids are formed, enabling their removal by gravity settling (Long et al., 2002). Thus, the properties of the flocs, especially their size, density and structure, which affect the settling rate, are of great importance for equipment design.

This thesis is concerned with Alberta bitumen and asphaltenes. The molecular composition of the Alberta bitumen is best described in terms of the solubility classes (Strausz, 1989) and is shown in Fig. 1.1. The most easily described classes are the saturates and aromatics. The saturate fraction consists of varieties of alkyl cycloalkanes from 1 to 6 rings (17% of the bitumen), and many of them are part of homologous series (Yarranton, 1997). The aromatic fraction of the bitumen consists primarily of monoaromatic (10% of the bitumen) and di- and tri-nuclear aromatic hydrocarbons (9% of the bitumen). The aromatic fraction contains a small amount (<1% of the bitumen) of sulfur and nitrogen heteroatoms in the form of benzothiophenes, alicyclic sulfides, alkylated benzoquinilines and carbazoles (Yarranton, 1997). Again many homologous series are observed.

The resins are a mixture of heterocycles (40% of the bitumen) and a small amount (1-2% of the bitumen) of carboxylic acids. The carboxylic acids are a homologous series of tricyclic terpenoid acids, pentacyclic hopanoid acids and trace amounts of *n*-alkanoic acids. There are many heteroatom homologous series in the resins including benzofluorenones, cyclic sulfides, alkyl benzocarbozoles and alkyl benzoquinolines (Yarranton, 1997). However, the resin species have higher molar mass, greater polarity and lower H/C ratios. Hence, the difference between resins and aromatics is not as clear as that between saturates and aromatics.

The distinction between resins and asphaltenes is less clear. The chemical species that make up each class are similar. The molecular nature of the asphaltenes fraction has been the subject of numerous investigations, but determining the actual structures of the constituents of the asphaltenes fraction proved to be difficult due to the self-organization of the heavier parts and the almost continuous distribution of the molecular properties (Murgich et al., 1999). Figure 1.2 shows a modified structure of asphaltenes presented by Murgich et al., 1999. Asphlatenes, on average, have higher molar mass, higher heteroatom content and lower H/C ratios than the resins (Koots and Speight, 1975). The resins and asphaltenes probably form a continuum of like chemical species with increasing average molar mass (Cimino et al., 1995). Asphaltenes and resins can exhibit complex properties and phase behavior.

To avoid the difficulties inherent in studying a system as complex as bitumen, one can examine a simpler model system possessing the key characteristics of the original one. Therefore, a model system will be designed to examine asphaltenes precipitation in organic solvents mixture. The phase behavior of asphaltenes in toluene/heptane mixtures resembles that of asphaltenes in bitumen except that asphaltene-resin interactions are not accounted for. Therefore, toluene/heptane/asphaltenes was selected as the model system and toluene/heptane/bitumen was studied to mimic the commercial system. It should be kept in mind that the effect of water droplets might need to be examined separately.

1.2 Research Objectives

The purpose of the thesis is to study the precipitation process and the characteristics of asphaltene aggregates. Although the aggregation kinetics of colloidal particles has been a subject of extensive experimental studies during the last decade, the mechanism of aggregation and the process of formation of fractal aggregates for asphaltene particles were not investigated intensively. The main objective of the thesis is to determine the kinetics of aggregation of suspended "primary" particles of asphaltenes in hydrocarbon solutions. It is found that when a concentrated solution of asphaltenes in toluene is added to excess heptane, the precipitated asphaltene grows from sub-micron size primary particles to orders of magnitude larger size flocs in real time (or, within few minutes). The thesis presents results of experimental and theoretical studies concerning the aggregation and fragmentation kinetics of asphaltene particles under shear. The work is of substantial significance to engineering research since various operations in petroleum industries are performed under shear flow and strongly affected by asphaltenes aggregation, flocculation, and sedimentation.

This study is the first step to investigate asphaltenes flocculation of a model system using optical microscopy. The microscopic technique described in the thesis is ideally suited for the study of suspensions containing solid asphaltene particles in the micron size range, which associate to form aggregates of several microns in diameter, and provides information concerning particle aggregation kinetics, floc compactness, fractal structure, and settling properties. These investigations meet the other objectives of the thesis, which is to predict the properties of asphaltene aggregates in terms of their structure and settling behavior. From a commercial viewpoint, the present study provides information on the significance of shear rate, asphaltenes concentration, and solvent composition for asphaltenes precipitation, which are essential for proper process design and material handling. The objectives can be restated as the following:

1. Measure and theoretically describe the growth kinetics of asphaltene precipitates in toluene/heptane mixtures in a model system.

2. Investigate the effects of shear history on aggregates breakage and reformation mechanisms to acquire knowledge about their strength.
3. Study the aggregate settling behavior and structure to understand their properties.

1.3 Thesis Outline

Chapter 1 serves as a general introduction to the subject of asphaltenes precipitation and its commercial application. This chapter is intended to provide the background and the motivation for this research, and to place the subsequent chapters in context.

The body of the thesis is set in paper format and is presented in chapter 2 to 6. Asphaltenes aggregation kinetics, the first thesis objective, is addressed in Chapters 2 and 3. The materials and experimental methods used in these consecutive chapters are presented in Chapter 2. The growth of asphaltene aggregates took place in a well-controlled, laminar shear flow of a Couette apparatus. The attainment of steady state by the flocculating suspension of asphaltenes as a function of shear rate is addressed in Chapter 2. Using population balance approach, a physical model is used to understand the aggregation and fragmentation processes. Chapter 3 examines the dynamic equilibrium between aggregate growth and breakup by monitoring the evolution of asphaltene flocs size distribution as a function of shear rate, solid particles content, and solvent composition.

The second thesis objective is dealt with in Chapter 4. Using a bench scale stirred tank and light transmittance technique, different shear schedules including the commercial cyclic- and tapered-shear, are employed to investigate the asphaltene aggregates reformation mechanism with bitumen.

The third thesis objective is considered in Chapters 5 and 6. In these Chapters, the settling velocities of aggregates are measured to discuss the relationship between the porosity and fractal structure of permeable asphaltene aggregates. The dynamic evolution of perimeter-based fractal dimension with shear, and two- and three-dimensional fractal dimension at different experimental conditions are measured to gain knowledge about aggregate compactness and tenuous structure. As the thesis is written in paper format, some repetitions in describing experimental methods could not be avoided.

Chapter 7 is a summary of Chapters 2-6 and includes a discussion of their relevance to asphaltenes precipitation and flocculation. Implications for treating the bitumen froth in gravity settling vessel are considered and recommendations for extending the work are made.

1.4 References

Cimino, R., Correra, S., Del Bianco, A., and Lockhart, T. P. (1995). In *Asphaltenes: Fundamentals and Applications*, ed. by Sheu, E. Y., and Mullins, O. C., Plenum Press, New York, Chapter III, p 97.

Firmin, K. (2000). *Muskeg River Mine Froth Treatment Process*. Shell Canada, CIM Meeting, Edmonton.

Koots, J. A., and Speight, J. G. (1975). Relation of Petroleum Resins to Asphaltenes, *Fuel*, 54 (3), 179-184.

Long, Y., Dabros, T., and Hamza, H. (2002). Stability and Settling Characteristics of Solvent-Diluted Bitumen Emulsions, *Fuel*, 81, 1945.

Strausz, O. P. (1989). *AOSTRA Technical Handbook of Oil Sands, Bitumen and Heavy Oils*. Ed. L. G. Hepler and C. His, AOSTRA Technical Publications Series # 6, Edmonton.

Yarranton, H. W. (1997). *Asphaltene Solubility and Asphaltene Stabilized Water-in-Oil Emulsions*. Ph.D. Thesis, University of Alberta, pp 02, 20-21.

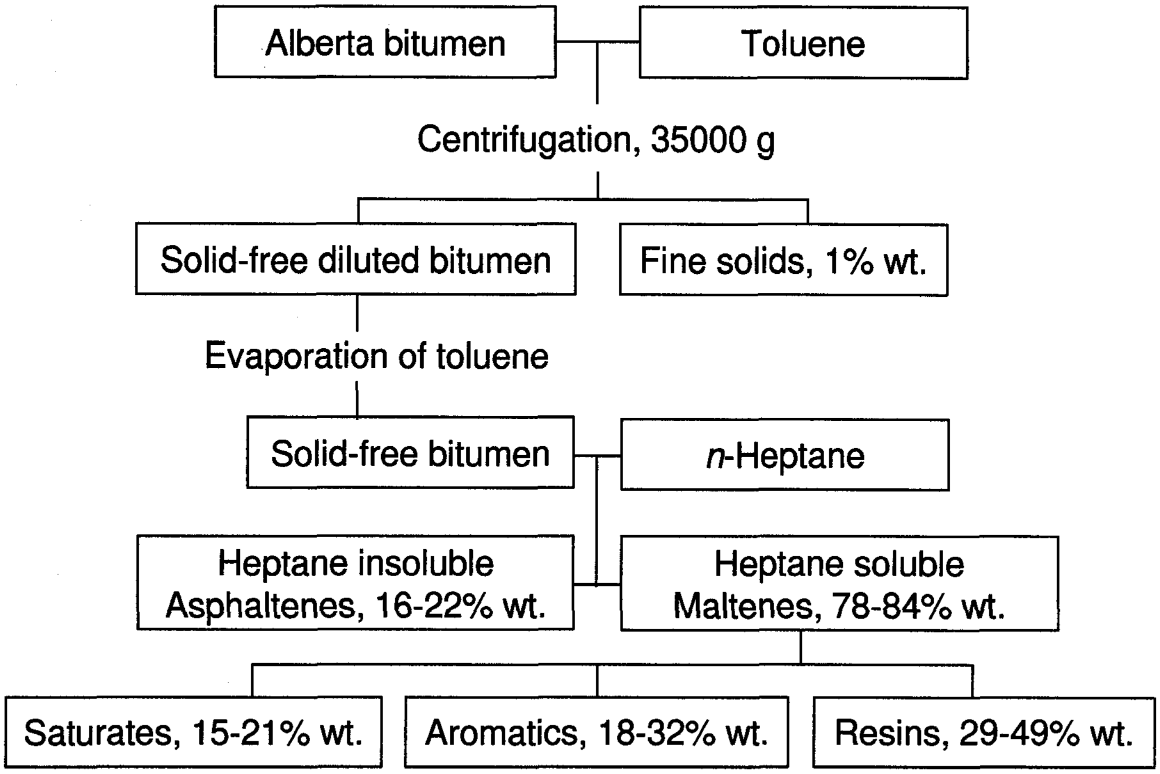

Figure 1.1. Simplified representation of the solubility classification of Alberta bitumens (Strausz, 1989).

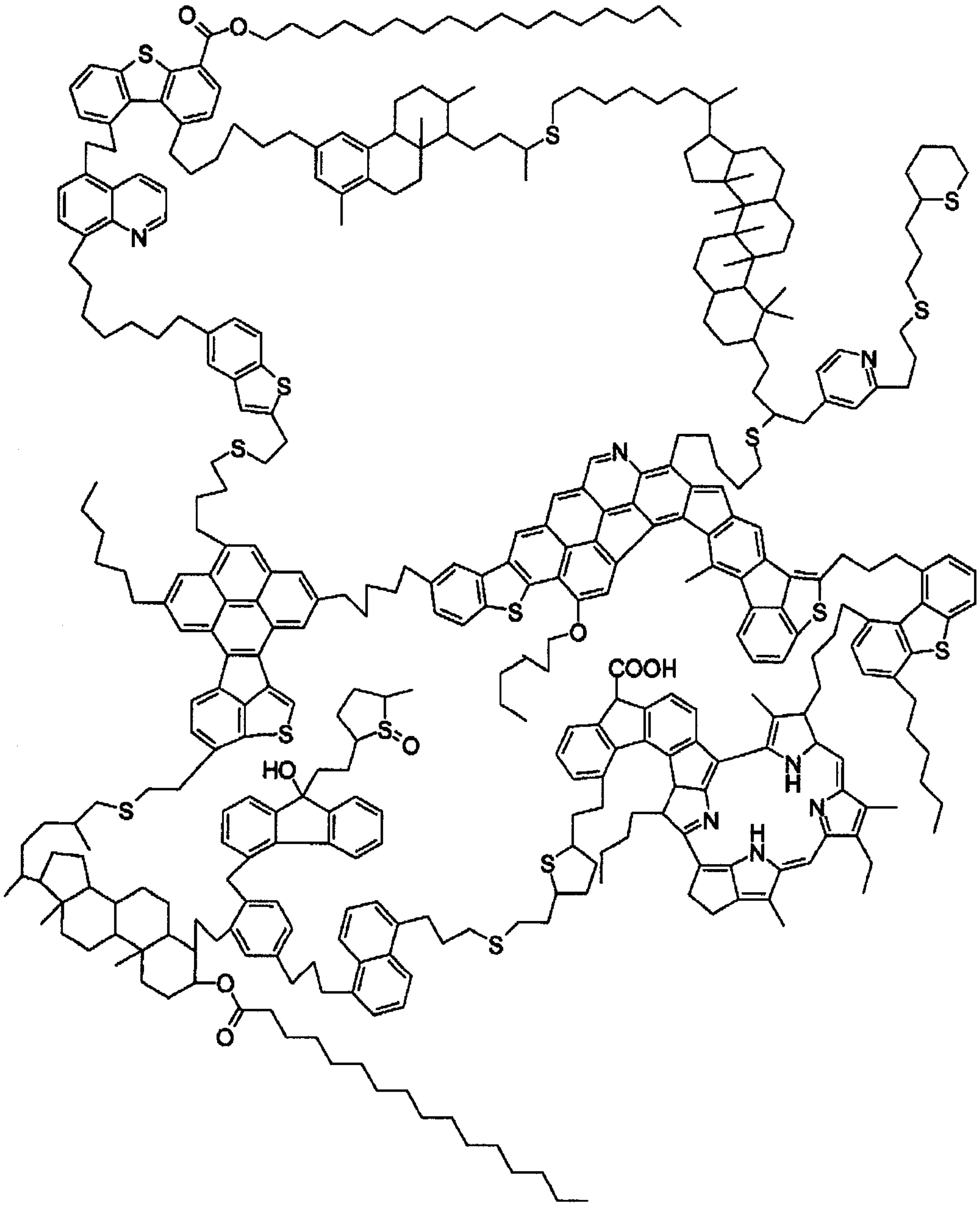

Figure 1.2. A hypothetical asphaltene molecule from Athabasca bitumen (Murgich et al., 1999).

Chapter 2

Asphaltenes Aggregation and Fragmentation: Couette Device*

2.1 Introduction

Petroleum asphaltenes have been a subject of extensive research. On the basis of solubility, asphaltenes are defined as the part of petroleum that is insoluble in *n*-alkanes and completely miscible in aromatic hydrocarbons such as toluene or benzene (Speight, 1990). This property is used for the extraction of asphaltenes. The above definition is in some sense arbitrary, as the molecular structure of asphaltenes varies significantly depending on their origin, method of oil recovery, and history of extraction (Burya et al., 2001). According to chemical structure, asphaltenes are aromatic multi-cyclic molecules surrounded and linked by aliphatic chains and heteroatoms; published molar mass data for petroleum asphaltenes range from 500 g/mol to a high of 50,000 g/mol (Long, 1981). The polarity and complex structure of asphaltenes lead to their self-association, flocculation, and precipitation during the course of heavy oil processing.

On one hand, the importance of asphaltenes in the petroleum industry is through its negative impact on various petroleum operations, such as exploration, production, transportation, and refining (Yen and Chilingarian, 1994; Sheu and Storm, 1995). For example, upon release of a well pressure asphaltenes may precipitate and plug the reservoir formation and well bore. On the other hand, a new technology is under development for cleanup operation of bitumen originating from the shallow oil sands deposits in northern Alberta, which takes advantage of asphaltenes propensity to aggregate. Asphaltenes, a high molecular weight constituent of bitumen, precipitate out

---

* Published in part: Rahmani, N. H. G., Dabros, T., and Masliyah, J. H., *AIChE* J., **49(7)**, 1645 (2003).

of a bitumen/light aliphatic hydrocarbon mixture and act as flocculant to the emulsified water droplets and fine solids. Very little is known about the mechanical properties (e.g. structure and yield strength) of the precipitated asphaltene aggregates. This paper focuses on determining these properties under dynamic conditions. The size range of studied aggregates is similar to the ones encountered in commercial systems as reported by Long et al. (2002).

The formation of colloidal asphaltenes associates in several organic solvents and in crude oil was observed for the first time more than half a century ago (Mack, 1932; Pfeiffer and Saal, 1940). It is postulated that in aromatic solvents, asphaltenes can form micelle-like aggregates above a certain concentration, known as the critical micelle concentration (CMC). The CMC data for asphaltenes in toluene have been determined using a variety of methods, such as measurement of surface tension (Rogacheva et al., 1980) and calorimetric titration (Andersen and Birdi, 1991; Sheu et al., 1992). The values obtained by various authors differ widely (e.g., the CMC in toluene is in the range from 0.10 to 3.24 gL^{-1}). This can be explained by the diversity of the techniques applied and by the variety of asphaltenes (origin, extraction, impurities) studied. Sheu and Storm (1995) have noted that asphaltenes in a good solvent below the CMC are in a molecular state, whereas above the CMC, asphaltene micelle formation occurs in a manner similar to that in surfactant systems but with less uniformity in their structure and more polydispersity. According to other investigations, the structure and the shape of asphaltenic micelle-like associates appear to be much more complicated than that of classic surfactant micelles (Drushel and Schultz, 1980, Yudin *et al.*, 1998). These studies indicate that asphaltene micelle-like associates are formed as a result of multiple interactions: aggregates about 2-

5 nm in size are present either in a molecular form or are formed by strong intermolecular attractive forces, while the larger particles are self-associates, formed from these small aggregates by a weaker interaction forces.

Though many studies have been conducted on the growth of colloidal asphaltene particles in hydrocarbon solutions, the flocculation of asphaltene particles under hydrodynamic shear flow has not been investigated. It bears a significant implication in industrial applications. The objective of the present chapter is to study the kinetics of aggregation of suspended "primary" particles of asphaltenes under controlled shear conditions. A mixture of toluene and *n*-heptane is often used to investigate the stability and the precipitation process of asphaltenes. At a certain threshold value of the ratio of *n*-heptane to toluene, the asphaltenes in solution becomes unstable and asphaltenes particles start to precipitate. It is found that when a concentrated solution of asphaltenes in toluene is added to excess heptane, the precipitated asphaltene grows from micron-size primary particles to aggregates that are orders of magnitude larger within few minutes.

In the present study, the growth of the asphaltenes flocs takes place in a well-controlled, laminar shear flow of a Couette device. Image analysis is used to measure the size of the aggregates in suspension. The present communication is a first step to study asphaltene flocculation for a model system using optical microscopy. It presents both experimental and theoretical studies of dynamics of aggregation and fragmentation for asphaltene particles under shear in an organic solvent. The growth of the aggregates is investigated as a function of various intensities of agitation (i.e., shear rate, G), solvent composition (i.e., ratio of toluene to *n*-heptane in the solution, T:H) and particle contents (i.e., volume fraction of particles, φ). It is shown how the variation in the applied shear rate leads to the change of parameters of a steady-state average aggregate size and the characteristic relaxation time required to achieve the steady state. A population balance approach is used to shed light on the effect of G, φ, and T:H in the aggregation and fragmentation processes. The model, developed in this work, well describes and explains the experimental observations and has two adjustable parameters: the porosity of the aggregates, ε, and the breakup coefficient for shear fragmentation, b. The values obtained for these two parameters are discussed. The microscopic technique described in the present paper is ideally suited for the study of suspensions containing solid asphaltenes particles in the sub-micron size range, which flocculate to form aggregates several microns in diameter. The technique also provides information on aggregation kinetics and aggregate size.

2.2 Material - Asphaltenes

The asphaltenes used in this study are derived from Syncrude vacuum-distillation-tower-feed Athabasca bitumen (bitumen that has been treated to remove most of the solids and water). However, the bitumen still contains mineral solids, which make up about 1 wt% of the bitumen. The "solids", which include fine clays, are insoluble in toluene (Yarranton, 1997). To remove the solids, the bitumen is first dissolved in toluene and centrifuged at 35,000g for 30 minutes. The supernatant liquid is recovered and evaporated until dry, "solids-free" bitumen remains. Asphaltenes are extracted from the "solids-free" bitumen with a 40:1 volume ratio of heptane to bitumen (solids-free). The mixture is stirred for 4 hours and left standing to allow the precipitated asphaltenes to settle overnight. Then the supernatant liquid is removed and the remaining precipitate is further diluted with heptane at a 4:1 volume ratio of heptane to asphaltene. After 4 hours, the final mixture is filtered using 0.22-μm *Millipore* filter paper and the remaining asphaltenes are washed thoroughly with heptane until the filtrate (i.e. heptane) becomes colorless. The precipitated asphaltenes are dried in a vacuum oven dryer at 23 kPa absolute pressure and 50°C. The drying process usually requires one week. The asphaltenes recovered in this method make up about 16 wt% of original bitumen.

Reagent-grade toluene and heptane were purchased from Fisher Scientific.

2.3 Apparatus

A schematic view of the Couette device (where the asphaltenes-solvent mixture is introduced) is shown in Fig. 2.1. This type of apparatus is used because under certain conditions it generates a well-defined shear field. Couette flow is preferable because if h<<d (where d is the inner Couette diameter and h is the gap width), a constant velocity gradient across the gap is achieved (Cummins et al., 1990).

The inner cylinder, with a diameter of 50 mm, is made of Teflon to provide better optical reflection. The outer cylinder, with an inner diameter of 60 mm, is made of Pyrex glass to allow the suspension to be observed. For the first set of experiments, the height of the cylinders is 200 mm, the annular gap between them is 5 mm, and the asphaltene suspension volume is 160 mL. For the second and third sets of experiments, the height of the cylinders is doubled to 400 mm, but the annular gap between them remains same (5 mm), and hence, the asphaltene suspension volume is 320 mL. Though all the experimental variables are same, more asphaltenes is precipitated for higher volume of asphaltene suspension in longer cylinder (as noticed from Table 2.1). The outer cylinder is fixed, while the rotational speed of the inner cylinder can be adjusted. For the three sets of experiments, the location of the observation area or control volume is 50 mm above the bottom of the cylinder. Images of asphaltenes aggregates in suspension are obtained using a microscope (Carl Zeiss Canada Ltd.) coupled with a CCD camera and a video recorder. Image analysis software (Sigma ScanPro 4) is used to calculate the geometrical properties of the aggregates from the captured images.

2.4 Sample preparation

2.4.1 Tests at different shear rates

Initially, dry asphaltenes powder is mixed with toluene to give an initial concentration of 1.0 g/L to achieve a good dispersion. The suspension is subjected to high-speed stirring for proper mixing and is labeled as a stock solution of toluene-asphaltene. Samples of this stock solution are diluted in toluene (if required) and then added with *n*-heptane in a beaker to give an initial asphaltenes concentration as desired (see Table 2.1). The suspension is stirred immediately at 300 rpm with a marine propeller for 15 s to ensure complete mixing. Though no baffle is placed in the beaker, aeration and evaporation of the solvent can be neglected due to low mixing intensity and short mixing time. Following the mixing, the asphaltenes solution is transferred into the outer glass cylinder, which is quickly snapped into the Couette device, and the rotation of the inner cylinder begins at a required rpm (see Fig. 2.2). This is considered as the starting time for aggregation. The experiments are carried out at a constant shear rate (G) ranging from 1.2–12.7 s^{-1}. Because of the limited optical resolution, the small asphaltene aggregates and their structural details became visible when the aggregates reached

Table 2.1. Amount of precipitated asphaltenes, asphaltenes concentration in solution and asphaltenes volume fraction for different experimental conditions

Average shear rate, G (s^{-1})	Ratio of toluene to *n*-heptane in the solution	Initial concentration of asphaltenes in toluene (mg/L)	Initial concentration of asphaltenes in toluene + *n*-heptane mixture (mg/L)	Final amount of precipitated asphaltenes (mg)	Particle concentration in toluene + *n*-heptane mixture (mg/L)	Particle volume fraction φ (x10^{-6})
1.2–12.7	1:15	1000	62.5	2.1 ± 0.3	12.8	10.81
2.5	1:15	1000	62.5	4.1 ± 0.4	12.8	10.81
2.5	1:7	1000	62.5	3.3 ± 0.3	10.3	8.60
2.5	1:3	1000	62.5	2.8 ± 0.2	8.8	7.29
2.5	1:7	1000	62.5	3.3 ± 0.3	10.3	8.60
2.5	1:7	750	46.9	1.7 ± 0.2	5.3	4.43
2.5	1:7	500	31.3	1.3 ± 0.2	4.1	3.38

approximately 30 μm. Hence, there is a time lag before the images can be captured due to lack of growth of the asphaltene aggregates to observable size.

Though the initial asphaltenes concentration was 62.5 mg/L, the amount of precipitated asphaltenes at the end of the experimental run is found to be significantly less than the initial amount added. After the stirring is stopped, the asphaltene aggregates are allowed to settle out of solution. The precipitated asphaltene aggregates are filtered using 0.22-micron *Millipore* filter paper. Since these aggregates are weak or fragile, great care must be taken in the measurement and handling of the flocs. Then the precipitate is dried in a vacuum dryer at 23 kPa absolute pressure and room temperature until the weight becomes constant. The asphaltenes recovered by this method is the precipitated amount and is used to calculate the volume of precipitate in solution assuming a density of 1200 kg/m^3 for solid asphaltenes (Yarranton, 1997). However, the actual volume of the precipitate is larger due to the porous structure of the asphaltene aggregates. It means that the average density of the aggregates is lower than 1200 kg/m^3.

2.4.2 Tests at different solvent compositions and asphaltene particle concentrations

Table 2.1 shows the amount of precipitated asphaltenes, asphaltenes particle concentration, and asphaltenes particle volume fraction (φ) in the solution for all experiments carried out at different conditions (set 1 to 3). From this table, it can be seen that the second set of experiments were carried out at a constant shear rate of 2.5 s^{-1} and an initial asphaltenes concentration of 62.5 mg/L, but the solvent composition (i.e., the ratio of toluene to heptane in the solution) varied. In the third set of experiments, the shear rate was set at 2.5 s^{-1} and the ratio of toluene to *n*-heptane was kept fixed at 1:7; the initial asphaltenes concentration varied from 62.5 mg/L to 31.3 mg/L.

2.5 Experimental studies

Peclet number is a measure of the relative strength of the fluid flow (convection) to Brownian motion (diffusion) (Elimelech et al., 1995):

$$Pe = \frac{U_0 a}{D_0} \tag{2.1}$$

where D_0 is the diffusion coefficient of a spherical particle of radius a subjected to a flow velocity characterized by U_0. Physically, the magnitude of the Peclet number indicates which of the two mechanisms (convection and diffusion) is dominant in the process of particle transport. Mathematically, it can be used to justify simplifications made to the equations governing the transport processes when carrying out theoretical calculations.

Small particles in suspension can be seen to undergo continuous random movement or Brownian motion. The diffusion coefficient (D_o) of a spherical particle is given by the Stokes-Einstein equation:

$$D_o = \frac{k_B T}{6\pi a \mu} \tag{2.2}$$

where k_B is the Boltzmann constant, T is the absolute temperature, a is the particle radius, and μ is the viscosity of the suspending liquid.

For a simple case of laminar shear flow, the appropriate characteristic flow velocity is given by

$$U_o = Ga \tag{2.3}$$

where G is the shear rate. Substituting Eqs. (2.2) and (2.3) into Eq. (2.1), the dimensionless group, Peclet number, can be written as

$$Pe = \frac{6\pi \mu G a^3}{k_B T} \tag{2.4}$$

When $Pe \ll 1$, only Brownian aggregation can be considered, whereas the Brownian contribution is negligible when $Pe > 10$. Depending on the mean aggregate size, Pe assumes different values, and for example, in this experimental study the Peclect number is found to be about 600 for particles with $a = 2.5$ micrometers and $G = 1\ s^{-1}$. This ensures that aggregation due to Brownian motion (i.e. perikinetic aggregation) can be neglected as compared with shear-induced (i.e. orthokinetic) aggregation (Oles, 1992; Serra et al., 1998).

When flows along curved walls are considered, it is found that a flow instability needs to be taken into account. The case of flow between two rotating concentric cylinders of which the inner cylinder is in motion and the outer cylinder is at rest affords an example of an unstable stratification caused by centrifugal forces. The fluid near the inner wall experiences a higher centrifugal force and shows a tendency to being propelled outwards. The stability of this type of flow was first investigated by Lord Rayleigh (1913) who assumed that the *fluid* was *non-viscous*. He found that the flow becomes unstable when the peripheral velocity, u, decreases with the radius, r, more strongly than $1/r$, that is, when

$$u(r) = \frac{const}{r^n}; \ with \ \ n > 1 \ \ (unstable) \tag{2.5}$$

The case of a viscous fluid was first investigated in detail by G. I. Taylor (Taylor, 1935) who used the framework of a linear theory for this purpose. When a certain Reynolds number is exceeded, vortices appear and their axes are located along the circumference. The conditions for the flow to become unstable can be expressed with the aid of a characteristic number known as the *Taylor number*, T_a, of the form

$$T_a = \frac{U_1 h}{\nu}\sqrt{\frac{h}{R_1}} = \frac{\omega R_1 h}{\nu}\sqrt{\frac{h}{R_1}} \geq 41.3; \ \text{(viscous instability)} \tag{2.6}$$

where h denotes the width of the gap, R_1 is the inner radius, and U_1 (= ωR_1) the peripheral velocity of the inner cylinder. With the present experimental arrangement, in which the gap has the dimension of d = 5 mm, the inner radius is R_1 = 25 mm, and the kinematic viscosity of the fluid is $\nu = 0.6143 \times 10^{-6}$ m^2/s, the vortices will appear at a critical angular velocity, ω_c = 0.454 rad/s, which corresponds to a critical Reynolds number, $Re_c = U_1 d/\nu$, of 92.

The most precise experiments on the determination of the critical Taylor numbers for the onset of instability, for the case of outer cylinder at rest, are those of Donnelly (Chandrasekhar, 1961). In carrying out the experiments, the speed of rotation of the inner cylinder was slowly increased from the lowest setting, keeping the outer cylinder near its null position all the time. The corresponding critical value of the angular velocity, ω, at which the flow in the gap between the two cylinders becomes unstable (i.e. laminar Taylor vortex flow onsets), is given by

$$\omega_c = \nu \left(\frac{3390 \left(R_2^2 - R_1^2 \right)}{4 R_1^2 \left(R_2 - R_1 \right)^4} \right)^{0.5} \tag{2.7}$$

where R_2 is the radius of the outer cylinder ($R_2 = 30$ mm). The critical angular velocity obtained from Eq. (2.7) is $\omega_c = 0.475$ rad/s, which is equivalent to an average shear rate, $G_{avg} = 3\ \text{s}^{-1}$ (from Eq. (2.10)) and a critical Reynolds number, $Re_c = 97$. Though Eqs. (2.6) and (2.7) are derived from two separate experiments conducted by different researchers, the results obtained from these equations match each other fairly closely. Instabilities generated when the velocity is higher than the above value can be clearly observed.

It should be stressed that the first appearance of neutral vortices at the limit of stability in accordance with Eq. (2.5) and the persistence of amplified vortices at higher Taylor numbers does not in any way imply that the flow has become turbulent. On the contrary, even if the limit of stability is exceeded by a large margin, the flow remains well ordered and laminar. Turbulent flow does not become developed until Taylor number, and therefore, Reynolds number vastly exceeding the limit of stability are attained. For the case of flow between two rotating concentric cylinders of which the inner cylinder is in motion and the outer cylinder is at rest, Schlichting (1979) characterized three regimes of flow, each circumscribed by the Taylor number, in the following way:

$T_a < 41.3$: laminar Couette flow,

$41.3 < T_a < 400$: laminar flow with Taylor vortices,

$T_a > 400$: turbulent flow.

From the definition of Taylor number and for the present experimental conditions, the corresponding angular velocity for the flow to become turbulent is $\omega_t = 4.40$ rad/s (i.e. $G_{avg} = 24\ \text{s}^{-1}$).

The average shear rate used in this study ranged from 1.2 to 12.7 s^{-1}; therefore the flow was in laminar region, but not stable for $G > 3\ \text{s}^{-1}$.

For laminar flow, an estimate of the mean shear rate is given by

$$G_{avg} = \frac{1}{R_2 - R_1} \int_{R_2}^{R_1} g\left(r\right)\, dr\ , \tag{2.8}$$

where $g\ (r)$ is

$$g\left(r\right) = \frac{2\omega R_1^2 R_2^2}{\left(R_2^2 - R_1^2\right) r^2} \tag{2.9}$$

and r is the radial distance. Integrating expression (2.8) it can be obtained

$$G_{avg} = \frac{2\omega R_1 R_2}{R_2^2 - R_1^2} \tag{2.10}$$

where ω is the angular velocity of the inner cylinder. Under the present experimental conditions, since the inner cylinder is rotating and the outer one is at rest, the local shear rate will be largest at the inner wall and lowest at the outer wall and percent variation in shear rate between local G_{max} and G_{avg} is about 16%.

2.6 Population balance model

2.6.1 Theory

The floc formation is a dynamic process and the two main processes that control the floc size distribution at any particular time are aggregate growth by coagulation and aggregate size reduction by fragmentation or erosion. In general, the rates of these two processes are not equal, and the mean size of the flocs either increases or decreases depending on whether aggregation or fragmentation is dominant. The steady state is then determined as a dynamic equilibrium between aggregation and fragmentation. It is known that the rate of aggregation is dependent on the rate at which collisions occur and on the probability of cohesion after collision, while the rate of fragmentation is dependent upon fluid shear and the probability of fragmentation in response to the imposed hydrodynamic stress.

Since the pioneering work of Smoluchowski (1917), the physical processes that control kinetics of particle aggregation have been quite well known. During the initial stages of shear-induced aggregation, particle growth is dominant and the average floc size increases rapidly. As the flocs grow and hydrodynamic stresses become of the order of the yield stress of the aggregates, the fragmentation becomes significant. Particle growth kinetics models attempt to describe how the size distribution of particles arises from inter-particle collisions. To model the rate of change of number concentration of particles of a given size due to the processes of aggregation and fragmentation, Austin (1971) and Friedlander (1977) proposed the following expression:

$$\frac{dn_i}{dt}=\frac{1}{2}\sum_{j+k=i}\alpha\beta_{jk}(V_j,V_k)n_jn_k-n_i\sum_{k=1}^{n_{\max}}\alpha\beta_{ki}(V_k,V_i)n_k-B_in_i+\sum_{j=i+1}^{n_{\max}}\gamma_{i,j}B_jn_j \qquad (2.11)$$

where n_i is the number concentration of flocs of size i (meaning that a single floc contains i number of primary particles), α is the collision efficiency or the fraction of collisions that result in aggregation, and β_{jk} is the collision frequency between particles of volume V_j and V_k. B_i is the fragmentation or breakup rate of flocs of size i, and $\gamma_{i,j}$ is the breakup distribution function defining the volume fraction of the fragments of size i originating from j-sized particles. Here, the index n_{max} represents the largest particle size that will form fragments of size i upon breakup.

The first term on the right hand side of Eq. (2.11) is the number increase arising from aggregation of smaller j- and k-sized particles. The factor 1/2 is necessary so that each possible particle combination is not counted twice. The second term accounts for losses due to association of the present particle of size i with any other particle of any size. The third term describes the loss of particles of size i by fragmentation, and the fourth term defines the formation rate of particles of size i by the fragmentation of larger particles.

The distribution of particles observable at any time under constant shear rate is deemed to arise from an initial distribution, which at time zero, should consist of only fully dispersed primary particles. While the number of flocs of a certain size can be reduced by aggregation to larger flocs as well as by fragmentation and erosion processes, the number of primary particles decreases only through aggregation to flocs. Primary particles, in turn, can only result from breakage or erosion of larger flocs.

The solution is analytically intractable, but numerically accessible by lumping particles into size classes, or bins, covering the whole range of particle sizes according to a geometric scale. The resulting geometric sectionalization approach was shown to be an unbiased approximation of the general aggregation and fragmentation problems (Gelbard et al., 1980; Landgrebe and Pratsinis, 1990). Therefore, the size domain considered is divided into ranges or bins to ease computation. Equations are used to describe the particle number concentration within each bin, which is represented by a characteristic volume V_i that is the average volume of the sizes contained within that bin:

$$V_i = \frac{u_{i-1} + u_i}{2} \tag{2.12}$$

where u_i is the upper boundary volume of bin i and u_{i-1} is the lower boundary volume. V_i is also a function of the previous section V_{i-1}:

$$V_i = \frac{fV_{i-1}}{1-\varepsilon} \tag{2.13}$$

where f is the sectional spacing and ε is the porosity of aggregates. In this study, a numerical technique is used to simulate the evolution of the particle size with $f = 2$ (Hounslow et al., 1988; Kusters et al., 1993; Spicer and Pratsinis, 1996), and for this specific case, Eq. (2.11) can be rewritten as

$$\frac{dN_i}{dt} = \sum_{j=1}^{i-2} 2^{j-i+1}\alpha\beta_{i-1,j}N_{i-1}N_j + \frac{1}{2}\alpha\beta_{i-1,i-1}N_{i-1}^2 - N_i\sum_{j=1}^{i-1} 2^{j-i}\alpha\beta_{i,j}N_j$$

$$- N_i\sum_{j=i}^{i_{max}} \alpha\beta_{i,j}N_j - B_iN_i + \sum_{j=i+1}^{i_{max}} \Gamma_{i,j}B_jN_j \tag{2.14}$$

where $\Gamma_{i,j}$ is the breakup distribution function from Eq. (2.11) modified to conserve volume within the framework of the sectional mode for the particular case of $f = 2$, and N_i is the number concentration of aggregates having characteristic volume V_i. For mathematical convenience four binary interaction mechanisms are considered in Eq. (2.14), as shown in Table 2.2. Calculations are carried out using 31 bins, from $i = 1$ to $i_{max} = 31$. In order to represent the whole population of particles, the number of equations that

Table 2.2. Binary interaction mechanisms for aggregation

First four terms in R.S. of equation 2.14	Birth or death in interval i	Collisions between particles in intervals	
1	Birth	i-1	$1 \longrightarrow i-2$
2	Birth	i-1	i-1
3	Death	i	$1 \longrightarrow i-1$
4	Death	i	$i \longrightarrow \infty$

needs to be solved is the same as the number of classes or bins. Volume conservation has been imposed in the model, which means that when a particle of size class *i* aggregates with a particle of size class *j*, a particle of size class *k* is formed whose volume is

$$V_k = V_i + V_j \tag{2.15}$$

The minimum size corresponds to the size of the primary particle observed in experiments at the early stage (Oles, 1992; Kusters et al., 1993). The main objective of this work is to establish a population balance model that describes the kinetics of aggregation and fragmentation of asphaltene particles.

2.6.2 Closure of model parameters and description of model

2.6.2.1 Collision efficiency (α):

According to the Smoluchowski model, the colloidal particles in the flow field are assumed to follow the fluid streamlines and collide with each other when the distance between the streamlines is less than the sum of the particle radii (Masliyah, 1994). However, during a collision between two particles, the particles experience hydrodynamic and repulsive or attractive colloidal forces. Taking these forces into account, a factor is introduced, called the orthokinetic collision efficiency, α, which shows the relation between the number of particle collisions that actually lead to aggregation and the total number of particle collisions. It is also known as the inverse of the stability ratio, W, (i.e., $\alpha = 1/W$) (Fuchs, 1934; van de Ven and Mason, 1977; Mishra et al., 1998). For aggregation in a shear field, Smoluchowski's rate was derived by neglecting Brownian motion, gravitation effects, colloidal forces, and hydrodynamic interactions.

In the present calculations, collision efficiency was assumed to be equal to 1 ($\alpha =$ 1). A similar assumption was also made by Spicer and Pratsinis (1996) and Serra and Casamitjana (1998), and can be justified by the fact that large colloidal aggregates have porous and fractal structures. As was pointed out by Jiang and Logan (1991), a higher aggregation frequency exists due to the fractal nature of the actual flocs. Hence, a higher value of the collision frequency (β_{ij}) may compensate for the reduction in the collision efficiency (α) and consequently the product of α and β_{ij} takes care of the inherent inadequacy of this assumption. However, it is important to point out that α is a complex function of the surface properties of the particles, the structure or diameter of the aggregates, hydrodynamic effects, and the prevailing colloidal forces (Higashitani et al., 1982; Burban et al., 1989). Various expressions exist relating α to system variables such as ionic strength, electrolyte concentration, and viscous retardation of collisions (Zeichner and Schowalter, 1979; Mousa and van de Ven, 1991; Han and Lawler, 1992). However, these expressions are not directly applicable in the present study, since the present system deals with organic solvents and complex structure of the precipitated asphaltene aggregates.

Serra and Casamitjana (1998) reported that a constant value for α that is independent of the shear rate is a reasonable assumption because α depends on the particle interactions and their physical properties, but not on the flow field. However, van de Ven and Mason (1977) computed trajectories of particles incorporating hydrodynamic and colloidal interactions for orthokinetic flocculation and found a dependence of collision efficiency on shear rate. In the absence of any repulsive force, a rigorous hydrodynamic analysis together with an empirical representation of the retarded van der Waals attraction led them to derive values of the limiting collision efficiency, α_o, for a range of conditions. The results can be well represented by a simple empirical expression involving the Hamaker constant, A, and the characteristic wavelength, λ,

$$\alpha_o = f(\lambda / a) C_A^{0.18} \tag{2.16}$$

where $C_A = A/36\pi\mu G a^3$, and $f(\lambda/a)$ is a function of the dispersion wavelength (since retardation effects were included) and the particle radius, a, for which some numerical values were given by van de Van and Mason (1977). This expression shows that the collision efficiency decreases as the particle size and shear rate increase. The dependence on shear rate means that the collision frequency varies as $G^{0.82}$, rather than being linearly dependent on shear rate, as in the Smoluchowski original theory. Accordingly, as aggregates grow, especially at high shear rate, there will be a corresponding decrease in α_o, which will tend to restrict further aggregation. However, the collision rate increases for larger particles (Eq. 2.18), so that the aggregation rate may not be greatly affected.

At distances smaller than a particle radius, it becomes increasingly difficult for the liquid between particles to drain out of the gap. Since van der Waals attraction becomes significant at separations smaller than 100 nm, the two effects counteract each other to a considerable extent when there is no repulsive force between the particles (Elimelech et al., 1995). Moreover, asphaltene aggregates have rather open, porous structures and it is very likely that hydrodynamic resistance is greatly reduced when the approaching surfaces are permeable to the liquid. The liquid can pass through the pores of the aggregates. Torres et al. (1991) developed an expression for the collision efficiency of porous flocs by taking into account the reduction of hydrodynamic interaction and attractive forces on porous relative to impermeable particles. On the basis of their analysis of encounters between equally sized fractal flocs they concluded that, as the hydrodynamically equivalent sphere radius is smaller than the actual size of the aggregate, hydrodynamic retardation effect can be neglected in kinetic calculations of coagulation. This is equivalent to setting α equal to unity for all possible encounters. Hence, it can be inferred that assuming collision efficiency equal to one results in acceptable error.

2.6.2.2 Collision frequency ($\beta_{i,j}$):

Aggregation occurs when two or more particles collide and adhere. Except for very concentrated suspensions, simultaneous encounters between three or more particles can be ignored. In order for two particles to aggregate (flocculate), they must first be brought into close proximity by a transport mechanism. Transport mechanisms give neighboring particles different velocities and cause 'collisions'. Whether or not the particles remain attached to each other after a collision depends on the net interparticle forces. The differences in the velocities of neighboring particles may result from

Brownian motion, spatial velocity variations within the fluid (i.e., fluid shear), and sedimentation (i.e., differential settling).

At the level of approximation used by Smoluchowski, the collision frequency function due to Brownian motion is

$$\beta_{i,j} = \frac{2}{3}\frac{k_B T}{\mu}\frac{(d_i + d_j)^2}{d_i d_j} \tag{2.17}$$

The collision frequency function due to fluid shear is

$$\beta_{i,j} = \frac{G}{6}(d_i + d_j)^3 \tag{2.18}$$

The collision frequency function due to differential settling is

$$\beta_{i,j} = \frac{\pi g}{72\mu}(d_i + d_j)^2 \left|\Delta\rho_i d_i^2 - \Delta\rho_j d_j^2\right| \tag{2.19}$$

where g is the acceleration due to gravity and $\Delta\rho_i = \rho_i - \rho$ is the effective density, which is the difference in density between the particle of size class i and the liquid medium.

The above kernel functions (Masliyah, 1994) can be used to assign relevant collision frequencies to different particle sizes and mass transport conditions; accordingly, different mechanisms are important at different stages of the flocculation process. Usually, if the particles are of submicrometer size, Brownian motion is appreciable. However, as the particles grow larger, Brownian aggregation becomes less important and shear-induced aggregation (or, orthokinetic aggregation) and differential settling take over (Levich, 1962). According to Logan and Wilkinson (1990), Brownian motion can be important for particles with diameters smaller than 1 μm, shear rate can be important in the range 1–40 μm, and differential settling may dominate for particles larger than 40 μm. However, the dominance of a particular collision mechanism depends not only on the particle size, but also strongly on the density difference between particle and liquid medium as well as intensity of the shear. Han and Lawler (1992) observed that for both orthokinetic aggregation and differential settling, the collision frequency was a strong function of particle size, dominated by the diameter of the larger of the two particles. The authors extended the analysis to compare collisions between all pairs of particles with sizes in the range 1–1000 μm. For a range of values of G, the authors found that differential settling was dominant only when one particle was quite large compared to the other. In all other cases, orthokinetic aggregation was the dominant mechanism. For the present study, the orthokinetic collision frequency (Eq. (2.18)) was used for the calculations. Other collision processes of Brownian motion and settling are deemed negligible to shear flow.

2.6.2.3 Fragmentation rate (B_i):

The fragmentation of aggregates is caused by hydrodynamic stresses. The most common breakage mechanisms are: (a) erosion of primary particles or small fragments from the floc surface, and (b) "bulgy deformation", rupture, or splitting of the floc (Pandya and Spielman, 1982; Chen et al., 1990). Erosion releases loosely bound particles from the surface of a compact floc having strong attachment force within the floc (Yeung, Gibbs, and Pelton, 1997). Splitting arises from pressure differences on the opposite sides of the floc that induce a shearing type of fragmentation (Parker et al., 1972).

The larger an aggregate becomes, the more susceptible it is to breakage. The fragmentation rate is given as a function of particle volume by Kapur (1972):

$$B_i = bV_i^d \tag{2.20}$$

where $d = 1/3$. This is consistent with the theoretical expectation that breakup rate is proportional to floc diameter (Boadway, 1978) and b is the breakup rate coefficient for shear-induced fragmentation (Pandya and Spielman, 1982):

$$b = b'G^y \tag{2.21}$$

where y is a constant inversely proportional to the aggregate strength and b' is a proportionality constant determined from data fitting. This type of power law relationship between aggregate size and shear rate is commonly used to correlate experimental (Parker et al., 1972) and simulation results (Chen et al., 1990).

2.6.2.4 Breakup distribution function ($\Gamma_{i,j}$):

Different types of breakup distribution functions ($\Gamma_{i,j}$) can be assumed for the sectional description of aggregation and fragmentation. Here, a binary breakage function is examined that describes the breakup of an aggregate into two parts of equal size (Chen et al., 1990).

$$\Gamma_{i,j} = \frac{V_j}{V_i}; \quad \text{binary breakage, so } j = i+1 \tag{2.22}$$

The expression for $\Gamma_{i,j}$ in Eq. (2.22) is only valid for f being equal to 2. All the breakage parameters in this model best describe fragmentation by splitting. Though splitting is less likely energetically, spatial velocity variations lead to a pressure gradient across the floc, making the splitting mode more significant than erosion for branched flocs that tend to divide into equal fragments (Yeung and Pelton, 1996). Higashitani et al. (2001) proposed a model in which the effective particle surface for the hydrodynamic drag force and the disturbance of neighboring particles in the flow field are taken into account to simulate the deformation and breakup process of various aggregates. The simulation confirmed the previous experimental observations that aggregates in shear fields are split into smaller fragments, but not eroded to individual particles from the aggregate surface.

2.6.2.5 Porosity of the aggregates (ε):

Substantial research indicates that flocs formed by aggregation may have a fractal structure. Unlike fractals that have increasing porosity as their size increases, Euclidean objects have a constant porosity (Meakin, 1988; Jiang and Logan, 1991; Gregory, 1997). Since fractal structure was not incorporated in the model, a constant porosity (ε) is assumed for aggregate formation from primary particles. For an aggregate made up of n spherical primary particles each of volume V_1, the porosity can be derived as

$$\varepsilon = 1 - \frac{nV_1}{V_a} \tag{2.23}$$

where V_a is the aggregate volume. In this model, the porosity of the aggregates, ε is used as an adjustable parameter and it can be expressed as

$$\varepsilon = -aG + c \tag{2.24}$$

where a and c are proportionality constants that are determined from data fitting. This type of linear relationship between aggregate porosity and shear rate can be used to correlate experimental and simulation results.

Eqs. (2.13, 2.18, 2.20 – 2.22, 2.24) provide closure to the population balance equation (Eq. (2.14)). The sectional model was solved numerically by a finite difference scheme using RK15s, an ordinary differential equation solver.

2.7 Results and Discussion

2.7.1 Effect of shear on the growth of asphaltene particles

Figure 2.3 shows the kinetics of asphaltene growth in terms of number mean aggregate diameter as a function of time for different shear rates. The characteristic dimension of an aggregate is the projected area diameter, $d_a = \sqrt{\frac{4A_a}{\pi}}$, where A_a is the projected area derived from image analysis. The number mean projected area diameter, d_{avg}, is defined as

$$d_{avg} = \frac{\sum_{i=1}^{i=k} \eta_i d_i}{\sum_{i=1}^{i=k} \eta_i} \tag{2.25}$$

where d_{avg} is a function of time, η_i is the number of particles counted in the i-th bin, d_i is the middle of the size range of the i-th bin, and k is the total number of bins. The number mean diameter is a good parameter to represent the progress of aggregation process.

Different shear rates (G) are used, in the range of 1.2–12.7 s^{-1}. A characteristic time-dependent behavior is found for all experiments. For all values of G, the aggregate size increases rapidly with time, consistent with the results of previous experimental studies (Oles, 1992; Spicer and Pratsinis, 1996). As explained earlier, due to the limited resolution of the microscope-camera system, particles with size around 30 μm will be considered to be the "primary" particles from which aggregation starts. The size and concentration of primary particles also defines our initial conditions for the population balance.

As shown in Fig. 2.3, the growth of the polydispersed asphaltenes primary particles in the suspension appears to be a strong function of the shear rate. The rate of growth of the flocs is greater at higher shear, which can explain the earlier appearance of primary flocs of the same size, about 30 μm, at the higher shear, as well as the by slight change in the slopes of the size versus time curves. As the shear rate is increased, the collision rate increases. Consequently, the aggregate mean size increases more rapidly and the slopes become steeper. For shear rates higher than 8.4 s^{-1}, not much growth is observed. At times greater than 10 to 25 min (depending on the shear rate), the aggregates pass through a maximum size. During the growth phase of the flocs, as the concentration of large flocs increases, breakup becomes more significant. In addition, it is found that the system reaches maximum size state more rapidly when the shear rate is increased, with the size of the aggregates being smaller. This suggests that, as the shear rate is increased, the flocs become more likely to break due to the hydrodynamic shear force. Similar behavior is supported by other studies, such as Burban et al. (1989), Oles (1992), Spicer and Pratsinis (1996), and Serra et al. (1998). After this stage, the mean aggregate size starts to decline until it reaches a steady state size. However, this behavior was initially thought to be a mere artifact due to differential settling of the flocs beyond these times. In such a case, since the flocs are denser than the liquid medium, the larger flocs would settle out of the observation region after certain time, leaving only the smaller aggregates. In order to test this hypothesis, the cylinders in the Couette device were made twice as long. If the rates of aggregation and fragmentation become equal after the flocs attain the maximum size, the longer cylinder should provide a broader maximum size plateau before the observed size would start declining solely due to settling. However, if a similar curve is found as that in Fig. 2.3, it should prove that aggregation is overtaken by fragmentation or, possibly, restructuring.

In Figures 2.4(a) and 2.4(b), the mean aggregate size as a function of time is shown for the two cylinders under the same experimental conditions, i.e., shear rate, asphaltenes particle concentration, and toluene-to-heptane ratio in the solution are kept the same. The mean aggregate size variations with time are found to be similar when the observation points are located 15 cm (200-mm cylinder) and 35 cm (400-mm cylinder) below the top surface in the cylinders. This means that, regardless of where the measurements are taken, what is observed is the net result of breakup-restructuring and aggregation, and not due to settling. Hence, the observed maximum in aggregate size is not an artifact of the experimental apparatus. The maximum in the aggregate size can be explained as a result of breakage-restructuring of the large flocs produced initially to form more compact structures. Under constant shearing, large open flocs become more compact as the flocs restructure or fragment and reform more durable structures (Bouyer et al., 2001; Spicer et al., 1996).

2.7.2 Effect of asphaltene particles concentration on floc growth

Figure 2.5 shows the effect of particle concentration on the growth of asphaltenes flocs. All three experiments are carried out at a shear rate of 2.5 s^{-1} and toluene-to-heptane ratio of 1:7. It can be observed from the figure that a higher particle concentration corresponds to a smaller relaxation time for visible floc formation and increases the initial aggregation rate (observed from the initial slopes of the curves) by decreasing the average distance between particles, thus reducing the characteristic time between collisions. The dynamic balance between the floc growth and breakage determines the average floc size that is attained at steady state. Increasing φ leads to an increase in the aggregation rate to a much greater extent than the fragmentation rate and consequently, a larger steady state floc size is reached. However, no significant difference in steady state floc size is observed for asphaltenes particle concentrations of 5.3 and 4.1 mg/L. A larger φ also results in a faster attainment of the maximum floc size than at lower asphaltene concentrations because of the accelerated kinetics of both aggregation and fragmentation.

Yudin et al. (1998) investigated the kinetics of asphaltene aggregation in toluene and *n*-heptane mixtures with dynamic light scattering. They reported a CMC value of about 3 g/L for asphaltenes in toluene and varied the concentration of asphaltenes in toluene from 1 to 10 g/L. The aggregation kinetics was measured upon adding the near precipitation threshold concentration of *n*-heptane. Two types of kinetic behaviors were observed. The noted size range for asphaltene aggregates was less than 5 microns. At a concentration of asphaltenes in toluene lower than the CMC, the aggregates were formed from "asphaltene molecules" and the character of the aggregation was solely determined by diffusion-limited aggregation (DLA). Above the CMC, the aggregates were formed from micelles and reaction-limited aggregation (RLA) took place at least in the initial stage of particle growth. As the asphaltene concentration increased, the micelles became larger and the potential barrier became higher. That is why the RLA rate slowed down with increasing asphaltene concentration, which was exactly opposite of DLA process.

In the present study all asphaltene solutions in toluene are dilute, less than 1 g/L, i.e. well below the CMC. Similarly as in the case of DLA process, higher aggregation rate and larger floc size are observed for higher asphaltene concentrations. Under the present conditions, an excess of heptane is added to destabilize the system. Therefore, the kinetics is governed by hydrodynamic shear-induced aggregation.

2.7.3 Effect of solvent composition on the growth of asphaltene particles

Figure 2.6 represents the effect of the ratio of toluene to *n*-heptane in the solution on the growth rate of asphaltene flocs. The shear rate was set at 2.5 s^{-1} and the initial asphaltenes particle concentration was 62.5 mg/L for all experiments. A lower ratio of toluene to *n*-heptane means lower solubility of asphaltenes and, accordingly, greater quantities of precipitated asphaltenes are observed at the end of an experiment. The amount of precipitate, which is always significantly less than the initial amount added to the solution, is used to determine the particle concentration in the solution (Table 2.1). Hence, a lower toluene-to-heptane ratio results in higher particle concentration in the solution. Therefore, a behavior similar to that in Fig. 2.5 is found, i.e., lower toluene-to-heptane ratio provides faster aggregation rate. Though a large variation in the maximum aggregate size is observed, there is a smaller difference in the steady state floc size for different solvent compositions. Hence for a fixed stirring speed, increasing the ratio of heptane in the solution greatly enhanced the aggregation rate and marginally enlarged the steady state floc size.

2.8 Theoretical Modeling

2.8.1 Determination of number concentration for primary asphaltene particles

During an experimental run, the first few images captured at the beginning (or, at that particular time) were used to provide the initial size distribution of the asphaltene particles. At the end of the experiment, the asphaltenes aggregates were filtered and dried in a vacuum oven dryer at 23 kPa absolute pressure and 22°C (room temperature) to determine the mass of the precipitated solid asphaltenes particles. Assuming a density of 1200 kg/m^3 for solid asphaltenes (Yarranton, 1997), the volume of the primary asphaltenes particles was calculated. Since the well-mixed suspension is homogeneous at the beginning, the size distribution of primary particles from captured images is assumed to be uniform throughout the suspension. Hence, the initial number concentration of primary asphaltene particles in the solution can be calculated (see Appendix A).

2.8.2 Comparison of Model and experiment

Given an initial distribution of particles, Eq. (2.14) was solved using a finite difference scheme for each of the 31 size classes until a steady state size is reached. It can be observed from Eqs. (2.13, 2.18, 2.20 – 2.22, 2.24) that, except for the breakup rate coefficient, b and the porosity of the aggregates, ε, other model parameters (i.e., V_i, d_i, N_i, $\beta_{i,j}$, and $\Gamma_{i,j}$) can be obtained from experimental conditions. Simulations were conducted for different values of G, φ, and T:H.

In Fig. 2.7, model predictions for asphaltenes aggregate growth as a function of time for various values of shear rates are represented for the asphaltenes volume fraction, $\varphi = 10.8\times10^{-6}$, corresponding to an initial number concentration of asphaltene particles equal to $N_1 = 3.0\times10^4$, $N_2 = 1.8\times10^4$, and $N_3 = 0.5\times10^4$ cm^{-3} (see Appendix A). In the model, the porosity of the aggregates, ε, and the breakup coefficient, b, are used as adjustable parameters and it is intuitive to represent the variations of ε and b with shear rate, G. Values of ε and b are determined by matching the model predicted floc mean diameter with the experimental data for the aggregation of primary asphaltene particles at various shear rates, G = 1.2–12.7 s^{-1}. In Figs. 2.8 and 2.9, the variations of the fitting parameters, b and ε, with G are represented. In this case, a power relationship, $b = b'G^y$, and a linear relationship, $\varepsilon = -aG+c$, provide a good fit for the experimental data. The parameters b', y, a, and c are determined by regression analysis of ε and b as functions of G. In Fig. 2.7, the results predicted by the model with $b' = 2\times10^{-5}$, $y = 0.61$, $a = 0.07$, and $c = 0.94$ are compared to the experimental data over the whole range of G.

In Fig. 2.10, model predictions with the predetermined fitting parameters for asphaltenes aggregate growth at different particle concentrations are represented with and without breakup. For the case of no breakage, b is set to zero. Without breakage, asphaltene aggregates continue to grow monotonically. Whereas, with breakage, a maximum in the aggregate diameter versus time curve is observed as a result of the competition between aggregate growth and breakage. It can be observed from Fig. 2.10 that fragmentation greatly affects the average size of the flocs, which is understood from the greater difference between the maximum floc size predicted by the model without breakup and the steady state floc size with breakup.

For the case of asphaltene concentration of 10.3 mg/L, there is the largest difference between the attained maximum aggregate size and the steady state size due to floc fragmentation. Whereas in the case of a lower asphaltenes concentration, this effect is less noticeable. Hence, it can be inferred that by reducing the asphaltenes concentration in the solution, the strength of the flocs is increased and they become less susceptible to breakage. Though restructuring of the aggregates can also explain the presence of the maximum size, the present PBE model did not include any term describing restructuring and only fragmentation was able to describe the time evolution of the number mean aggregate size very well.

In Fig. 2.11, model predictions including breakup and without breakup are represented for asphaltene aggregates growth at different solvent compositions. Again for the case of no breakage, $b = 0$. It is clear from the plots of both Figs. 2.10 and 2.11 that the initial aggregate growth is not affected by breakage where the mean aggregate diameter increases with time at the same rate whether aggregate breakage is present or not. However, the steady state aggregate size is affected by breakage. This is especially true when there is a significant maximum in the aggregate size. It can be observed from model results that the solvent composition has a dominant effect on the kinetics of floc growth and the magnitude of aggregate breakup, but no significant impact on the final steady state floc size (see Fig. 2.11).

The two parameters b' and y can be related to the strength of the floc, which depends on flocculants type and concentration, surface properties of the primary particles, floc structure, and suspension medium. All of these factors need to be related to the values of b' and y in order to provide a more mechanistically based description of the floc breakup kinetics. This work also confirms that a simple power law description (Eq. 2.21) is a useful kinetic model of floc breakup. However, the breakup rate coefficient, b, is found to be independent of asphaltene particles volume fraction, φ, and toluene-to-heptane ratio in the solution, T:H, at least for present conditions. In the experimental regime, the range for particle volume fraction is about $3.4–10.8\times10^{-6}$, and the solution can be considered very dilute. Hence, *b* is found to be constant with φ though the number of collisions and the rate of nonlinear breakup increase with higher φ.

On the other hand, the porosity of the aggregates, *ε*, is found to be weakly dependent on φ and T:H. As mentioned earlier, the ratio of toluene-to-heptane (T:H) in the solvent determines the solubility of asphaltenes particles. At lower toluene-to-heptane ratio, asphaltenes become less soluble in the solution and, therefore, asphaltene particles volume fraction (φ) increases in solution. The model takes into account the effect of T:H in the solution as the effect of φ in the solution. The variation in φ and T:H changes the initial primary particles concentration and sizes in the solution and are determined experimentally by image analysis. This gives the initial condition of population balance model. At higher φ values in the solution, more large aggregates are formed due to higher number of collisions and the average aggregate size is higher (Figs. 2.10 and 2.11). Moreover from these figures, it is observed that the large aggregates are more susceptible to breakage due to their loosely bound structures. Accordingly, a higher porosity is found with increasing φ in the solution (Fig. 2.12).

2.9 Conclusions

This work provides new information on the kinetics of asphaltenes flocculation in the model system. It demonstrates the use of a population balance approach to describe the flocculation phenomena in organic solvents. An experimental study was carried out on the effects of shear rate, particle concentration, and solvent type or composition during aggregation of primary asphaltene particles. The dynamic evolution of asphaltene aggregates growth was monitored by image analysis of the digitized images. Asphaltenes seem to be unique in terms of forming a maximum in the floc size evolution. After a certain period of time, the floc size distribution reached a steady state size distribution as a result of the competition between aggregation and fragmentation. Increased shear enhanced the aggregation rate as determined from image analysis. The average steady state floc size always decreased with increasing shear. Increasing the asphaltenes concentration or reducing the ratio of toluene to heptane in the solution increased the floc growth rate and the steady state floc size.

A population balance model is used in order to understand the dynamics of the aggregation/fragmentation process. The model uses two fitted parameters: the porosity of the aggregates, ε, and the breakup coefficient for shear fragmentation, b. Both the parameters, b and ε, depend on flow characteristics (i.e. shear rate, G). The relations, $b = b'G^y$ and $\varepsilon = -aG+c$, fit well with the experimental data. The value of b was found independent of asphaltene particle volume fraction (φ) in the experimental regime for very dilute suspensions, whereas, ε was found to increase with an increase in the φ values due to very loosely bound structure of asphaltene aggregates.

From commercial viewpoint, the present study provides information on the significance of shear rate, particle concentration and solvent composition in asphaltenes floc formation, which are essential for proper process design and material handling.

2.10 Nomenclature

a	particle radius (m)
A	Hamaker constant (J)
A_a	aggregate projected area (μm^2)
b	breakup coefficient for shear fragmentation
B_i	fragmentation or breakup rate of flocs of size i (s^{-1})
C_A	empirical expression involving the Hamaker constant, A, and the characteristic wavelength, λ ($C_A = A/36\pi\mu Ga^3$)
CMC	critical micelle concentration (gL^{-1})
d	inner Couette diameter (mm)
d_a	aggregate projected area diameter (μm)
d_{avg}	number mean projected area diameter (μm)
d_i	average diameter of the particle sizes contained within bin i (μm)
DLA	diffusion-limited aggregation
D_0	diffusion coefficient of a particle of radius a_0 (m^2/s)
f	sectional spacing
g	acceleration due to gravity (m/s^2)
G	shear rate (s^{-1})
G_{avg}	mean shear rate (s^{-1})
G_{max}	maximum shear rate at the rotating cylinder wall of Couette device (s^{-1})
h	width of the gap between the cylinders in Couette device (mm)
i_{max}	number of classes or bins
k_B	Boltzmann constant, $k_B = 1.381 \times 10^{-23}$ J/K
N_i	number concentration of aggregates in bin i having characteristic volume V_i (# / cm^3)
N_{total}	total number concentration of aggregates in all bins (# / cm^3)
n	number of spherical primary particles each of volume V_1 in the aggregate
n_i	number concentration of flocs of size i (meaning that a single floc contains i number of primary particles)
n_{max}	the largest particle size that will form fragments of size i upon breakup

Pe	Peclet number, $Pe=\frac{6\pi\mu G a_o^3}{k_B T}$
r	radius
R_1	radius of the inner cylinder (mm)
R_2	radius of the outer cylinder (mm)
Re	Reynolds number, $Re = U_i d/\nu$
Re_c	critical Reynolds number
RLA	reaction-limited aggregation
t	time, s
Δt	time interval
T	absolute temperature (K)
T:H	toluene-to-heptane ratio in solvent mixtures (or, solvent composition)
T_a	Taylor number
u	peripheral velocity (m/s)
U_1	peripheral velocity of the inner cylinder (m/s)
u_i	upper boundary volume of bin i
u_{i-1}	lower boundary volume of bin i
U_o	flow velocity of a particle of radius a_o (m/s)
V_1	volume of a spherical primary particle (μm^3)
V_a	aggregate volume (μm^3)
V_i	average volume of the particle sizes contained within bin i
W	stability ratio

Greek

φ	solid particle contents (i.e., volume fraction of particles)
ε	porosity of the aggregates
μ	viscosity of the suspending liquid (Pa·s)
ω	angular velocity of the inner cylinder (rad/s)
ν	kinematic viscosity of the fluid (m^2/s)

α	collision efficiency or the fraction of collisions that result in aggregation
α_o	limiting collision efficiency
λ	characteristic wavelength
ρ	density of the fluid (kg/m^3)
ω_c	critical angular velocity (rad/s)
η_i	number of particles counted in the *i*-th bin
ρ_i	density of the particle of size class *i* (kg/m^3)
$\gamma_{i,j}$	breakup distribution function defining the volume fraction of the fragments of size *i* originating from *j*-sized particles
$\Gamma_{i,j}$	breakup distribution function
β_{ij}	collision frequency between particles of volume V_i and V_j (cm^3/s)
ω_t	angular velocity for the flow to become turbulent (rad/s)
$f(\lambda/a)$	a function of the dispersion wavelength (including retardation effects)

2.11 Literature Cited

Adler, P. M. (1981). Heterocoagulation in shear flow. *J. Colloid Interf. Sci.*, 83(1), 106.

Andersen, S. I. and K. S. Birdi. (1991). Aggregation of Asphaltenes as Determined by Calorimetry. *J. Colloid Interf. Sci.*, 142, 497.

Austin, L. G. (1971). A Review: Introduction to the Mathematical Description of Grinding as a Rate Process. *Powd. Tech.*, 5, 1.

Boadway, J. D. (1978). Dynamics of Growth and Breakage of Alum Floc in Presence of Fluid Shear. *J. Env. Eng. Div.: Proc. ASCE*, 104, 901.

Bouyer, D., A. Line, A. Cockx, and Z. Do-Quang. (2001). Experimental Analysis of Floc Size Distribution and Hydrodynamics in a Jar-Test. *Chem. Eng. Res. Des.*, 79, 1017.

Burban, P. Y., W. Lick, and J. Lick. (1989). The Flocculation of Fine-Grained Sediments in Estuarine Waters. *J. Geophys. Res.*, 94, 8323.

Burya, Y. G., I. K. Yudin, V. A. Dechabo, V. I. Kosov, and M. A. Anisimov. (2001). Light-scattering Study of Petroleum Asphaltene Aggregation, *Applied Optics*, 40 (24), 4028.

Chadrasekhar, S. (1961). *Hydrodynamic and Hydromagnetic Stability*. Clarendon, Oxford, 330.

Chen, W., R. R. Fisher, and J. C. Berg. (1990). Simulation of Particle size Distribution in an Aggregation-Breakup Process. *Chem. Eng. Sci.*, 45, 3003.

Cummins, P. G., E. Staples, B. Millen, and J. Penfold. (1990). A Couette Shear Flow Cell for Small-Angle Neutron Scattering Studies. *Meas. Sci. Technol.*, 1, 179.

Drushel, H. V., and W. W. Schultz. (1980). *Second Chemical Congress of North America*.

Elimelech, M., J. Gregory, X. Jia, and R. A. Williams. (1995). *Particle Deposition and Aggregation: Measurement, Modelling and Simulation*, Butterworth-Heinemann Ltd, Oxford.

Friedlander, S. K. (1977). *Smoke, Dust, and Haze*, Wiley, New York.

Gelbard, F., Tambour, Y., & Seinfeld, J. H. (1980). Sectional representations for simulating aerosol dynamics. *Journal of Colloid and Interface Science, 76 (2),* 541-556.

Gregory, J. (1997). The Density of Particle Aggregates. *Wat. Sci. Technol.*, 36 (4), 1.

Gregory, J., and Li, G. B.. (1991). Flocculation and Sedimentation of High-Turbidity Waters. *Water. Res.*, 25 (9), 1137.

Han, M. Y., and D. F. Lawler. (1992). The (relative) Insignificance of G in flocculation. *J. Am. Water Works Assoc.*, 84, 79.

Higashitani, K., Iimura, K., & Sanda, H. (2001). Simulation of deformation and breakup of large aggregates in flows of viscous fluids. *Chemical Engineering Science*, 56, 2927-2938.

Higashitani, K., K. Yamauchi, Y. Matsuno, and G. Hosokawa. (1982). Kinetic Theory of Shear Aggregation for Particles in a Viscous Fluid, *J. Chem. Eng. Japan*, 15, 299.

Hounslow, M. J., R.L. Ryall, and V. R. Marshall. (1988). A Discretized Population Balance for Nucleation, Growth, and Aggregation. *AIChE J.*, 34, 1821.

Jiang, Q., and B. E. Logan. (1991). Fractal Dimensions of Aggregates Determined from Steady state Size Distributions. *Environ. Sci. Technol.*, 25 (12), 2031.

Kapur, P. C. (1972). Self-Preserving Size Spectra of Comminuted Particles. *Chem. Eng. Sci.*, 27, 425.

Kusters, K. A., S. E. Pratsinis, S. G. Thoma, and D. M. Smith. (1993). Ultrasonic Fragmentation of Agglomerate Powders. *Chem. Eng. Sci.*, 48, 4119.

Landgrebe, J. D., and S. E. Pratsinis. (1990). A Discrete-Sectional Model for particulate production by Gas-Phase Chemical Reaction and Aerosol Aggregation in the Free-Molecular Regime. *J. Colloid Interf. Sci.*, 139, 63.

Long, R. B. (1981). The Concept of Asphaltenes. *Adv. Chem. Ser.*, 195, 48.

Long, Y., T. Dabros, and H. Hamza. (2002). Stability and Settling Characteristics of Solvent-Diluted Bitumen Emulsions, *Fuel*, 81, 1945.

Lord Rayleigh. (1913). On the stability or instability of certain fluid motions. *Scientific papers,* 6, 197-204.

Mack, C., "Colloid Chemistry of Asphalts," *J. Phys. Chem.*, **36**, 2901 (1932).

Masliyah, J. H. (1994). *Electrokinetic Transport Phenomena*. Pub. No. 12, AOSTRA, Edmonton.

Meakin, P. (1988). Fractal Aggregates. *Adv. Coll. Int. Sci.*, 28, 249.

Mishra, V., S. M. Kresta, and J. H. Masliyah. (1998). Self-Preservation of the Drop Size Distribution Function and Variation in the Stability Ratio for Rapid Coalescence of a Polydisperse Emulsion in a Simple Shear Field. *J. Colloid Interf. Sci.*, 197, 57.

Mousa, H., and T. G. M. van de Ven. (1991). Stability of Water-In-Oil Emulsions in Simple Shear Flow 1.Determination of the Orthokinetic Coalescence Efficiency. *Colloids Surf.*, 60, 19.

Oles, V. (1992). Shear-Induced Aggregation and Breakup of Polystyrene Latex Particles. *J. Colloid Interf. Sci.*, 154, 351.

Pandya, J. D. and L. A. Spielman. (1982). Floc Breakage in Agitated Suspensions: Theory and Data Processing Strategy. *J. Colloid Interf. Sci.*, 90, 517.

Parker, D. S., W. J. Kaufman, and D. Jenkins. (1972). Floc Breakage in Turbulent Flocculation processes. *J. San. Eng. Div.: Proc. ASCE*, 98, 79.

Pfeiffer, J. P., and R. N. J. Saal. (1940). Asphaltic Bitumen as Colloid System. *J. Phys. Chem.*, 44, 139.

Rogacheva, O. V., R. N. Gimaev, V. Z. Gubaidullin and D. K. Khakimov. (1980). Study of Surfactant Activity of Asphaltenes in Petroleum Residues. *Kolloid. Zh.*, 42 (3), 586.

Schlichting, H., Gersten, K. (1979). *Boundary-layer theory.* Springer-Verlag Berlin Heidelberg, New York, pp 503.

Serra, T., and X. Casamitjana. (1998). Effect of the Shear and Volume Fraction on the Aggregation and Breakup of Particles. *AIChE J.*, 44 (8), 1724.

Shue, E. Y., M. M. De Tar, D. A. Storm, and S. J. DeCanio. (1992). Aggregation and Kinetics of Asphaltenes in Organic Solvents, *Fuel*, 71, 299.

Sheu, E. Y., and D. A. Storm. (1995). Colloidal Properties of Asphaltenes in Organic Solvents. in *Asphaltenes - Fundamentals and Applications*, edited by Sheu, E. Y., and Mullins, O. C., Plenum Press, New York.

Smoluchowski, M. (1917). Versuch Einer Mathematischen Theorie der Koagulations Kinetis Kolloider Losungen. *Z. Physik. Chem.*, 92, 129.

Speight, J. G. (1990). *Fuel Science and Technology Handbook,* Marcel Dekker, New York, pp 1193.

Spicer, P. T., and S. E. Pratsinis. (1996). Coagulation and Fragmentation: Universal Steady State Particle Size Distributions. *AIChE J.*, 42, 1612.

Taylor, G. I. (1935). Statistical theory of turbulence, parts 1-4. *Proceedings royal society London A,* 151, 421-478.

Torres, F. E., Russel, W. B., and Schowalter, W. R. (1991). Floc structure and growth kinetics for rapid shear coagulation of polystyrene colloids. *J. Colloid Interf. Sci.*, 142, 554-574.

van de Ven, T. G. M., and S. G. Mason. (1977). The microrheology of colloidal dispersions. VII. Orthokinetic doublet formation of spheres. *Colloid & Polymer Science,* 255, 468-479.

Van Durren, F. A. (1968). Defined Velocity Gradient Model Flocculator. *J. Sanitary Eng. Div.*, 4, 6076.

van Smoluchowski, M. (1917). Versuch einer mathematischen theorie der koagulations kinetik kolloider lösungen. *Z. Physik. Chem.*, 92, 156.

Yarranton, H. W. (1997). *Asphaltene Solubility and Asphaltene Stabilized Water-in-Oil Emulsions*. Ph.D. Thesis, Department of Chemical and Materials Engineering, University of Alberta, pp 66.

Yen, T. F., and G. V. Chilingarian (editor), (1994). *Asphaltenes and Asphalts, 1*, Elsevier, Amsterdam .

Yeung, A., Gibbs, A., and Pelton, R. (1997). Effect of Shear on the Strength of Polymer-Induced Flocs. *J. Colloid Interf. Sci.*, 196, 113-115.

Yeung, A., and Pelton, R. (1996). Micromechanics: A New Approach to Studying the Strength and Breakup of Flocs. *J. Colloid Interf. Sci.*, 184, 579-585.

Yudin, I. K., G. L. Nikolaenko, E. E. Gorodetskii, E. L. Markhashov, V. A. Agayan, J. V. Sengers and M. A. Anisimov. (1998). Crossover Kinetics of Asphaltene Aggregation in Hydrocarbon Solutions, *Physica A*, 251, 235.

Zeichner, G. R., and Schowalter, W. R. (1979). Effects of hydrodynamic and colloidal forces on the coagulation of dispersions. *Journal of Colloid and Interface Science*, 71, 237.

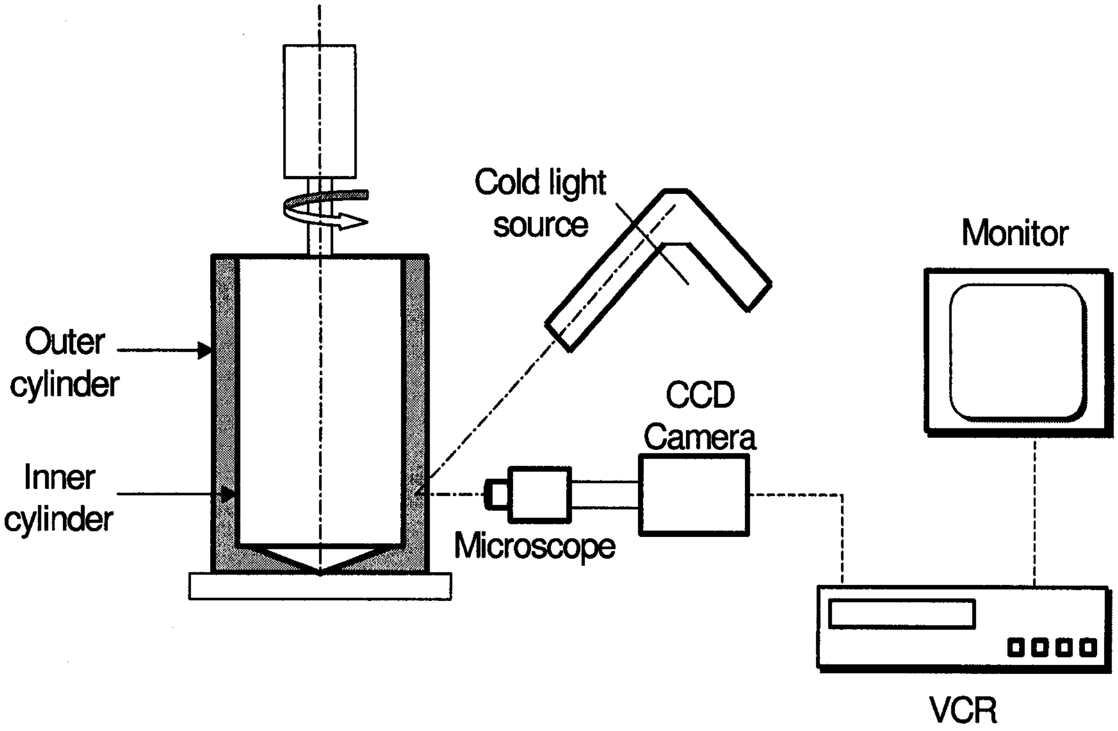

Figure 2.1. Schematic of the experimental set-up.

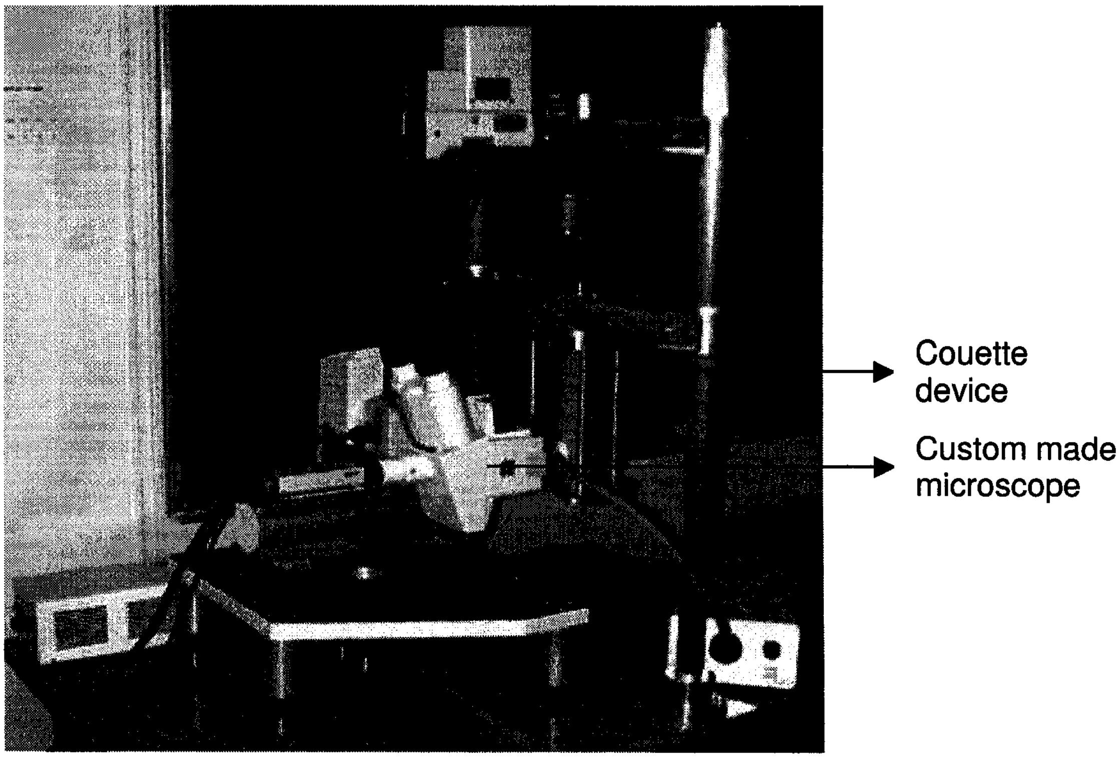

Figure 2.2. Photograph of the Couette device.

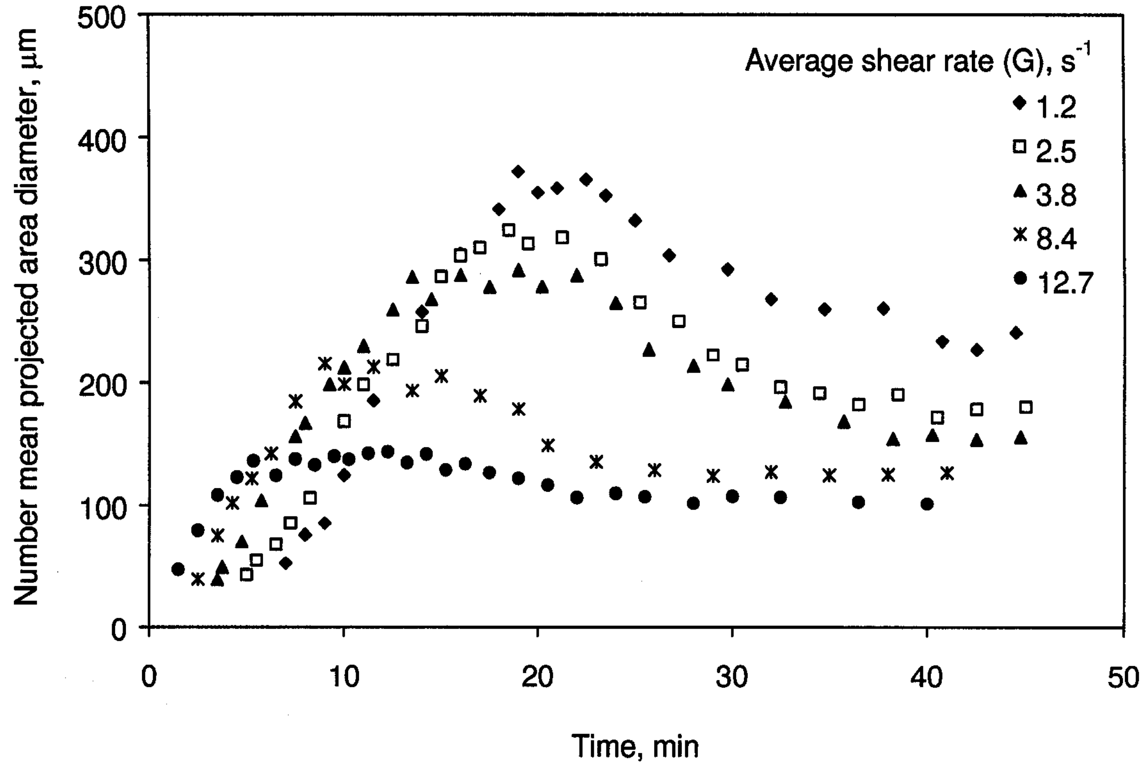

Figure 2.3. Kinetics of asphaltenes aggregation under shear at toluene-to-heptane solvent ratio (T:H) of 1:15 and particle concentration of 12.8 mg/L.

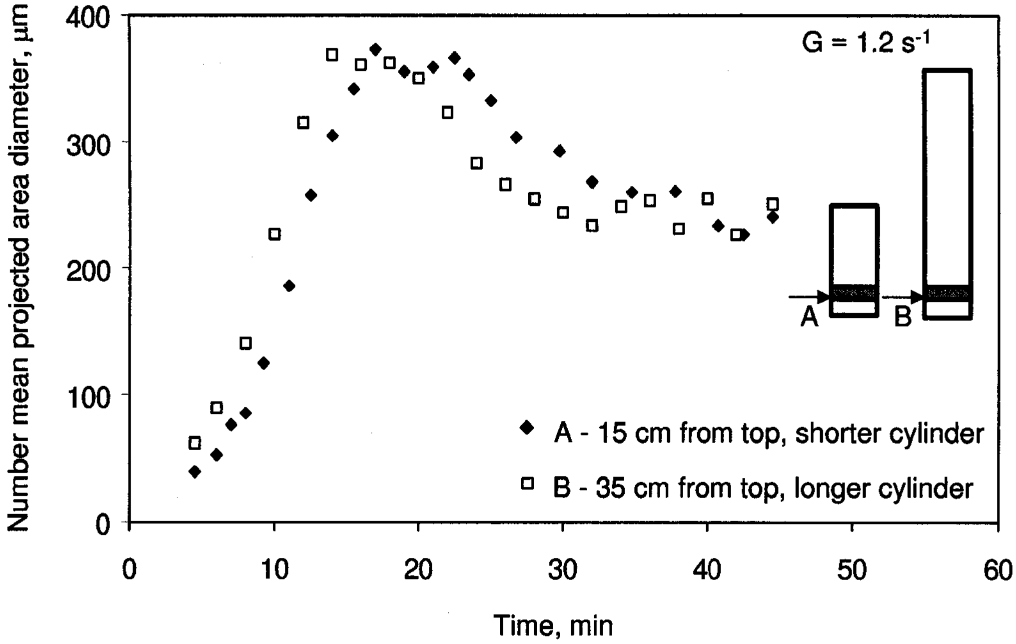

(a)

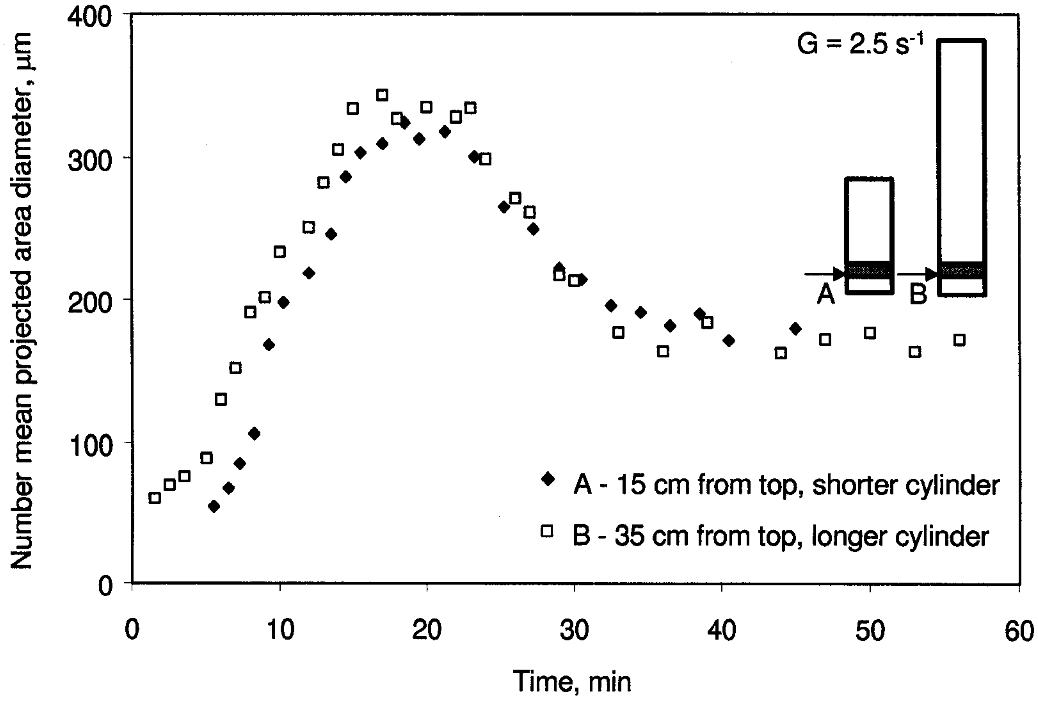

(b)

Figure 2.4. Growth kinetics comparison between different observation locations at T:H = 1:15, and asphaltene particle concentration=12.8 mg/L.
(In Figure 2.4(a), $G = 1.2\ s^{-1}$, and in 2.4(b), $G = 2.5\ s^{-1}$)

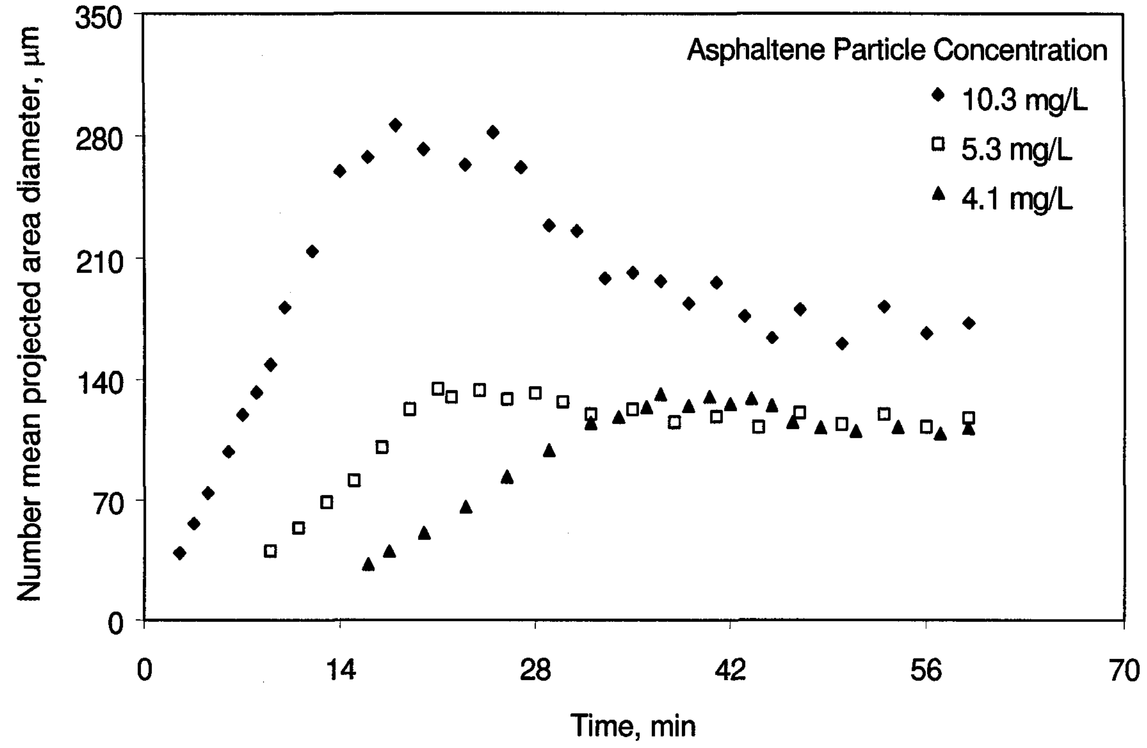

Figure 2.5. Evolution of average aggregate diameter versus time at different concentrations of asphaltene particles at T:H = 1:15, and $G = 2.5\ s^{-1}$.

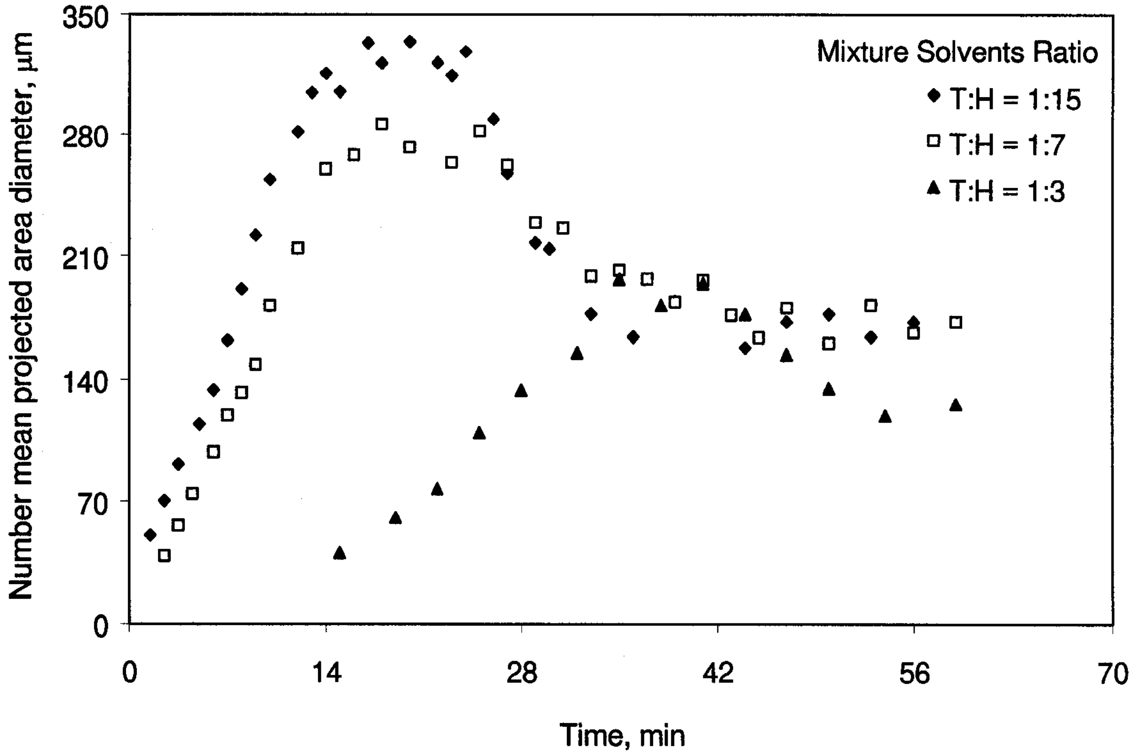

Figure 2.6. Evolution of average aggregate diameter versus time at different toluene to heptane ratios in the solution (T:H) and at $G = 2.5\ s^{-1}$.

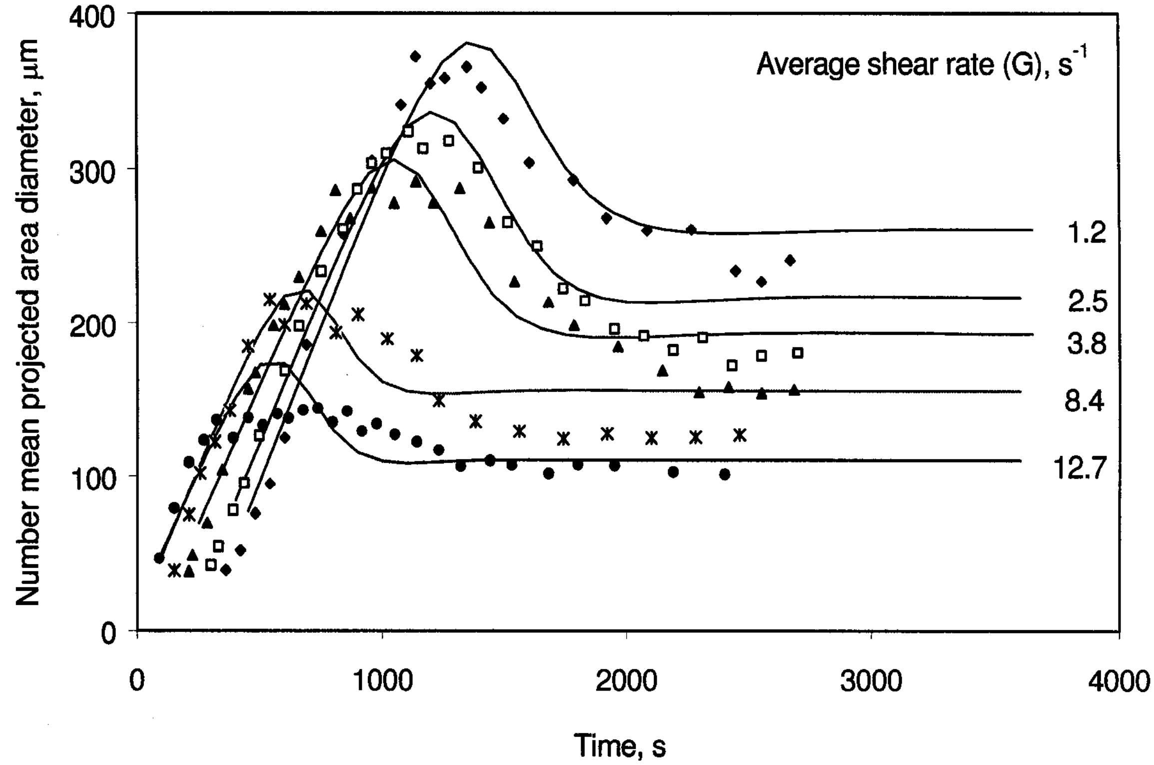

Figure 2.7. Model prediction versus experimental data for growth kinetics of asphaltene aggregates under shear at toluene to heptane solvent ratio (T:H) of 1:15 and particle concentration of 12.8 mg/L. Solid curves were calculated by solving population balance equation (Eq. 2.14) from the model.

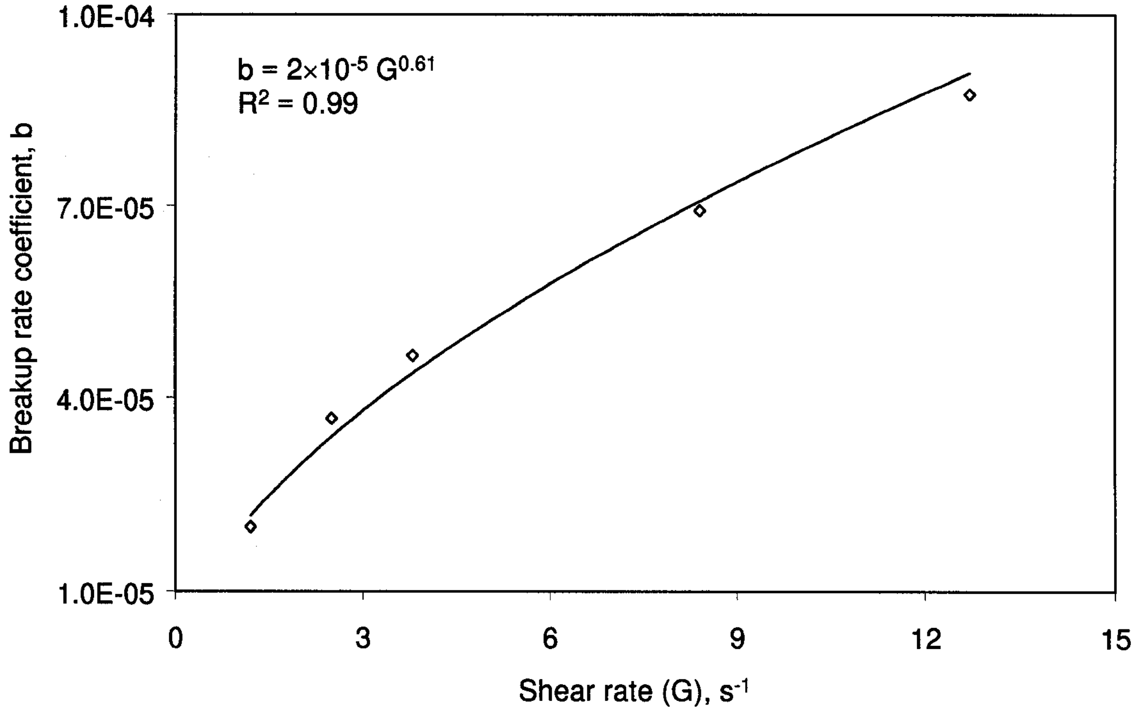

Figure 2.8. Relationship between the breakup rate coefficient, *b*, and the shear rate, *G*, at the particle volume fraction, $\varphi = 10.8 \cdot 10^{-6}$.

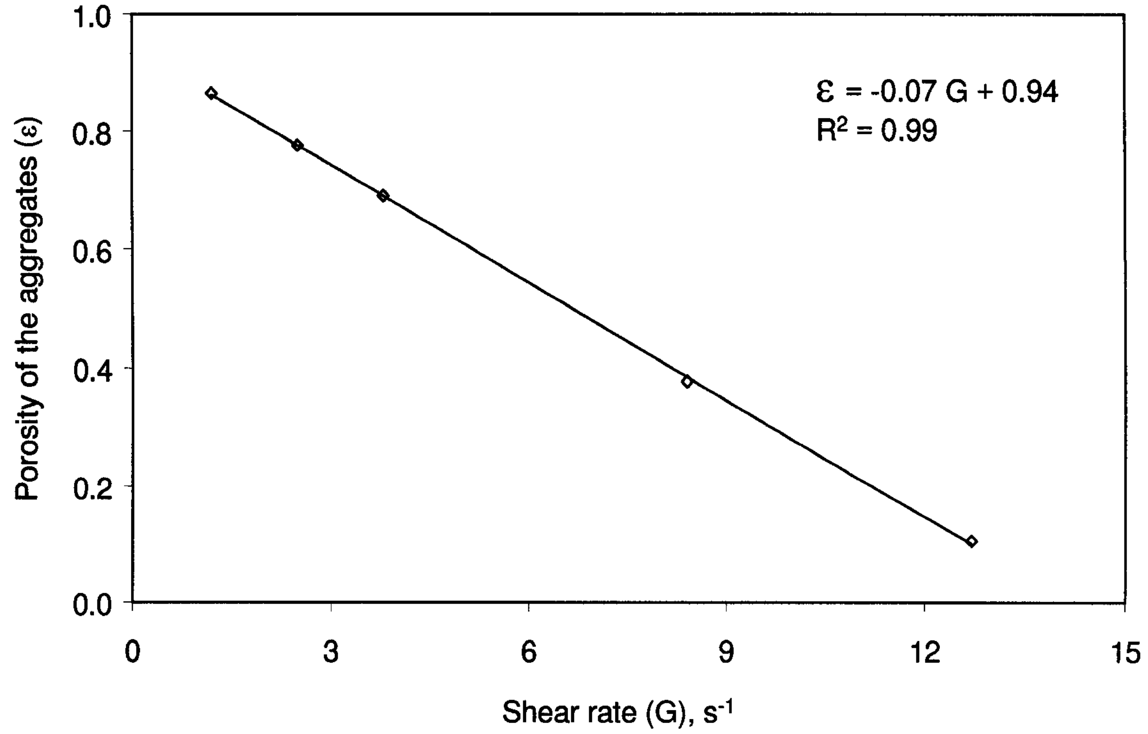

Figure 2.9. Relationship between the porosity of the aggregates, ε, and the shear rate, G, at the particle volume fraction, $\varphi = 10.8 \times 10^{-6}$.

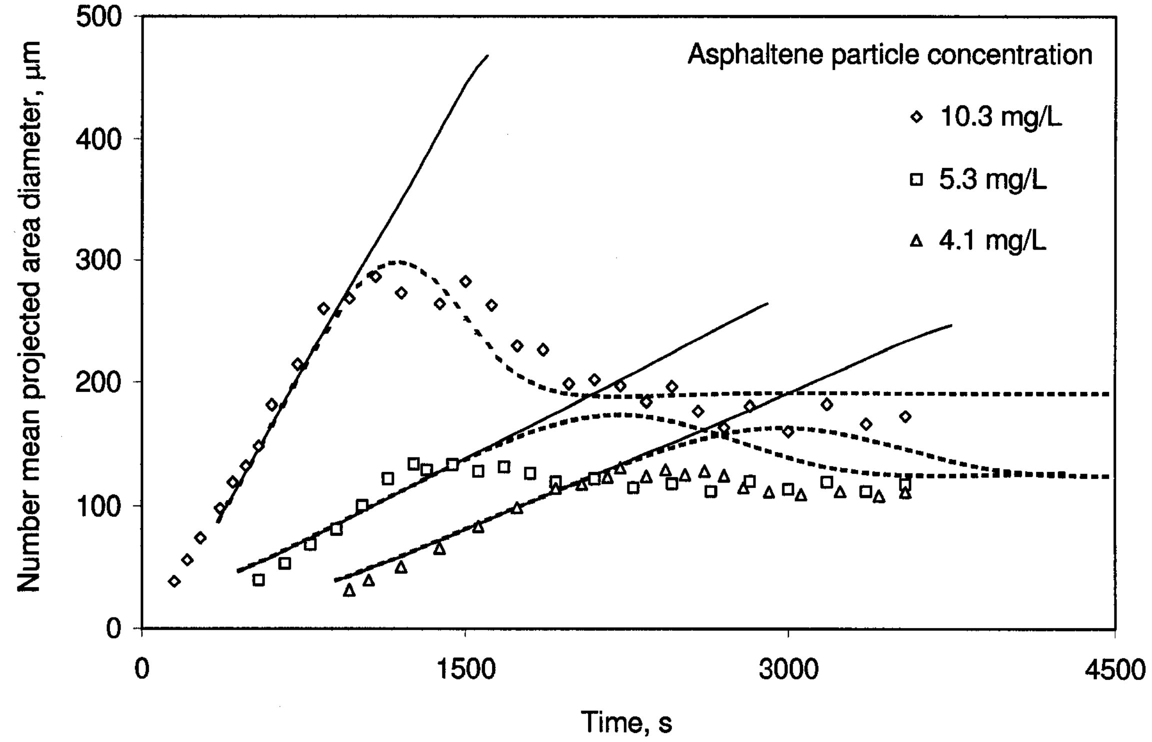

Figure 2.10. Model prediction versus experimental data for growth kinetics of aggregates at $G = 2.5\ \mathrm{s}^{-1}$ and at different concentrations of asphaltene particles. Curves are drawn from the model.
Solid lines – without breakage at all asphaltene particle concentrations, and dashed lines – with breakage for all asphaltene particle concentrations.

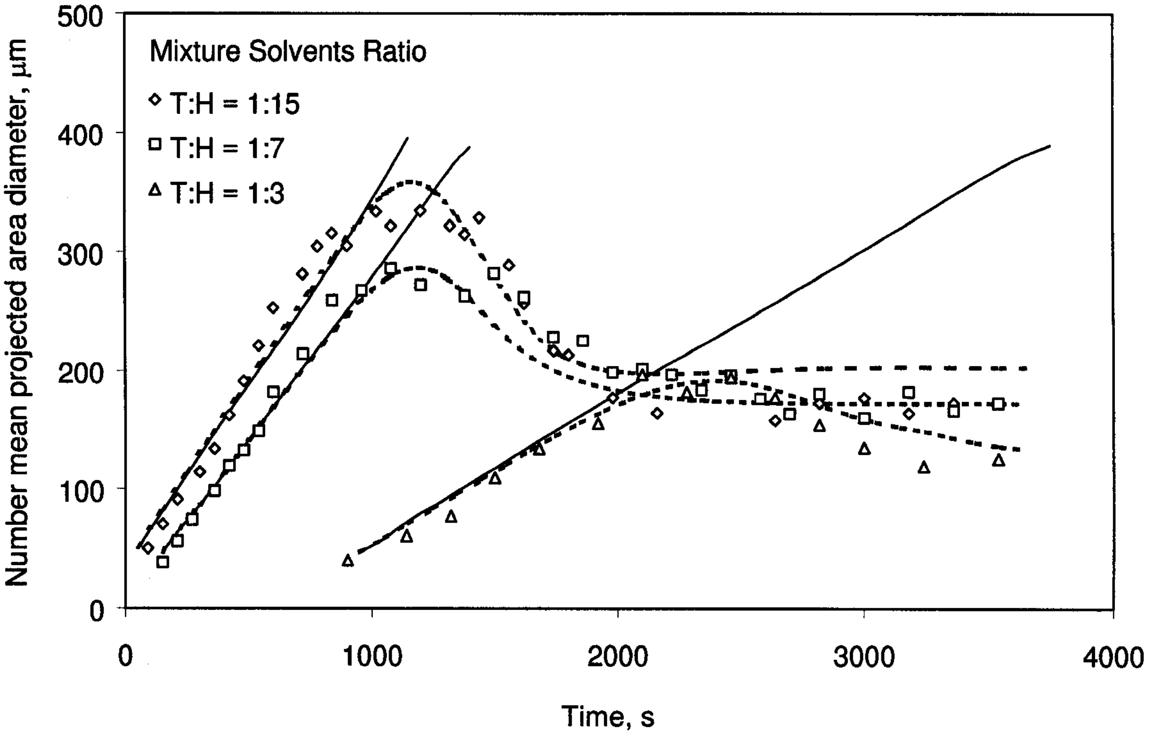

Figure 2.11. Model prediction versus experimental data for growth kinetics of asphaltene aggregates at $G = 2.5\ \mathrm{s}^{-1}$ and at different ratios of toluene to heptane in solution. Curves are drawn from the model.
Solid lines – without breakage at all solvent compositions, and
dashed lines – with breakage for all solvent compositions.

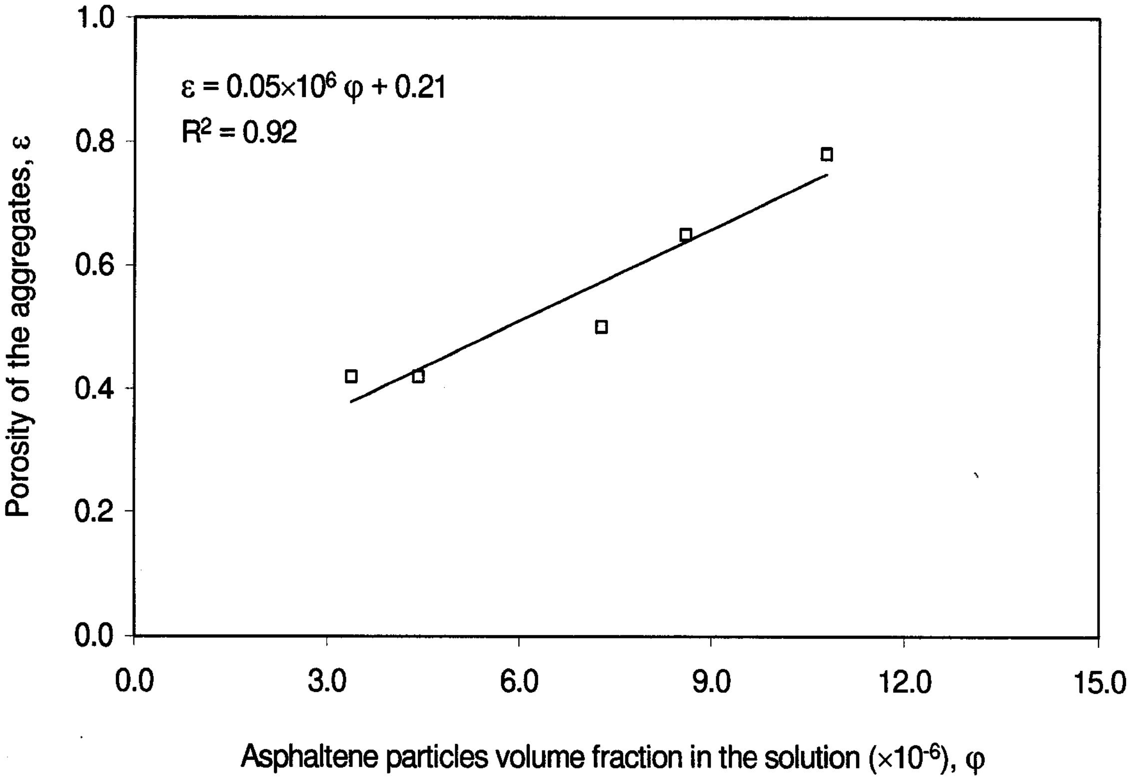

Figure 2.12. Relationship between the porosity of the aggregates, ε, and the asphaltene particles volume fraction in the solution, φ, at the shear rate, $G = 2.5\ \mathrm{s}^{-1}$.

Chapter 3

Evolution of Aggregate Size Distribution: Couette Device[1]

3.1 Introduction

Many chemical processes, such as water treatment, offshore oil drilling, pharmaceutical products separation and heavy oil extraction, involve precipitation and flocculation as one or more key steps of the overall operation. Precipitation occurs through several steps, namely nucleation, particle growth, and eventually aggregation and breakup. Since the process is fast, mixing at various scales plays a crucial role in determining the final floc size distribution and floc morphology.

Simultaneous coagulation and fragmentation of the suspended phase by fluid shear is encountered in many industrial processes involving polymerization, liquid-liquid dispersion, emulsification and flocculation. Most flocculators are operated under shear to ensure thorough mixing and high collision frequency between particles, and, therefore, rapid floc growth. Various experiments carried out with sediment particles (Lick and Lick, 1988; Tsai et al., 1987) and with latex particles (Oles, 1992; Pandya and Spielman, 1982) show that the aggregation of particles is a dynamic process. The particle size distribution at any particular time is determined by the rates at which individual particles aggregate and disaggregate. If the rates of aggregation and fragmentation are different the average size of the distribution increases or decreases depending on which process is dominant. As the particles become larger, they become more vulnerable to breakage due to hydrodynamic stresses. The steady state is reached when the fragmentation rate

---

[1] A version of this chapter is accepted in Chemical Engineering Science.

balances the aggregation rate and the floc size distribution no longer changes with time (Reich and Vold, 1959; Spicer and Pratsinis, 1996a). The aggregation process is also known as agglomeration, agglutination, coagulation, or flocculation. These terms are used in different ways depending on the area of application and on the supposed mechanism of aggregation. To a large extent, flocculation is used as a generic term covering all aggregation processes (Gregory, 1989).

Although the aggregation kinetics of colloidal particles has been the subject of extensive experimental study during the last decade, the mechanism of aggregation and the process of aggregate formation for asphaltene particles have not been investigated in detail. Asphaltene molecules are lyophobic with respect to low-molecular-weight paraffin hydrocarbons, and lyophilic with respect to aromatic hydrocarbons and resins (Sachanen, 1945). Both aromatic hydrocarbons and resins are readily absorbed by asphaltenes and act as stabilizing agents for the asphaltene molecules, that is, inhibiting aggregation of the molecules. Therefore, the addition of low-molecular-weight paraffin hydrocarbons destabilizes these molecules and leads to flocculation and precipitation of the asphaltenes. The asphaltene molecules consequently aggregate and form larger flocs (Ferworn et al., 1993).

Van Smoluchowski (1917) developed the first theoretical model describing the kinetics of coagulation due to Brownian motion or in a simple shear flow. Today his models are still the basis for many more advanced or specific kinetic models of coagulation. Shortly after its publication, the model was confirmed by experiments for a range of different applications. Many of the subsequent investigations were conducted for pure coagulation processes either involving Brownian diffusion (Shilov et al., 1995) or by the relative motion and collision of the particles in laminar flow (Arp and Mason, 1976) or the impact of the different sections of the turbulent energy spectrum in turbulent flow (Saffman and Turner, 1956; Higashitani et al., 1982; Wiesener, 1992). Generally, population balances are number continuity equations characterizing the number N of particles having distinct properties u_i, as a function of time t. To describe a flocculation process the particle volume V can be used to determine the characteristic particle size. On the basis of a population balance model the floc size distribution (FSD) resulting from the growth of aggregates can be predicted for a given geometry of the flocculation reactor and known process conditions. Lu and Spielman (1985) and Spicer and Pratsinis (1996a) used population balance models that included simultaneous floc formation and breakage.

In the present study, a Couette apparatus is used to apply well-controlled, uniform shear to a suspension of asphaltene particles in toluene-heptane solvents mixture. Experiments are performed in the range of shear rates from 1.2–12.7 s^{-1}, ratios of toluene-to-heptane in the solvent mixture from 1:3–1:15 and asphaltene particle concentrations of 4.1–10.3 mg/L. Image analysis is used to measure the size of the aggregates in suspension. The size range of the aggregates studied is similar to that of the ones encountered in commercial systems as reported by Long et al., 2002. Mikkelsen and Keiding (1999) recently provided a novel view of the evolution of activated sludge floc by suggesting that the effects of shear and solids content on floc size could be interpreted as the result of a flocculation-deflocculation balance. Using a similar conceptual framework, the present study aims at examining in detail the dynamic equilibrium between floc growth and floc breakup by monitoring the evolution of asphaltene floc size distributions as a function of stirring condition, solvent composition, and solid particles content. A theoretical analysis of the experimental results is presented.

In the present chapter, the time rate of change of the particle size distribution as affected by aggregation and fragmentation due to fluid shear is investigated. Data in the form of floc size distribution as a function of time is obtained. In the literature, the number-based size distribution of asphaltene flocs in hydrocarbon solvent mixture is not explored yet. However, some authors have observed bimodal number-based size distributions (Parker, Kaufman & Jenkins, 1971) for activated sludge flocs, whereas some investigators have described activated sludge floc size distributions with either a lognormal equation (Barbusinski & Koscielniak, 1995) or a power-law model (Li and Ganczarczyk, 1991). Numerous papers have shown that, in the asymptotic regime of floc growth predicted on binary encounters between clusters in suspension, the mathematical solution of von Smoluchowski aggregation equations yields a gamma function (Friedlander, 1977; Hunt, 1982; Sposito, 1997). Gamma functions are also applicable to steady-state size distributions obtained for various simultaneous binary aggregation and fragmentation processes (Meakin & Ernst, 1988; Cohen, 1992; Spicer & Pratsinis, 1996a; McCoy & Madras, 1998). A population balance approach is used to shed light on the effects of shear rate (G), solvent composition (toluene-to-heptane ratio in the solution, T:H), and solid particle volume fraction (φ) in the kinetics of flocculation. Both theoretical and experimental investigations are performed on the dynamic evolution of FSD as affected by aggregation and fragmentation due to fluid shear. Approximate values for the coefficients appearing in the population balance equations were determined in the previous chapter and applied for the model predictions of FSD.

3.2 Results and Discussions

3.2.1 Floc Size Distributions

3.2.1.1 Shear effect on the evolution of aggregate size

Experimental measurements of floc size distribution are made using photography and subsequent image analysis. It is important to emphasize that this technique is an in-situ and non-intrusive technique. In addition, the Couette device is completely closed; thus, for example, pumps do not disturb the flow. However, the image acquisition technique gives only two-dimensional information (i.e., perimeter, area, and shape factor) on the floc size.

Figure 3.1 exhibits the kinetics of asphaltene growth in terms of number mean aggregate diameter as a function of time for different shear rates. The characteristic length of an aggregate is denoted as the projected area diameter, which is derived from image analysis. The number mean diameter, d_{avg}, can be defined as

$$d_{avg} = \frac{\sum_{i=1}^{i=k} \eta_i d_i}{\sum_{i=1}^{i=k} \eta_i} \tag{3.1}$$

where d_{avg} is a function of time, η_i is the number of particles counted in the i-th bin, d_i is the middle of the size range of the i-th bin, and k is the total number of bins. The number mean diameter is a good parameter to represent the complete growth process in image analysis and is used as the characteristic size. The following observations can be deduced from Fig. 3.1:

(1) As flocculation begins, aggregation dominates and the floc increases in size and reaches a maximum size as fragmentation becomes significant and balances aggregation.

(2) After reaching a maximum, the mean floc size decreases to a steady-state size. This happens either due to fragmentation of the large fragile flocs (Burban et al., 1989) or due to reorganization of the floc structures under the flow stress (Bouyer et al., 2001; Spicer and Pratsinis, 1996b). Under constant shear, large open flocs become more compact as the flocs restructure or fragment and re-form into more durable and stable structures (Selomulya et al., 2001). The population balance model also predicted similar behavior of passing through the maximum size before dropping to the steady-state size plateau, without taking into account the restructuring effect. This was attributable to the breakage of larger aggregates. At this late stage of coagulation, the primary particles were nearly depleted and further growth could not be achieved.

(3) Increasing the shear rate increases the aggregation and fragmentation rates. Higher shear provides a higher aggregation rate (or growth rate) initially in the aggregation-dominated regime (understood from the earlier appearance of primary flocs of the same size, about 30 μm, at the higher shear, as well as the slightly steeper slopes of the average aggregate diameter vs time curves) and, later on, results in a smaller steady-state floc size as a result of the increased fragmentation rate (about 200 μm at 2.5 s^{-1} and 120 μm at 12.7 s^{-1}). The combined result of the accelerated aggregation and fragmentation is a more rapid attainment of steady state by the suspension (about 6 min at 12.7 s^{-1} vs more than 35 min at 2.5 s^{-1}).

The population balance model allows determination of the effect of the shear rate, G, on the floc size distribution. Given an initial distribution of particles, Eq. (2.14) is solved using a finite difference scheme for each of the 31 size classes until a steady-state size is reached (see Chapter 2). It can be observed from Eqs. (2.13, 2.18, 2.20 – 2.22, 2.24) that, except for the breakup rate coefficient, b, and the porosity of the aggregates, ε, other model parameters (i.e., V_i, d_i, N_i, $\beta_{i,j}$, and $\Gamma_{i,j}$) can be obtained experimentally. Simulations were conducted for different values of G, φ, and T:H.

In Fig. 3.2, model predictions for evolution of asphaltene aggregates size distribution at different instants for $G = 8.4\ \mathrm{s}^{-1}$ are represented for the asphaltene volume fraction, $\varphi = 10.8\times10^{-6}$, corresponding to an initial number concentration of asphaltene particles equal to $N_1 = 3.0\times10^4$, $N_2 = 1.8\times10^4$, and $N_3 = 0.5\times10^4\ \mathrm{cm}^{-3}$ (see Appendix A). In the model, the porosity of the aggregates, ε, and the breakup coefficient, b, are used as adjustable parameters and it is intuitive to represent the variations of ε and b with shear rate, G. Values of ε and b are determined by matching the model-predicted floc mean diameter with the experimental data for the aggregation of primary asphaltene particles at various shear rates, $G = 1.2–12.7\ \mathrm{s}^{-1}$. A power relationship, $b = b'G^y$, and a linear relationship, $\varepsilon = -aG + c$, provide a good fit for the experimental data. The parameters b', y, a, and c are determined by regression analysis of ε and b as functions of G (see Chapter 2). In Fig. 3.2, the results predicted by the model with $b' = 2\times10^{-5}$, $y = 0.61$, $a = 0.07$, and $c = 0.94$ are compared to the experimental data for three different instants at $G = 8.4\ \mathrm{s}^{-1}$. Relative number frequency, also defined as number fraction (i.e. ratio of number of particles in the i-th bin to the total number of particles in all bins, $N_\mathrm{i} / N_\mathrm{total}$), is plotted against average aggregate diameter of the i-th bin, d_i $(=(6V_\mathrm{i}/\pi)^{1/3})$. The experimental FSDs are compared to the predictions of the population balance model describing simultaneous aggregation and fragmentation. As growth occurs the particle distribution changes as shown in Fig. 3.2.

The symbols represent the experimental measurements. Initially, aggregation dominates and the primary particles rapidly collide and grow. Once flocculation has begun, experimental observations indicate that the particle size distribution evolves rapidly from narrow monodispersity and broadens into larger sizes as particle collisions form flocs. After about 7 min (Fig. 3.2(b)), the experimental FSDs form the mode (i.e. the peak of the relative number frequency curve, at which the frequency density is a maximum) around 120 μm shifting from the primary particle mode of about 35 μm at 1.5 min (Fig. 3.2(a)). The primary particle mode is depleted by collisions with the larger flocs and the larger mode is formed. As the flocs grow larger, they become more susceptible to breakage and hence, at about 26 min (Fig. 3.2(c)), the floc size distribution mode shifts to about 70 μm and the size distribution becomes narrower. After that, the FSD no longer changes significantly, indicating that a steady state has been attained as a result of the balance between aggregation and fragmentation. The solid lines show the numerical results obtained by the population balance model. The model could not completely describe the FSDs as observed by the image analysis. The theory does not allow for 'a' maximum in the FSDs, rather the model describes the size distribution of the larger flocs.

Experimental (Fig. 3.3a) and model predictions (Fig. 3.3b) of asphaltene aggregates size distribution at steady state for three different values of shear rate, *G*, are represented for asphaltene particles volume fraction in the solution, $\varphi = 10.8\times10^{-6}$. As can be seen in Fig. 3.3(a), the steady-state FSD is shifted towards smaller sizes for higher values of G as a result of the increased significance of fragmentation (Eq. 2.21). In spite of the significant effect of shear on the breadth of the FSDs, their shapes are remarkably similar. Increasing the shear rate does not affect the shape or width of the steady-state FSD.

The steady-state floc size distributions in Fig. 3.3(a) are plotted in normalized form in Fig. 3.3(b) to remove the scaling effects of the shear rate, G. Despite the different kinetic behaviors at the three different shear rates, the distributions collapse to a single curve when scaled by the steady-state, number mean floc diameter (d_{ss}). This indicates that the normalized steady-state FSD is independent of the applied shear rate.

3.2.1.2 Effect of Asphaltenes concentration on the evolution of floc size

The effect of the solid asphaltenes concentration (or volume fraction) on the evolution of number mean floc diameter, d_{avg}, is shown in Fig. 3.4. Increasing φ increases the initial aggregation rate by reducing the average distance between particles and thus reducing the characteristic time between collisions, but it does not significantly influence the floc fragmentation rate because collisional breakage is assumed negligible (De Boer et al., 2000; Oles, 1992). The dynamic balance between floc growth and breakage determines the average floc size that is attained at steady state. As aggregation has a second-order power dependence on particle number concentration and fragmentation has linear dependence on particle number concentration, increasing φ increases the aggregation rate to a much greater degree than the fragmentation rate and a larger steady-state floc size is reached.

The larger φ also results in a faster attainment of steady state than at lower solids fractions because of the more rapid increase in the aggregation rate compared to the fragmentation rate. Oles (1992) observed with dispersion of polystyrene latex in 1.16 mol NaCl and ultrapure water solution that the time required to attain steady state was of the order of hours for $\varphi = 10^{-5}$, whereas Gregory and Li (1991) found that flocculating particles of kaolin clay in tap water reached a steady state at $\varphi = 0.1$ in only a few minutes.

In Fig. 3.5(a), the steady-state size distribution is plotted as a function of the asphaltene particles concentration in solution. Increasing particle concentration produces a broader FSD at steady state because the aggregation and fragmentation rates are both enhanced at larger solids fractions. The FSD shifts towards a larger size because the increased solids fraction enhances the aggregation rate more significantly than the fragmentation rate. This is seen more clearly in Fig. 3.5(b), which shows the effect of solids volume fraction on the steady-state floc size distributions after being scaled with the steady-state, number mean floc diameter (d_{ss}) both experimentally and theoretically. From experimental observations, increasing φ extends the floc size distribution to larger floc sizes. Hence, it can be inferred that increasing the solid asphaltene fraction increases the aggregation rate, increases the steady-state floc size, and broadens the steady-state floc size distribution. However, as shown in Fig. 3.5(b), the model describes the steady-state FSD at different φ to fall on a nearly single curve when normalized by the corresponding d_{ss} value obtained at a particular φ. This indicates that the normalized steady-state FSD weakly depends on the solid asphaltene particles concentration.

3.2.1.3 Effect of solvent composition on the growth of asphaltene flocs

The effects of the ratio of toluene-to-heptane (T:H) in the solution on asphaltenes flocculation are demonstrated in Fig. 3.6, which shows the number mean aggregate diameter as a function of time for a single shear rate of 2.5 s^{-1} and for the initial asphaltene particles concentration of 62.5 mg/L. Lower T:H means lower solubility of asphaltenes and, accordingly, greater quantities of precipitated asphaltenes are observed at the end of an experiment. The amount of precipitate, which is always significantly less than the initial amount added to the solution, is used to determine the particle concentration in the solution (Table 2.1). Hence, a lower toluene-to-heptane ratio results in higher particle concentration in the solution. Therefore, a behavior similar to that in Fig. 3.4 is found, i.e., lower T:H provides faster aggregation. Though large variations in the characteristic relaxation time and the maximum aggregate size are observed, there is a smaller difference in the steady-state floc size for different solvent compositions. Hence, for a fixed rotational speed, increasing proportion of heptane in the solution has a dominant effect on the kinetics of aggregate growth and the magnitude of aggregate breakup, but a lesser impact on the steady-state average aggregate size.

Figure 3.7(a) shows the steady-state floc size distributions for asphaltenes at different solvent compositions and Fig. 3.7(b) shows the comparison between experimental and numerical results in dimensionless form. The symbols show experimental data and the lines indicate the model predictions with the predetermined fitting parameters (b and ε) as found by the regression analysis of b and ε as functions of shear rate, G. However, the initial number concentration of "primary" particles changed due to different solvent compositions, which was accounted for by the model in terms of asphaltene particle concentrations in solution. The steady-state distributions in Fig. 3.7(a) become narrow with increasing T:H in the solution, as fewer collisions occur with decreasing asphaltene particle concentration. As shown in Fig. 3.7(b), upon normalization, the experimental FSDs do not collapse to a single curve when the three distributions are compared with each other. Higher heptane content in solution broadens the steady-state floc size distribution. However, as the model accounts for the effect of T:H in the solution as the effect of φ in the solution, a similar behavior is predicted as shown in Fig. 3.5(b), i.e. the steady-state FSDs at different T:H values fall to a nearly single curve when normalized by the corresponding d_{ss} values. Similarly, it can be inferred that the normalized steady-state FSD weakly depends on the ratio of toluene-to-heptane (T:H) in the solution.

3.3 Conclusions

This study provides information on the kinetics and evolution of asphaltene aggregate size distribution in the model system. It demonstrates the use of a population balance approach to describe asphaltene flocculation phenomena in organic solvents. The model predicts the floc size distributions as a function of time resulting from the flocculation of suspended asphaltene particles in a laminar flow field. The effects of shear rate, particle concentration, and solvent type or composition during flocculation of asphaltene particles were investigated. The model prediction of the aggregate size evolution compares well with the experimentally observed values, given the assumptions made in the theoretical work and the constraints/uncertainties involved in the experimental work.

After sufficiently long times, the floc size distribution reaches a steady-state that reflects a dynamic equilibrium between floc formation and floc rupture. At higher shear, the rate of breakage increases so that a greater number of smaller flocs exist in the suspension. Hence, increased shear reduces the average steady-state floc size.

The kinetics of aggregation according to the population balance equation depends on the square of concentration of particles. At reduced solids concentration, the aggregation frequency is decreased, since fewer collision partners are available. Accordingly, increasing the asphaltene concentration or increasing the proportion of heptane in the solvent mixture increases the floc growth rate and the steady-state floc size.

The normalized steady-state floc size distribution is same with respect to shear and appears to be nearly the same for different asphaltene particles concentration or toluene-to-heptane ratios in the solution, as described by the population balance model. However, experimental observations indicate that at a fixed fluid shear rate, increasing the asphaltene particle concentration in the solution broadens the steady-state floc size distribution as increased particle collisions enhance floc growth to a much greater extent than floc breakage. Reducing the ratio of toluene to heptane in the solution has a similar effect on the steady-state floc size distribution.

From a practical viewpoint, the present study provides information on the significance of shear rate, particle concentration, and solvent composition on the evolution of asphaltene floc growth and size distribution, which helps in the design of mixing vessel and its operating parameters.

3.4 Nomenclature

b	breakup coefficient for shear fragmentation
d_{avg}	number mean projected area diameter (μm)
d_i	average diameter of the particle sizes contained within bin i
d_{ss}	steady-state, number mean projected area diameter (μm)
FSD	floc size distribution
G	shear rate (s^{-1})
N	number concentration of particles (# / cm^3)
N_i	number concentration of aggregates in bin i having characteristic volume V_i (# / cm^3)
N_{total}	total number concentration of aggregates in all bins (# / cm^3)
t	time, min
T:H	toluene-to-heptane ratio in solvent mixtures (or, solvent composition)

Greek

φ	solid particle contents (i.e., volume fraction of particles)
ε	porosity of the aggregates
η_i	number of particles counted in the i-th bin
$\Gamma_{i,j}$	breakup distribution function
β_{ij}	collision frequency between particles of volume V_i and V_j (cm^3/s)

3.5 References

Arp, P.A., and Mason, S.G. (1976). Orthokinetic collisions of hard spheres in simple shear flow. *Canadian Journal of Chemistry,* 54, 3769–3774.

Barbusinski, K., and Koscielniak, H. (1995). Influence of substrate loading intensity on floc size in activated sludge process. *Wat Res, 29,* 1703-1710.

Bouyer, D., Line, A., Cockx, A., and Do-Quang, Z. (2001). Experimental Analysis of Floc Size Distribution and Hydrodynamics in a Jar-Test. *Chem. Eng. Res. Des.*, 79, 1017.

Burban, P. Y., Lick, W., and Lick, J. (1989). The Flocculation of Fine-Grained Sediments in Estuarine Waters. *J. Geophys. Res.*, 94, 8323.

Cohen, R. D. (1992). The self-similar cluster size distribution in random coagulation and breakup. *Journal Colloid Interface Science, 149*, 261-270.

De Boer, D. H., Stone, M. and Levesque, L. M. J. (2000). Fractal Dimensions of Individual Flocs and Floc Populations in Streams. *Hydrol. Process.*, 14, 653.

Ferworn, K. A., Svrcek, W. Y., and Mehrotra, A. K. (1993). Measurement of Asphaltene Particle Size Distributions in Crude Oils Diluted with n-Heptane. *Ind. Eng. Chem. Res.*, 32, 955.

Friedlander, S. K., "*Smoke, Dust, and Haze:Fundamentals of Aerosol Behaviour*", Wiley, New York, 1977.

Gregory, J. (1989). Fundamentals of flocculation. *Critical Reviews in Environmental Control*, 19(3), 185-230.

Gregory, J., and Li, G. B. (1991). Flocculation and Sedimentation of High-Turbidity Waters. *Water. Res.*, 25 (9), 1137.

Higashitani, K., Yamauchi, K., Matsuno, Y., and Hosokawa, G. (1982). Kinetic Theory of Shear Coagulation for Particles in a Viscous Fluid. *J. Chem. Eng. Japan*, 15, 299.

Hunt, J. R. (1982). Self-similar particle-size distributions during coagulation: theory and experimental verification. *Journal of Fluid Mechanics*, *122*, 169-185.

Li, D. H., and Ganczarczyk, J. J. (1991). Size distribution of activated sludge flocs. *Journal of Water Pollution Control Federation. 63*, 806.

Lick, W., and Lick, J. (1988). Aggregation and Disaggregation of Fine-Grained Lake Sediments. *J. Great Lakes Res.*, 14, 514.

Long, Y., Dabros, T., and Hamza, H. (2002). Stability and settling characteristics of solvent-diluted bitumen emulsions. *Fuel*, 81, 1945-1952.

Lu, C. F., and Spielman, L. A. (1985). Kinetics of Floc Breakage and Aggregation in Agitated Fluid Suspensions. *J. Colloid Interf. Sci.*, 103, 95.

McCoy, B. J. and Madras, G. (1998). Evolution to similarity solutions for fragmentation and aggregation. *Journal Colloid Interface Science, 201*, 200-209.

Meakin, P., and Ernst, M. H. (1988). Scaling in aggregation with breakup simulations and mean-field theory. *Phys Rev Lett, 60*, 2503-2506.

Mikkelsen, L. H., and Keiding, K. (1999). Equilibrium aspects of the effect of shear, solids content on aggregate deflocculation. *Adv Colloid Interface Sci, 80*, 151-182.

Oles, V. (1992). Shear-Induced Aggregation and Breakup of Polystyrene Latex Particles. *J. Colloid Interface Sci.*, 154, 351.

Pandya, J. D., and Spielman, L. A. (1982). Floc Breakage in Agitated Suspensions: Theory and Data Processing Strategy. *J. Colloid Interface Sci.*, 90, 517.

Parker, D. S., Kaufman, W. J., and Jenkins, D. (1972). Floc Breakage in Turbulent Flocculation processes. *J. San. Eng. Div.: Proc. ASCE*, 98, 79.

Parker, D. S., Kaufman, W. J., and Jenkins, D. (1971). Physical conditioning of activated sludge floc. *Journal of Water Pollution Control Federation*. 43, 1817-1833.

Rahmani, N.H.G., Dabros, T., and Masliyah, J.H. (2003). Characterization of asphaltenes aggregation and fragmentation in a shear field. *AIChE Journal*, 49 (7), 1645-1655.

Reich, I. and Vold, R. D. (1959). Flocculation-deflocculation in agitated suspensions. I. Carbon and ferric oxide in water. *Journal Physical Chemistry, 63*, 1497-1501.

Sachanen, A. N. (1945). *Chemical Constituents of Petroleum*, Reinhold, New York.

Saffman, P. G., and Turner, J. S., (1956). On the collision of drops in turbulent clouds. *Journal of Fluid Mechanics*, 1, 16–30.

Selomulya, C., Amal, R., Bushell, G., and Waite, t. D. (2001). Evidence of shear rate dependence on restructuring and breakup of latex aggregates. *Journal of Colloid and Interface Science*, 236, 67–77.

Shilov, V., Lichtenfeld, H., and Sonntag, H. (1995). Fast coagulation of nearly spherical ferric oxide (haematite) particles. Part II: Theoretical contribution to the fast coagulation of particles with different surface curvature. *Colloids and Surfaces, A: Physicochemical and Engineering Aspects* 104 (1995), pp. 321–325.

Spicer, P. T., and Pratsinis, S. E. (1996a). Coagulation-Fragmentation: Universal Steady State Particle Size Distributions. *AIChE J.*, 42, 1612-1620.

Spicer, P. T., and Pratsinis, S. E. (1996b). Shear-Induced Flocculation: The Evolution of Floc Structure and the Shape of the Size Distribution at Steady State. *Wat. Res.*, 30 (5), 1049.

Sposito, G. (1997). Scaling invariance of the von Smoluchowski rate law. *Colloids Surface A: Phys Eng Aspects, 120*, 101-110.

Tsai, C. H., Iacobellis, S., and Lick, W. (1987). Flocculation of Fine-Grained Lake Sediments due to a Uniform Shear Stress. *J. Great Lakes Res.*, 13, 135.

van Smoluchowski, M. (1917). Versuch einer mathematischen theorie der koagulations kinetik kolloider lösungen. *Z. Physik. Chem.*, 92, 156.

Wiesener, M. R. (1992). Kinetics of aggregate formation in rapid mix. *Water Research*, 26, 379–387.

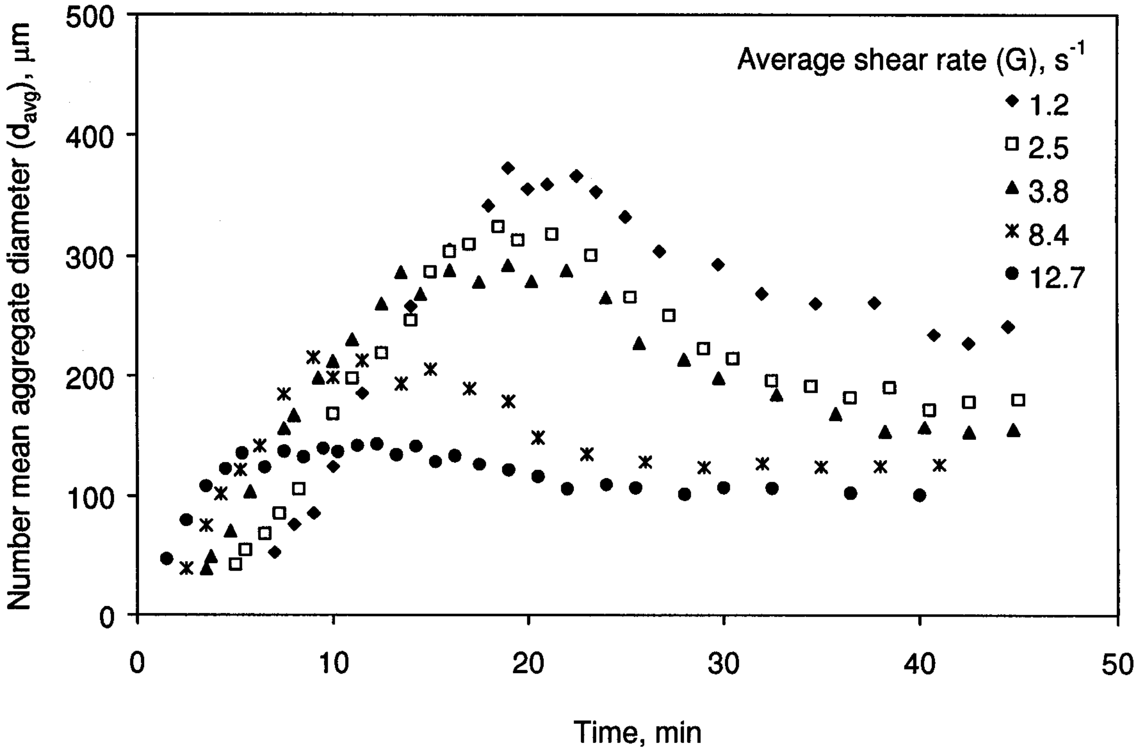

Figure 3.1. Growth kinetics of asphaltene aggregates under shear at toluene-to-heptane solvents ratio (T:H) of 1:15 and particle concentration of 12.8 mg/L.

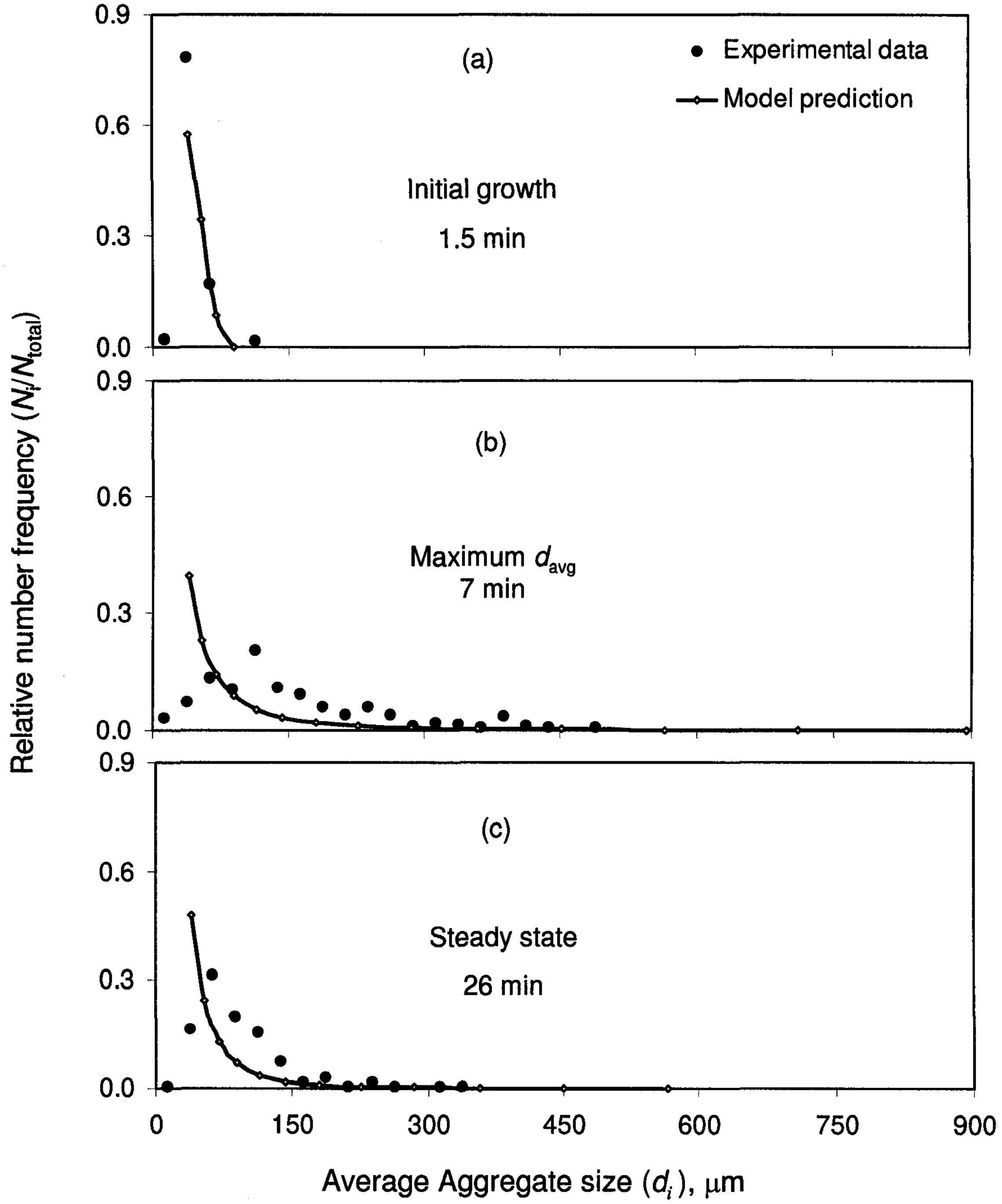

Figure 3.2. Asphaltene FSDs at various stages of growth under shear rate of $G = 8.4\ s^{-1}$ at toluene-to-heptane (T:H) ratio of 1:15 in the solvent mixture and particle concentration of 12.8 mg/L.

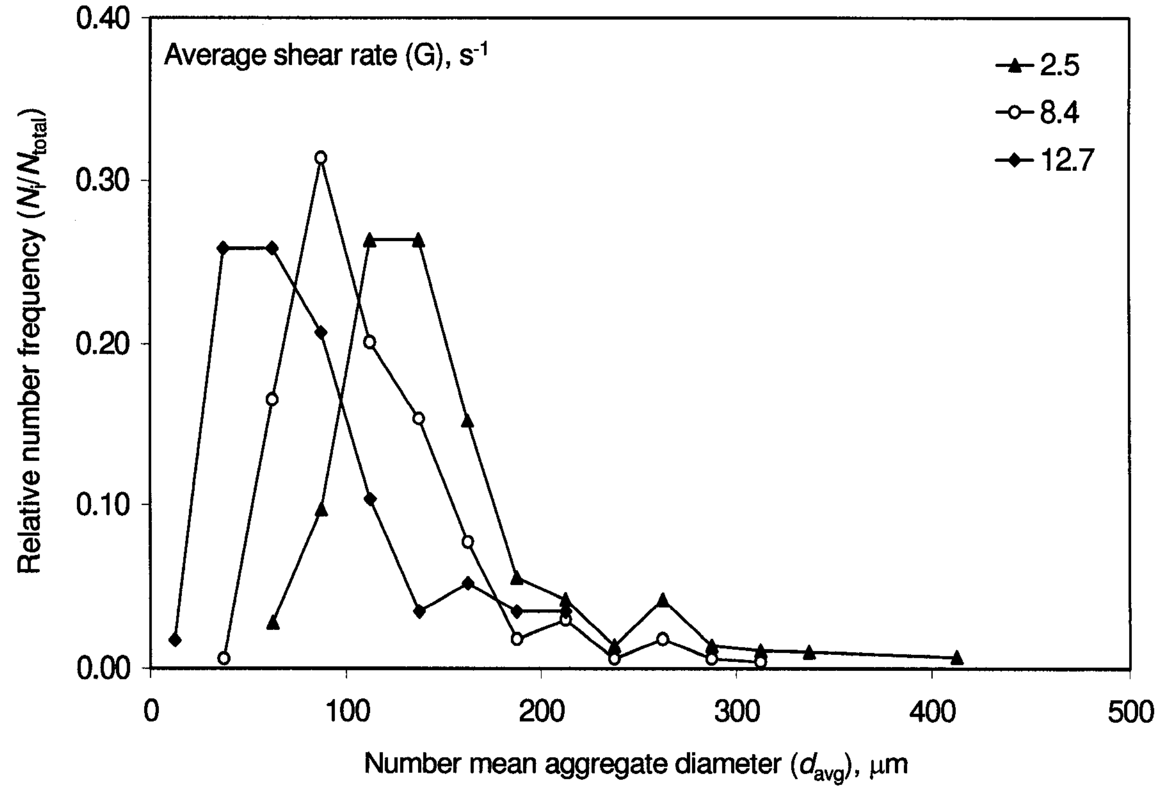

Figure 3.3 (a). Experimental asphaltene FSDs at steady state as a function of shear rate for toluene-to-heptane ratio (T:H) of 1:15 and particle concentration of 12.8 mg/L. Increased shear shifts the floc size distribution towards smaller overall floc size.

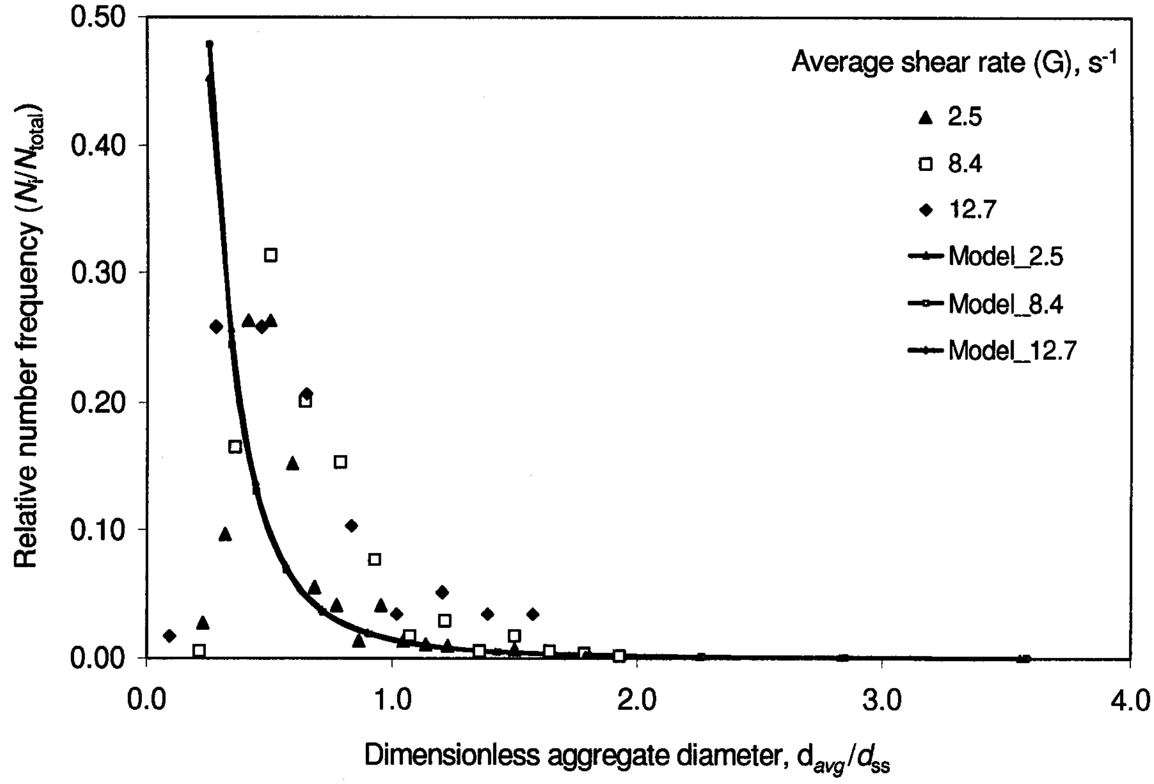

Figure 3.3 (b). Asphaltene FSDs at steady state as a function of shear rate for T:H of 1:15 and particle concentration of 12.8 mg/L. Normalized form of the steady state FSD. The model predicted curves collapse to a single curve and are independent of the applied shear rate.

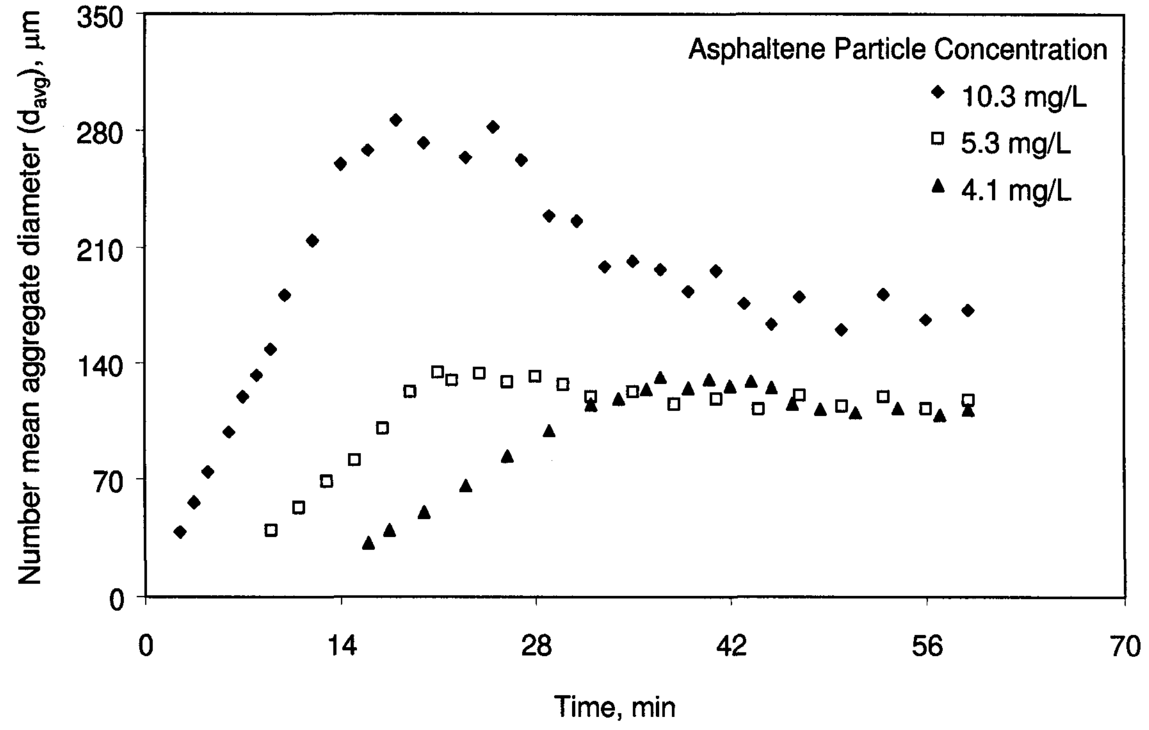

Figure 3.4. Evolution of number average aggregate diameter vs time at different concentrations of asphaltene particles at $G = 2.5\ s^{-1}$ and toluene-to-heptane ratio (T:H) of 1:7 in the solvent mixture.

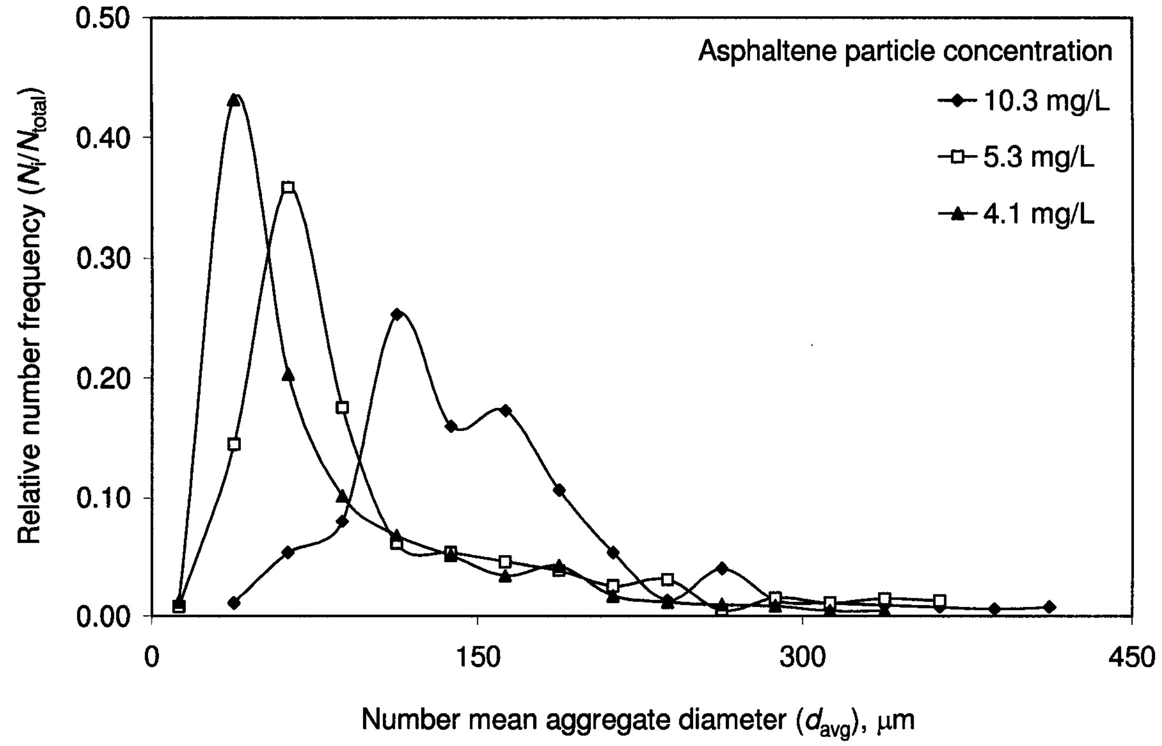

Figure 3.5 (a). Steady state FSD as a function of asphaltenes particle concentration at a shear rate of 2.5 s^{-1} and T:H of 1:7. Increased particle concentration broadens the size distribution by increasing the overall floc size.

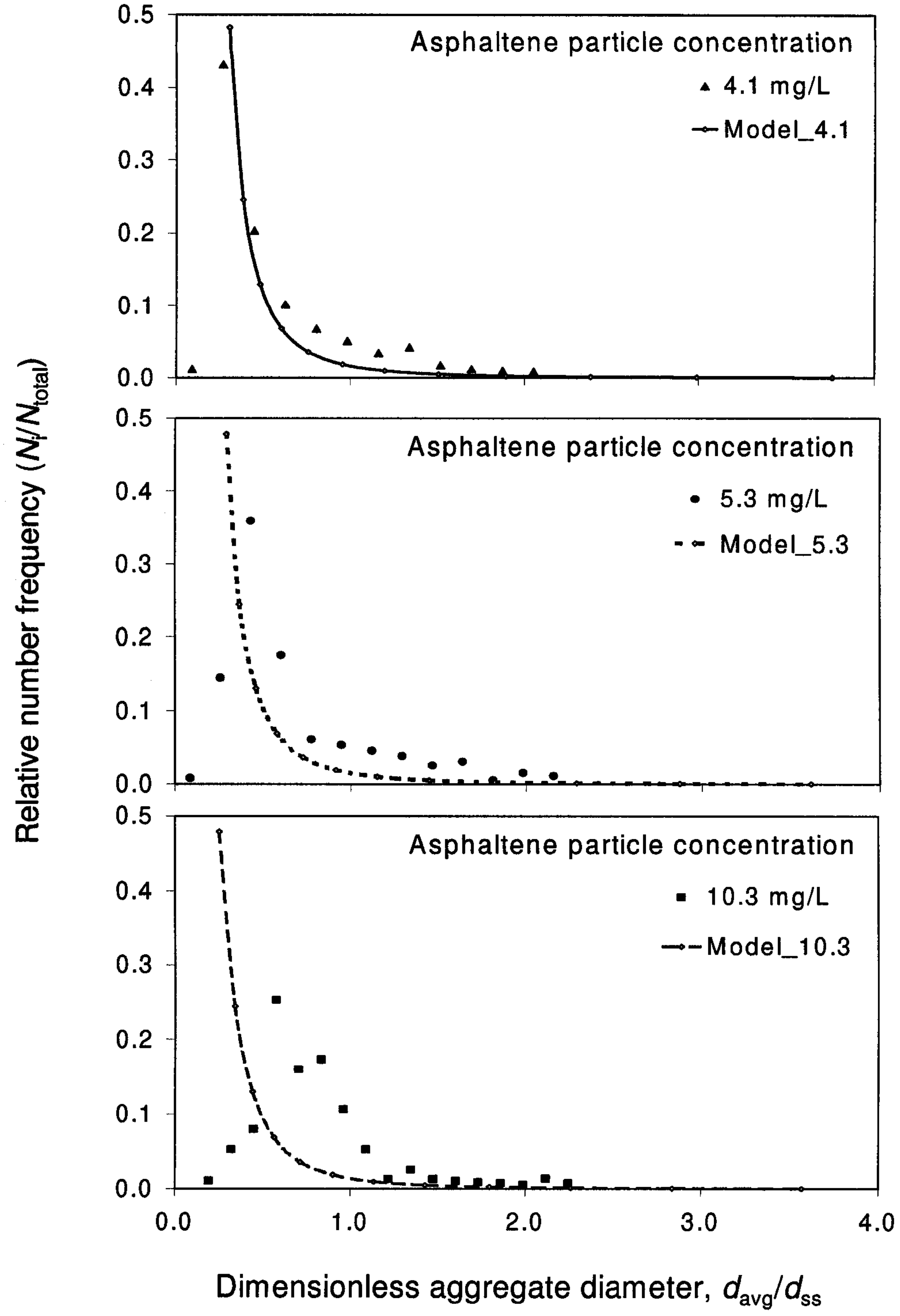

Figure 3.5 (b). Normalized form of the steady-state floc size distribution as a function of asphaltenes particle concentration at a shear rate of 2.5 s^{-1} and T:H of 1:7. Experimental observations indicate that reducing asphaltene concentration in solution narrows the normalized size distribution, whereas the model describes the steady-state FSD at different φ to fall on a nearly single curve.

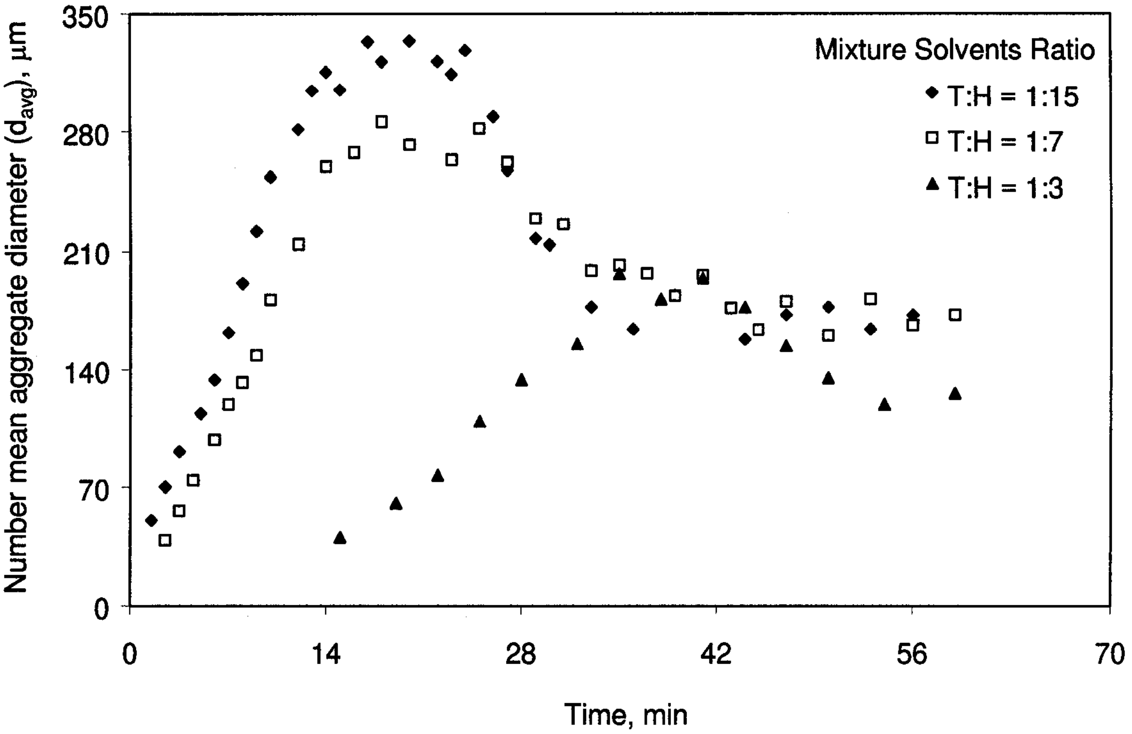

Figure 3.6. Evolution of number mean aggregate diameter vs time at different T:H values in the solution at $G = 2.5\ s^{-1}$.

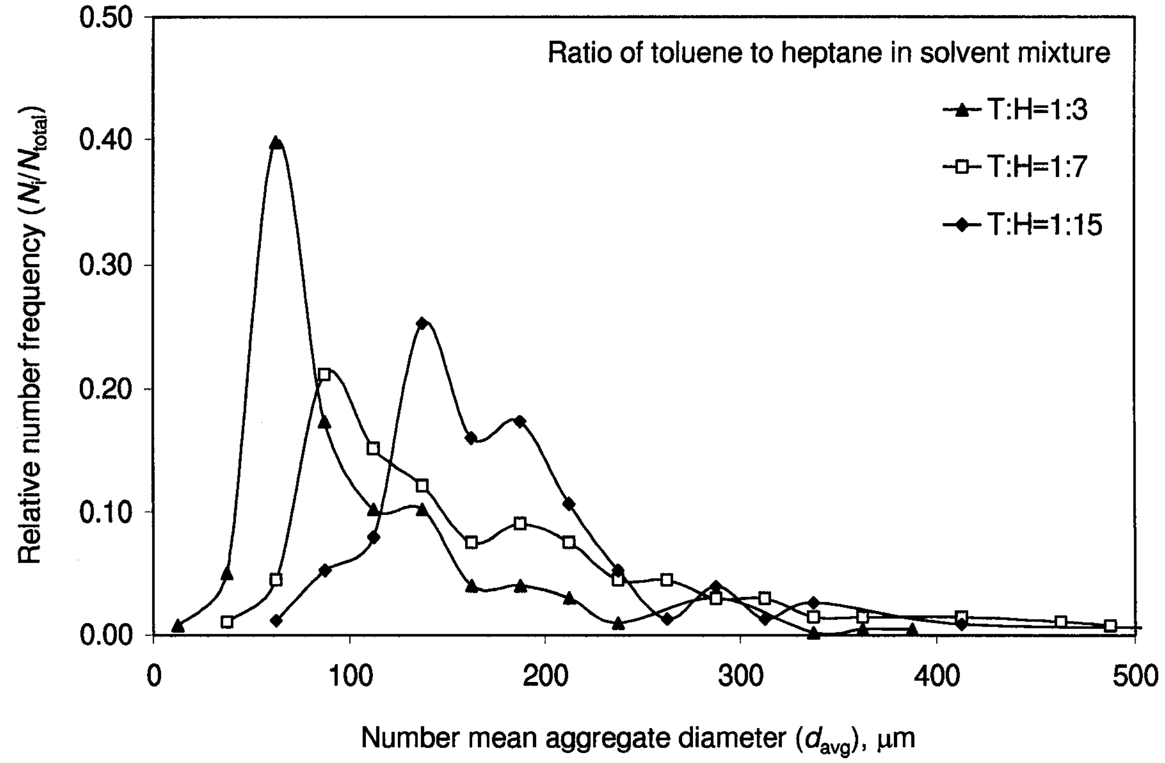

Figure 3.7(a). Steady-state asphaltene FSDs as a function of solvent composition (i.e. T:H in the solution) at a shear rate of 2.5 s^{-1}. Increased toluene-to-heptane ratio reduced the particle concentration in the solution and narrows the FSD by decreasing the overall floc size.

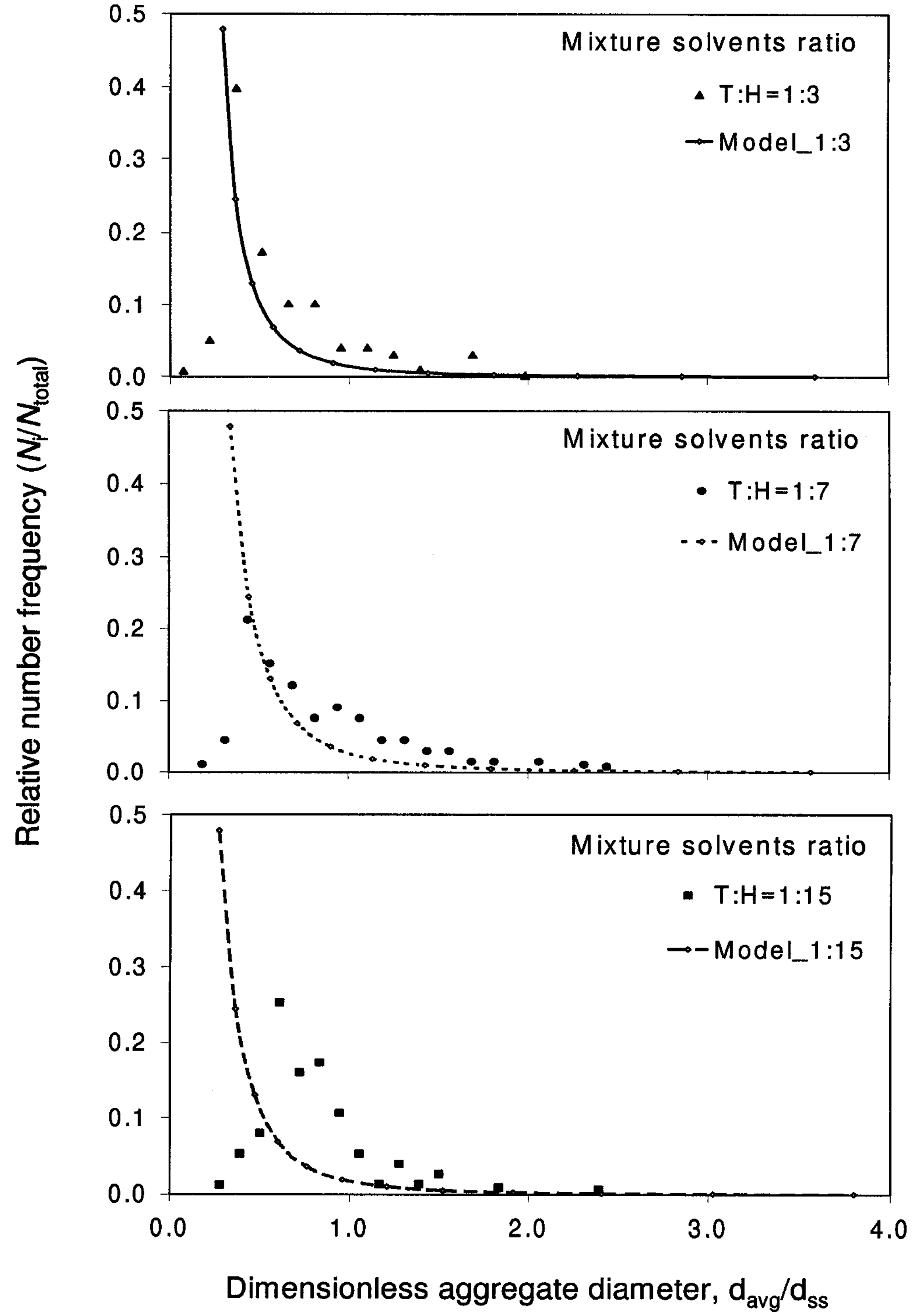

Figure 3.7(b). Normalized form of the steady-state FSD as a function of solvent composition (i.e. toluene-to-heptane ratio (T:H) in the solution) at a shear rate of 2.5 s^{-1}. The steady-state FSDs described by the PBE model at different T:H values fall to a nearly single curve when normalized by the corresponding d_{ss} values.

Chapter 4

Asphaltenes Aggregation: Stirred Tank

4.1 Introduction

4.1.1 Flocculation

The recovery and removal of suspended fine particles are essential to heavy oil processing, water treatment, mineral processing, and production of biological commodities like detergent enzymes. Flocculation is an important step in many solid-liquid separation processes. Common unit operations such as filtration, flotation, and sedimentation become more effective as the size of the particles is increased. If the particles to be removed are too small for effective separation, their size can be increased substantially by causing them to form aggregates. This aggregation process is variously known as *agglomeration*, *coagulation*, or *flocculation*. These terms are used in different ways depending on the area of application and on the supposed mechanism of aggregation. In particular, there is a lack of agreement in the distinction between the terms *coagulation* and *flocculation*. To a large extent, *flocculation* is used as a generic term covering all aggregation processes (Gregory, 1989).

The whole process of flocculation can be divided into two parts: rapid mixing and aggregate formation. The principal aim of the rapid mixing step is to quickly and uniformly disperse the primary particles. The formation of aggregates is achieved by appropriate agitation, so the particles collide and stay together. Collisions among particles can be caused by three well defined transport mechanisms, such as, Brownian or perikinetic flocculation due to the thermal energy, velocity gradient or orthokinetic flocculation due to the bulk fluid motion, and differential settling due to a larger particle overtaking and colliding with a slower settling particle. As flocs grow larger, fluid shear stresses can also break the flocs into smaller fragments (fragmentation) and the breakage tends to occur at the weakest points in the floc structure. This produces fragments that are stronger and more compact but smaller than the parent floc (Thomas, 1964). Thus, aggregation increases the average floc size, but decreases its average compactness, while fragmentation decreases the average floc size and increases the average floc compactness. The optimization of a flocculation process, therefore, depends on the relative rates of collisions and breakage. After a characteristic time of shear-induced flocculation, a steady state is reached between aggregation and fragmentation and the number average floc size no longer changes (Reich and Vold, 1959; Spicer et al., 1998). Floc structures can also be made more compact by shear-induced breakage or restructuring (Thomas, 1964; Francois, 1987; Jullien and Meakin, 1989; Clark and Flora, 1991; Spicer et al., 1996). The growth, breakage and restructuring processes govern the development of floc sizes and structures and all three may occur within the complex shear field of a stirred tank. Hence, the orthokinetic flocculation is the prime interest of the engineers for both research and practical applications.

The need for measurements of in-situ size distribution and geometry of particles has long been recognized in the chemical, biological and other process industries. Optical techniques along with modern advances in rapid computerized data acquisition and storage capabilities make imaging techniques particularly attractive for the in-situ study of dynamic systems. Previous work (Clark and Flora, 1991; Spicer et al., 1996; Serra and Casamitjana, 1998) has employed different techniques to characterize the aggregate properties. Image analysis, whether *in situ* (Clark and Flora, 1991), offline (Spicer et al., 1996), or online (Serra and Casamitjana, 1998), has been used extensively to measure the size of aggregates in terms of their characteristic length and the shape of aggregates in terms of their aspect ratio or shape factor. The use of in-situ/on-line techniques for the study of asphaltene aggregates is important due to the extremely fragile nature of these aggregates.

The state of aggregation and dynamics of aggregates in a flocculating suspension can be measured by particle counters (e.g. Lawler et al., 1983; Francois, 1988; Amirtharajah and O'Melia, 1990). But, they are expensive and are not suitable for obtaining immediate and continuous information about the state of aggregation. On the other hand, simple but sensitive technique has been developed to monitor the state of aggregation of colloidal suspensions (Gregory, 1985). The technique is based on measurement of turbidity fluctuations in flowing suspensions and provides instantaneous information about the state of aggregation. When a flowing suspension is illuminated by a narrow light beam, the transmitted light measured by a photo-detector gives two outputs, a mean value (i.e. the large dc component) and a small fluctuating (ac) signal. It was shown by Gregory (1985) that the ratio of the r.m.s (root mean square) of the fluctuating A.C. component to the mean D.C. signal is roughly proportional to the size of the aggregates flowing through the detector and to the square root of their concentration. This ratio, referred to as *flocculation* or *coagulation index*, can give instantaneous information on the state of aggregation of particle suspension at a given stage of the flocculation process. Although the ratio value does not provide any quantitative information on the aggregate size, the relative increase in this value is a useful indicator of the degree of flocculation. For a given suspension, it can be said that larger ratio value implies larger aggregate size. The technique described above has been successfully applied to study the dynamics and mechanisms of coagulation of dilute and concentrated suspensions with polymeric coagulants (e.g. Gregory, 1988; Li and Gregory, 1991; Ching et al., 1994; Burgess et al., 2000). In this chapter, it is shown that this technique can be applied to study the kinetics of asphaltenes aggregation in toluene-heptane mixtures. It is further demonstrated that this method can give valuable insights into the mechanisms of particle aggregation, fragmentation and reformation. Besides, the present study provides additional information on the average size of asphaltene aggregates by calibrating the ratio values from PDA using an on-line image-based technique.

4.1.2 Asphaltene

Asphaltene is defined as the fraction of a crude oil, which is insoluble in light saturated oils such as pentane and comprises the heaviest components of the oil (Sheu and Storm, 1995). The soluble part is usually called the maltene and also comprises many components ranging from light saturated, aromatic molecules to heavier "resins". Indeed, the borderline between asphaltenes and resins is a matter of definition, and remains somewhat arbitrary. Many experiments reported to date indicate that the solubility of asphaltenes in the oil, as well as in conventional non-polar solvents, presents intriguing features suggesting aggregation in a colloidal state. Various models were proposed for aggregation and precipitation with only limited success in accounting for the experimental facts. Porte et al. (2003) considered the current literature reported on asphaltene solubilization so far and proposed a new description, demanding that it should not be contradicted by any one of the listed facts found in literature. In their description, asphaltene aggregation and precipitation are controlled by different intermolecular forces. In good apolar solvents, aggregation is induced by strong specific interactions (e.g. hydrogen bonds) originating at the periphery of the asphaltene molecules: they drive the reversible association in two-dimensional sheets, a morphology which is consistent with reported scattering and viscosity data. As long as the quality of the solvent is sufficiently good, the aggregates remain dispersed at equilibrium. As the solubility parameter of the solvent is shifted to become a bad apolar solvent, weak nonspecific van der Waals dispersion attractions between the aggregates determine precipitation. This statement of different forces driving aggregation and precipitation, respectively, is the most important ingredient of this description.

It is widely agreed to date that asphaltenes are present in oil in an aggregated state. Regarding the mechanism leading from aggregation to true flocculation, two opposite hypotheses have been summarized by Cimino et al. (1995). In the lyophobic model (Leontaritis and Mansoori, 1987; Stephenson, 1990), asphaltenes are considered as essentially insoluble in the oil and in common solvents. They remain dispersed as colloidal particles "stabilized" by the "resins", which are less aromatic. The resins are adsorbed at the surface of the aggregates and provide steric stabilization against flocculation. Addition of light paraffinic compounds makes the solution a better solvent for the resins: they dissociate from the aggregates, and eventually, the asphaltene aggregates flocculate. The opposite lyophilic model postulates that asphaltene aggregates are solvated by the surrounding media, with which they constitute a single phase in thermodynamic equilibrium (Hirschberg et al., 1984; Buckley et al., 1999). Resins play no special role, and flocculation is determined by changes in the interactions between the aggregate and the solvating medium. In both approaches, the solvating power of the oil is of major importance. Still to date, both the aggregate morphology and the flocculation mechanism of asphaltenes remain controversial.

The physical nature and the process of aggregate formation for asphaltene particles have not been investigated for larger size scales. The purpose of this study is to understand the kinetics of aggregation of suspended "primary" particles of asphaltenes in hydrocarbon solvents. Generally, a mixture of toluene and n-heptane is often used to investigate the stability and the precipitation process of asphaltenes. Using the light transmittance technique of PDA, the aggregation in a bench-scale stirred tank is examined. The growth of the aggregates is investigated as a function of shear rate, ratio of toluene to n-heptane in the solvent mixture, asphaltene concentration, and bitumen concentration. Different shear schedules are used to investigate the aggregate breakage and reformation mechanisms and to get a qualitative definition about the strength of these flocs. The effect of the presence of maltenes on kinetics of asphaltenes aggregation is studied. The characteristics of the aggregates in terms of growth kinetics and size are evaluated for cyclic-shear and tapered-shear flocculation, a technique often applied in water treatment. The effect of shear history on the growth of asphaltene aggregates could be understood.

4.2 Theory of Turbidity Fluctuations

4.2.1 Photometric Dispersion Analyzer (PDA 2000)

The principles of the optical technique used in this study and its application to flocculation processes have been described previously (Gregory, 1985; Gregory and

Nelson, 1986). They developed a new approach to test flocculation qualitatively using Photometric Dispersion Analyzer (PDA). The instrument is a sensitive, on-line, flow-through detector, which gives a rapid indication of the state of aggregation of particles in a flowing suspension. The theory of PDA is based on Beer-Lambert law and assumes Poisson distribution of particle number in a flowing suspension. The Beer-Lambert law can be given as follows (Gregory and Nelson, 1986; Ching et al., 1994)

$$I/I_0 = V/V_0 = \exp(-NCL) \tag{4.1}$$

where, I is the transmitted light intensity, I_0 is the incident light intensity; N is the number concentration of particles; C is the average scattering cross section of the suspended particles; and L is the optical path length. In practice the light intensity is converted at the detector to a proportional voltage. So voltage outputs V and V_0 correspond to I and I_0 respectively, where V is the time averaged d.c. voltage for transmitted light intensity and V_0 is the time averaged d.c. voltage corresponding to the incident light intensity. In a suspension illuminated by a light beam with cross sectional area A and length L, the average number of particles (n) contained in the illuminated volume equals NAL (i.e. $n = NAL$). Hence, Eq. (4.1) can be represented as,

$$V = V_0 \exp(-NCL) = V_0 \exp(-nC/A) \tag{4.2}$$

As the suspension flows through the cell, the actual number of particles crossing the light beam will show a random variation about the mean value, n, as the sample is continually renewed by the flow (Gregory, 1985). This variation of the particle number will follow a Poisson distribution so that the standard deviation about the mean equals the square root of the mean (Std. dev. = $n^{1/2}$). It has also been shown by Gregory (1985) and Gregory and Nelson (1984, 1986) that the random variation in the number of particles in the illuminated volume of a flowing suspension leads to corresponding fluctuations in transmitted light intensity and proportional voltage reading. The simplest measure of a fluctuating signal is its r.m.s value, and for developing the theory of PDA, they considered only the fluctuating component of the transmitted light intensity (or its corresponding AC voltage) after separating it from the mean (dc) value (Fig. 4.1) and the V_{rms} can be given by

$$V_{\mathrm{rms}} = V \sinh (n^{1/2}C/A) \qquad (4.3)$$

Gregory and Nelson (1984) noted that for fairly dilute suspensions (< 100 mg/l solids), the quantity $n^{1/2}C/A$ will be much less than unity in which case, $\sinh (n^{1/2}C/A) \cong (n^{1/2}C/A)$ by the linear approximation, and

$$V_{\mathrm{rms}} = V (n^{1/2}C/A) \qquad (4.4)$$

In principle, the scattering cross-section C could be calculated from light scattering theory, but this is difficult except in certain limiting cases. If the particles are very small (so that the radius is very much less than the light wavelength), then Rayleigh theory can be applied. However, for the particles we are concerned with, large asphaltene aggregates, this would not be a realistic approach. For much larger particles (a few μm), a simple diffraction or 'light blockage' approach is valid (Friedlander, 1977; Gregory and Nelson, 1984), and the scattering cross-section is then just twice the geometric cross-sectional area of a particle (i.e. $C = 2\pi a^2$). Intermediate particle sizes require application of the much more elaborate Mie theory.

When particles aggregate, the r.m.s. value should change for two reasons:

- the number concentration decreases, and
- the scattering cross section increases.

These have opposing effects on the r.m.s. value, but it can be shown that, in virtually all cases of practical interest, the net effect is a substantial increase in fluctuations and hence, in the measured r.m.s. value.

It is convenient to present Eq. (4.4) in terms of the particle number concentration, N, rather than the average number in the illuminated beam, n, and to introduce a dimensionless term, R, which is the ratio of V_{rms} to the mean value V:

$$R = (V_{\mathrm{rms}}/V) = (L/A)^{1/2} N^{1/2} C \tag{4.5}$$

Dividing the r.m.s. value by the d.c. value provides the ratio value, R, that is essentially immune to such problems as electronic drift and contamination ("fouling") of optical surfaces. These effects change the d.c. and r.m.s. values in the same relative way, so that the ratio value is unaffected. This is a major advantage in the monitoring of highly turbid suspensions, where flow-through turbidity measurements can be very seriously affected by fouling.

Gregory and Nelson (1984), from theoretical considerations, have shown that the rms value or the ratio value would vary as either the sixth root ($j^{1/6}$) or the square root ($j^{1/2}$) of the aggregation number (j) (i.e. on average, j number of primary particles combine to form one aggregate), depending on whether coalesced-sphere aggregates (Fig. 4.2 (a)) or extended aggregates (Fig. 4.2 (b)) are assumed. Real aggregates will be intermediate between these two extremes (Fig. 4.2 (c)). Extended aggregates will cause the maximum ratio value, but their mass density may be minimum.

Eq. (4.5) was developed for mono-dispersed suspension; for a hetero-dispersed suspension, the ratio R, referred to as flocculation index (FI), can be modified to (Gregory and Nelson, 1986)

$$R = \left(\frac{L}{A}\right)^{1/2} \left(\Sigma N_i C_i^2\right)^{1/2} \tag{4.6}$$

where N_i and C_i are the number concentration and scattering cross-section of particles of size i, respectively. The above equation demonstrates that the fluctuating signal still depends on the square root of particle number concentration (N) and on the first power of the scattering cross section (C). Moreover, the C value is highly dependent on the size of the suspended particles (as shown before). An analysis of the term $(\Sigma N_i C_i^2)^{1/2}$ in Eq. (4.6) reveals that smaller particles have a negligible effect on R, and that, in a coagulating suspension, the larger aggregates have a dramatic influence on R (Gregory and Nelson, 1986; Ching et al., 1994). This means that as flocculation progresses, the value of R increases. Although the ratio (R) does not provide quantitative information on aggregate size, the relative increase in the R value is a useful indicator of the degree of flocculation. For a given suspension, it can be assumed that larger R value implies larger aggregate size. However, the ratio values (R) can be calibrated in terms of floc diameter by the image analysis of captured microphotography and hence the flocculation index can be interpreted as the number mean, projected area diameter. For this research, the PDA outputs are combined with the microscopic images to acquire quantitative information on the size of asphaltene aggregates.

The PDA 2000 instrument has three outputs:

- The d.c. value, corresponding to the average transmitted light intensity (and hence related to the turbidity of the suspension);
- The r.m.s. value of the fluctuating (a.c) component;
- The ratio value, R = (r.m.s./d.c.)

The outputs are sampled at a frequency of 1 Hz and displayed graphically in real time. The instrument setting was such that the d.c. voltage reading for only *n*-heptane solvent was always 7.5 Volt and then the asphaltene-toluene solution was added to heptane. All of the experiments were conducted under similar conditions, so that useful comparisons could be made. The ratio output is the most useful for fairly dilute suspensions, for which the d.c. value may change only slightly as flocculation proceeds. In typical cases, the ratio value may increase by a factor of five or more before flocs have grown to a visible size. The rate of increase of R may be taken as an empirical measure of the rate of flocculation.

4.3 Materials and Analysis

Asphaltenes aggregation in toluene and heptane mixtures was studied with three different feed sources.

- Asphaltenes that was previously extracted and purified from Athabasca bitumen as described in section 4.3.1.
- Athabasca Bitumen containing natural level of asphaltenes that was extracted from bitumen-froth using naphtha in the commercial froth treatment plant. It is known as the Coker feed bitumen.
- Athabasca Bitumen containing natural level of asphaltenes that was extracted from oil-sands using toluene in the laboratory. It is known as solvent-extracted bitumen.

4.3.1 Preparation of asphaltene solution

The asphaltenes used in this study are derived from Syncrude vacuum-distillation-tower-feed Athabasca bitumen (bitumen that has been treated to remove most of the solids and water). However, the bitumen still contains mineral solids, which make up about 1 wt% of the bitumen. The "solids", which include fine clays, are insoluble in toluene (Yarranton, 1997). To remove the solids, the bitumen is first dissolved in toluene and centrifuged at 35,000g for 30 minutes. The supernatant liquid is recovered and evaporated until dry, "solids-free" bitumen remains. Asphaltenes are extracted from the "solids-free" bitumen with a 40:1 volume ratio of heptane to bitumen (solids-free). The mixture is stirred for 4 hours and left standing to allow the precipitated asphaltenes to settle overnight. Then the supernatant liquid is removed and the remaining precipitate is further diluted with heptane at a 4:1 volume ratio of heptane to asphaltenes. After 4 hours, the final mixture is filtered using 0.22-μm Millipore filter paper and the remaining asphaltenes are washed thoroughly with heptane until the filtrate (i.e. heptane) becomes colorless. The precipitated asphaltenes are dried in a vacuum oven dryer at 23 kPa absolute pressure and 50°C. The drying process usually requires one week. The asphaltenes recovered in this method make up about 16 wt% of original bitumen. Reagent-grade toluene and heptane, used in the extraction, were purchased from Fisher Scientific.

Dry asphaltenes powder is mixed with toluene to give an initial concentration of 3.0 g/L to achieve a good dispersion. The suspension is subjected to high speed stirring for proper mixing and then allowed to stand in a mason jar for overnight. This is retained as a stock of asphaltene-toluene solution.

Table 4.1. Physical Properties of Solvents Used

Solvent	Boiling point (^{0}C)	Density at 20^0 C (kg/m^3)	Viscosity at 20^0 C Pa.s
Toluene	110.6	866.9	0.59×10^{-3}
n-Heptane	98.4	683.7	0.42×10^{-3}

For the first set of aggregation experiments, samples of this stock solution are diluted in toluene and then *n*-heptane is added to give an initial asphaltenes concentration of 62.5 mg/L. A constant stirring speed of 36 rpm is employed. In this set of experiment, the solvent composition (i.e., the volume ratio of toluene-to-heptane (T:H) in the solution) is varied. In the second set of experiments, the stirring speed was set at 75 rpm and the volume ratio of toluene to n-heptane is kept fixed at 1:5. The initial asphaltenes concentration is varied between 62.5 mg/L and 93.75 mg/L.

4.3.2 Preparation of bitumen solution

In most of the experiments, solvent extracted bitumen and coker feed bitumen are used. First the bitumen was dissolved in toluene and the solution was added to excess heptane to investigate asphaltenes aggregation. In this set of experiments, the volume ratio of toluene to *n*-heptane is kept fixed at 1:5, but the stirring speed is varied between 75 to 160 rpm and the initial bitumen concentration is varied between 625 to 1125 mg/L. Corresponding asphaltenes concentration in the solution varied between 100 to 180 mg/L (assuming 16 wt% asphaltenes in bitumen).

4.3.3 Apparatus

A Photometric Dispersion Analyzer (PDA 2000, Rank Brothers, UK) is used to provide real time on-line information on changes in turbidity of the flowing suspension and the state of aggregation, which can then be used to determine the kinetics of aggregation. A qualitative indication of the floc size, as the experiment progresses, is also possible. A schematic view of the experimental setup for monitoring the kinetics of asphaltenes aggregation by PDA 2000 is shown in Fig. 4.3. Aggregation tests are carried out in a bench scale stirred tank reactor equipped with a sampling tube, which passes through PDA 2000 and an observation cell. The flow rate in the tube is controlled by the peristaltic pump. Images of asphaltenes aggregates while passing through the glass flow-through tube are obtained using a microscope (Carl Zeiss Canada Ltd.) coupled with a CCD camera and a video recorder. Image analysis software (Sigma ScanPro 4) is used to calculate the geometrical properties of the aggregates from the captured images. The electric mixer motor is mounted on a steel support, which is rigidly placed on the top of the reactor. The impeller, which is a standard 45° angle four-blade pitch turbine, is attached to the motor via a 6 mm diameter steel rod, and the suspension is mixed by the impeller with the presence of baffle (Fig. 4.4). The center of the impeller is positioned at at 1/3 of the tank height from the bottom. Similar to the present impeller, most pitched-blade turbines are rotated so that the direction of pumping is downward. This type of axial flow creates good top-to-bottom motion in the tank, which results in good mixing. Simple inversion of the impeller face does not change the pumping direction to upward, rather reversing the direction of rotation or changing the angle of the blades will make a pitch-blade impeller up-pumping. It is possible to vary the speed and time of both the rapid mix and slow stirring phases by using a variable speed motor controller (RZR 50, Caframo, Ontario, Canada).

4.3.4 Stirred tank flow field characterization

The parameter most frequently used to express energy input in a stirred tank is the mean velocity gradient, G_{avg}, as given by Camp and Stein (1943):

$$G_{avg} = (P_{liq}/\mu V_t)^{1/2} = (\varepsilon / \nu)^{1/2} \tag{4.7}$$

where P_{liq} is the energy dissipated into the liquid (watts), μ is the dynamic viscosity of the suspending fluid (Pa·s), V_t is the suspending fluid volume in the stirred tank where the energy is applied (m^3), ε (=P/M) is the energy dissipation rate per unit mass (m^2/s^3), M is the mass of fluid (kg), and ν (=μ/ρ) is the kinematic viscosity of the fluid (m^2/s), where ρ is the density of the fluid (kg/m^3). Whereas "the velocity gradient, or G-value, concept is a gross, simplistic, and totally inadequate parameter for design of mixers" (Amirtharajah, 1978), as there are currently no other design approaches available, this parameter is used to design mixer units (Monk and Trussell, 1991).

According to Godfrey et al. (1989) and Clark and Flora (1991), the rate of dissipation of energy is given by

$$\varepsilon = P_o N_{\text{rps}}^3 D_{\text{imp}}^5 / V_t \tag{4.8}$$

where P_o is the impeller power number (dimensionless), N_{rps} is the impeller rotational rate (rps or s^{-1}), and D_{imp} is the impeller diameter (m). Lately, Chapple et al. (2002) reported variation of power number with Reynolds number for three impeller diameters of down-pumping four bladed 45^0 pitched blade impellers. Though there is a gap in data points for the impeller Reynolds number ($Re_{\text{imp}} = N_{\text{rps}} D_{\text{imp}}^2 \rho / \mu$) between 4×10^3 and

1×10^4, the power number varied between 1.1 to 1.3 for impeller Reynolds number ranging from 1×10^3 to 2×10^5. Since the D/T ratio (here T is the tank diameter, m) is equal to 0.43 for the employed pitch-blade impeller and lies between 0.33 and 0.50 as reported by Chapple et al. (2002), an average power number equal to 1.2 is used for the present work. The impeller Reynolds number varied from 2×10^3 to 35×10^3 in the present work. In other words, the impeller Reynolds number was larger than 10^3 in all experiments, resulting in a constant P_o value (=1.2) for the four-bladed, pitched-blade (45^0) impeller (also shown in p. 63, Fig. 3-16 in Oldshue, 1983). The Kolmogorov microscale, η, characterizing the length scale of the energy dissipating turbulent eddies is (Spielman, 1978)

$$\eta = (\nu^3 / \varepsilon)^{1/4} \tag{4.9}$$

The flow conditions within a stirred tank are non-homogeneous (Cutter, 1966), thus the G_{avg} in Eq. (4.7) does not characterize the local velocity gradient (i.e., in the impeller or bulk zones of the mixing tank) or the velocity fluctuations experienced in the stirred tank (Cleasby, 1984; Clark, 1985). It is used solely as a basis for comparison of the various shear rates effect on the aggregation process.

4.3.5 Experimental Procedure

Asphaltenes suspension in toluene-heptane solvent mixture was first mixed at 660 rpm for 15 seconds to break up any agglomerates. The impeller was then set to the desired speed (N_{rps}). For the present study, the impeller diameter (D_{imp}) is 0.045 m, fluid volume in the tank (V_t) is 960×10^{-3} m^3, and for a toluene-to-heptane volume ratio (T:H) of 1:5 in the solvent mixture, the density and viscosity of the suspending fluid is 714.7

kg/m^3 and 0.45×10^{-3} Pa·s, respectively. Hence, combining Eqs. (4.7) & (4.8), the impeller Reynolds number and the volume averaged shear rate (G_{avg}) are calculated using a power number, $P_o = 1.2$, and are shown in Table 4.2. The impeller speeds were chosen carefully to eliminate floc sedimentation. The impeller rotational velocity (N_{rps}) was measured using an optical tachometer (Ono Sokki HT-446).

Table 4.2. Range of Reynolds number and average shear rate for present study

Impeller rotational speed, N_{rps} (rev/s)	Impeller Reynolds number, Re_{imp} ($Re_{\text{imp}} = N_{\text{rps}} D_{\text{imp}}^2 \rho / \mu$)	Average shear rate, s^{-1} $G_{\text{avg}} = \left(\frac{P_o N_{\text{rps}}^3 D_{\text{imp}}^5}{V_t} / \frac{\mu}{\rho} \right)^{1/2}$
36 / 60	1.9×10^3	10
75 / 60	4.0×10^3	28
110 / 60	5.9×10^3	50
160 / 60	8.6×10^3	87
265 / 60	14.3×10^3	186
400 / 60	21.5×10^3	345
660 / 60	35.4×10^3	730

The flocculating suspension is sampled through tygon tubing of 3.0 mm diameter, by means of a peristaltic pump (Masterflex C/L, Cole Parmer) at a rate of about 8.5 mL/min. The pump is located upstream of the flow-through imaging cell to prevent shearing of the aggregates in the pinch portion of the pump prior to size measurements. For all the experiments, samples are withdrawn for recycling from the same location in the tank, about midway between the impeller and the bottom of the tank. This is the location of the re-circulation zone for an axial flow impeller and will provide an accurate sampling of the bulk of the stirred tank (Oldshue, 1983; Clark and Flora, 1991). The tygon tube is held by the cell of the PDA which houses two precisely aligned fiber-optic probes. The optical fibers carry the incident and transmitted light as shown in Fig. 4.5. The light source is a high intensity light-emitting diode and the transmitted light is continuously monitored by a sensitive photodiode. The output from the photodiode is converted to a voltage which consists of a large d.c. component, corresponding to the average transmitted light intensity, together with a small a.c. component or ripple due the fluctuations of the transmitted light as a result of the variations of particle number in the flowing suspension. The dc component is then eliminated by passing the signal through a suitable capacitor and can be seen as output on the display dial of the PDA by depressing the 'DC' switch. The ac component is separated from the d.c. component and amplified by a factor of up to 100. In this way, fluctuations of the order of 1 mV or less in a d.c. signal of 10V can be analyzed. A converter derives the root mean square (r.m.s.) value of the fluctuating ac signal, which can be seen on the display dial by depressing the 'RMS' switch. The PDA also calculates automatically the ratio of r.m.s. to d.c. value and this ratio value can be seen on the display dial of the PDA by depressing the 'RATIO' switch. All outputs can be smoothed by depressing the 'FILTER' switch of the PDA. The display dial shows only the instantaneous value, which existed when the switch was depressed. Both d.c. and r.m.s. readings can be adjusted by use of precision 10-turn gain controls, enabling a wide range of suspension concentrations and conditions to be monitored. The sensitivity of the device can be increased by increasing the rms gain or decreasing the dc gain. Throughout the present study, the PDA instrument was calibrated before each experiment using pure *n*-heptane in the reactor through a flow-through recycle system with the help of a peristaltic pump. The r.m.s. and d.c. gain values were kept constant to set same sensitivity of the equipment for all experiments.

4.3.6 Aggregation Monitoring

The flocculating suspension was monitored continuously by the photometric dispersion analyzer (PDA 2000). Measurements are carried out directly in the transparent tygon tubing by the instrument as the ratio value, R. This ratio value (R) is also known as flocculation index (FI) in the literature, and the present study uses FI notation. Although this is a dimensionless quantity, its value depends on the instrument setting, which in this study was kept constant, and on the tubing transparency, which is assured by using a new tube for each experiment. Hence, for this study, the flocculation index (FI) values are directly comparable, even though the absolute index values are arbitrary (in the range from 0-2.5). The sample is returned to the flocculation vessel after passing through the detector. It should be noted that the pump is located after the detector, so that possible issues of floc break-up by the peristaltic action are minimized. Under the present conditions, the sample takes about 5 seconds to pass from the vessel to the detector, so that a rapid indication of the effect of any change can be noted. The output from the PDA 2000 is converted to digital form through data acquisition board and Labview and the data are stored in a personal computer spreadsheet for subsequent analysis.

4.3.7 Calibration of Ratio value

From the determination of a relationship between the PDA ratio value and the photographic floc size measurement with image analysis, a real time on-line quantitative indication of floc size can be obtained. A linear relationship (Eq. 4.10) is used in the present study to fit the experimental data for asphaltene aggregates (Fig. 4.6).

$$d_{\mathrm{avg}} = a(\mathrm{FI}) + b \tag{4.10}$$

where FI is the flocculation index (i.e. Ratio value output of the PDA), d_{avg} is the number-mean, projected area diameter of the aggregates from captured image; a and b are the fitted parameters of the straight line. The number mean, projected area diameter, d_{avg}, can be defined as

$$d_{avg} = \frac{\sum_{i=1}^{i=k} \eta_i d_i}{\sum_{i=1}^{i=k} \eta_i} \tag{4.11}$$

where d_{avg} is a function of time, η_i is the number of particles counted in the i-th bin, d_i is the middle of the size range of the i-th bin, and k is the total number of bins. The number mean diameter is a good parameter to represent the complete growth process in image analysis and is used as the characteristic size. The coefficients (a and b) are determined by the least square regression analysis. The standard error is applied as the y-axis error bar of experimental data and also to determine the coefficients of the regression line. The relationship, which is developed between the on-line measurement of asphaltene aggregate size and the on-line output parameter, R value of the PDA, is calibrated for two different shear rates to verify reproducibility (Fig. 4.6). Using this relationship the effect of different variables on aggregate size can be studied on-line in real time.

4.3.8 Aggregation Procedure

Initially, 840 mg of bitumen was dissolved in 160 mL of toluene and the solution was added to 800 mL of n-heptane in the stirred tank. Initial high speed stirring at 660 rpm for 15 seconds was provided for proper mixing and homogeneous precipitation of primary asphaltene particles. It can be observed from results that particle growth start from zero flocculation index, which confirms that 15-second rapid stirring is sufficient to completely disperse the primary particles. Then for constant shear experiments, slow stirring at a fixed value ranging from 36 to 160 rpm, were set to allow for floc formation.

For cyclic-shear experiments, the typical stirring conditions were set as following. The aggregates were first allowed to grow at a low stirring speed. Then they were fragmented at a higher stirring speed until the broken aggregates reach a new steady state. The stirring speed was then lowered again, thereby, allowing the formation of the aggregates at the new low stirring speed. The same cycle was repeated few times in order to study the reversibility of floc formation and breakage. For tapered-shear flocculation, the stirring speed was gradually reduced and at each shear rate, a new steady state aggregate size was formed. Continuous sampling and monitoring by PDA was carried out throughout the experiment.

4.4 Results and Discussion

4.4.1 Effect of solvent composition on the growth of asphaltene aggregates

Flocculation of fairly dilute suspensions in a stirred vessel gives a PDA ratio value (R), which varies with time in a manner shown in Fig. 4.7. A similar time-dependent behavior is found for all experiments. The figure represents the effect of the ratio of toluene to n-heptane in the solution on the growth rate of asphaltene aggregates. The stirring speed was set at 36 rpm and asphaltene concentration was 62.5 mg/L for all tests. Fig. 4.7 shows the kinetics of asphaltene particles growth in terms of the flocculation index (FI) as a function of time for a given stirring speed.

Four different solvent compositions were used, i.e. toluene-to-heptane ratio of 1:2, 1:3, 1:5, and 1:7. A large impact of solvent compositions on the aggregate growth was observed. Fig 4.7 shows that from the very beginning, the aggregate growth rate was rapid for higher heptane content in the solution and, similarly, the characteristic relaxation time was significantly smaller. A lower ratio of toluene to n-heptane means lower solubility of asphaltenes and, accordingly, results in a higher particle concentration in the solution. Therefore, a lower toluene-to-heptane ratio provides greater aggregation rate. After heptane addition as aggregation starts, there is a period during which the flocculation index (FI) increases slowly and can be defined as the characteristic relaxation time. This period is followed by a much more rapid rise of the FI until it reaches a maximum. This behavior can be understood in terms of the kinetics of floc growth and break-up in stirred reactors (orthokinetic flocculation). In the early stages, the flocs are very small and collision rates, which depend on cubic power of the particle diameter, are low. With increasing floc size Smoluchowski theory (Elimelech et al., 1995) predicts an increasing collision rate and hence a more rapid flocculation takes place. As flocs grow larger further growth is restricted by the effective shear rate in the stirred vessel and the strength of the flocs. Effectively, flocs growth to a limiting size is determined by the shear rate, the nature of the flocculant and the size of the primary particles (Muhle, 1993). After passing through this limiting size (or, maximum value) for the case of toluene to heptane ratio of 1:7, the average floc size shows a significant decline (similar behavior is also observed by Gregory and Li, 1991, for kaolin clay–tap water system) before leveling off and reaches the final, steady state value. The maximum in the aggregate size can be explained as a result of breakage and also possible restructuring of the large porous flocs produced initially to form more compact structures. Under constant shearing, large open flocs become more compact as the flocs restructure or fragment and reform more durable structures (Bouyer et al., 2001; Spicer et al., 1996). Secondly, as aggregates pass through the regions of high and low shear rates in a stirred tank, reorganization and restructuring can both occur. Restructuring is likely the most prevalent compaction mechanism when a steady state is reached between aggregation and fragmentation during flocculation (Spicer et al., 1998). After several minutes, the aggregates reached a steady state size, which was found to decrease greatly with increasing toluene to heptane ratio in the solution. Though a large variation in the maximum aggregate size is observed for different solvent compositions, there is no significant difference in the final, steady state floc size for toluene-to-heptane ratio of 1:5 and 1:7.

Figure 4.8 also shows that solvent composition has a dramatic effect on the growth of asphaltene aggregates from bitumen. All three experiments are carried out at the stirring speed of 75 rpm and initial bitumen concentration of 875 mg/L. The ratio values are interpreted in terms of the number-mean, projected area diameter of the flocs by the image analysis of captured microphotographs (described in section 4.3.7) and are represented on the right hand secondary y-axis. The growth rate is higher when the solvent mixture is richer in heptane. A maximum in the aggregate size was also observed at the toluene to heptane ratio of 1:7. Also in this case, the aggregates reached a maximum size very rapidly and then went through restructuring or reorganization.

4.4.2 Effect of particle concentration on aggregate growth

Aggregation of asphaltenes suspension in toluene-heptane solvent mixture for various initial asphaltenes concentration gives results as shown in Fig. 4.9. The stirring speed was set at 75 rpm and toluene-to-heptane ratio was 1:5 for both experiments. As the asphaltene particle concentration increases there is a significant increase in the rate of rise of the FI value and an increasing plateau value, indicating larger flocs. It can be observed from Fig. 4.9 that a higher particle concentration provides a smaller relaxation time for visible floc formation and increases the initial aggregation rate (observed from the initial slopes of the curves) by decreasing the average distance between particles, thus reducing the characteristic time between collisions. The dynamic balance between the floc growth and breakage determines the average floc size that is attained at steady state. Increasing particle volume fraction in the suspension (φ) leads to an increase in the aggregation rate to a much greater extent than the fragmentation rate and consequently, a larger steady state floc size is reached. A larger φ also results in a faster attainment of maximum floc size than at lower asphaltenes volume fraction because of the accelerated kinetics of both aggregation and fragmentation. This behavior is in excellent qualitative agreement with experimental literature data. Oles (1992) observed with dispersion of polystyrene latex in 1.16 mol NaCl and ultrapure water solution that the time required to attain steady state was of the order of hours for $\varphi = 10^{-5}$, whereas Gregory and Li (1991) found that flocculating particles of kaolin clay in tap water reached a steady state at φ =

0.1 in only a few minutes. A similar behavior is observed in Fig. 4.7, where lower toluene-to-heptane ratio in the solution (i.e. higher particle concentration) provides faster aggregation rates. A maximum in the average floc size is found for both the curves. After the attainment of the maximum floc size, the average floc diameter begins to decrease as a result of the floc restructuring or reorganization. Restructuring is likely the most prevalent compaction mechanism when a steady state is reached between aggregation and fragmentation during flocculation.

Figure 4.10 shows the effect of initial bitumen concentration on the growth of asphaltene flocs. All three tests are carried out at a stirring speed of 75 rpm and toluene-to-heptane ratio of 1:5. Heptane insoluble asphaltenes content of the Athabasca bitumen is about 16 wt.%. The initial bitumen concentration varied from 625 mg/L to 1125 mg/L. It can be noticed that higher bitumen concentration gives earlier and faster aggregation (from the slopes of the curves) as well as larger floc sizes. Also, there is significant difference in the final, steady state floc size for different initial bitumen concentrations in solution. It can be inferred from Fig. 4.10 that at a bitumen concentration of 1125 mg/L, more open and porous asphaltene aggregates are formed rapidly as a maximum in the average floc size was observed, after which the floc diameter began to decrease as a result of the floc breakage and also possibly restructuring.

4.4.3 Effect of stirring speed on floc growth

The plots in Fig. 4.11 exhibit the kinetics of asphaltene aggregates growth under shear. A large influence of stirring speed on the aggregate steady-state size was observed. Three different stirring speeds were used, i.e. 75, 110 and 160 rpm. Initially the aggregate growth rate was rapid and it was nearly the same within the range of the applied stirring speed. After few minutes the aggregates reached a steady state size, which was found to decrease with increasing stirring speed.

4.4.4 Effect of bitumen source on asphaltene floc growth

Figure 4.12 shows the effect of bitumen source on asphaltenes aggregation. For the froth-extracted bitumen, the bitumen was obtained after froth treatment using naphtha from the commercial oil-sands extraction plant. For the case of solvent-extracted bitumen, the bitumen was extracted from oil sands using toluene in the laboratory. In both cases, the stirring speed was kept at 75 rpm, toluene-to-heptane volume ratio was 1:5, and the initial bitumen concentration was 875 mg/L. Though the extraction procedure is completely different for the two types of bitumen, they are totally identical for asphaltenes aggregation, both in terms of growth kinetics and average aggregate size.

4.4.5 Effect of Maltenes

The molecular composition of the Athabasca Bitumen is best described in terms of the solubility classes. In terms of the weight percent, the classes are –Saturates (15-21%), Aromatics (18-30%), Resins (29-49%), and Asphaltenes (16-22%) (Yarranton, 1997). The heptane soluble part of bitumen (i.e. saturates, aromatics, and resins, collectively) is known as maltenes. After asphaltenes precipitation has taken place through the addition of heptane to the bitumen, redissolution is observed when heptane is evaporated from the bitumen-heptane mixture. The aromatic high-molecular-weight asphaltenes are peptized by the maltenes (most likely the resins contained in the maltenes) (Ignasiak and Strausz, 1978). Similarly, once asphaltene is precipitated in heptane and separated by filtration, asphaltene can be resolubilized in toluene even in the absence of maltenes. However, it should be noted that redissolution may sometimes be very slow (Roux et al., 2001). Although the presence of resins is not a prerequisite, resins efficiently co-solubilize asphaltenes: addition of extra maltenes often prevents precipitation or even permits re-solubilization of precipitates (Sheu and Storm, 1995).

Figure 4.13 reveals important information about the effect of maltenes on asphaltenes aggregation. It demonstrates the difference in asphaltenes aggregate growth between two systems containing the same asphaltene concentrations. The stirring speed is kept at 75 rpm, and the toluene-to-heptane ratio is 1:5. The upper curve shows the kinetics of asphaltene aggregates growth with extracted asphaltenes in toluene-heptane mixture and the asphaltenes concentration used was 93.75 mg/L. The lower curve exhibits the growth of asphaltene aggregates with bitumen in same solvent mixture having a bitumen concentration of 625 mg/L. It has been reported that the heptane insoluble asphaltenes content of Athabasca bitumen is 16±1 wt.%. Even if the lowest weight percentage of asphaltenes content is considered, i.e. 15 %, it gives an equivalent asphaltenes concentration of about 94 mg/L in the used bitumen concentration of 625 mg/L. Hence, for both the experiments, the asphaltenes concentration can be assumed to be the same. But, a large difference in growth kinetics is observed, though the final, steady state aggregate size is found to be the same after sufficiently long time. It implies that the presence of maltenes plays a very significant role in the aggregation kinetics of asphaltenes, which is important to know from practical viewpoint.

4.5 Practical Implications

4.5.1 Cyclic shear

The effect of shear history on the evolution of the asphaltene floc size is investigated by PDA during cyclic-shear flocculation in a stirred tank. Flocs produced by cyclic-shear flocculation are grown at constant stirring speed of 110 rpm for 60 minutes, then are fragmented at 660 rpm for 15 seconds and are re-formed (re-grown) at 110 rpm. The same cycle is repeated three times. Fig. 4.14 shows the evolution of average aggregate size (d_{avg}) during cyclic-shear growth of asphaltenes aggregates. As shown in Fig. 4.14, the particle size increases rapidly while aggregation dominates at early times and reaches steady state value of 70 μm. At 60 min, d_{avg} drops immediately to a minimum value of about less than 40 μm during the fragmentation period. After 15 s of fragmentation, as the stirring rate is returned to 110 rpm, the aggregates grow to a new steady-state size. In Fig. 4.14, the new steady-state average aggregate size (d_{avg}) is about 50, 47, and 44 μm for each cycle, respectively. The steady state floc size is found to be smaller for each subsequent cycle. At certain stirring speed, there appears to be no unique "steady-state aggregate size", it depends on the shear history of the aggregates. It is observed that a change in the applied shear rate drives the suspension from one steady state to a new steady state. By lowering or raising the shear rate, larger or smaller aggregates are formed, respectively. When the aggregates (flocs) attained the first steady state, they were fragmented using high shear and then if the original shear rate was re-applied, two types of behavior have been observed experimentally by the researchers: reversible and irreversible behavior.

It has been reported that for particle suspensions destabilized by increase of the ionic strength (i.e. adding NaCl), when the original shear rate is re-applied, the steady state average floc size returns to its original steady state value. Such suspensions exhibit reversible floc dynamics because floc fragmentation and re-growth do not affect the van der Waals binding forces between primary particles (Kusters, 1993). The steady state floc size distribution (FSD) for reversible systems is independent of initial conditions (Chen et al., 1990).

When the flocculant is a precipitated solid (i.e. $Al(OH)_3$) or polymer, the suspension exhibits irreversible floc dynamics. Francois (1987) studied kaolin- $Al(OH)_3$ floc fragmentation and reformation at various shear rates in stirred tanks. In all cases, flocs formed again but did not attain their previous steady state average size. He explained this finding as floc formation by a multi-level progression: primary particles combined to form dense microflocs, which in turn combined to form the next level and so on. Leu and Ghosh (1988) flocculated kaolin suspensions with a polyelectrolyte and observed a similar behavior: flocs are reformed after intense fragmentation but did not attain their original steady state average size. They attributed this behavior to the detachment of polymer chains from kaolin particles, resulting in reduced collision efficiency and, thus, smaller aggregates. Clark and Flora (1991) studied cycled-shear flocculation of polystyrene-$Al(OH)_3$ flocs by image analysis of flocs microphotographs. The flocs, formed at 35 s^{-1}, fragmented at 150-1800 s^{-1}, and re-formed at 35 s^{-1}, exhibited increasingly compact structures but no clear size variation trend was observed. Glasgow and Liu (1995) found that kaolin-polymer flocs were more dense following cyclic-shear flocculation with cyclic introduction of additional flocculant.

The irreversibility of aggregates during cyclic shear is most likely the result of particle-flocculant bond breakage during fragmentation. Once broken, these bonds are not able to reform to their previous extent, reducing the efficiency of subsequent aggregate-aggregate attachments (Leu and Ghosh, 1988). Extensive numerical simulations indicate that a reduction in the collision efficiency of aggregates produces more compact, smaller structures relative to the case when collisions are 100% successful. This results from the need for the colliding aggregates to interpenetrate further than before if successful collisions are to occur (Clark and Flora, 1991; Meakin, 1988). Thus, intense shearing produces fragmentation that, by breaking the particle-flocculant bonds in turn reduces the "stickiness" of the resulting fragments. As a result, the efficiency of subsequent collisions is reduced and smaller, more compact aggregate structures are produced by these collisions.

As aggregates pass through regions of high and low shear rates in a stirred tank, both reorganization and restructuring can occur. Restructuring is likely the most prevalent compaction mechanism when a steady state is reached between aggregation and fragmentation during flocculation. As a result, the deliberate application of a cyclic shear schedule is an excellent way to study the incidental long-term microscopic aging effects brought about by many passes of aggregates through the higher shear impeller region of a stirred tank. This is because intentionally higher shear rates reduce the Kolmogorov microscale to the extent that most particles are fragmented and the cyclic-shear effect is more homogeneous.

Irreversible flocculation offers a simple method of increasing floc compactness and suggests that some degree of floc fragmentation by fluid shear may not always be undesirable. In addition, this type of cycling of the average floc structure has been shown to have profound effects on the viscosity of more concentrated suspensions (Stewart and Sutton, 1984; 1986; Mills et al., 1991; Tsutsumi et al., 1994). As a result it is of interest to accurately characterize floc compaction and determine the best means of bringing it about.

Collectively, Fig. 4.15 shows the results from three different experiments. Once the flocs are formed and reached steady state at 75 rpm, the stirring speed is increased to either 160, 400 or 660 rpm. After the increase in the stirring speed the flocs break-up rapidly and their size decreases. The higher the breakage shear rate, the lower the minimum value of average aggregate size (d_{avg}) as a result of increased fragmentation. After a complete breakage of the flocs, a new steady state re-establishes itself. In Fig. 4.15, the new steady-state average floc size is about 45 μm for the breakage shear rate of 160 rpm, and the other two new steady-state average floc size is less than 40 μm (i.e. below the calibration range) for breakage shear rate equal to 400 and 660 rpm. The stirring speed is then reduced to 75 rpm and again a new steady state aggregate size is reached. This is significantly smaller than the original (i.e. previous) one ($d_{\text{avg}} \cong 100$ μm), indicating that the employed suspension exhibits *irreversible* behavior. The flocs do not grow to their original size prior to the initial increase in the stirring speed. A repeat in increasing and decreasing the stirring speed gives new steady state floc sizes. In all cases, the final floc size is smaller. However, the steady-state floc size at 75 rpm for three separate curves in each cycle was found to be almost same though the small fragment sizes (or, microflocs) were significantly different from each other due to three separate fragmentation stirring speeds applied.

4.5.2 Tapered shear

The results shown in Figs. 4.14 and 4.15 indicate that even a small step increase in the applied shear rate can produce smaller but more compact flocs. The latter can be inferred from the settling behavior of flocs produced at different shear rates and is discussed in the next chapter. This may have some interesting implications in floc removal from suspensions since this is the primary goal of using flocculation in most chemical processes. As the goal is usually to make large and compact flocs, an optimal shear rate schedule may exist with respect to floc sedimentation. Thus, it is useful to compare the above cyclic-shear flocculation method with more traditional methods.

The concept of tapered-shear flocculation, i.e. the gradual reduction of the applied shear rate in order to minimize fragmentation but maximize mixing and particles collision rate, has been used to improve flocculation performance. In theory, tapered-shear flocculation should perfectly exploit floc irreversibility because it tends to form flocs from compact microflocs versus open structures resulting from conventional constant shear flocculation.

Figure 4.16 shows the evolution of average aggregate size (d_{avg}) during a typical tapered-shear flocculation experiment using four stirring speeds, 265 rpm, 160 rpm, 110 rpm, and 75 rpm, applied for more than 35 minutes each. Initially, a rapid initial growth is observed as particle collisions increase the average floc size. After about 7 minutes, the floc growth rate slows down and the average floc size reaches a smaller steady-state value, which is below the minimum calibration range of 40 μm. Subsequent steady states are obtained with gradual decrease in the stirring speed. After about 35 minutes, when the stirring rate is reduced to 160 rpm, the average floc size increases to level off at a value that is less than 40 μm (i.e. below the calibration range). At 80 minutes, further reduction of stirring speed to 110 rpm causes another increase in the floc size, but still less than 40 μm (i.e. below the calibration range). Finally, at 125 minutes, reduction of the stirring speed to 75 rpm further increases d_{avg} to a final steady state value of about 50 μm. Floc growth always takes place upon decreasing the stirring speed. But the final steady state aggregate size obtained at 75 rpm by tapered-shear (≅ 50 μm) is almost half the size of the steady state d_{avg} (≅ 95 μm) reached during aggregation at constant stirring speed of 75 rpm (Fig. 4.16). This is due to exposure of the aggregates to high shear for a time sufficient to reduce the "stickiness" (which might be due to loss of active sites or change of surface structures) between particle attachments such that the flocs re-form rather poorly. This behavior indicates that there is an upper limit to the irreversibility benefits to flocculation and that an optimal shear cycle may exist for a given system. Furthermore, cyclic-shear flocculation may be more economical than tapered-shear flocculation because of the smaller energy input required, as high shear is applied for only a short period. This short fragmentation period can be specially advantageous in bio-separations where excessive shearing should be avoided to minimize rupture of fragile cells (Shamlou and Tichener-Hooker, 1993).

4.6 Conclusions

An experimental study was carried out on the effects of initial asphaltene concentration, solvent type and composition, and shear schedule during aggregation of asphaltenes in a stirred tank. The effect of shear history on the evolution of the asphaltenes aggregate size was investigated during cyclic- and tapered- shear flocculation. The evolution of the average floc size was monitored by the Photometric Dispersion Analyzer (PDA). The ratio output of the PDA was calibrated by image analysis of the captured photographs of asphaltene flocs. Dynamic monitoring by PDA provides instantaneous information on floc growth, break-up and re-formation. After a certain period of time, the average floc size reached a steady state size as a result of the competition between aggregation and fragmentation. An increase in the stirring speed decreased the steady state size of the aggregates, but the characteristic relaxation time was almost identical within the applied range of shear rates. For a fixed stirring speed, increasing volume fraction of particles as well as increasing the ratio of heptane in the solution greatly enhanced the aggregation rate and increased the final, steady state floc size.

Whether aggregation takes place with extracted asphaltenes or with bitumen, it can be inferred from the aggregation kinetics that, above a critical concentration of asphaltenes in the toluene-heptane solvent mixtures, the same aggregates exhibit restructuring or reorganization after the attainment of the maximum size. The kinetics of restructuring is more pronounced when the aggregates are produced from extracted asphaltenes.

Cyclic- and tapered- shear schedule generally decreases the floc size. A change in the applied stirring speed drives the floc size from one steady state to a new steady state. Once the flocs attained the first steady state during cyclic shear flocculation, they were fragmented using high stirring speed. After that when the original stirring speed was restored, *not fully reversible* behavior was observed. The irreversibility of aggregates during cyclic shear is most likely the result of particle-aggregate bond breakage during fragmentation. Once broken, the resulting fragments attain reduced "stickiness" (which might be due to loss of active sites or change of surface structures) and are not able to form again to their previous extent, thus reducing the efficiency of subsequent aggregate-aggregate attachments. Hence "shear history" plays an important role in achieving the final, steady state floc size.

Cyclic and tapered- shear flocculation appears more advantageous than constant-shear flocculation for production of fast settling particles for particle removal by inertial processes (settling, centrifugation, etc.).

4.7 Nomenclature

A	cross-sectional area of the light beam in PDA
C	average scattering cross section of the suspended particles (m^2)
d_{avg}	number mean projected area diameter (μm)
d_i	average diameter of the particle sizes contained within bin i (μm)
D_{imp}	impeller diameter (m)
FI	flocculation index (i.e. Ratio value output of the PDA)
G_{avg}	mean shear rate (s^{-1})
I	transmitted light intensity
I_o	incident light intensity
L	optical path length (mm)
M	mass (kg)
n	average number of particles in the optical cell ($=NAL$)
N	number concentration of particles
N_{rps}	impeller rotational rate (rps or s^{-1})
PDA	photometric dispersion analyzer
P_{liq}	energy dissipated into the liquid (Watts)
P_o	impeller power number

R	ratio value, (r.m.s./d.c.)
Re_{imp}	impeller Reynolds number, $Re=N_{rps}D_{imp}^{2}\rho/\mu$
V	time averaged d.c. voltage for transmitted light intensity
V_o	time averaged d.c. voltage corresponding to the incident light intensity
V_{rms}	time averaged r.m.s. voltage of the PDA
V_t	suspending fluid volume in the stirred tank (m^3)

Greek

μ	viscosity of the suspending liquid (Pa·s)
ν	kinematic viscosity of the fluid (m^2/s)
ε	energy dissipation rate per unit mass (m^2/s^3)
ρ	density of the fluid (kg/m^3)
η	Kolmogorov microscale (μm)
η_i	number of particles counted in the *i*-th bin

4.8 Literature Cited

Amirtharajah, A. (1978). Design of Rapid-Mix Units. *In Water Treatment Plant Design for the Practicing Engineer*, ed. by R. L. Sanks. Ann Arbor Science, Michigan.

Amirtharajah, A. and O'Melia, C. R. (1990). Coagulation Processes: Destabilization, Mixing, and Flocculation. *In Water Quality and Treatment*. McGraw-Hill, NY.

Bouyer, D., Line, A., Cockx, A., and Do-Quang, Z. (2001). Experimental Analysis of Floc Size Distribution and Hydrodynamics in a Jar-Test. *Chem. Eng. Res. Des.*, 79, 1017.

Buckley, J. S., Hirasaki, G. J., Liu, Y., Von Drasek, S., Wang, J. X., and Gill, B. S. (1998). Asphaltene precipitation and solvent properties of crude oils. *Pet. Sci. Technol.,* 16, 251.

Burgess, M. S., Phipps, J. S., and Xiao, H. (2000). Flocculation of PCC Induced by Polymer/Microparticle Systems: Floc Characteristics. *Nordic Pulp and Paper Research Journal*, 15 (5), 572-578.

Camp, T.R. and Stein, P.C. (1943). Velocity gradient and internal work in fluid motion. *J. Boston Soc. of Civ. Engrs.*, 30(4), 219-237.

Chapple, D., Wall, A., Afacan, A., and Kresta, S. M. (2002). The effect of impeller and tank geometry on power number for a pitched blade turbine. *Trans IChemE*, 80(A), 364-371.

Chen, W., Fisher, R. R., and Berg, J. C. (1990). Simulation of Particle size Distribution in an Aggregation-Breakup Process. *Chem. Eng. Sci.*, 45, 3003.

Ching, H. W., Tanaka, T. S., and Elimelech, M. (1994). Dynamics of Coagulation of Kaolin Particles with Ferric Chloride. *Wat. Res.*, 28(3), 559-569.

Cimino, R., Correra, S., Del Bianco, A., Lockhart, T. P. (1995). In *Asphaltenes: Fundamentals and Applications*; Sheu, E. Y., Mullins, O. C., Plenum Press, New York, Chapter III, p 111.

Clark, M. M., and Flora, J. R. V. (1991). Floc Restructuring in Varied Turbulent mixing. *J. Colloid Interf. Sci.*, 147 (2), 407.

Clark, M. M. (1985). Critique of Camp and Stein rms Velocity-Gradient. *J. Env. Eng. Div. – ASCE,* 111(6), 741-754.

Cleasby, J. L. (1984). Is Velocity-Gradient a Valid Turbulent Flocculation Parameter. *J. Env. Eng.,* 110(5), 875-897.

Cutter, L. A. (1966). Flow and turbulence in a stirred tank. *AIChE J.*, 12, 35-45.

Elimelech, M., Gregory, J., Jia, X., and Williams, R. A. (1995). Particle Deposition and Aggregation. Measurement, Modelling and Simulation. Chapter 6, Butterworth Heinemann, Oxford.

Francois, R. J. (1987). Strength of Aluminum Hydroxide Flocs. *Wat. Res.*, 21(9), 1023.

Francois, R. J. (1988). Growth Kinetics of Hydroxide Flocs. *J. Am. Wat. Wks. Ass.*, 80, 92-96.

Friedlander, S. K. (1977). *Smoke, Dust, and Haze*, Wiley, New York.

Glasgow, L. A., and Liu, S. X. (1995). Effects of Dosing Regimen and Agitation Profile upon Floc Characteristics. *Chem. Eng. Commun.*, 132, 223-237.

Godfrey, J. C., Obi, F. I. N., and Reeve, R. N. (1989). Measuring Drop Size in Continuous Liquid-Liquid Mixers. *Chem. Eng. Prog.*, 85 (12), 61-69.

Gregory, J., and Li, G. B. (1991). Effects of Dosing and Mixing Conditions on Polymer Flocculation of Concentrated Suspensions. *Chem. Eng. Comm.*, 108, 3-21.

Gregory, J. (1989). Fundamentals of flocculation. *Critical Reviews in Environmental Control*, 19(3), 185-230.

Gregory, J. (1988). Polymer Adsorption and Flocculation in Sheared Suspensions. *Colloids and Surfaces*, 31, 231-253.

Gregory, J., and Nelson, D. W. (1986). Monitoring of Aggregates in Flowing Suspensions. *Colloids and Surfaces*, 18, 175.

Gregory, J. (1985). Turbidity fluctuations in flowing Suspensions. *J. Colloid Interf. Sci.*, 105, 357.

Gregory, J., and Nelson, D. W. (1984). A New optical Method for Flocculation Monitoring. in *Solid-Liquid Separation*, ed. by J. Gregory, Ellis Horwood, England, 172-182.

Hirschberg, A., de Jong, L. N. J., Schipper, B. A., Meijer, J. G. (1984). *SPE J.*, paper SPE11202, p 283.

Ignasiak, T. M. and Strausz, O. P. (1978). Reaction of Athabasca asphaltene with tetralin. *Fuel*, 57, 617-621.

Jullien, R., and Meakin, P. (1989). Simple Models for the Restructuring of Three-Dimensional Ballistic Aggregates. *J. Colloid Interf. Sci.*, 127, 265-272.

Kusters, K. A., Pratsinis, S. E., Thoma, S. G., and Smith, D. M. (1993). Ultrasonic Fragmentation of Agglomerate Powders. *Chem. Eng. Sci.*, 48, 4119.

Lawler, D. F., Izuieta, E., and Kao, C. P. (1983). Changes in Particle Size Distributions in batch Flocculation. *J. Am. Wat. Wks. Ass.*, 75, 604-612.

Leontaritis, K. J., and Mansoori, G. A. (1987). *SPE International Symposium on Oilfield Chemistry*; Society of Petroleum Engineers: Richardson, TX, paper SPE 16258.

Leu, R. J., and Ghosh, M. M. (1988). Poly-electrolyte Characteristics and Flocculation. *J. Am. Water Works Assoc.*, 80 (4), 159.

Li, G. B., and Gregory, J. (1991). Flocculation and Sedimentation of High-Turbidity Waters. *Water. Res.*, 25(9), 1137-1143.

Meakin, P. (1988). Fractal Aggregates. *J. Colloid Interf. Sci.*, 28 (4), 249.

Mills, P. D. A., Goodwin, J. W., and Grover, B. W. (1991). Shear Field Modification of Strongly Flocculated Suspensions – Aggregate Morphology. *Colloid Polym. Sci.*, 269 (9), 949.

Monk, R. D. G., and Trussell, R. R. (1991). Design of Mixers for Water Treatment Plants: Rapid Mixing and Flocculators. *In Mixing in Coagulation and Flocculation,* ed. by Amirtharajah, A., Clark, M. M., and Trussell, R. R. American Water Works Association Research Foundation, Denver, Colorado.

Muhle, K. (1993). Floc Stability in Laminar and Turbulent Flow. in Coagulation and Flocculation, ed. by Dobias, B., Marcel Dekker, New York.

Oldshue, J. Y. (1983). Fluid Mixing Technology. McGraw–Hill, New York.

Oles, V. (1992). Shear-Induced Aggregation and Breakup of Polystyrene Latex Particles. *J. Colloid Interf. Sci.*, 154, 351.

Porte, G., Zhou, H., and Lazzeri, V. (2003). Reversible Description of Asphaltene Colloidal Association and Precipitation. *Langmuir,* 19 (1), 40 -47.

Reich, I. & Vold, R. D. (1959). Flocculation-deflocculation in agitated suspensions. I. Carbon and ferric oxide in water. *Journal Physical Chemistry, 63*, 1497-1501.

Roux, J. N., Broseta, D., Demé, B. (2001). SANS study of asphaltene aggregation: Concentration and solvent quality effects. *Langmuir*, *17*, 5085.

Serra, T., Colomer, J., and Casamitjana, X. (1998). Effect of the Shear and Volume Fraction on the Aggregation and Breakup of Particles. *AIChE J.*, 44 (8), 1724.

Shamlou, P. A. and Tichener-Hooker, N. (1993). Turbulent Aggregation and Breakup of Particles in liquids in Stirred Vessels. in *Processing of Solid-Liquid Suspensions*, ed. by P. A. Shamlou, Butterworth Heinemann, Oxford, 1-25.

Sheu, E. Y., and Storm, D. A. (1995). Colloidal properties of asphaltenes in organic solvents. In *Asphaltenes*: *Fundamentals and Applications,* ed. by E. Y. Sheu, and O. C. Mullins, Plenum Press, New York, Chapter I, p 1.

Spicer, P.T., Pratsinis, S.E., Raper, J.A., Amal, R., Bushell, G., and Meesters, G.M.H. (1998). Effect of Shear Schedule on particle Size and Structure during Flocculation in Stirred Tanks. *Powder Technol*, 97, 26-34.

Spicer, P. T., Keller, W. and Pratsinis, S. E. (1996). The Effect of Impeller Type on Floc Size and Structure During Shear-Induced Flocculation. *J. Colloid Interf. Sci.*, 184, 112.

Spielman, L. A. (1978). Hydrodynamic aspects of Flocculation. In *The Scientific Basis of Flocculation,* ed. by K. J. Ives, Sijthoff, and Noordhoff, The Netherlands.

Stephenson, W. K. (1990). *Pet. Eng. Int., 6,* 24.

Stewart, R. F., and Sutton, D. (1984). Control of Structure in Particulate Solids Suspensions. in *Solid-Liquid Separation*, ed. by J. Gregory, Ellis Horwood Ltd., Chichester, 111.

Thomas, D. G. (1964). Turbulent Disruption of Flocs in Small Particle Size Suspensions. *AIChE J.*, 10, 517-523.

Tsutsumi, A., Yoshida, K., Yui, M., Kanamori, S., and Shibata, K. (1994). Shear Viscosity Behavior of Flocculated Suspensions. *Powder Technol.*, 78 (2), 165.

Yarranton, H. W. (1997). *Asphaltene Solubility and Asphaltene Stabilized Water-in-Oil Emulsions*. Ph.D. Thesis, University of Alberta, pp 20,66.

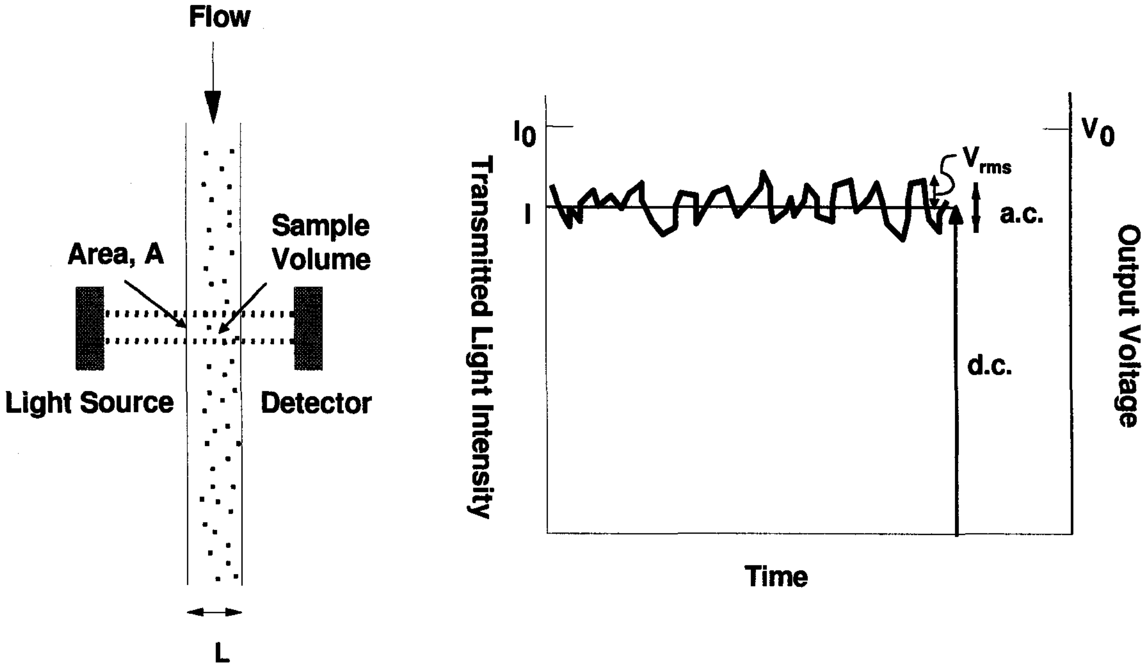

Figure 4.1. Principle of the PDA monitoring technique (Gregory and Nelson, 1984). The intensity of light transmitted through a flowing suspension shows random fluctuations about the mean. The r.m.s value of the fluctuations is monitored continuously.

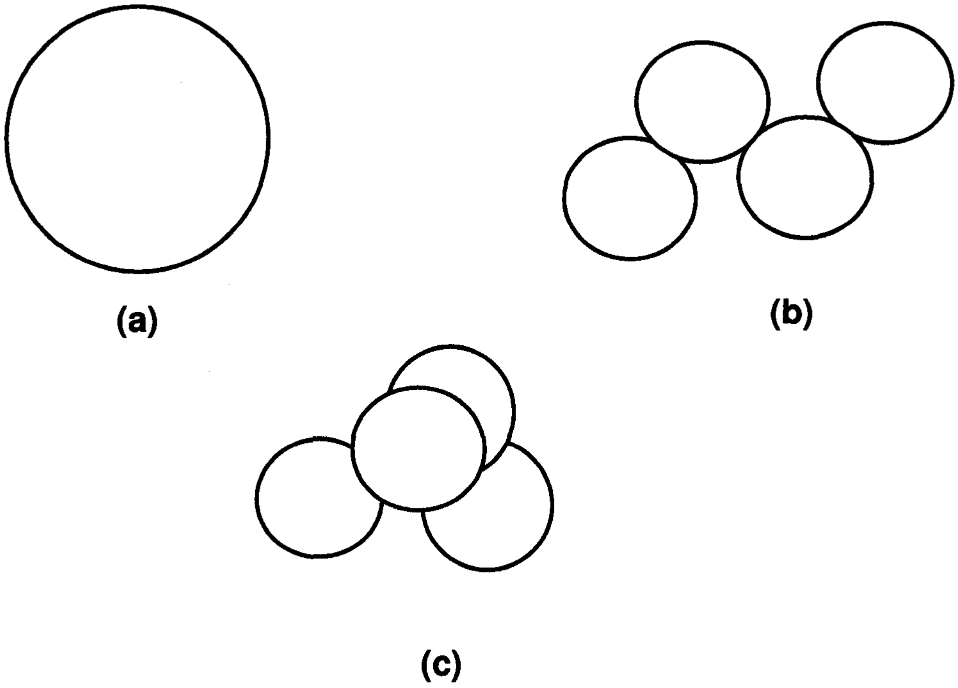

Figure 4.2. Forms of aggregates composed of four equal spheres. (a) Coalesced sphere, (b) Extended aggregate (e.g. aligned by flow), (c) Randomly oriented aggregate (Gregory and Nelson, 1984).

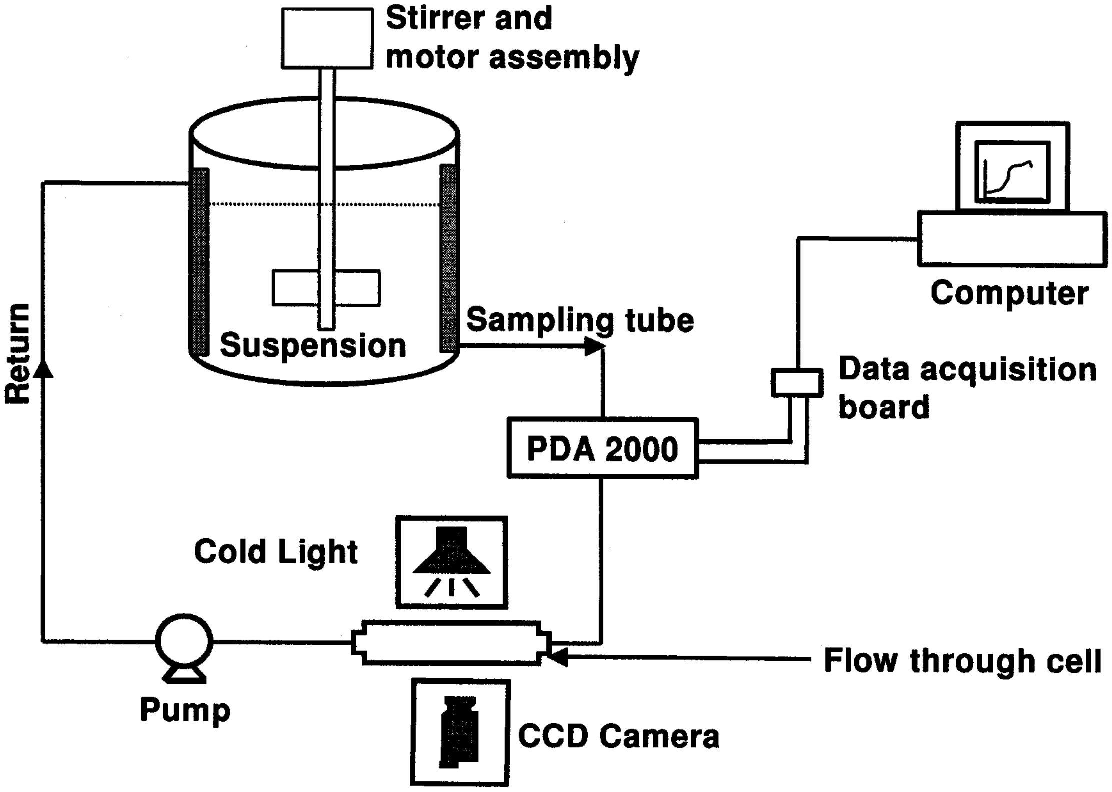

Figure 4.3. Schematic of the experimental setup to monitor the kinetics of asphaltenes flocculation by the PDA 2000.

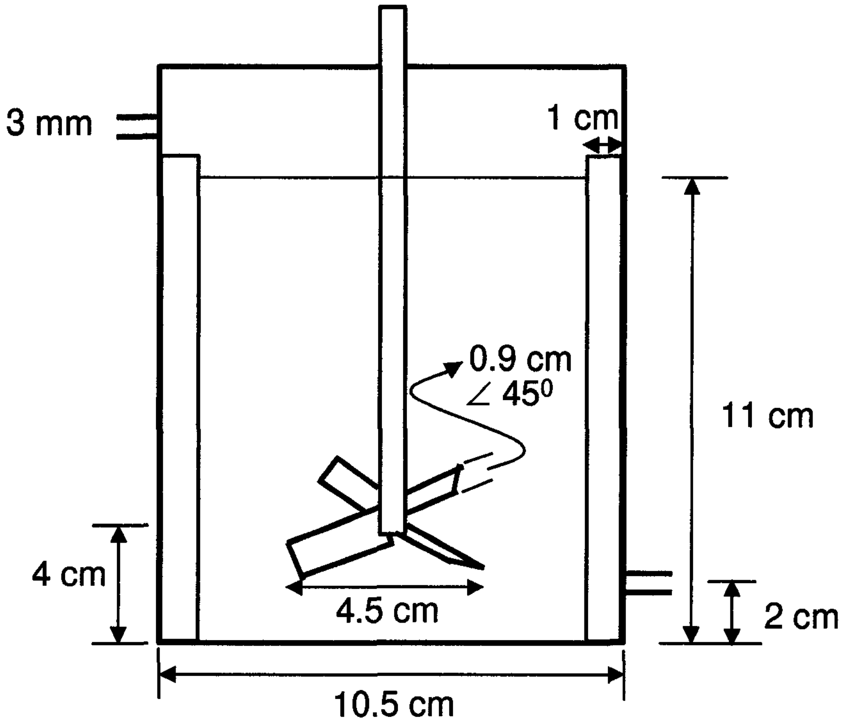

Figure 4.4. Schematic diagram of the stirred tank and the 45° angled 4-blade pitch turbine used for the asphaltene flocculation experiments.

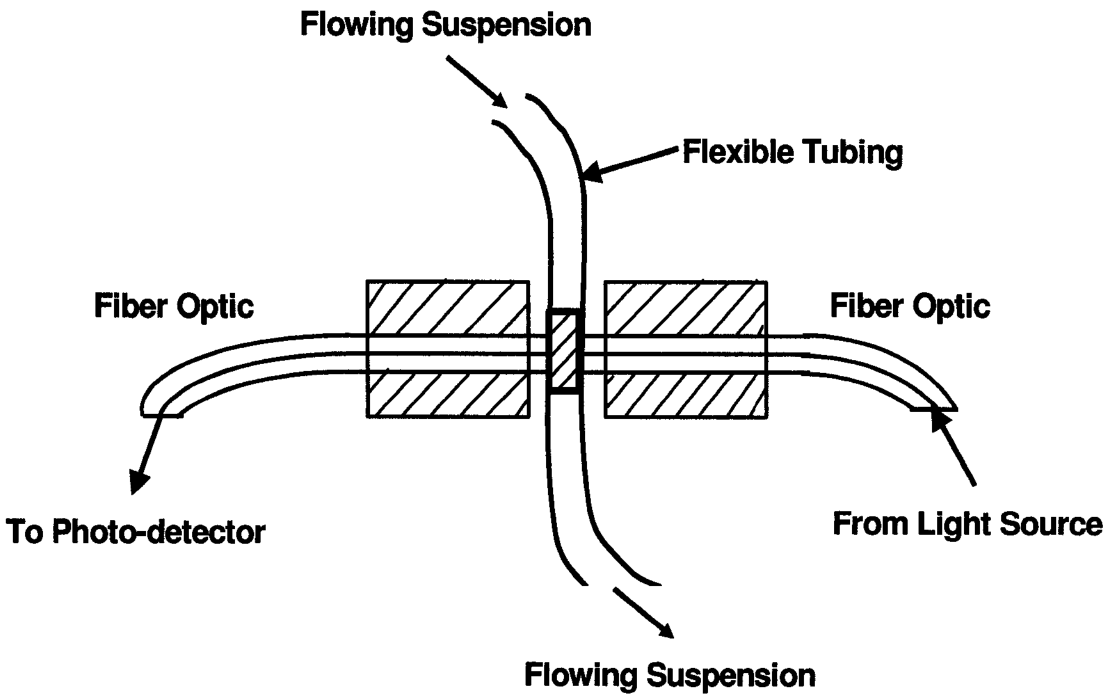

Figure 4.5. Schematic of the flow cell of PDA.

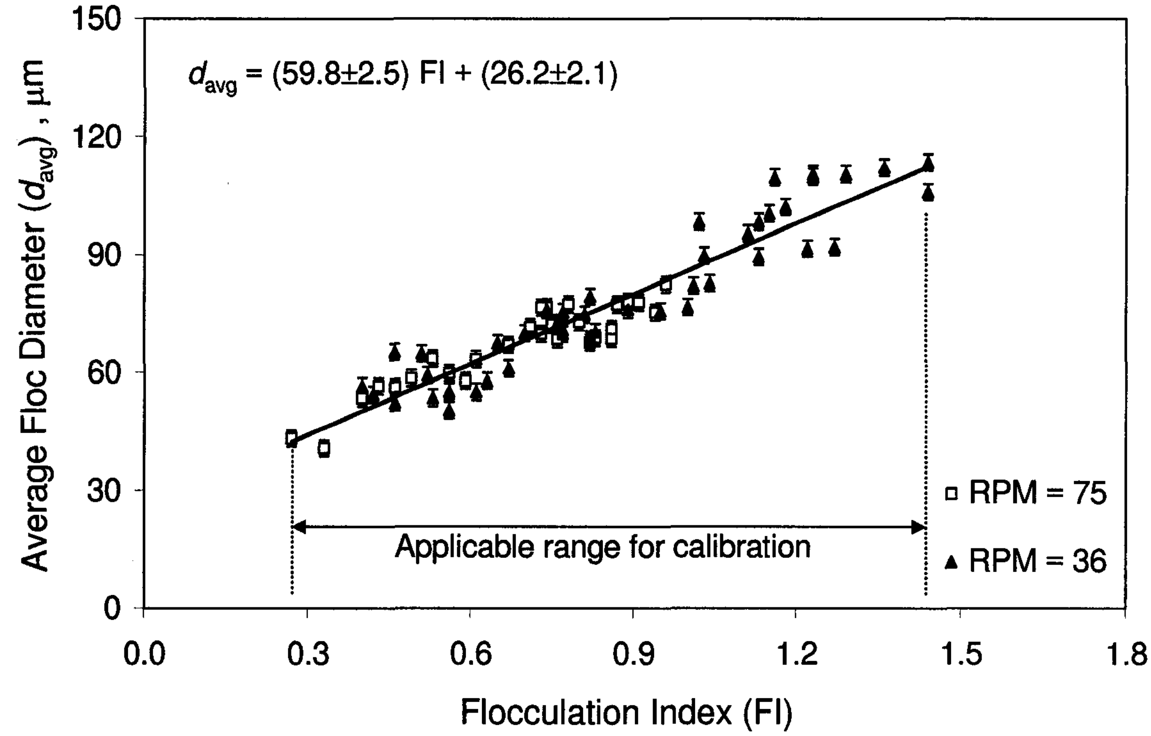

Figure 4.6. Relationship between the floc size and the ratio value. This calibration is used for on-line monitoring the growth of asphaltene flocs in real time. Flocculation tests are carried out with extracted and purified asphaltenes at toluene-to-heptane ratio (T:H) of 1:5 in solvents mixture and initial asphaltenes concentration of 62.5 mg/L. The standard error is applied as the y-axis error bars of experimental data and is also shown for the coefficients of the regression line.

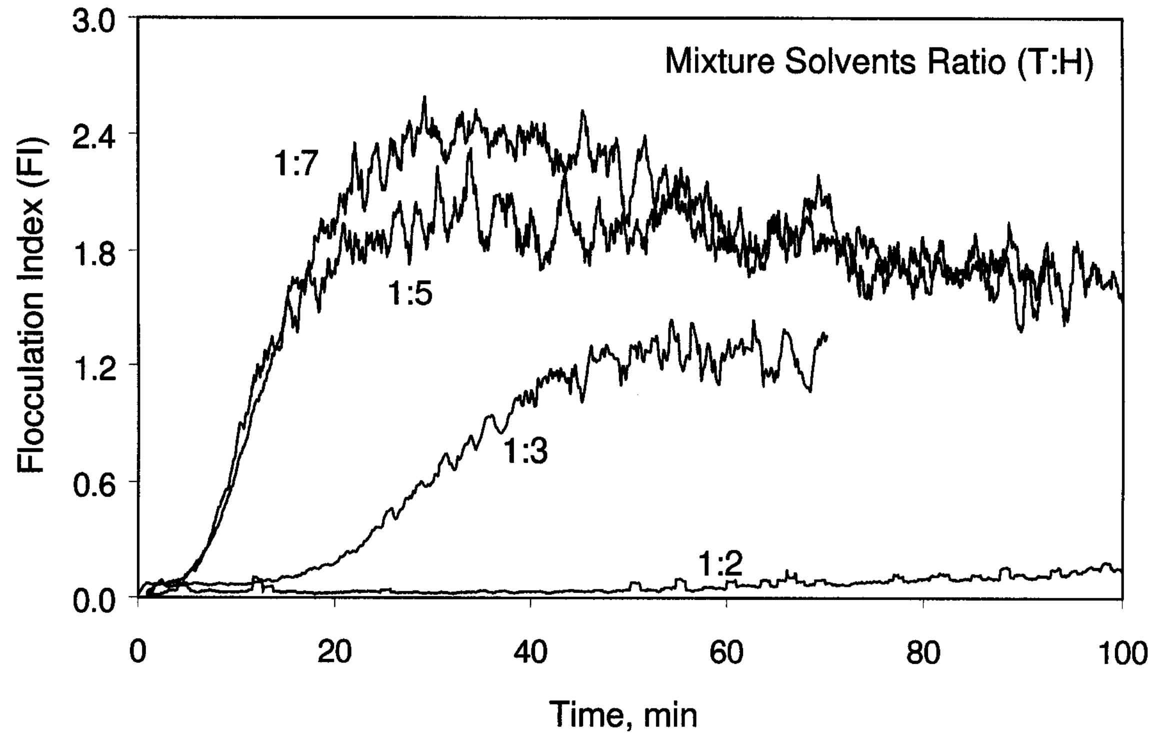

Figure 4.7. Evolution of FI value with time for asphaltene aggregates at various solvent compositions (i.e. toluene-to-heptane ratio in solvent mixtures). Flocculation tests are carried out with extracted asphaltenes at stirring speed of 36 rpm, and initial asphaltenes concentration of 62.5 mg/L.

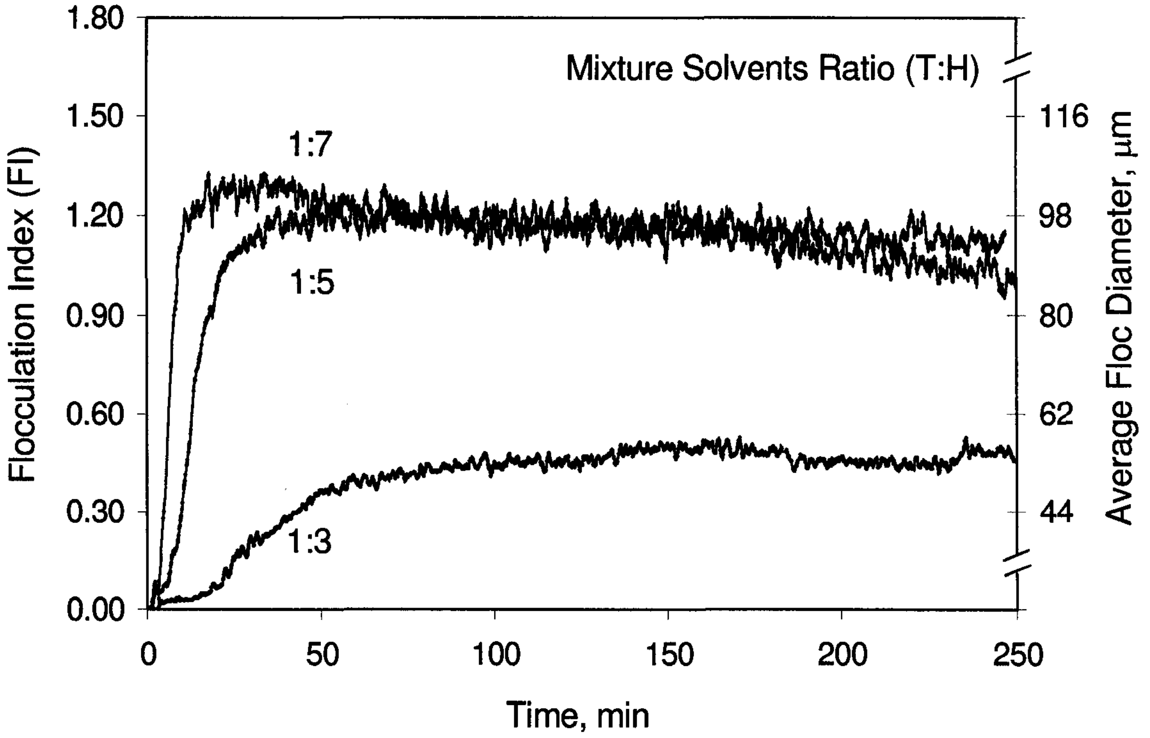

Figure 4.8. Effect of solvent compositions on the kinetics of asphaltenes flocculation from bitumen at a stirring speed of 75 rpm, and initial bitumen concentration of 875 mg/L (which has an equivalent asphaltenes concentration of 875×0.16 = 140 mg/L).

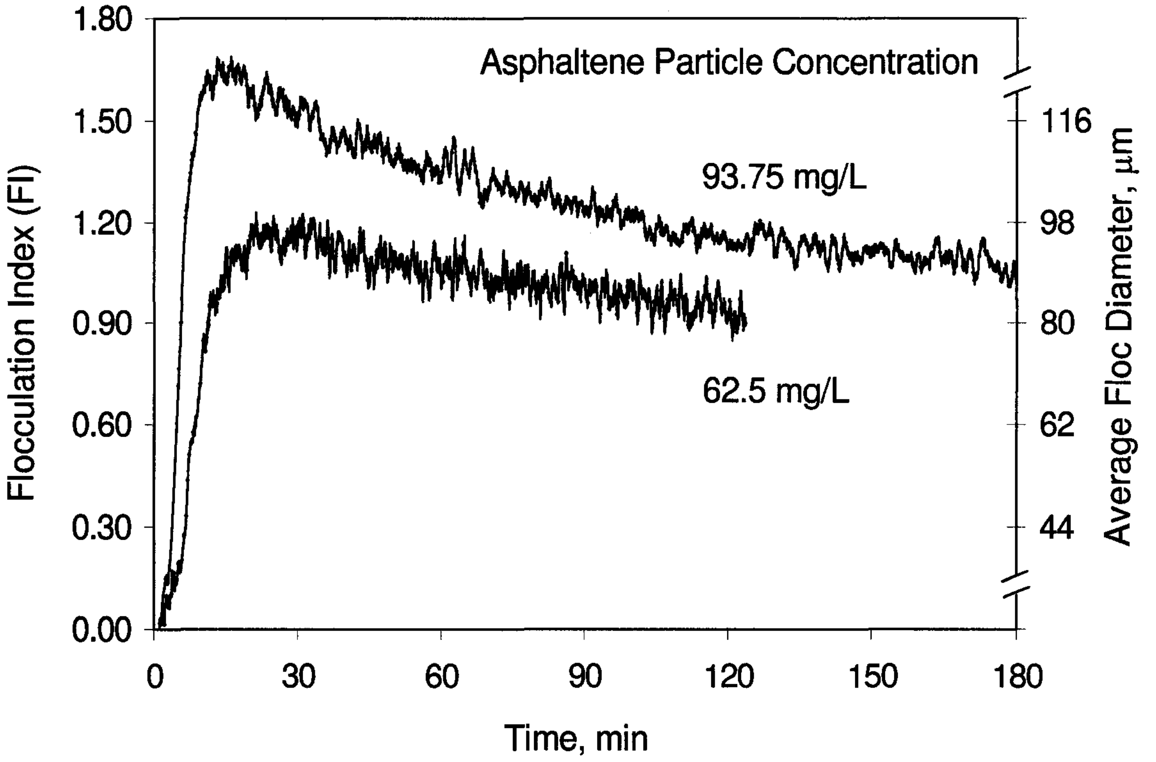

Figure 4.9. Plot of average aggregate size versus time for asphaltenes flocculation with extracted asphaltenes at a stirring speed of 75 rpm, and toluene-to-heptane solvent volume ratio of 1:5.

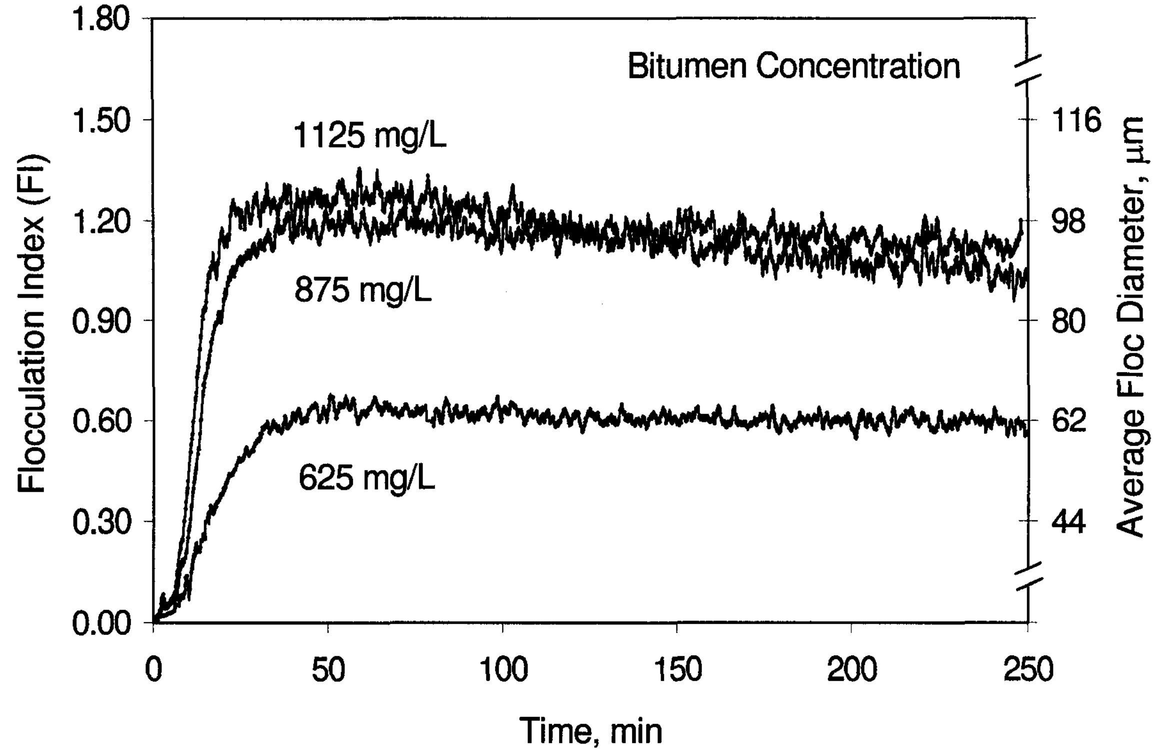

Figure 4.10. Comparison of the growth of aggregate size for various initial bitumen concentrations at a stirring speed of 75 rpm, and toluene-to-heptane solvent ratio of 1:5.

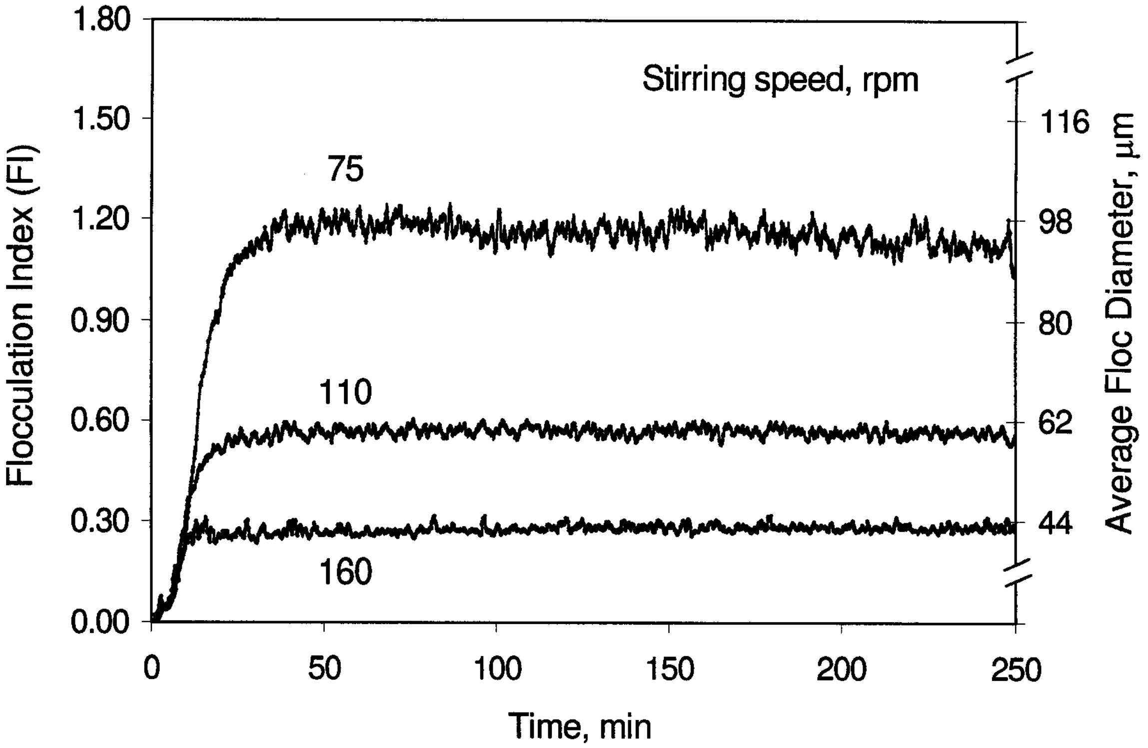

Figure 4.11. The evolution of the FI value and average floc size, d_{avg}, as a function of time for flocculation of asphaltenes at various stirring speeds (75–160 rpm) in a solvent mixture having toluene-to-heptane ratio of 1:5 and initial bitumen concentration of 875 mg/L. After attainment of steady state, d_{avg} no longer changes with time.

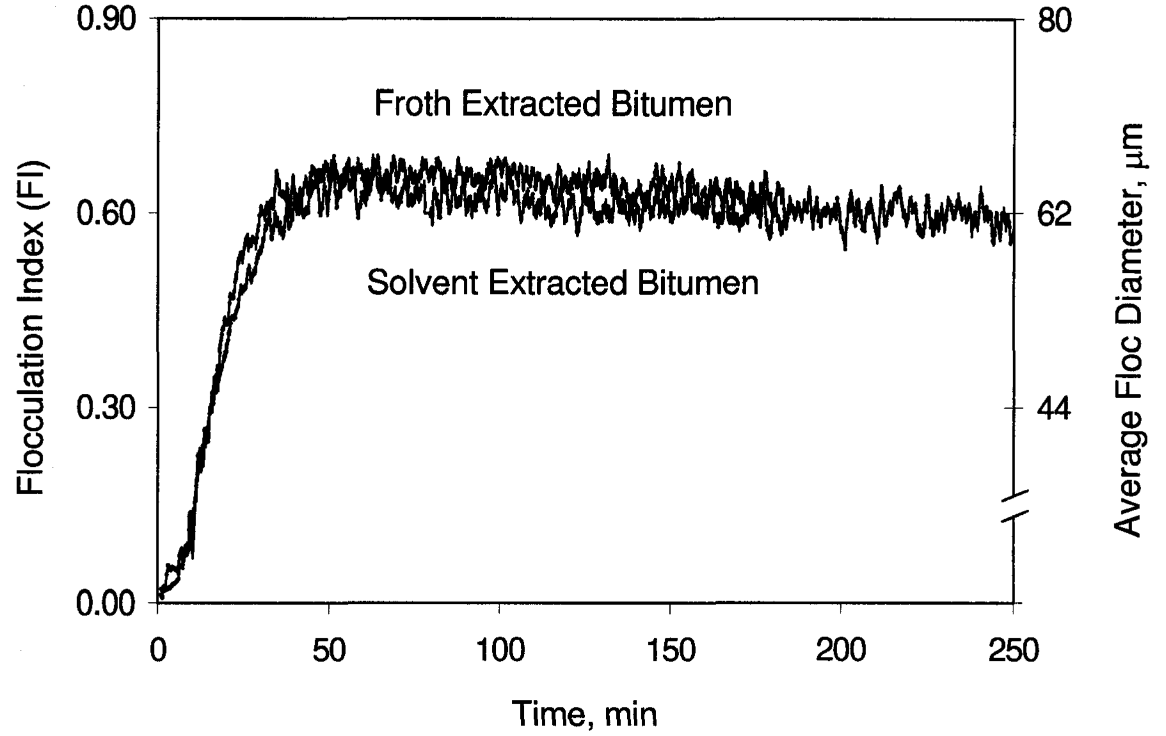

Figure 4.12. Effect of differently extracted bitumen on growth of asphaltene aggregates at a stirring speed of 75 rpm, toluene-to-heptane solvents ratio of 1:5, and initial bitumen concentration of 875 mg/L.

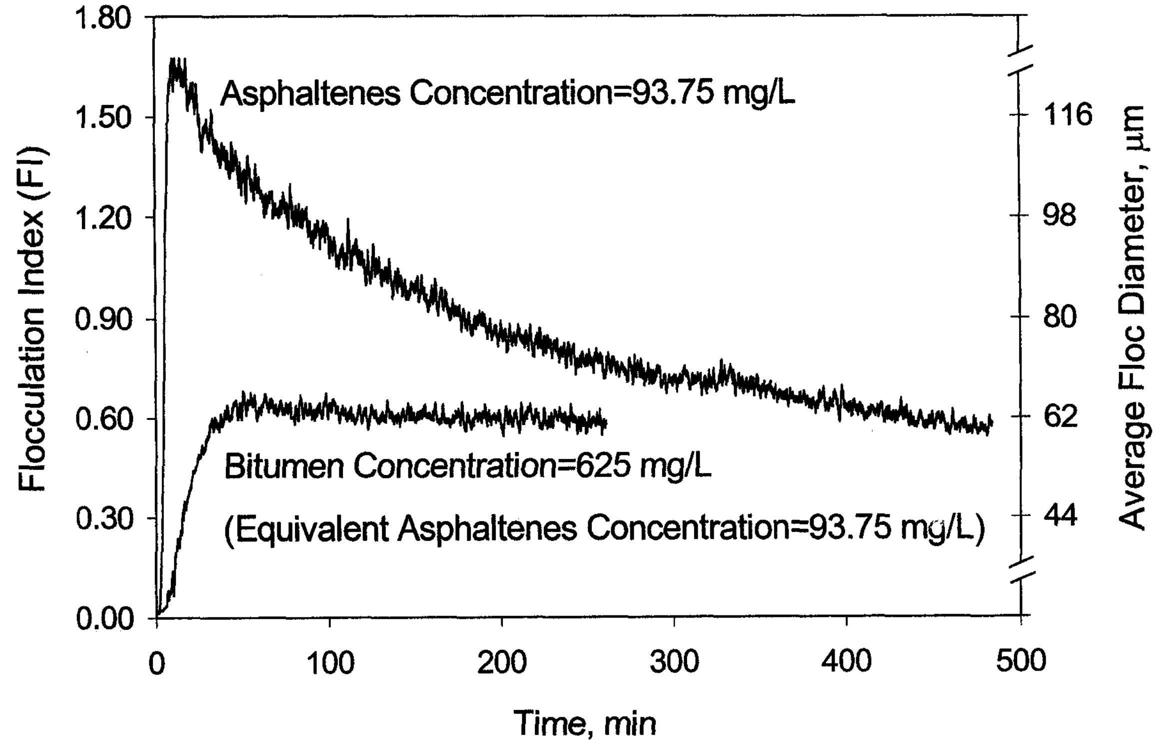

Figure 4.13. Plot of FI value and average floc diameter vs time. It shows the effect of maltenes on the growth of asphaltene aggregates at a stirring speed of 75 rpm, and toluene-to-heptane solvents ratio of 1:5. Though maltenes severely retard the kinetics of asphaltene aggregates growth, after sufficient long time, the final, steady-state size is observed to be the same. The effect of breakage and possibly restructuring is pronounced on the aggregates produced from extracted asphaltenes.

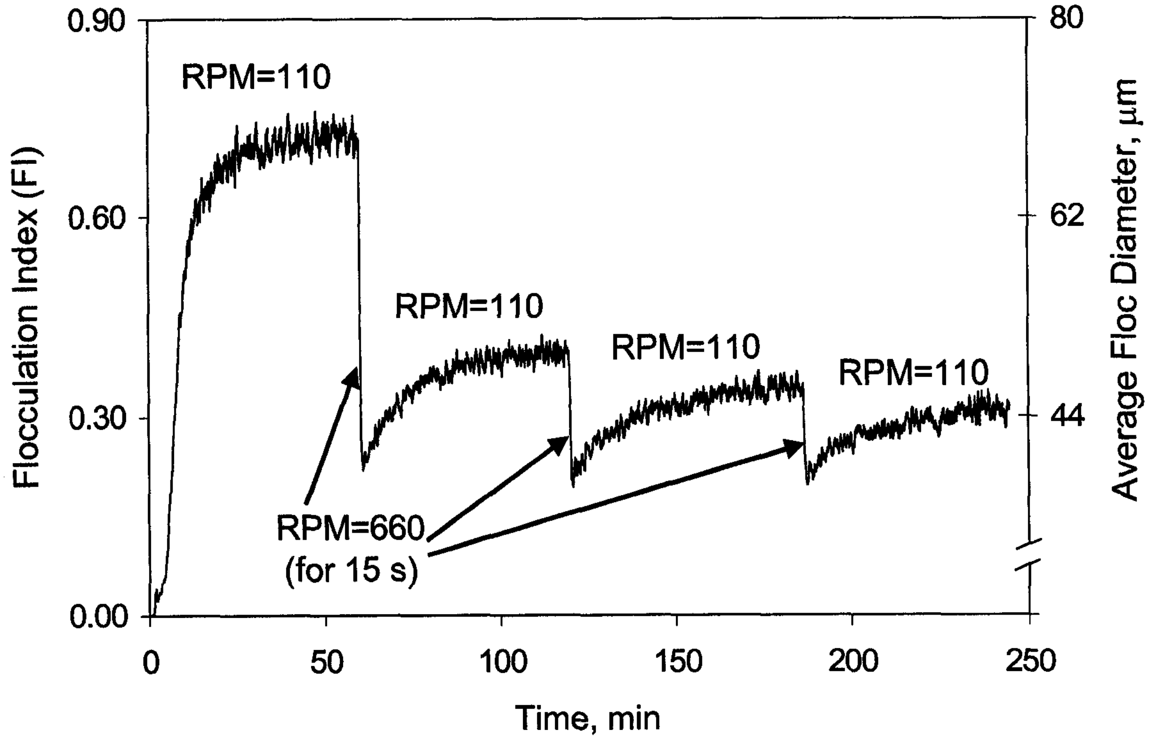

Figure 4.14. Effect of cyclic-shear on the evolution of FI and average aggregate size (d_{avg}). The flocs are grown for 60 minutes at the stirring speed of 110 rpm; toluene to heptane ratio of 1:5; and initial bitumen concentration of 1000 mg/L; and are fragmented at 660 rpm for 15 seconds. Repeated application of breakage stirring speed gradually decreases the size of fragments produced and the final floc size attained.

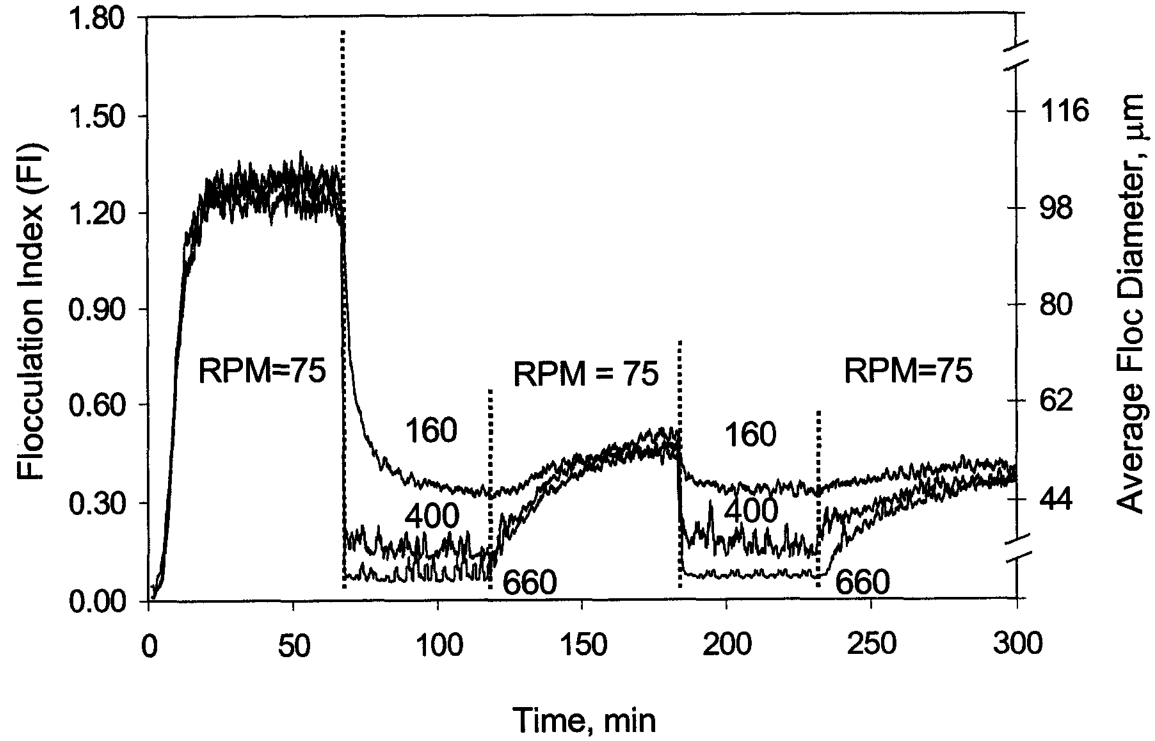

Figure 4.15. Effect of cyclic-shear flocculation on the FI and average floc size (d_{avg}) at a toluene-to-heptane ratio of 1:5 in solvents mixture, and initial bitumen concentration of 1000 mg/L. Increasing the fragmentation stirring speed from 160 to 660 rpm decreases the size of fragments produced and the steady state floc size attained. Re-application of original stirring speed of 75 rpm increases the size of the aggregates and a new steady state size is reached following re-growth and this size is significantly smaller than the previous steady state size at 75 rpm.

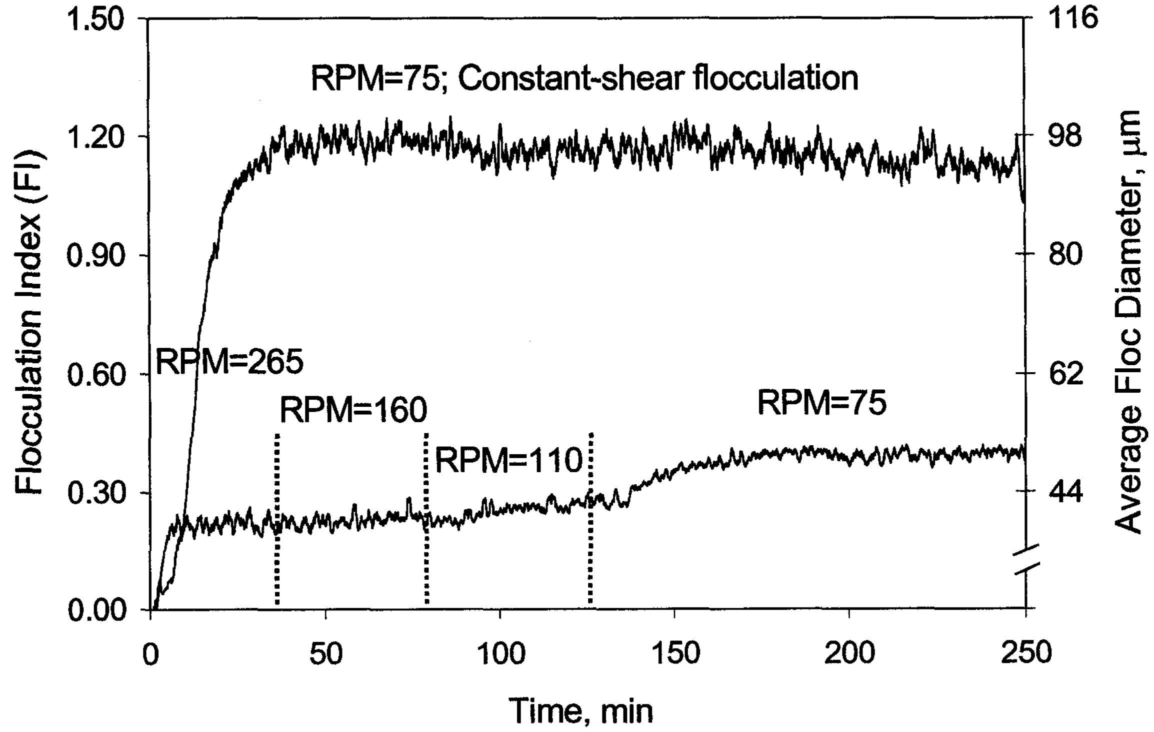

Figure 4.16. Evolution of FI during tapered-shear flocculation at a toluene-to-heptane solvents ratio of 1:5, and initial bitumen concentration of 1000 mg/L. Initially the floc size increases during rapid aggregation and reaches a steady state at 265 rpm (after about 8 min). As the stirring speed is reduced, the floc size increases and finally a new steady-state size (about 50 μm) is reached at 75 rpm. The upper curve shows the evolution of FI and average floc size (d_{avg}) during constant-shear flocculation at 75 rpm in a solvent mixture having toluene-to-heptane ratio of 1:5 and initial bitumen concentration of 875 mg/L (the steady-state size is about 95 μm).

Chapter 5

Settling Behavior of Asphaltene Aggregates

5.1 Introduction

Particle aggregation and transportation by gravity sedimentation are important in both engineered treatment systems and natural waters. For example, in bitumen froth treatment process using paraffinic solvents, asphaltene particles aggregation is necessary prior to particle removal by solid-liquid separation processes (Long et al., 2002). The precipitated asphaltenes would act as flocculant to the emulsified water droplets and fine solids in the diluted froth and form agglomerates combining all together. Altering the mass, surface area, and number concentration of particles can substantially affect their removal by gravity sedimentation in settling vessel. Information pertaining to the settling velocity of individual asphaltene aggregates is important for the study of mixed water, asphaltene, and fine solids settling and for the determination of average effective density of the aggregates. It may be possible to correlate the velocity of a cluster-cluster aggregate to the velocity of a primary cluster (Li and Ganczarczyk, 1987). Aiba et al. (1965) and Bradley and Krone (1971) indicated that the average settling velocity of activated sludge suspended solids could be empirically expressed as a linear function of the settling velocity of individual particles. The coefficient of this function might be either a constant or a variable, which depends on the concentration of the solids.

Aggregate size and density (or, porosity) are the most important factors that influence the efficiency of aggregate removal from suspensions. It is well known that aggregate size and density (or, porosity) are often mutually dependent, and can be expressed by some empirical relationships, such as – a power law type relation. In addition, shape or structure also affects the behavior of aggregated particles, particularly with regard to settling rates (Namer and Ganczarczyk, 1994; Jiang and Logan, 1996; Johnson et al., 1996) and collision efficiency (Jiang and Logan, 1991; Wiesner, 1992). Solids removal efficiency by sedimentation or filtration depends on the structure of the aggregates, as this determines the relationship between aggregate size and density. Besides, changes in aggregate structure within a suspension affect macroscopic properties, like viscosity (Gillespie, 1983) and density (Spicer et al., 1996). Porosity of the aggregates also determines the quality of the aggregate compactness (Pierre et al., 1995).

In recent years, many studies have shown that the irregular aggregate shapes can be described in terms of fractal geometry concepts. A complete characterization of a particle suspension should include a description of the fractal dimension of the aggregates (Jiang and Logan, 1991, Gorczyca and Ganczarczyk, 1996). Fractal geometry concept is useful in describing the rugged surface of large, irregular, porous aggregates that are not well defined by Euclidean geometry. In this concept, area and volume are not generally calculated by raising the characteristic length of an object to an integer power. Heterogeneously (non uniformly) packed objects with irregular boundaries can be defined by nonlinear relationships where the properties of the object scale with a characteristic length dimension raised to a power called the fractal dimension (Wiesner, 1992; Grijspeerdt and Verstraete, 1997; Logan, 1999; Gardner et al., 1998). For example, the aggregate porosity (also, effective density) and aggregate size can be expressed by the following power-law relationships:

$$1-\varepsilon \propto l_a^{D-3} \tag{5.1}$$

$$\rho_{eff} = (\rho_a - \rho_l) \propto l_a^{D-3} \qquad (5.2)$$

where ε is the aggregate porosity; (1-ε) is the solid volume fraction in an aggregate; l_a is the characteristic size of the aggregate (e.g. longest dimension is used for present study); ρ_{eff} is the aggregate effective density; ρ_a is the aggregate density; ρ_l is the density of the liquid, and *D* is the 3-dimensional fractal dimension for a self-similar structure. In Eqs. (5.1) and (5.2) the number 3 represents the Euclidean dimension for the three dimensional space. Since the fractal dimension is usually less than the Euclidean dimension, Eqs. (5.1) and (5.2) indicate that the aggregate porosity increases and the effective density decreases as the aggregate size increases (Huang, 1993).

The basic understanding of the structure and properties of fractal aggregates is due to the computer simulations (Meakin, 1988). Computer models have been developed by many investigators, such as – Vold (1963), Sutherland (1967), Goodarz-Nia (1977), Lagvankar and Gemmell (1968), Meakin (1984), and Mountain *et al.* (1986). These studies have shown that the fractal dimension depends on the condition of aggregate formation and that *D* may range from less than 1.7 to 3.0 (Rogak and Flagan, 1990). On the other hand, a number of experimental studies on the floc/aggregate porosity or density-size relationship have been performed by many investigators for flocs formed from a variety of materials: Lagvankar and Gemmell (1968) for $Fe_2(SO_4)_3$ flocs; Matsumuto and Mori (1975) for bentonite and alum flocs; Magara et al. (1976), Tambo and Watanabe (1979), Li and Ganczarczyk (1987), and Lee and Hsu (1994) for activated sludge flocs; Glasgow and Hsu (1984) for kaolin-polymer flocs; Gibbs (1985b) for clay flocs; Tambo and Watanabe (1979) for aluminum flocs; Weitz and Oliveria (1984) for gold colloid flocs; Klimpel and Hogg (1986) for quartz flocs; Gibbs (1985a) and Burban et al. (1990) for river sediment flocs; Li and Logan (1997) for latex microbeads aggregation; and Alldrege and Gotschalk (1988), Kajihara (1971), Logan and Hunt (1987), Hawley (1982), and McCave (1975) for marine aggregates. These studies have shown that the power law for floc porosity (or effective density) is valid at least over a limited range of floc size. In the experimental studies mentioned above, various methods had been used for measuring the floc density, e.g. equivalent density method (Lagvankar and Gemmell, 1968; Gibbs, 1985a, 1985b), isopycnic centrifugation (Dammel and Schroeder, 1991; Knocke et al., 1993), interference microscopy (Andreadakis, 1993), Oden balance method and photo-extinction method (Matsumuto and Mori, 1975); and free settling test (Tambo and Watanabe, 1979; Li and Ganczarczyk, 1987; Huang, 1993; Lee and Hsu, 1994). Among these methods, free settling test is the most widely used method in the literature because of its simplicity and low cost (Lee et al., 1996).

The information obtained in a free settling test is the equivalent diameter and the terminal settling velocity of a single aggregate. Assuming that the aggregate is moving steadily in the medium, a force balance equation is used for estimating the aggregate density (and also aggregate porosity). Based on the constructed aggregate 'size-density' relationship, Li and Ganczarczyk (1989) and Jiang and Logan (1991) proposed that an aggregate is a highly porous fractal-like object made of many primary particles. Fractal dimension is a quantitative measure of how the primary particles occupy the aggregate interior space. Beside the aggregate diameter and terminal velocity data, the information about several parameters are required in the force balance equation, such as - drag coefficient (Huang, 1993); primary particle density (Lee, 1994b); and the correction factor for advection flow (Logan and Hunt, 1987; Li and Ganczarczyk, 1988).

Very few studies have so far been concerned with the physical aspects of asphaltenes flocculation and little is known regarding the morphological characteristics of asphaltene flocs and the relation between their structure and settling properties. In order to gain knowledge on the physical and morphological aspects of the flocculation process of asphaltenes, this chapter presents an experimental study using microscopic and optical monitoring techniques and paying attention to the structure of the asphaltene aggregates and their settling rate. For efficient removal of asphaltene aggregates from a suspension, it is crucial to understand the settling behavior of the fractal aggregates. Due to difficulty in describing the irregular shape and varying porosity of these aggregates, it is extremely hard to have a single equation that can accurately describe their sedimentation rates. However, it is possible that by combining the equations developed so far, better prediction can be obtained.

The focus of this chapter is to examine the applicability of appropriate permeability model and the several assumptions made in a free settling test. The study involves performing the measurements of settling velocities for several aggregates within a glass-settling column and investigating the relationship among the porosity, permeability and settling velocity of fractal aggregates. An aggregate-settling model that can consider the effect of creeping flow through the aggregate on its settling velocity is employed in the aggregate porosity calculations. Settling velocity measurements indicate an inverse relationship between aggregate size and density. The reduced aggregate density with increasing size is usually attributed to the entrainment of fluid into the aggregate structure (Tambo and Watanabe, 1979). These porous aggregates further collide with each other to form increasingly more porous structures (Spicer et al., 1996). Results for the aggregate porosities and fractal dimensions are discussed.

5.2 Theoretical Background

The settling behavior of aggregates is dependent on the drag force and permeability of the aggregates, which can be considered to behave as porous media. Darcy's law is the oldest model used to describe the flow of fluid through porous media. It is therefore important to understand Darcy's law when describing the settling behavior of porous aggregates.

For low Reynolds number flow of Newtonian fluid outside of the aggregate, the flow field can be found by solving the Stokes equation (Happel and Brenner, 1965):

$$\mu \nabla^2 \boldsymbol{u} = \nabla p \tag{5.3}$$

and for incompressible fluids

$$\nabla \cdot \boldsymbol{u} = 0 \tag{5.4}$$

where μ is fluid viscosity; $\boldsymbol{u}$ is fluid velocity vector; and p is fluid pressure referred to a datum plane. Here the usual notations are followed as lightface Italic for scalar quantity, and boldface Italic for vector quantity (Bird et al., 1994).

The equation of motion most widely adopted to describe creeping Newtonian flow through an isotropic porous medium is the empirical Darcy law

$$-\frac{\mu}{k} \hat{\boldsymbol{u}} = \nabla \bar{p} \tag{5.5}$$

with the incompressibility condition assuming the form

$$\nabla \cdot \hat{\boldsymbol{u}} = 0 \tag{5.6}$$

where ^ denotes an ensemble-averaged quantity within the porous medium, ¯ denotes an interstitial-averaged quantity within the porous medium, and k is the permeability in the porous medium region.

Darcy equation offers good representation of low-porosity systems, but it not particularly suited for describing high-porosity systems, such as flocs, especially in the proximity of their surfaces. When a viscous fluid flows past the surface of a porous medium, the effect of viscous shear can penetrate beneath the permeable surface to form a sort of boundary layer in the porous medium (Beavers and Joseph, 1967). Darcy's law in not compatible with the existence of such a region because on macroscopic stress term is associated with it. Such considerations led the groups of Ooms et al. (1970) and Neale et al. (1973) to the conclusion that Brinkman's equation (Brinkman, 1947) is preferable to Darcy's law when examining the flow through highly porous permeable flocs (up to porosity value of 0.999; Adachi and Kamiko, 1993):

$$-\frac{\mu}{k}\hat{\boldsymbol{u}}+\mu\nabla^2\hat{\boldsymbol{u}}=\nabla\bar{p} \tag{5.7}$$

where ∇^2 is the Laplacian operator. The higher-order of Eq. (5.7) with respect to Eq. (5.5) permits to specify continuity of both velocity and hydrodynamic stress on the boundaries, thus enabling the prediction of a boundary layer inside the floc with thickness of the same order of magnitude as $\sqrt{k}$. It indicates that Darcy's law is valid everywhere except in the immediate vicinity of fluid-particle surface.

Experimental confirmations of the good results obtained applying Brinkman's equation to describe the motion of homogeneous floc was given by Matsumuto and Suganuma (1977) and Masliyah and Polikar (1980) with their measurements of the settling velocities of porous spheres made by steel wool and plastic foam, respectively.

5.2.1. Dimensionless Drag Force Factor or Permeability Correction Factor (Ω)

By solving Brinkman's flow equation (Eq. 5.7) inside the aggregate and Stokes flow equation (Eq. 5.3) outside of the aggregate and coupling them on the aggregate surface, Brinkman obtained coefficient, Ω, which accounts for the reduction of the drag force in the case of a permeable sphere settling (Neale et al., 1973):

$$\Omega = \frac{\text{Resistance experienced by a permeable sphere of diameter } d_a}{\text{Resistance experienced by an impermeable sphere of diameter } d_a} \tag{5.8}$$

Based on the Brinkman's extension of Darcy's law, the expression for Ω is derived to give (Neale et al., 1973):

$$\Omega = \frac{2\beta^2[1-(\tanh\beta)/\beta]}{2\beta^2+3[1-(\tanh\beta)/\beta]} \tag{5.9}$$

where β is known as the normalized aggregate diameter (Huang, 1993) or the dimensionless permeability of the porous aggregate (Li and Logan, 1997) or the permeability factor (Li and Logan, 2001) and is expressed by:

$$\beta = \frac{d_a}{2\sqrt{k}} \tag{5.10}$$

and k is the aggregate permeability (m^2) and d_a is the aggregate diameter. The validity of Eq. (5.9) had been experimentally verified by Matsumuto and Suganuma (1977). A direct application of Eq. (5.9), nevertheless, requires the knowledge about aggregate permeability, whose evaluation is usually based on permeability models.

Flow through an aggregate can reduce its drag, resulting in a settling velocity faster than that of otherwise identical but impermeable sphere predicted using Stokes' law (Hawley, 1982; Li and Ganczarczyk, 1988). The settling velocity of a permeable aggregate, U, can be related to that predicted by Stokes' law, U_s (Matsumoto and Suganuma, 1977; Johnson et al., 1996), by

$$\Gamma = \frac{U}{U_S} = \frac{\beta}{\beta - tanh\beta} + \frac{3}{2\beta^2} \tag{5.11}$$

As a matter of fact, Eq. (5.11) is the reciprocal of Eq. (5.9), i.e. $\Gamma = 1/\Omega$.

It is also found in the literature that the flow through an aggregate can be expressed in terms of the fluid collection efficiency, η, defined as the ratio of the interior flow passing through the aggregate to the flow approaching it. When Brinkman's extension of Darcy's law is used to describe the interior flow, the fluid collection efficiency of an aggregate (Adler, 1981; Chellam and Wiesner, 1993; Li and Logan, 1997) is

$$\eta = \frac{9(\beta - \tanh\beta)}{2\beta^3 + 3(\beta - \tanh\beta)} \tag{5.12}$$

From Eqs. (5.11) and (5.12), it can be noted that the parameters, Γ and η, are solely functions of the permeability factor, β. Both Γ and η increase as the β factor decreases. For impermeable particles as β approaches infinity, Γ=1 and η=0. As the aggregate permeability increases, β decreases, and Γ and η increase.

5.2.2. Permeability (*k*)

Various models published in the literature for determining permeability, *k*, (Veerapaneni and Wiesner, 1996; Lee et al., 1996; Tang and Raper, 2002) are listed in Table 5.1. These permeability models consider the shape of primary particles to be either spherical or fibrous particles. All equations are in the form of $k = d_p^2 * f(\varepsilon)$, where $f(\varepsilon)$ is a function of aggregate porosity, and d_p is the characteristic length for the primary particles, both are unknown in a free settling test. The important feature of Table 5.1 is that both d_p and ε are to be known in order to evaluate k.

Masliyah and Polikar (1980) experimentally obtained the permeability of porous spheres by measuring the pressure drop, ΔP, on a plug of materials over a distance Δz. Then using Darcy's law, which can also be expressed as follows

$$U = - \frac{k}{\mu} \frac{\Delta P}{\Delta z} \tag{5.13}$$

the value of permeability, k, was obtained from the slope of a plot of $-\Delta P$ vs $\mu U \Delta z$. However, as explained before, Darcy's law is not appropriate to be used for high porosity materials. This means that the determination of permeability, as shown above, is not accurate for highly porous aggregates.

Matsumuto et al. (1978) employed Davies correlation for estimating the aggregate permeability. Li and Ganczarczyk (1992) compared the permeabilities calculated from Carman-Kozeny equation and Davies correlation. Large differences occurred depending on the model applied. Huang (1993) used Brinkman model to estimate permeability and concluded from experimental data that the calculated fractal dimension will not be affected when the aggregate flow-through effect is considered. The validity of Brinkman model was also tested by Matsumoto and Suganuma (1977) and Li and Logan (1997) using the results from settling experiments of steel wool flocs and latex micro sphere flocs, respectively. Matsumoto and Suganuma (1977) found that the Brinkman model is effective for modelling sedimentation of high porosity flocs, up to 0.999. Rogak and Flagan (1990) also proposed an expression for permeability based on the fractal nature of floc. Chellam and Wiesner (1993) had examined Rogak and Flagan's model. In addition the information about the primary particle themselves, the way these particles occupying

Table 5.1. Permeability models available in the literature*

Model	Primary particle shape	Permeability function
Brinkman (1947)	Sphere	$k=\frac{d_p^2}{72}[3+\frac{4}{1-\varepsilon}-3\sqrt{\frac{8}{1-\varepsilon}-3}]$
Carman-Kozeny (1937)	Sphere	$k=\frac{\varepsilon^3}{5S_o^2(1-\varepsilon)^2}$
Dilute Limit (1957)	Sphere	$k=\frac{d_p^2}{18(1-\varepsilon)}$
Happel (or Cell model) (1958)	Sphere	$k=\frac{d_p^2}{18\gamma^3}\frac{3-4.5\gamma+4.5\gamma^5-3\gamma^6}{3+2\gamma^5}$
Howells, Hinch, Kim & Russel's model (1985)	Sphere	$k=\frac{d_p^2}{18\gamma^3}[1+2.12\gamma^{1.5}+2.11\gamma^3\ln(\gamma^3)+16.456\gamma^3+......]$
Happel (1959)	Fiberous	$k=\frac{d_p^2}{32\phi}[-\ln\phi+\frac{\phi^2-1}{\phi^2+1}]$
Davies (1952)	Fiberous	$k=\frac{d_p^2}{4}[\frac{1}{16\phi^{3/2}(1+56\phi^3)}]$
Iberall (1950)	Fiberous	$k=\frac{3}{16}\frac{\varepsilon}{1-\varepsilon}d_p^2\frac{2-\ln(\mathrm{Re}_p)}{4-\ln(\mathrm{Re}_p)}$

---

* The symbol d_p = primary particle diameter (m); ε = porosity of floc; $\phi = 1-\varepsilon$ = solid fraction of floc; $\gamma = \phi^{1/3}$; S_o = specific surface area of the primary particle = $6/d_p$ (m^{-1}); $Re_p = d_pU\rho_l / \mu\varepsilon$ = Reynolds number based on the primary particle and internal flow velocity.

the floc space is also required in their model. Veerapaneni and Wiesner (1996) proposed an estimate of the floc permeability by assuming a radial porosity distribution. A simple model coupling the Happel's cell model with fractal geometry is used to estimate the permeability of the aggregate as a function of radial distance. They expressed the non-homogeneous porosity by considering that the porosity of fractal aggregates increases with the distance away from the center of gyration. They showed that the Carman-Kozeny model is only valid when the porosity, ε, is less that 0.5.

Lee et al. (1996) compared Brinkman, Happel, and Carman-Kozeny permeability models using computer simulation. They recommended that for aggregates, the Brinkman or Happel model is the most appropriate. They demonstrated that floc permeability is sensitive to permeability models and parameters, such as the diameter of the primary particle. Increasing the floc diameter would also increase the permeability. Therefore, it is important to develop a model, which covers a wide range of floc diameters. It was proposed that a combination of Stokes' law with permeability models, such as Brinkman or Happel, could potentially be used to describe the settling behavior of permeable aggregates. The validity of the Brinkman model should further be examined by comparison with experimental results from different systems.

5.2.3. Porosity (ε)

The porosity of an aggregate (ε) is defined as the fractional void space with respect to the bulk volume that is constituted by interconnecting pores. This concept can be written in a mathematical form in terms of the number of primary particles in the aggregate, n, volume of a primary particle, V_1, and the volume of the aggregates, V_a, as follows:

$$1-\varepsilon=\frac{nV_1}{V_a} \tag{5.14}$$

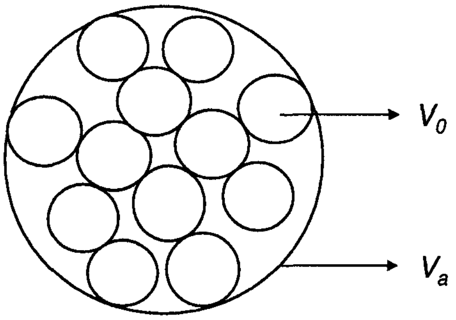

Assuming that an aggregate consists only of two parts, solid particles and liquid, then according to the mass balance in the aggregate, the aggregate porosity (ε) can be related to its density by the following expression:

$$1-\varepsilon=\frac{\rho_a-\rho_l}{\rho_p-\rho_l}=\frac{\rho_{eff}}{\rho_p-\rho_l} \tag{5.15}$$

where ρ_a, ρ_l, and ρ_p are density of aggregates, suspending liquid, and primary particles, respectively. This equation shows the relationship between the porosity, ε, and the aggregate effective density, ρ_{eff}. It is very difficult to obtain the value of the density of an aggregate, ρ_a. Hence, the porosity cannot readily be calculated from Eq. (5.15) and different methods (such as - electrozone sensing technique, and settling velocity) have been used by the researchers to determine the aggregate porosity.

Calculation of porosity based on Eqs. (5.14) and (5.15) assumes that the distribution of pores within the aggregates are homogeneous. However, real fractal aggregates may have nonhomogeneous distribution of primary particles (Veerapaneni and Wiesner, 1996). The variation is due to the chemical and physical mechanisms causing the flocculation (Meakin, 1988; Gregory, 1989). For example, the aggregation of small and more densely packed aggregates into larger and less dense aggregates (cluster–cluster aggregation), growth processes where smaller particles (or clusters) are attached to the exterior of 'seed' aggregates (similar to particle–cluster aggregation) (Veerapaneni and Wiesner, 1996). As a result, the size of pores inside aggregates tends to increase with aggregate size; the pores are larger around the outside of the aggregates. Although the porosity of aggregates does not necessarily vary radially, the model proposed by Veerapaneni and Wiesner (1996), might give better approximation of the porosity since it does not assume homogeneous distribution of porosity within the aggregates.

5.2.4. Drag coefficient (C_D)

For an incompressible Newtonian fluid flow in the creeping flow region, the drag force, F_D, exerted by the suspending liquid on a permeable object can be expressed in terms of the suspending liquid viscosity, μ, resistance coefficient, K, and settling velocity, U (Concha and Almendra, 1979a):

$$F_D = \mu K U \Omega \tag{5.16}$$

where Ω is defined in Eq. (5.9). If the shape of the object is spherical then $K=3\pi d_a$.

The dimensionless drag force for a spherical solid body, which is known as the drag coefficient, C_D, is defined as (Concha and Almendra, 1979a):

$$C_D = \frac{F_D}{\frac{\pi}{8}\rho_l U^2 d_a^2} \tag{5.17}$$

For a Reynolds number ($Re = Ud_a/\nu$, where ν is the kinematic viscosity of suspending liquid) much less than unity ($Re \ll 1$), the drag coefficient is expressed as:

$$C_D = \frac{24}{\mathrm{Re}} \tag{5.18}$$

A more widely used correlation of the drag coefficient for an isolated solid sphere in the laminar flow regime (Schiller and Nauman, 1935) is known as:

$$C_D = \frac{24}{\mathrm{Re}}(1 + 0.15\mathrm{Re}^{0.687}) \qquad \mathit{for}\, \mathrm{Re} < 1000 \tag{5.19}$$

Haider and Levenspiel (1989) attempted to derive an expression for drag coefficient for nonspherical particles. It was derived from the expressions obtained by Clift and Gauvin (1970) and Turton and Levenspiel (1986), which were based on experimental data; and by fitting the experimental drag data for nonspherical particles obtained by Pettyjohn and Christiansen (1948). The following expression was obtained by Haider and Levenspiel (1989), which can be used for $\mathrm{Re} < 2.6\times10^5$:

$$C_D = \frac{24}{Re}\left(1 + B_1 Re^{B_2}\right) + \frac{B_3}{\left(1 + \frac{B_4}{Re}\right)} \tag{5.20}$$

where B_1, B_2, B_3, and B_4 are functions of sphericity ,ψ, which is defined as follows (Pettyjohn and Christiansen, 1948):

$$\psi = \frac{A_s}{A_{ns}} \tag{5.21}$$

A_s and A_{ns} are surface area of spherical and non-spherical particles of equal volume and density. Eq. (5.20) is applicable across all flow regimes, and is based on the experimental data for rigid impermeable particles.

Tang and Raper (2002) demonstrated that the more non-spherical a particle is, the higher the drag force exerted by surrounding liquid. This would make a non-spherical particle settle slower than a spherical particle of the same density and volume. Eq. (5.20) reduces to Stokes' drag coefficient, $C_D = 24/Re$, as sphericity approaches unity. Haider and Levespiel (1989) claimed that Eq. (5.20) accurately predicts the drag coefficients for non-spherical particles having sphericity larger than 0.67 as the values were very close to experimental data. However, since Eq. (5.20) was derived for individual particles, the use of this equation for porous medium such as fractal aggregates is yet to be examined.

5.3 Governing equations for aggregate-settling model

In an experiment of settling through an unbounded fluid, the size and settling velocity of the aggregates are measured in a quiescent glass column. It will be referred as free-settling test in the rest of the chapter. Assuming that the settling of each individual aggregate satisfies Stokes' law, the porosity (ε) of an aggregate is determined from:

$$1-\varepsilon=\frac{18\mu U}{g(\rho_p-\rho_l)d_a^2} \tag{5.22}$$

where U is the measured aggregate settling velocity; d_a is the aggregate diameter; μ is the dynamic viscosity of liquid medium; g is the gravity acceleration; ρ_l is the density of liquid medium; and ρ_p is the density of primary particles in the aggregate.

Eq. (5.22) is questionable because Stokes' law is only valid for an impermeable, spherical particle. Since an aggregate has highly porous structure, the ambient fluid will penetrate the aggregate; the settling velocity of the aggregate is, therefore, higher than that of an impermeable particle with the same size and the same effective density as the aggregate (Neale et al., 1973; Matsumoto and Suganuma, 1977; Masliyah and Polikar, 1980). Considering these effects, in general, the force balance for an aggregate moving steadily in an infinite medium can be described by the equation (Neale et al., 1973; Li & Ganczarczyk, 1992; Huang, 1993):

$$U=\left[\frac{4}{3}\frac{g(1-\varepsilon)}{\Omega C_{\mathrm{D}}}\frac{\rho_{\mathrm{a}}-\rho_l}{\rho_l}d_{\mathrm{a}}\right]^{1/2} \tag{5.23}$$

Then the porosity of the aggregate can be obtained as:

$$\frac{(\rho_a-\rho_l)}{(\rho_p-\rho_l)}=(1-\varepsilon)=\frac{3\rho_l\Omega C_D}{4g(\rho_a-\rho_l)d_a}U^2 \tag{5.24}$$

where C_{D} is the drag coefficient; ρ_a is the aggregate density; and Ω is the ratio of the resistance experienced by an aggregate to that of an equivalent solid sphere. Except for the aggregate diameter and terminal velocity data, which are available from experimental measurements, four unknowns are present in the Eq. (5.24), ρ_{p}, Ω, C_{D}, and ε/ρ_{eff}. To estimate aggregate porosity or effective density, other three values (ρ_p, Ω, and C_{D}) are required.

5.3.1 Determination of model parameters

In most studies, ρ_p is assumed to be equal to ρ_s, the dried solid density (Tambo and Watanabe, 1979; Huang, 1993). However, in activated sludge with a large amount of internal water, the bound water and the solid phase will move together and behave like a particle (Kawasaki et al., 1991; Lee, 1994). In such a case, the primary particle density is a function of bound water content, which complicates the analysis (Lee, 1994). For the present study, ρ_p is assumed to be equal to ρ_s.

Brinkman permeability model is used for this work as it has been reported in the literature that among the existing models, it predicts well for highly porous aggregates (up to 99% porosity), which is applicable for our case. So, the permeability equations used for the present study are

$$\Omega = \frac{2\beta^2[1-(\tanh\beta)/\beta]}{2\beta^2+3[1-(\tanh\beta)/\beta]} \tag{5.9}$$

$$\beta = \frac{d_a}{2\sqrt{k}} \tag{5.10}$$

$$k = \frac{d_p^2}{72}[3+\frac{4}{1-\varepsilon}-3\sqrt{\frac{8}{1-\varepsilon}-3}] \tag{5.25}$$

Since the experimentally observed Reynolds number ranged from 0.006 to 0.136, the maximum difference between two correlations for drag coefficient (Eqs. 5.18 and 5.19) is 3.8% for the working range of *Re*. Hence, for the present study, the correlation used is

$$C_D = \frac{24}{Re} \tag{5.18}$$

Eqs. (5.9, 5.10, 5.25, 5.18) provide closure to the present aggregate-settling model. They were substituted into Eq. (5.24) and assuming d_p is known, the equation contains only one unknown, the aggregate porosity or density. So, finally the settling equation (Eq. (5.24)) becomes of the form $f(\varepsilon) = 0$, which can be solved numerically.

5.4 Experimental Method

5.4.1 Preparation of asphaltene aggregates

The asphaltenes used in this study are derived from Syncrude vacuum-distillation-tower-feed Athabasca bitumen (bitumen that has been treated to remove most of the solids and water) using standard procedure (see Chapter 4). The aggregates used in the free-settling tests were produced in a bench scale continuous stirred tank reactor of 1.0 L in volume at different fluid shear rates (36, 75, and 160 rpm). It was shown in Table 4.2 that 36 rpm is equivalent to $Re_{\mathrm{imp}} = 1.9\text{x}10^3$, $G_{\mathrm{avg}} = 10\ \mathrm{s}^{-1}$; 75 rpm is equivalent to $Re_{\mathrm{imp}} = 4.0\text{x}10^3$, $G_{\mathrm{avg}} = 28\ \mathrm{s}^{-1}$; 160 rpm is equivalent to $Re_{\mathrm{imp}} = 8.6\text{x}10^3$, $G_{\mathrm{avg}} = 87\ \mathrm{s}^{-1}$; and 660 rpm is equivalent to $Re_{\mathrm{imp}} = 35.5\text{x}10^3$, $G_{\mathrm{avg}} = 730\ \mathrm{s}^{-1}$. The volume averaged shear rate G_{avg} is calculated using a power number, $P_{\mathrm{o}} = 1.2$, for the employed 45° angle four-blade pitch turbine and turbulent flow ($Re_{\mathrm{imp}} > 10^3$) (p. 63, Fig. 3-16 in Oldshue, 1983), and combining Eqs. (4.7 & 4.8).

For the first set of flocculation experiments, samples of dried asphaltene are dissolved in toluene and then added with *n*-heptane, to give an initial asphaltene concentration of 62.5 mg/L in the solution and the solvent composition (i.e., the ratio of toluene to heptane in the solution) is fixed at 1:5 volume ratio, but the stirring speed varied as 36 and 75 rpm in two different experiments, respectively. In the second set of experiments, the ratio of toluene to n-heptane is kept fixed at 1:5, and the initial bitumen concentration is 1000 mg/L, but the stirring speed varied as 75 and 160 rpm during cyclic shear flocculation.

In performing the flocculation test, the sample suspension of asphaltenes in a 1:5 ratio of toluene-heptane solvent mixture is first mixed at 660 rpm for 30 seconds to break up any agglomerates. The impeller is then set to the desired speed to produce a constant average fluid shear and allow floc formation. This type of axial flow creates good top-to-bottom motion in the tank resulting in good mixing.

5.4.2 Settling apparatus and experiment

The experimental apparatus for the settling of asphaltene aggregates consists of a pyrex glass column (Fig. 5.1). The column is 350 mm in height to ensure that the terminal settling velocity could be reached, and 30 mm in width to neglect the wall effect on aggregate settling (Johnson et al., 1996). After the average aggregate diameter reached a steady-state size (which is known from the previously performed growth kinetics experiments by PDA), samples were withdrawn from the stirred tank at certain time intervals (every 15 minutes). A small amount (about 3 mL) of suspension containing aggregates is gently transferred into the top of the settling column using a rubber dropper bulb with a 10-ml pipette tip cut midway to minimize breakup of the aggregates. The column was filled with toluene and heptane solvent mixture at a volume ratio of 1:5, which is the same as the original system. Images of asphaltene aggregates, while passing through the observation region in the glass-settling column, were obtained using a microscope objective (Carl Zeiss Canada Ltd.) coupled with a CCD camera and a video recorder. A cold fiber optic light was placed on the same side of the column from the camera to provide reflected-lighting from the white background on the other side of the column, which produces clear and sharp pictures.

5.4.3 Analysis

The video recordings were obtained on a VHS High Grade Video Tape. Snappy Video Snapshot installed under Windows XP was used to grab and digitize the chosen frames of the recordings. Sigma Scan Pro automated image analysis software was used to determine the shape, size and settling velocity of the aggregates from the captured images. To determine the aforementioned parameters, sequences of a few frames were grabbed and digitized at various observation times. An identical procedure was always applied in image analysis of the grabbed frames. Since the background light intensity varied continuously depending on the number and size of the aggregates passing through the observation region, the automatic gray scale filtering could not be used. So, the objects on a frame were filled using manual drawing of the boundaries for geometric characterization. Several parameters (such as - area, projected area diameter, major axis / longest dimension, shape factor etc.) were determined for each aggregate. Projected area diameter of an aggregate (d_a) is defined as:

$$d_a = \left(\frac{4 \cdot Area}{\pi} \right)^{1/2} \tag{5.26}$$

This is the diameter of a fictitious circular object that has the same projected or cross-sectional area as the irregular object being measured. Finally, the image analysis software scales the major and minor axes of the ellipse so that it has almost the same area as the image (Allen, 1997). The major axis of the fitted ellipse is used in this chapter as the major length scale to characterize the aggregate structure in terms of fractal dimension. The geometric characteristics and distance between the aggregates at two different captured photographs were measured by image analysis system. To interpret image sizes correctly, a graduated microscale was photographed to determine the number of pixels corresponding to a given standard length for each set of experiments.

To determine the aggregate settling velocity, frame i and i+1 were captured and processed using the image analysis software. Frame i is captured when the aggregate enters the viewing area, and frame $i+1$ is captured at the last moment when the aggregate is about to leave the viewing area. As a result two positions (i.e. initial and final positions) of an aggregate within a known time interval of Δt (number of fields advanced at normal playback speed times 1/30 s) were obtained on frame *i and* $i+1$, and the distance between two positions of every aggregate was measured. The settling velocity, U, of an aggregate was calculated as:

$$U = \frac{\sqrt{(y_2 - y_1)^2}}{\Delta t} \tag{5.28}$$

where (x_2, y_2) and (x_1, y_1) are coordinates of the center of an aggregate on frame $i+1$ and i, respectively, and Δt is the time interval between the frames. It was observed from the experiments that the horizontal movement of the aggregates (i.e. $x_2 - x_1$) was negligible compared to the verticle movement (i.e. $y_2 - y_1$). Knowing the magnification, traveling distance and time between the aggregates, the terminal settling velocities were calculated.

In the present experiment, asphaltene aggregates are introduced to the settling column by a pipette in the form of 3-mL suspension from the stirred-tank flocculator directly. Because of the presence of a large number of aggregates in the 3-mL suspension, some would pass through the narrow illuminated area and are captured by the continuous video recording. This method/technique is effective in combined measurements of size and settling velocity of asphaltene aggregates.

5.5 Results and Discussion

5.5.1 Settling velocities in toluene-heptane solvent mixtures

During this study, the settling velocities and sizes of asphaltene aggregates are measured. The area-equivalent diameter of the aggregates are in the range from 20 to 200 μm, and the settling velocities are in the range from about 100 to 600 μm/s, corresponding to the Reynolds number ranging from 0.006 to 0.136. The settling velocities are shown in Figs. 5.2(a) and 5.2(b) as function of the projected area diameter of the aggregates. Other size characteristics like volume-equivalent diameter or surface-area-equivalent diameter could not be derived from image analysis measurements and are not considered.

Fig. 5.2(a) presents the relationship between projected area diameter and terminal settling velocity at two different shear rates (i.e. 36 and 75 RPM), where the aggregates are produced from extracted asphaltenes. The open circles are the observed settling velocities at 36 rpm and the solid squares are the data points at 75 rpm. With the projected area diameter as the size criterion, the data are quite scattered. No significant difference is observed in the settling velocities at the two different shear rates. If the solid (i.e. nonporous) spherical particles of similar diameters are considered, then the Stokes velocities would be at least a order of magnitude higher than the settling velocities observed in the experiments. This infers that the asphaltene aggregates are highly porous. It would be interesting to compare the observed settling velocities with Stokes' law estimates for the porous asphaltene aggregates, but the density of the aggregates is not known. The larger variance of experimental data, especially for larger aggregates (also observed by Namer and Ganczarczyk, 1994; Gorczyca and Ganczarczyk, 1996), may be caused either by the limitations of the experimental method used or by the real shape distribution of asphaltene aggregates within the same characteristic length. Further, particular errors may be introduced by using the experimentally determined porosity of the aggregates and a drag coefficient based on the approximating volume of aggregates.

Fig. 5.2(b) shows the settling velocities of asphaltene aggregates, produced from bitumen during ramped shear, initially at 75 rpm and then at 160 rpm. The solid squares are the observed settling velocities at 75 rpm and the open triangles are the data points at 160 rpm. It can be noted that for same projected area diameter of the aggregates (d_a), the observed settling velocities at 160 rpm are significantly higher that those found at 75 rpm. It implies that higher shear produces more compact and denser aggregates. This is in agreement with the concept of "mechanical syneresis" described by Yusa (1977), as shrinkage and densification of loose and bulky aggregates occur due to shear force being applied locally, unevenly, and fluctuating over the surface of the aggregates. This is also consistent with experimental results of Klimpel and Hogg (1986) for quartz flocs and Huang (1993) for drilling mud flocs.

It is observed from the experimental results that, in some cases, the aggregate-settling velocities did not increase as the aggregate sizes increased. This can probably be explained by the irregular shapes of the aggregates, which have significant effects on the settling velocities of non-spherical particles. The effect of fluid drag force on the velocity of a particle is twice as great for nonspherical particles as for spherical particles (Lerman, 1979; Ozturgut and Lavalle, 1984). Furthermore, aggregates with the same volume but different shapes, can settle at different rates. According to Lerman (1979), the expected settling rates, from fastest to slowest, are for sphere, cylinder, needle, and disc, respectively. Thus, a disc-shaped or cylinderical floc may settle more slowly than a spherical floc with the same volume, even though the longest dimension of the disc or cylinder may be larger than that of the spherical floc. Moreover, floc-settling velocity is also affected by the settling orientations of the flocs because the drag force depends on the area facing the settling direction, whereas the effective gravitational forces only depend on the volume. This influence may exist in asphaltene aggregate-settling tests that usually take place in a creeping flow region, since non-spherical particles can settle at many possible orientations in this region (Allen, 1981). Floc orientation also affects the settling direction. If a flat, disc, or needle-shaped particle starts settling down in such an orientation with the longest dimension of the particle neither parallel nor perpendicular to the vertical direction, the particle path would have certain horizontal components. This explains why some flocs were observed to settle along a tortuous path even in quiescent conditions. However, in this analysis, the influence of the possible flow through the floc that also affects the drag force has been taken into consideration by solving Eqs. (5.9), (5.10), (5.18), and (5.25).

5.5.2 Porosity and effective density of asphaltene aggregates

The aggregate porosities are calculated according to Eq. (5.24) and are plotted against projected area diameter in Fig. 5.3(a). In the calculation of aggregate porosities, the values for different variables are used as $\rho_p = 1200$ kg/m^3 (assuming solid asphaltenes as primary particle), $\rho_l = 714.5$ kg/m^3, and $\mu = 0.45$ mPa·s (which corresponds to toluene and heptane solvent mixture of 1:5 volume ratio at temperature of 20° C). A range of d_p values equal to 0.1, 1.0, and 5.0 μm are used to calculate aggregate porosities, as it was not possible to determine to "primary" particle size due to experimental constraints. Once the porosity of the aggregates is known, the effective density can be estimated as shown by Eq. (5.15). The obtained porosities are used to determine aggregate effective densities and are shown in Fig. 5.3(b). The effective density is known in various names in literature, such as – hydrodynamic, apparent, excess, buoyant, and envelope.

The observed relationship between the porosity of the aggregates and their projected area diameter confirms the general increase of aggregate porosity with increasing size, with a significant decrease in porosity over the 50 μm size range of the aggregates (Fig. 5.3(a)). Higher porosity of the aggregates with an increasing characteristic length indicates that the structure of the aggregates possesses a space-filling capacity in which the non-solid portion is relatively high, and the projected area, is therefore, not completely filled (Namer and Ganczarczyk, 1993). This phenomenon is also confirmed from the smaller values of the experimentally observed 3-D fractal dimensions ($D < 2$) (see Fig. 5.7).

It can be seen from Fig. 5.3(a) that the solid concentration at which the aggregates are formed has no distinguishable effect on aggregate porosity. It is inferred as the porosities calculated at 75 rpm from experimental observations (shown by plus and shaded plus symbols for d_P = 0.1 μm; cross and shaded cross symbols for d_P = 1.0 μm; star and shaded star symbols for d_P = 5.0 μm) represent aggregates formed at two different initial particle concentrations. For the present experimental study, the porosity was found to be fairly independent of the d_p values used. The aggregates formed with bitumen had higher particle concentration (bitumen conc. = 1000 mg/L, which is roughly equivalent to asphaltene particle conc. ≅ 160 mg/L) than aggregates formed with extracted asphaltenes (asphaltene particle conc. = 62.5 mg/L). However, no difference in aggregate porosities was observed. Although some scattering exists, the data suggest that for the same size, the aggregates formed at different solid particle concentrations but at the same fluid shear rate may have the same porosity. Moreover, the shift to lower porosities (Fig. 5.3 (a)), i.e. higher effective densities (Fig. 5.3(b)), for smaller aggregates is mostly observed at higher shear rates (understood from the dominance of open symbols in Fig. 5.3) and is caused by their more compact structures.

The experimental data indicated the dependence of the terminal settling velocity in a free-settling regime upon the irregular, fractal structure of the aggregates. Most of the larger asphaltene aggregates (in this study > 100 μm) possess higher settling velocities (Fig. 5.2(a)) and Reynolds number, although their effective density is very low (Fig. 5.3(b)). This experimental observation suggests that the fractal nature of the aggregates has an influence on terminal settling velocity.

5.5.3 Permeabilities of asphaltene aggregates

The permeability of asphaltene aggregates was calculated using Brinkman model (Eq. 5.26) with $\rho_p = 1200$ kg/m^3, numerically determined porosity values from Eq. (5.25) and $d_p = 0.1$, 1.0, and 5.0 μm and is demonstrated in Fig. 5.3. At the smaller aggregate size, the permeability increases rapidly with increasing aggregate diameter. Then smaller linear increase is observed at comparatively larger aggregate sizes. Within the aggregate diameter range studied, permeability (k) has varied from 10^{-17} to 10^{-9} m^2. Calculations also demonstrated that based on the same parameters (ρ_P and d_P), higher shear rates reduce permeabilities by compaction of the aggregate size (Fig. 5.4). Lee et al. (1996) has reported a comparison of six different permeability models. They found that for a specific aggregate size, the k values calculated from various models usually vary within a range of two to three orders of magnitude. The permeabilities from Happel or Brinkman model are lower than the estimations by Carman-Kozeny model for spherical primary particle shape.

With the calculated aggregate permeability, β values are shown in Fig. 5.5. Though scattering greatly, when the aggregate size is smaller than about 50 μm, β values show a clear ascending trend with decreasing aggregate size. Above this 50 μm size range threshold, β values are found to be almost constant with aggregate diameter. Since β is inversely proportional to k value, based on the same parameters (ρ_p and d_P), β value is larger at higher shear rates. Li and Ganczarczyk (1992) defined a critical β value of 10.9, below which the aggregate can be viewed permeable aggregate. Since ρ_p is constant and d_P is the only variable parameter for calculations in present work, in Fig. 5.5 with d_P = 5.0 μm, almost all the aggregates produced at different shear rates are permeable. Whereas with d_p = 0.1 μm, all aggregates become impermeable and the aggregates produced with d_p = 1.0 μm fall close to the borderline range between permeable and impermeable. Based on this estimation, it can be noticed from Fig. 5.5 that a larger aggregate is not always more permeable than a smaller aggregate.

Since it was not possible with the present experimental arrangement to determine an exact value for d_p, a range of d_p values were studied to accommodate the real d_p value for the aggregates on somewhere of the parameter space studied. Hence, possible error for aggregate permeability estimation will be as high as few orders of magnitude. Caution must be paid, therefore, to any conclusion drawn from the aggregate permeability information thus obtained.

From Eq. (5.9), the correction factor Ω is obtained and is depicted in Fig. 5.6. It can be observed from the figure that as the aggregate permeability factor β exceeds approximately 100, Ω approaches unity. It indicates that the aggregate can be assumed as a impermeable sphere. However, at smaller β values (approximately < 50), the correction associated with permeable structure of the aggregates is significant (i.e. the Ω value is less than unity). For example, at the experimentally observed aggregate Reynolds number ranging from 0.006 to 0.136, Ω is 0.98 at $\beta = 50$, Ω is 0.42 at $\beta = 2$, and at the critical β value of 10.9 (Li and Ganczarczyk, 1992), Ω is 0.90. Hence, $\Omega = 1$ assumption for β values above the critical value produces negligible error ($\leq 10\%$). It implies that when the aggregate becomes larger, or when the aggregate is produced at a lower shear rate, β value decreases and Ω also decreases accordingly. Wu and Lee (1998) numerically evaluated the hydrodynamic drag force exerted on an individual floc moving steadily through an quiescent Newtonian fluid and demonstrated that the complete Ω versus β curve over a wide range of Reynolds number is sigmoid-like, with the nonporous sphere ($\Omega = 1$) and the "no-sphere" ($\Omega = 0$) conditions as two extremes.

5.5.4 Fractal dimensions (D_3) of asphaltene aggregates

Since the longest dimension (l_a) and the settling velocity (U) of the aggregate have been measured independently for each aggregate, these data have been used to estimate aggregate effective density (ρ_{eff}) as a function of aggregate characteristic size (l_a) (Eq. 5.2). A number of researchers have investigated the relationship between effective density and a characteristic aggregate length using various techniques and observed a large variability in the dependency of ρ_{eff} on the aggregate length (Sternberg et al., 1999). This has a major influence on predictions of aggregate settling velocity in practical situations. In the present study of asphaltene aggregates settling behavior, the difference in the slopes of Fig. 5.7 can be explained by the evolution of fractal nature of the aggregates under shear. Three-dimensional fractal dimension, D_3 (also used as D), can be used to quantify the disorder aspect or the packing factor of an object. Its value varies from 1 to 3, where a value of 3 corresponds to a solid spherical structure. A distinct property of a fractal is power law behavior. Hence, when an aggregate is fractal, it means that the effective density of the cluster varies with the diameter, according to the expression in Eq. (5.2). Fig. 5.7 shows a log-log plot of effective density versus longest dimension for permeable asphaltene aggregates. The straight lines in Fig. 5.7 are the least square fitted lines for data and according to the relationship in Eq. (5.2), the slopes of these straight lines give a measure of the fractal dimension of the aggregates (Lee and Hsu, 1994). The standard error is applied in determining the slopes from the regression lines.

Figures 5.7 (c) and 5.7 (d) represent asphaltene aggregates formed with bitumen at 75 and 160 rpm, respectively. Based on the same aggregate diameter, at 160 rpm, the aggregate effective density is significantly higher (Fig. 5.7 (d)) and the observed settling velocities are distinctly faster (Fig. 5.2 (b)) than those observed at 75 rpm. This implies that asphaltene aggregates form more compact structures at a higher shear. However, surprisingly, we didn't observe any significant difference in 3-D fractal dimension between 75 rpm (1.30 ± 0.15) and 160 rpm (1.42 ± 0.12) (see Table 5.2). This might be due to scattering of experimental data points for a very narrow aggregate size range (20 – 90 μm) studied.

Figures 5.7 (a) and 5.7 (b) represent asphaltene aggregates formed with extracted asphaltenes at 75 and 36 rpm respectively and no significant difference in the fractal dimension can be observed. However, when the permeable aggregate structures are considered at 75 rpm, the fractal dimension observed for asphaltene aggregates formed with extracted asphaltenes (2.00 ± 0.38) is appreciably higher than that with bitumen (1.30 ± 0.15). Since the solid concentration at which the aggregates are formed has no distinguishable effect on aggregate porosity/density (see Fig. 5.3), the significant difference in the aggregate structure might be happening due to the difference in aggregation mechanism in the presence of other compounds in bitumen (e.g. bitumen contains resins, aromatics and saturates along with asphaltenes).

Table 5.2. 3-D Fractal dimensions under various conditions for all data

Model for dimensionless drag force factor (Ω)	Asphaltene aggregates formed with Asphaltene (62.5 mg/L)		Asphaltene aggregates formed with Bitumen (1000 mg/L) (Equivalent asphaltene conc. ≅ 1000×0.16 = 160 mg/L)	
	36 rpm (G_{avg}=10 s^{-1})	75 rpm (G_{avg}=28 s^{-1})	75 rpm (G_{avg}=28 s^{-1})	160 rpm (G_{avg}=87 s^{-1})
	D_3 ± S. E.	D_3 ± S. E.	D_3 ± S. E.	D_3 ± S. E.
Impermeable ($\Omega = 1$)	1.68 ± 0.20	1.59 ± 0.42	1.33 ± 0.15	1.44 ± 0.12
Permeable (Brinkman model; Ω from Eq. 5.9)	1.87 ± 0.19	2.00 ± 0.38	1.30 ± 0.15	1.42 ± 0.12

Table 5.2 shows the calculated fractal dimensions at different conditions assuming both permeable and impermeable aggregates. It can be observed from Table 5.2 that when the asphaltene aggregates are formed with bitumen (right half of the Table 5.2), the obtained fractal dimension is insensitive to the permeability model or the parameter set applied, due to the high β (or near unity Ω) values of comparatively smaller size

aggregates. However, the obtained fractal dimension is significantly higher when the permeability of the aggregates is accounted for and when extracted asphaltenes are used for aggregate formation (left half of the Table 5.2). It shows again that the effect of permeability on the settling velocity of an aggregate cannot be neglected at the lower values of β. Previously, the effect of permeability on the settling velocity of a porous sphere was theoretically discussed by Ooms et al. (1970), Sutherland et al. (1970) and Neale et al. (1973); and Matsumoto and Suganuma (1977) experimentally showed that the effect of permeability on the settling velocity of a highly porous aggregate could not be neglected.

Since the correlations for drag coefficient (C_D) and Ω values for a permeable sphere under creeping flow condition have a sound theoretical base, the free-settling test for smaller flocs provides a qualitatively valid aggregate density approximation. As a matter of fact, no direct evidence against the validity of the free-settling test on aggregates with Reynolds number less than unity is found (Lee et al., 1996).

5.6 Conclusions

A remotely operated video system comprising a quiescent settling column, cold illuminating light, and frame grabber of video recording has been used to collect time-lapse sequences of settling aggregates. Image analysis of the video images collected on the computer provides independent estimates of particle size, shape, and settling velocity.

Suspended-aggregate sizes range from 20 μm (lower limit of detection) to 200 μm. Measurements of the aggregate settling velocity for the data set range from 100 to 600 μm/s. Experimental data on the relationship between terminal settling velocities of asphaltene aggregates and their projected area diameters demonstrated that the asphaltene aggregates are highly porous, and higher shear rate produces more compact and denser aggregates. Apparently, the asphaltene particles form larger and "fluffy" aggregates at lower shear rates (e.g. 36 rpm).

Although many researchers have attempted to develop equations to calculate drag coefficients and settling velocities of fractal aggregates, no single equation can best describe the settling behavior of fractal aggregates. The main reason for this is that it is extremely difficult to take into account the permeability and irregular shape of these aggregates. However, the evolution of the aggregate structure can be presented using the aggregate mass fractal dimension, D, and the aggregate effective density can be used to characterize the aggregate removal rates. Hence, the present study involved performing the measurements of settling velocities for several aggregates within a glass-settling column and investigating the relationship among the porosity, permeability and settling velocity of fractal aggregates.

The simulation shows that the aggregate permeability is a strong function of the parameter d_p used. For the same d_p value, the permeability increased with increasing aggregate diameter, or increased at lower shear rates. However, large uncertainty may exist in such permeability estimation due to assumptions used in d_p and ρ_p values. A direct and reliable method for permeability measurement is greatly needed.

Using the Brinkman permeability model, the size and settling-velocity measurements were used to compute the effective density of aggregates as a function of aggregate size. The porosity of the aggregates is found to increase with an increase in their size. Higher porosity of the aggregates with an increasing characteristic length indicates that the structure of the aggregates possesses a space-filling capacity in which the non-solid portion is relatively high, and the projected area, is therefore, not completely filled. This phenomenon supports the smaller values of the experimentally observed 3-D fractal dimensions ($D < 2$). Within the data range of present experimental study, the porosity was found to be weakly dependent of the d_p values used. For the same size, the aggregates formed at different solid particle concentrations but at the same fluid shear rate exhibited almost the same porosity. For smaller aggregates, lower porosities were observed mostly at higher shear rates and are caused by their more compact structures.

In spite of the fact that the density of aggregates with a diameter larger than 100 μm has almost the density of the liquid medium (i.e. very low effective density), they showed relatively high terminal settling velocities due to their fractal structure and very high porosity that resulted in significant reduction of the drag coefficient.

5.7 Nomenclature

A_{ns}	surface area of non-spherical particles (m^2)
A_s	surface area of spherical particles (m^2)
C_D	drag coefficient
D_3	three-dimensional fractal dimension (also used as D)
d_a	aggregate projected area diameter (μm)
d_p	primary particle diameter (μm)
F_D	drag force (N)
g	acceleration due to gravity (m/s^2)
G_{avg}	mean shear rate (s^{-1})
k	permeability (m^2)

K	resistance coefficient
l_a	aggregate longest dimension (μm)
n	number of spherical primary particles each of volume V_1 in the aggregate
p	fluid pressure (Pa)
Re	Reynolds number, $Re = Ud_a / \nu$
Re_{imp}	impeller Reynolds number, $Re = N_{rps} D_{imp}^2 \rho / \mu$
Re_p	Reynolds number based on the primary particle and internal flow velocity through the pores, $Re_p = d_p U \rho_l / \mu\varepsilon$
S_o	specific surface area of the primary particle ($= 6/d_p$, m^{-1})
t	time, s
Δt	time interval
$\boldsymbol{u}$	fluid velocity vector
U	settling velocity of a permeable aggregate (μm/s)
U_s	settling velocity predicted by Stokes' law (μm/s)
V_1	volume of a spherical primary particle (μm^3)
V_a	aggregate volume (μm^3)

Greek

ε	porosity of the aggregates
μ	viscosity of the suspending liquid (Pa·s)
ν	kinematic viscosity of the fluid (m^2/s)
η	fluid collection efficiency
Ω	drag force factor or permeability correction factor
Γ	$1/\Omega$.
β	normalized aggregate diameter or permeability factor
η	fluid collection efficiency
ψ	sphericity
ϕ	solid fraction of floc ($= 1-\varepsilon$)

γ	$\phi^{1/3}$
ρ_{a}	aggregate density (kg/m^3)
ρ_{eff}	aggregate effective density (kg/m^3)
ρ_l	density of the liquid (kg/m^3)
ρ_{p}	density of solid primary particle (kg/m^3)
ρ_{s}	dried solid density (kg/m^3)

5.8 Literature Cited

Adachi, Y., Kamiko, M. (1993). Sedimentation of a polystyrene latex floc. *Powder Technol.*, 78, 129–135.

Adler, P. M. (1981). Streamlines In and Around Porous Particles. *J. Colloid Interf. Sci.*, 81(2), 531-535, 1981.

Aiba, S., Humphrey, A. E., and Millis, N. F. (1965). *Biochemical Engineering.* University of Tokyo Press, Tokyo.

Alldrege, A. L., and Gotschalk, C. (1988). In situ settling behavior of marine snow. *Limnol. Oceanogr.*, 33(3), 339-351.

Allen, T. (1997). *Particle Size Measurement, Vol. 1,* Chapman and Hall, London.

Andreadakis, A. D. (1993). Physical and chemical properties of activated sludge floc. *Wat. Res.*, 27, 1707-1714.

Beavers, G. S., and Joseph, D. D. (1967). Boundary conditions at a naturally permeable wall. *J. Fluid. Mech.*, 30, 197-207.

Bird, R. B., Stewart, W. E., and Lightfoot, E. N. (1994). *Transport Phenomena.* John Wiley & Sons, New York.

Bradley, R. A., and Krone, R. B. (1971). Shearing effects on settling of activated sludge. *J. Sanit. Engng. Div. Am. Soc. Civ. Engrs.*, 97, 59-79.

Brinkman, H.C. (1947). A calculation of the viscous force exerted by a flowing fluid on a dense swarm of particles, *Appl. Sci. Res., Sect. A 1*, 27–34.

Burban, P. Y., Xu, Y. J., Mcneil, J., and Lick, W. (1990). Settling speeds of flocs in fresh water and seawater. *J. Geophys. Res.*, 95, 18213-18220.

Chellam, S. and Wiesner, M. R. (1993). Fluid mechanics and fractal aggregates. *Wat. Res.*, 27, 1943-1946.

Clift, R., Gauvin, W.H. (1970). *Australasian Chemical Engineering Conference*.

Concha, F., Almendra, E.R. (1979a). Settling velocities of particulate systems, 1. Settling velocities of individual spherical particles. *Int. J. Miner. Process.*, 5, 349–367.

Concha, F., Almendra, E.R. (1979b). Settling velocities of particulate systems, 2. Settling velocities of suspensions of spherical particles. *Int. J. Miner. Process.*, 6, 31–41.

Dallavalle, J.M. (1943). *Micromeritics*, Pitman, New York.

Dammel, E. E., and Schroeder, E. D. (1991). Density of activated sludge solids. *Wat. Res.*, 25, 841-846.

Gardner, K. H., Theis, T. L., and Young, T. C. (1998). Colloid Aggregation: Numerical Solution and Measurements. *Colloids Surf. A: Physicochem. Aspects,* 141, 237-252.

Gibbs, R. J. (1985a). Estuarine flocs: Their size, settling velocity, and density. *J. Geophys. Res.*, 90, 3249–3251.

Gibbs, R. J. (1985b). Settling velocity, diameter, and density for flocs of illite, kaolinite, and montmorillonite. *J. Sedimentary Petrology*, 55(1), 65-68.

Gillespie, T. (1983). The effect of aggregation and particle-size distribution on the viscosity of Newtonian suspensions. *J. Colloid Interface Sci.*, 94(1), 166–173.

Glasgow, L. A., and Hsu, J. P. (1984). Floc characteristics in water and wastewater treatment. *Particulate Science and Technology*, 2, 285–303.

Goodarz-Nia, I. (1977). Floc density, porosity and void ratio in colloidal systems and aerosols. *J. Colloid Interface Sci.*, 62(1), 131–141.

Gorczyca, B., and Ganczarczyk, J. (1996). Image Analysis of Alum Coagulated Mineral Suspensions, *Environ. Technol.,* 17, 1361-1369.

Gregory, J., "Polymer Adsorption and Flocculation in Sheared Suspensions," Colloids and Surfaces, 31, 231-253 (1988).

Grijspeerdt, K., and Verstraete, W. (1997). Image analysis to estimate the settleability and concentration of activated sludge. *Wat. Res.*, 31(5), 1126-1134.

Haider, A., Levenspiel, O. (1989). Drag coefficient and terminal velocity of spherical and non-spherical particles, *Powder Technol.*, 58, 63–70.

Happel, J., and Brenner, H. (1965). *Low Reynolds Number hydrodynamics*. Englewood Cliffs, Prentice-Hall, N.J.

Hawley, N. (1982). Settling velocity distribution of natural aggregates. *J. Geophys. Res.*, 87, 9489-9498.

Huang, H. (1993). Porosity-size relationship of drilling mud flocs: Fractal structure. *Clays and Clay Minerals*, 41(3), 373-379.

Jiang, Q., and Logan, B. E. (1996). Fractal dimensions of aggregates produced in laminar and turbulent shear devices. *J. Am. Water Works Assoc.*, 88(2), 100-113.

Jiang, Q., and Logan, B. E. (1996). Fractal dimensions of aggregates determined from steady-state size distributions. *Environ. Sci. Technol.*, 25(12), 2031-2037.

Johnson, C. P., Li, X., and Logan, B. E. (1996). Settling Velocities of Fractal Aggregates, *Environ. Sci. Technol.*, 30, 1911-1918.

Kajihara, M. (1971). Settling velocity and porosity of large suspended particle. *J. Oceanogr. Soc, Jpn.*, 27, 158-162.

Kawasaki, K., Matsuda, A., and Mizukawa, Y. (1991). Compression characteristics of excess activated sludges treated by freeze-and-thawing process. *J. Chem. Eng. Jpn.*, 24(6), 743-748.

Klimpel, R. C., and Hogg, R. (1986). Effects of flocculation conditions on agglomerate structure, *J. Colloid Interf. Sci.*, 113(1), 121-131.

Knocke, W. R., Dishman, C. M., and Miller, G. F. (1993). Measurement of chemical sludge floc density and implications related to sludge dewatering. *Wat. Environ. Res.*, 65, 735-743.

Lagvankar, A. L. and Gemmell, R.S. (1968). A size-density relationship for flocs. *J. AWWA*, 60, 1040-1046.

Lapple, C.E. (1951). Fluid and Particle Mechanics, University of Delaware Publ., Newark, vol. 284, p. 284.

Lee, D.J., Chen, G.W., Liao, Y.C., and Hsieh, C.C. (1996). On the free-settling test for estimating activated sludge floc density, *Wat. Res.*, 30, 541–550.

Lee, D. J., and Hsu, Y. H. (1994). Fast freeze/thaw treatment on activated sludge: floc structure and sludge dewaterability. *Environ. Sci. Technol.*, 28, 1444-1449.

Lee, D. J. (1994). Measurement of bound water in waste activated sludges: use of the centrifugal settling method. *J. Chem. Tech. Biotechnol.*, 61, 139-144.

Lerman A. (1979). *Geochemical Processes: Water and Sediment Environment.* Wiley, New York.

Li, D. H., and Ganczarczyk, J. (1992). Advective transport in activated sludge flocs. *Wat. Environ. Res.*, 64, 236-240.

Li, D. H., and Ganczarczyk, J. (1989). Fractal geometry of particle aggregates generated in water and waste-water treatment processes, *Environ. Sci. Technol.*, *23*, 1385-1389.

Li, D. H., and Ganczarczyk, J. (1988). Flow through activated sludge flocs. *Wat. Res.*, 22, 789-792.

Li, D. H., and Ganczarczyk, J. (1987). Stroboscopic determination of settling velocity, size and porosity of activated sludge flocs, *Wat. Res.*, 25(9), 1137-1143.

Li, X. Y., and Logan, B. E. (2001). Permeability of Fractal Aggregates. *Wat. Res.*, 35(14), 3373-3380.

Li, X. Y., and Logan, B. E. (1997). Collision Frequencies between Fractal Aggregates and Small Particles in a Turbulently Sheared Fluid. *Environ. Sci. Technol.*, 31(4), 1237-1242.

Long, Y., Dabros, T., and Hamza, H. (2002). Stability and Settling Characteristics of Solvent-Diluted Bitumen Emulsions, *Fuel*, 81, 1945.

Logan, B. E. (1999). *Environmental Transport Processes.* John Wiley and Sons, New York, 443-453.

Logan, B. E., and Hunt, J. R. (1987). Advantages to microbes of growth in permeable aggregates in marine systems. *Limnol. Oceanogr.*, 32(5), 1034-1048.

Magara, Y., Nambu, S., Utosawa, K. (1976). Biochemical and physical properties of an activated sludge on settling characteristics, *Wat. Res.*, 10, 71–77.

Masliyah, J.H., and Polikar, M. (1980). Terminal velocity of porous spheres. *Can. J. Chem. Eng.*, 58, 299–302.

Matsumoto, K., Mori, Y. (1975). Settling velocity of floc - new measurement method of floc density, *J. Chem. Engrs., Jpn.*, 8(2), 143-147.

Matsumoto, K., Suganuma, A. (1977). Settling velocity of a permeable model floc. *Chem. Eng. Sci.*, 32, 445–447.

Matsumoto, K., Suganuma, A. and Kunii, D. (1978). Effect of permeablity on the settling velocity of an actual floc. *Chem. Eng. Sci.*, 32, 445–447.

McCave, I. N. (1975). Verticle flux of particles in the ocean. *Deep Sea Res.*, 22, 491-502.

Meakin, P. (1988). Fractal Aggregates. *Adv. Colloid Interface Sci.*, 28 (4), 249-331.

Meakin, P. (1984). Effects of cluster trajectories on cluster-cluster aggregation: A comparison of linear and Brownian trajectories in two- and three- dimensional simulations. *Phys. Rev. A: Gen. Phys.*, 29, 997-999.

Mehaute, B.L. (1976). An Introduction to Hydrodynamics and Water Wave, Springer-Verlag, New York, pp. 89–97.

Mountain, R. D., Mulholland, G. W., and Baum, H. (1986). Simulation of aerosol agglomeration in the free molecular and continuum flow regimes. *J. Colloid Interf. Sci.*, 114, 67-81.

Namer, J., and Ganczarczyk, J.J. (1994). Fractal Dimensions and Shape Factors of Digested Sludge Particle Aggregates, *Water Poll. Res. J. Canada*, 29(4), 441-455.

Namer, J., and Ganczarczyk, J.J. (1993). Settling properties of digested sludge particle aggregates, *Wat. Res.*, 27(8), 1285-1294.

Neale, G., Epstein, N., and Nader, W. (1973). Creeping flow relative to permeable spheres. *Chem. Eng. Sci.*, 28, 1865–1874.

Oldshue, J. Y. (1983). *Fluid Mixing Technology*. McGraw–Hill, New York, 1983.

Olson, R. (1960). Essentials of Engineering Fluid Mechanics, International Textbook, Scranton, Chap. 11.

Ooms, G., Mijnlieff, P. F., and Beckers, H. L. (1970). Frictional force exerted by a flowing fluid on a permeable particle, with particular reference to polymer coils. *J. Chem. Phys.*, 53, 4123.

Ozturgut, E. and Lavalle, J. W. (1984). New method of wet density and settling velocity determination for wastewater effluent. *Environ. Sci. Technol.*, 18, 947-952.

Pettyjohn, E.S., Christiansen, E.B. (1948). Effect of particle shape on free settling rates of isometric particles. *Chem. Eng. Prog.*, 44, 157.

Pierre, A. C., Ma, K., and Barker, C. (1995). Structure of kaolinite flocs formed in an aqueous-medium. Journal of Materials Sci., 30(8), 2176-2181.

Rogak, S.N., and Flagan, R.C. (1990). Stokes drag on self-similar cluster on spheres, *J. Colloid Interf. Sci.*, 134(1), 206–218.

Rubey, W.W. (1933). Settling velocities of gravel, sand, and silt particles, *Am. J. Sci.*, 225–325.

Spicer, P. T., Keller, W., and Pratsinis, S. E. (1996). The Effect of Impeller Type on Floc Size and Structure During Shear-Induced Flocculation. *J. Colloid Interf. Sci.*, 184, 112-122.

Sutherland, D.N. (1967). A theoretical model of floc structure. *J. Colloid Interf. Sci.*, 25, 373-380.

Sutherland, D.N., and Tan, C.T. (1970). Sedimentation of a porous sphere, *Chem. Eng. Sci.*, 25, 1948–1950.

Tambo, N., Watanabe, Y. (1979). Physical characteristics of flocs - I. The flocs density function and aluminium floc, *Wat. Res.*, 13, 409–419.

Tang, P., and Raper, J. A. (2002). Modelling the settling behaviour of fractal aggregates - a review. *Powder Technol.*, 123, 114-125.

Torobin, L.B., Gauvin, W.H. (1959). Fundamental aspects of solid–gas flow. Part 1. *Can. J. Chem. Eng.*, 37, 129–141.

Turton, R., Levenspiel, O. (1986). A short note on the drag correlation for spheres. *Powder Technol.*, 47(1), 83-86.

Veerapaneni, S.A., M.R. Wiesner, Hydrodynamics of fractal aggregates with radially varying permeability, J. Colloid Interface Sci. 177 1996 45–57.

Vesilind, P. A. (1994). The role of water in sludge dewatering. *Wat. Environ. Res.*, 66, 4–11.

Vold, M. J. (1963). Computer simulation of floc formation in a colloidal suspension. *J. Colloid Sci.*, 18, 684-695.

Weitz, D. A., and Oliveria, M. (1984). Fractal structures formed by kinetic aggregation of aqueous gold colloids. *Phys. Rev. Lett.*, 52, 1433-1436.

Wiesener, M. R. (1992). Kinetics of aggregate formation in rapid mix. *Water Research*, 26, pp. 379–387.

Wu, R. M. and Lee, D.J. (1998). Hydrodynamic drag force exerted on a moving floc and its implication to free-settling tests. *Wat. Res.*, 32, 760–768.

Yusa, M. (1977). Mechanisms of pelleting flocculation. *Inter. J. Mineral Processing*, 4, 293-305.

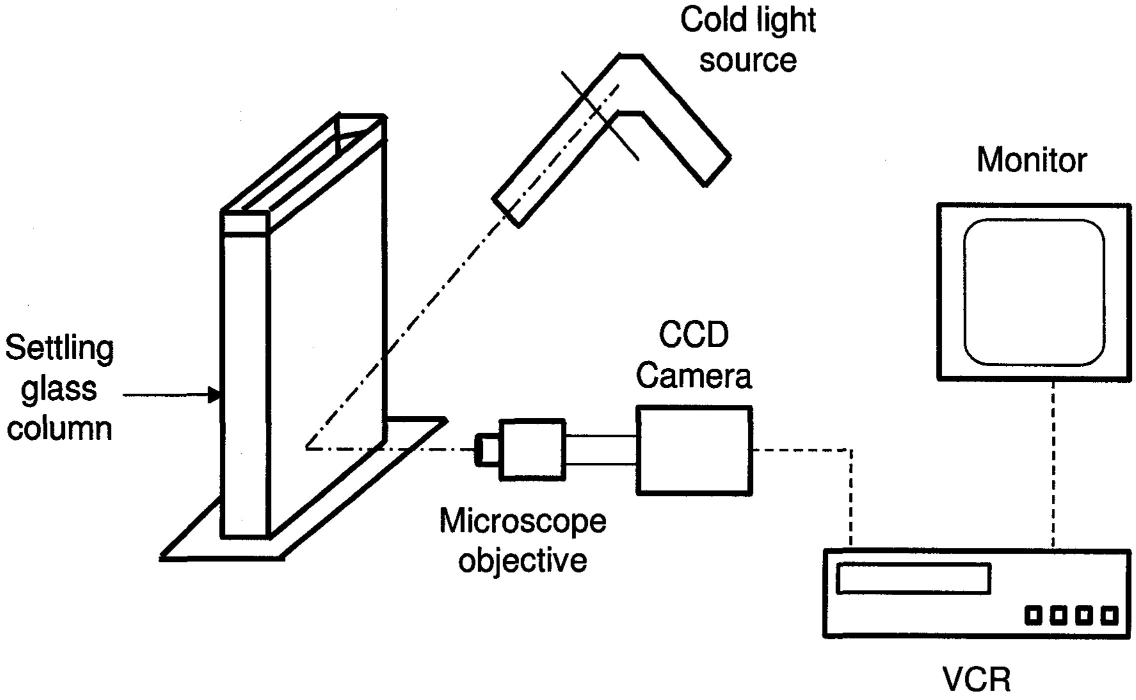

Figure 5.1. Experimental arrangement for aggregate settling velocity measurement.

(a)

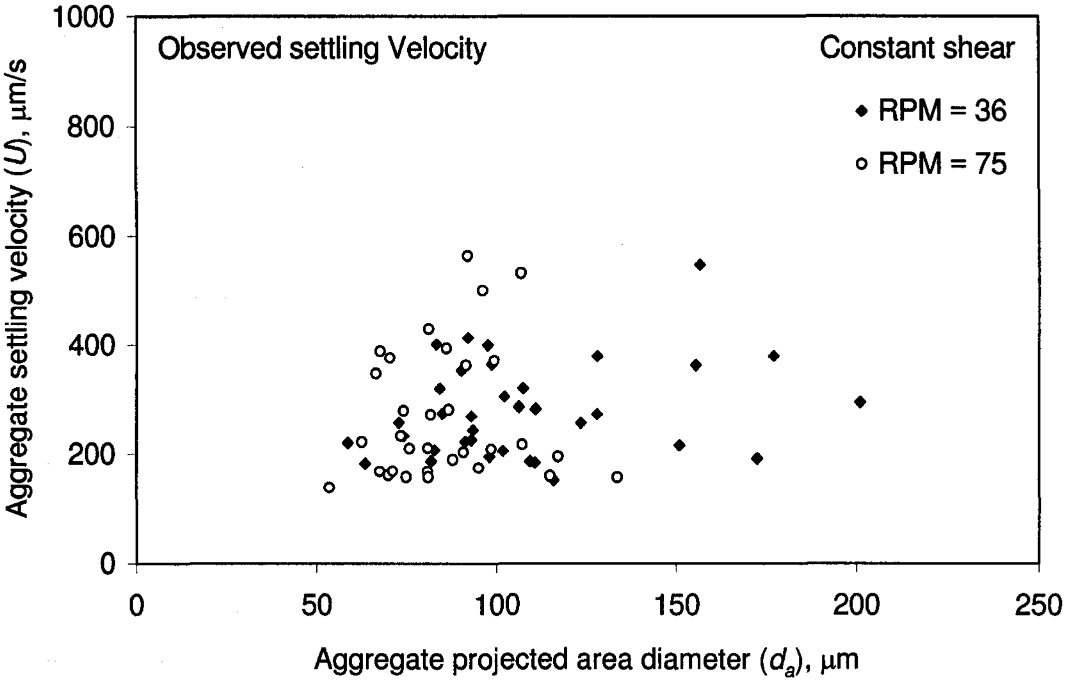

(b)

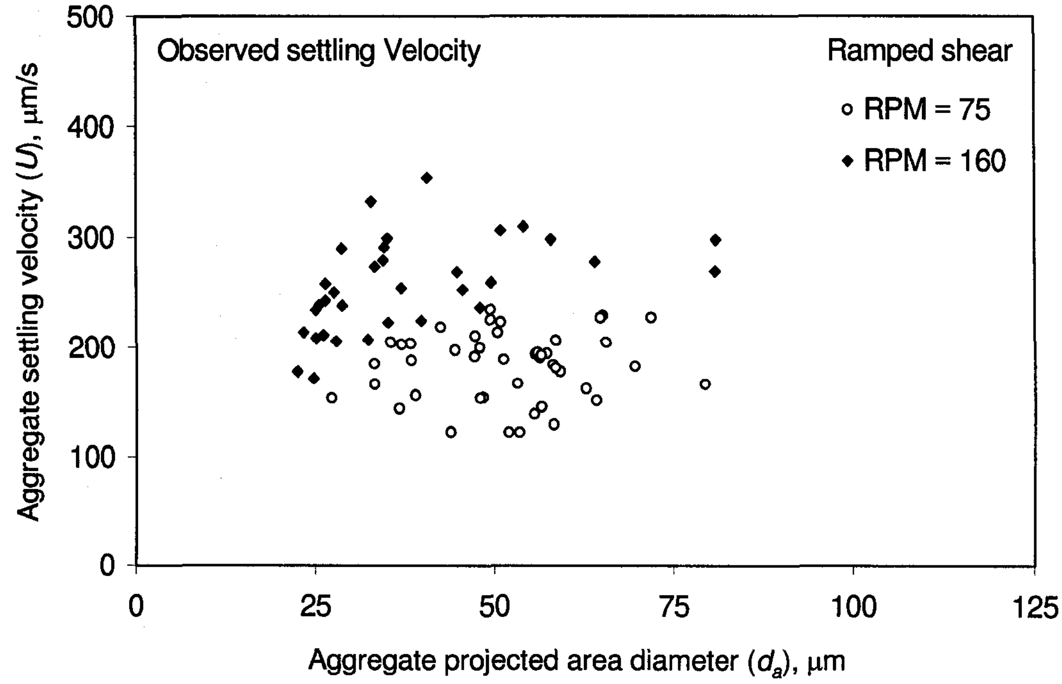

Figure 5.2. Aggregate settling velocity as a function of the projected area diameter at different shear rates for toluene-to-heptane solvent ratio (T:H) of 1:5.

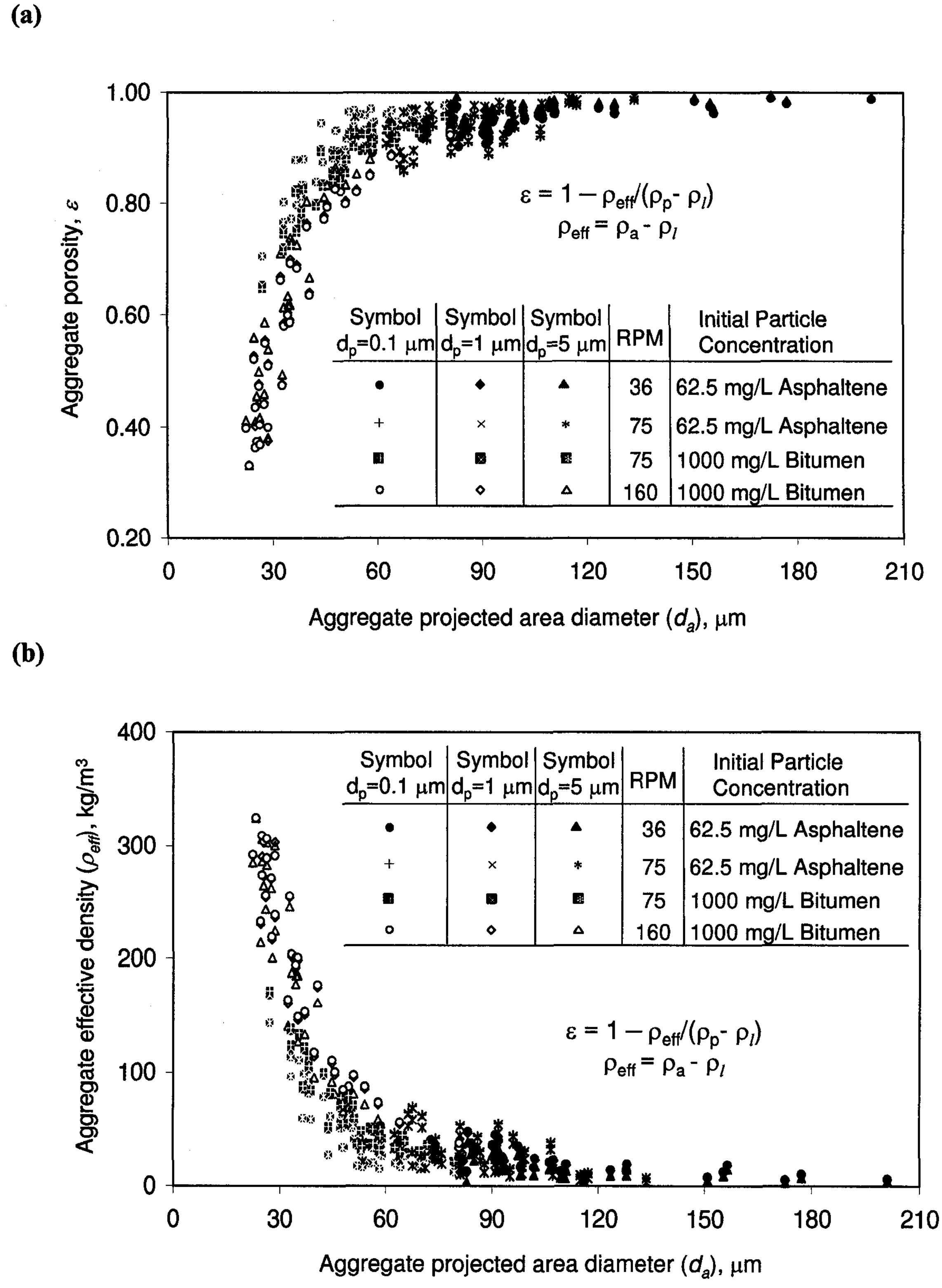

Figure 5.3. Scattered plot of porosity and effective density of asphaltene aggregates versus their projected area diameter for different experimental conditions.

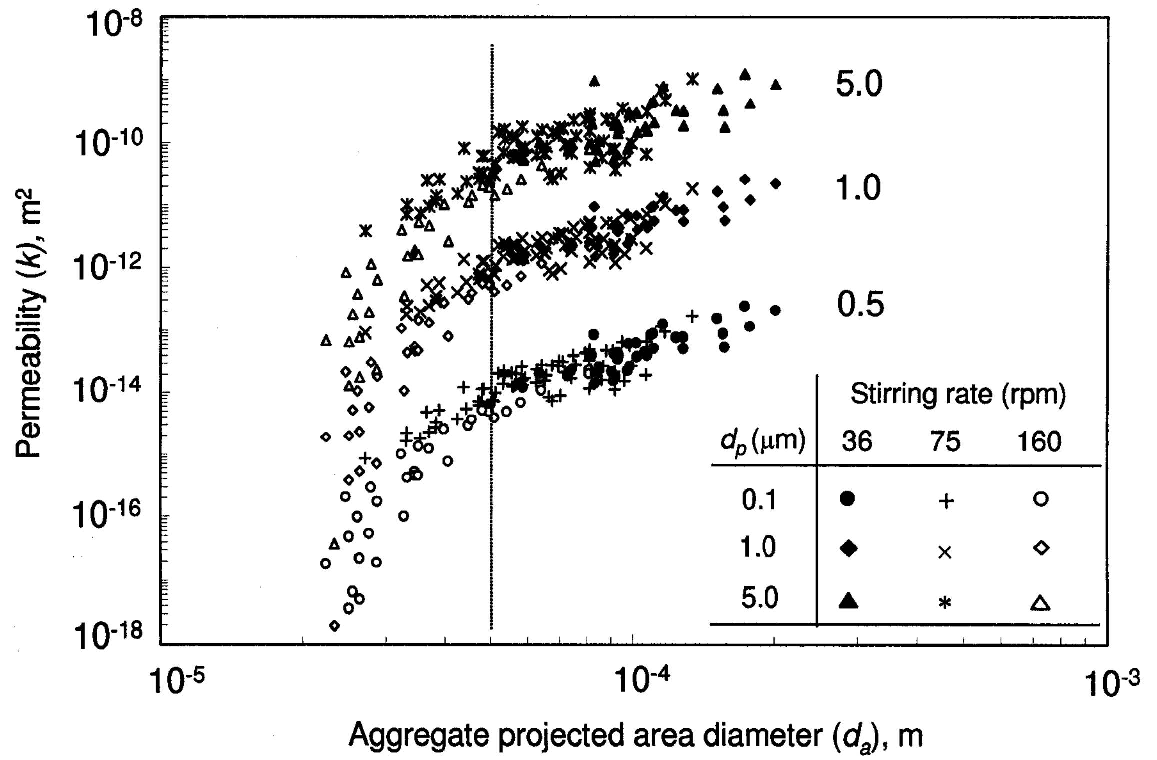

Figure 5.4. Aggregate permeability calculated from Brinkman model versus aggregate projected area diameter (d_a) at different shear rates and primary particle sizes (d_p).

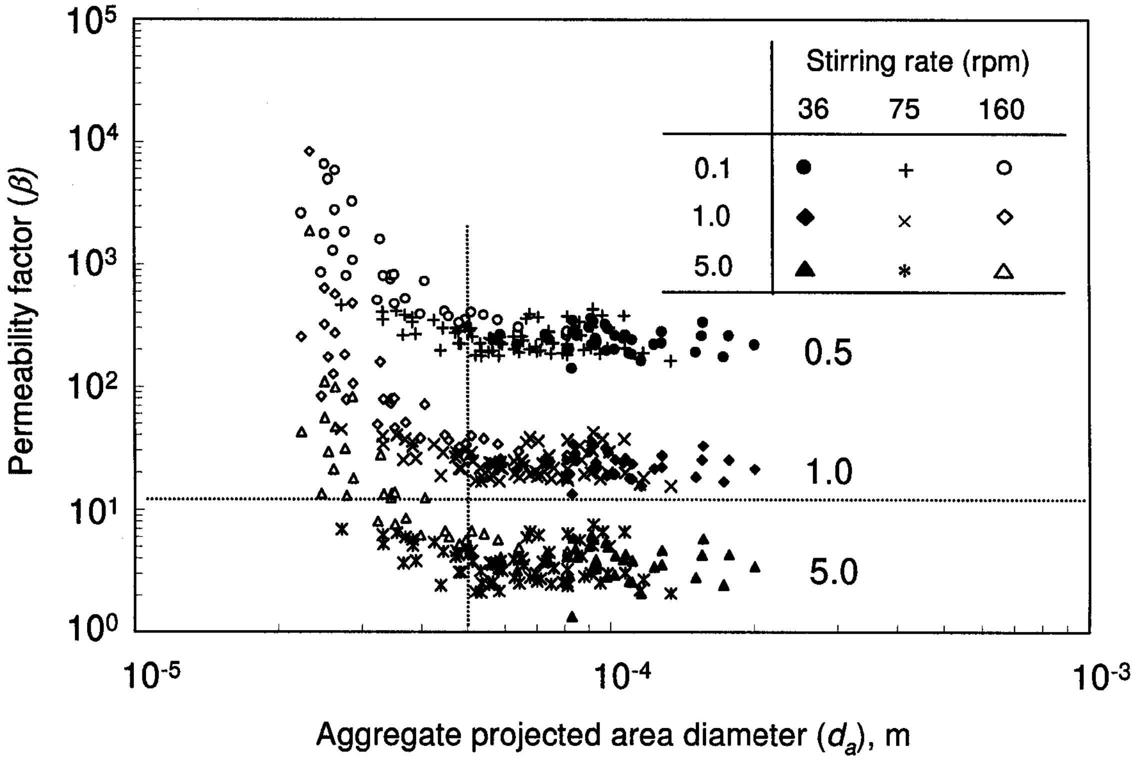

Figure 5.5. Permeability factor β, a dimensionless group, is plotted against aggregate projected area diameter (d_a). Brinkman model is used and a critical β value of 10.9 is shown by the horizontal dotted line.

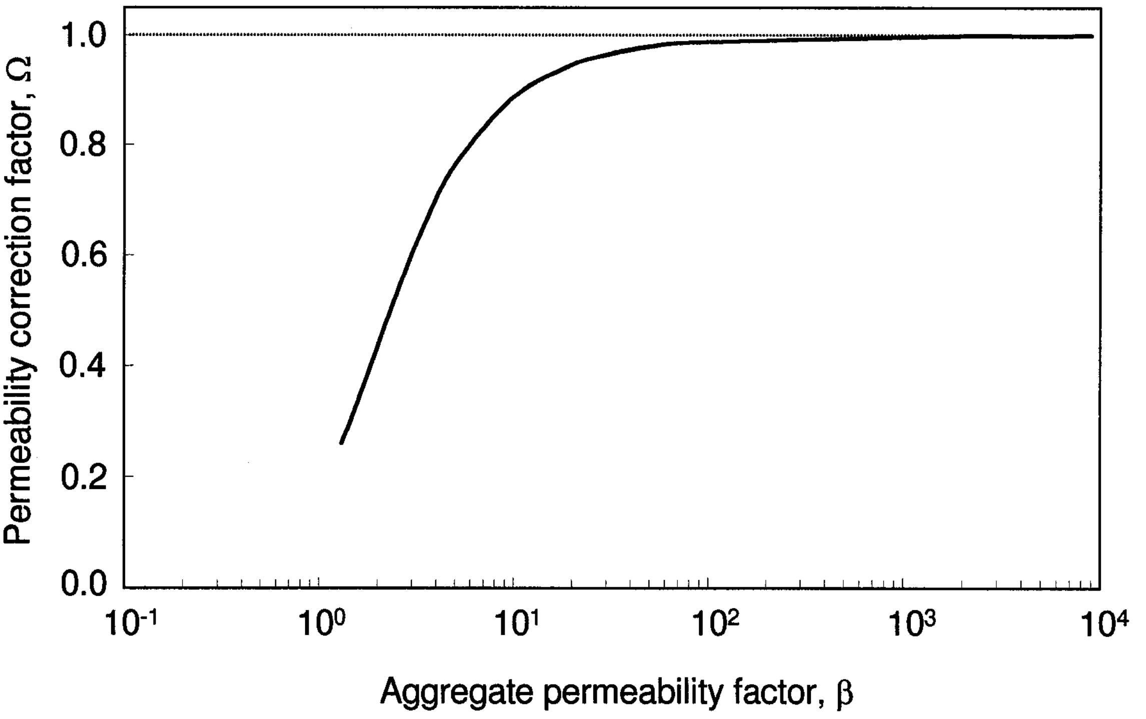

Figure 5.6. Plot of the permeability correction factor, Ω, vs the β values (Eq. 5.9). As the dimensionless aggregate permeability β exceeds approximately 100, Ω becomes unity.

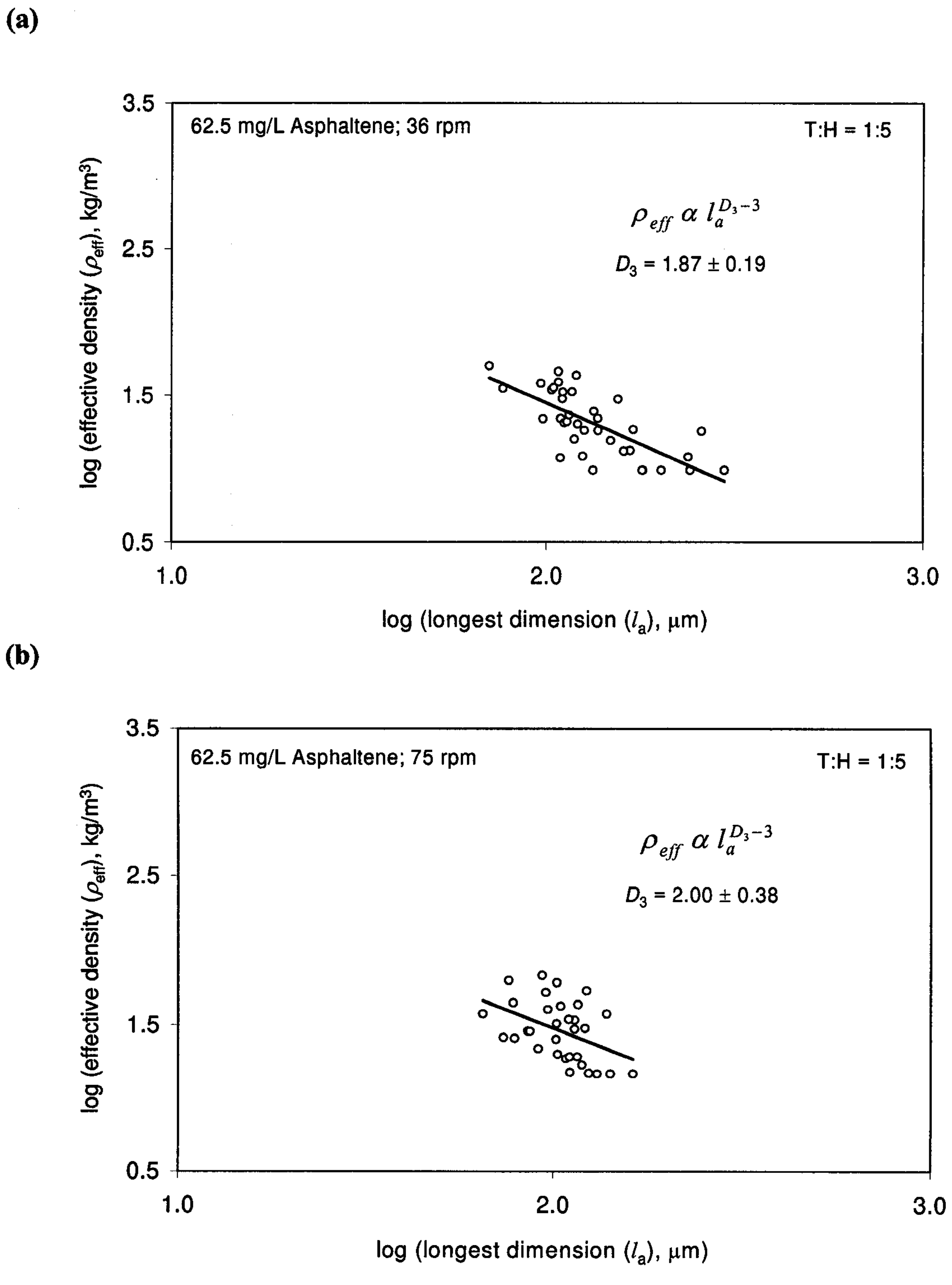

Figure 5.7. Relationship between the log of aggregate effective density (ρ_{eff}) and longest dimension (l_a) with the plot of non-linear regression model to determine three-dimensional fractal dimensions (D_3) of aggregates formed with pure asphaltenes.
(In Fig. 5.7(a), stirring rate = 36 rpm; and in 5.7(b), stirring rate = 75 rpm)

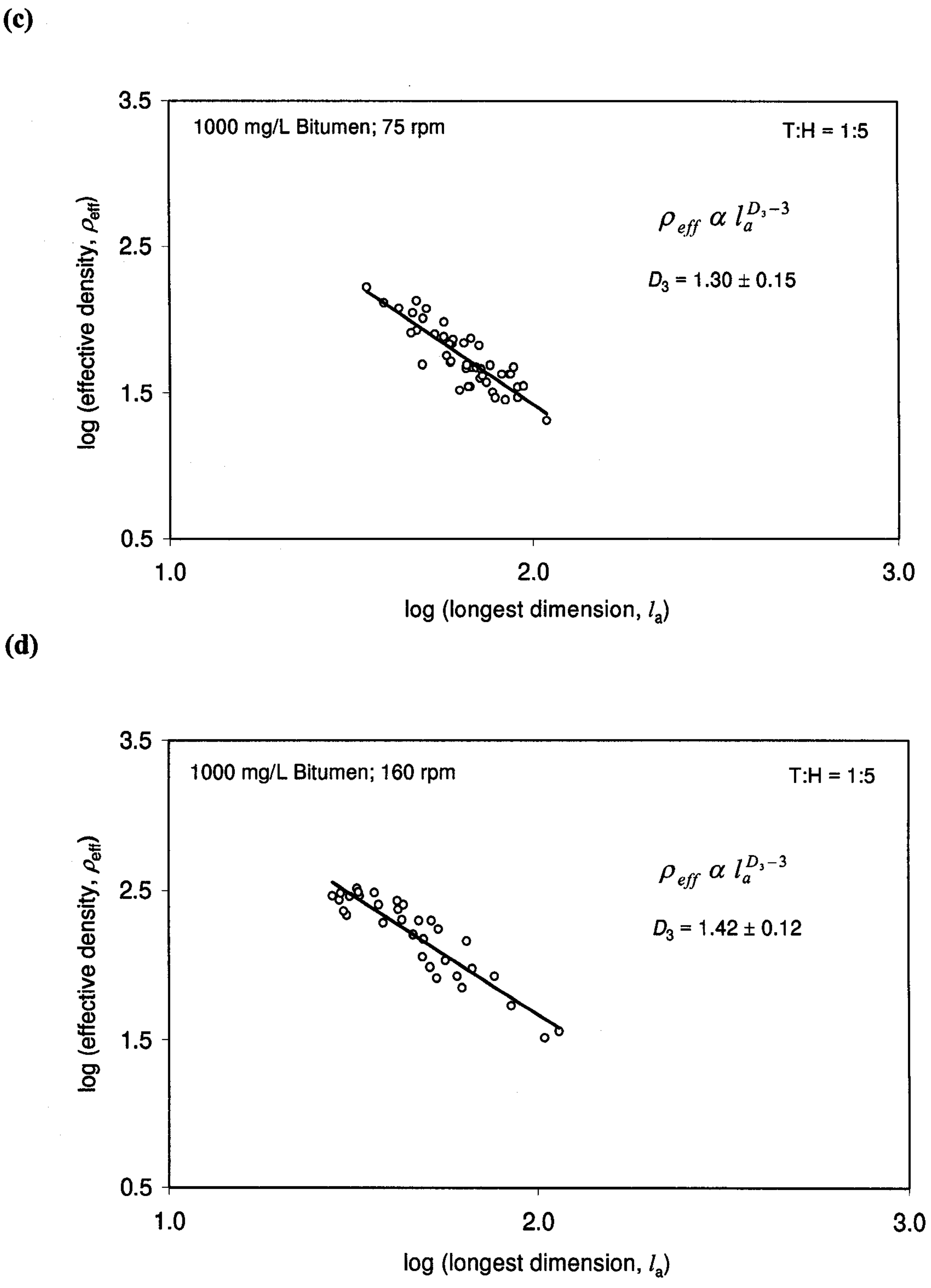

Figure 5.7. Relationship between the log of aggregate effective density (ρ_{eff}) and longest dimension (l_a) with the plot of non-linear regression model to determine three-dimensional fractal dimensions (D_3) of aggregates formed with bitumen.
(In Fig. 5.7(c), stirring rate = 75 rpm; and in 5.7(d), stirring rate = 160 rpm)

Chapter 6

Fractal Structure of Asphaltene Aggregates

6.1 Introduction

Apart from aggregate size distribution, aggregate structure has been known to be of great importance in solid-liquid separation processes such as filtration, sedimentation, and dewatering (Selomulya et al., 2001). The aggregate structure and consequently its density influence the strength of the aggregates (Gregory, 1997). This, in turn, indicates whether an aggregate can sustain the shear experienced during the flocculation process, and determines the final characteristic of the aggregates after they undergo growth, breakup, and possible restructuring (Spicer et al., 1996; Selomulya et al., 2001).

Although endeavors to present disordered forms and structures in mathematical terms had been made since the seventeenth century, a comprehensive approach to the subject was only recently developed by Mandelbrot (1983) and it is called the fractal analysis. Currently, fractal geometry is applied to a broad range of real systems and is utilized for the understanding of many physical phenomena. For particulate systems where the particles adhere to each other on contact, the resulting aggregates have a rugged irregular structure, which exhibits statistical self-similarity. These aggregates are described as fractal, and may be characterized by the calculation of the Hausdorff-Bisicovitch dimension, a quantity independent of size over the range where scaling occurs. Mandelbrot (1983) has termed this value as fractal dimension, D, and has defined a fractal object as one for which the Hausdorff-Bisicovitch dimension is less than the topological dimension. The concept of fractal geometry provides a mathematical framework for description of the structure of irregular flocs.

Image analysis techniques yield data on the basis (in the form) of two-dimensional images of the aggregates being studied, so that once the area and length have been calculated the most interesting feature is the irregularity of the perimeter. In general, there are two basic methods of characterizing aggregates from two-dimensional image data (Bower et al., 1997). The first method is to measure the fractal dimension of the aggregate boundary, and the second method is to consider the scaling relationship between either the perimeter and area, or number density and radius.

The first method employs such techniques as variable magnification, mosaic amalgamation, structured walk, dilation logic, and the equi-spaced method, all of which measure perimeter length as a function of resolution. A summary of the procedures involved and a comparison of the relative merits of each of these methods are given by Kaye et al. (1994).

The second method utilizes perimeter/area measurement (Lovejoy, 1982), nested squares, radius of gyration, and direct correlation, which are all indirect techniques of measuring the density fractal dimension. All these latter techniques have been used by Robinson and Earnshaw (1992) to characterize two-dimensional aggregates, and were found to be in good agreement. Indeed, the majority of the studies using fractal characterization in the current literature utilize one or several of these techniques.

It should be noted that the fractal dimension measured by the boundary method and the density method do not necessarily describe the same physical property of the aggregate, and so may have different values. In particular, they diverge at the morphological extremes of space-filling and tenuous aggregates. This is because the perimeter of a compact, space-filling aggregate is uniform and has a boundary fractal dimension approaching unity, whilst the corresponding density fractal dimension approaches two, the dimension of the plane. Consequently, as the aggregate becomes more porous and tenuous, filling more of the available space, the density fractal dimension is reduced. The aggregate boundary, however, is now more convoluted and irregular, and so its boundary fractal dimension increases.

Fractal dimensions relate aggregate size to some property in n-dimensions, where $n = 1,2$ or 3, and D_n is the fractal dimension in n-dimensions. For example, fractal dimensions of aggregates imbedded in one-, two- and three-dimensions are:

$$P \alpha l^{D_1} \tag{6.1}$$

$$A \alpha l^{D_2} \tag{6.2}$$

$$V \alpha l^{D_3} \quad or \quad V \alpha l^{D} \tag{6.3}$$

where l is the characteristic length scale, which can be taken either as the shortest, longest, geometric mean, or equivalent radius (based on area) (Gorczyca and Ganczarczyk, 1996) of an aggregate, P is the aggregate perimeter, A is the projected aggregate area, and V is the aggregate volume. The subscripts on D_n indicate the integer value of D_n for Euclidean geometry. If the subscript is omitted, it is understood that its value is 3, or $D_3 = D$. The fractal dimensions can be obtained from the slopes of log-log plots of the respective aggregate properties in Eqs. 6.1 to 6.3 and aggregate length. For Euclidean objects (e.g. a sphere), $D_1 = 1$, $D_2 = 2$, and $D_3 = 3$.

The perimeter of irregular objects is larger, and the cross-sectional area is smaller, than the corresponding properties of spheres of the same length. As the perimeter of fractal objects increases with particle size, their D_1 values are greater than unity. Similarly, fractal aggregates become less dense and more irregular as they increase in size and their $D_2 < 2$. These two fractal dimensions therefore quantify the rates at which perimeter and aggregate projected area increase with respect to particle maximum length.

Since the different fractal dimensions characterize how the aggregate properties change with size, their magnitude is related to aggregate morphology. Properties of aggregates that affect sedimentation rates, such as porosity, average density, and hydrodynamic radius, are primarily functions of D_2 and D_3. Aggregates tend to become more porous with increasing size resulting in two- and three- dimensional fractal dimensions that are usually less than their corresponding Euclidean values, i.e. $D_2 < 2$ and $D_3 < 3$.

For an aggregate made up of spherical primary particles of diameter d_p, the number of particles in the aggregate (N_P) is a function of the solid volume according to $N_P = V/(\pi d_p^3/6)$. Since $N_P \sim V$, Eq. (6.3) can also be written in terms of particle number as

$$N_P \, \alpha \, l^{D_3} \tag{6.4}$$

Particle size and shape affect the behavior of aggregated particles, particularly with regard to collision efficiency (Jiang and Logan, 1991) and settling rates (Gorczyca and Ganczarczyk, 1996). Heterogeneously (non uniformly) packed objects with irregular boundaries can be defined by nonlinear relationships where the properties of the object scale with a characteristic length dimension raised to a power called the fractal dimension (Wiesner, 1992; Grijspeerdt and Verstraete, 1997; Logan, 1999; Gardner et al., 1998). For example, the aggregate porosity (or, effective density) and characteristic length are consistent with power-law relationships:

$$1 - \varepsilon \sim l_a^{D_3 \text{-} 3} \tag{6.5}$$

$$\rho_{eff} = \rho_a - \rho_l \propto l_a^{D_3 \text{-} 3} \tag{6.6}$$

where ε is the aggregate porosity; (1-ε) is the solid volume fraction in an aggregate; l_a is the aggregate longest dimension; ρ_{eff} is the aggregate effective density; ρ_a is the aggregate density; ρ_l is the density of the liquid, and D_3 is the 3-dimensional fractal dimension for a self-similar structure. If the fractal relationship between aggregate size and porosity (i.e. $1 - \varepsilon \sim l_a^{D_3 - 3}$) is included in Stokes' equation, then this equation leads to the scaling relationship between settling velocity (*U*) and aggregate longest dimension (Jiang and Logan, 1991)

$$U \sim l_a^{D_3 - 1} \qquad (6.7)$$

Hence the fractal dimension, D_3, can also be derived from the slope of log-log plot of settling velocity and aggregate longest dimension. A few more scaling relationships between *U* and l_a exist in the literature for different ranges of Reynolds numbers and fractal dimensions (Logan, 1999). As the experimentally observed aggregate settling velocities fall in the Stokes' regime ($Re \ll 1$), for present study Eq. (6.7) is used to determine the 3-D fractal dimension of the aggregates.

For rapid coagulation, particles with small D_3 may be desirable (Logan, 1999; Gardner et al., 1998) while for gravity settling a large D_3 is preferred. Recently, fractal concepts have been used to explain higher observed settling velocities for large aggregates, relative to Stokes' settling (Johnson et al., 1996; Chakraborti et al., 2000). As indicated by Eq. (6.7), both aggregate size and fractal dimension influence the settling velocity, *U*. It was suggested that the internal flow through large pores within the fractal aggregates would likely contribute to faster settling velocities and enhanced coagulation between the aggregates and suspended particles (Li and Logan, 2000).

Morphological characterization of suspended aggregates can be achieved using a microscopic technique, which is complementary to macroscopic methods for characterizing flocculated suspensions. Methods that are widely used in industries to determine flocculation performance include measurement of sediment height, settling velocities of flocs, terminal sediment volume and conventional rheometry. Such techniques provide valuable information about the bulk behavior of suspensions, but it is difficult to extract information concerning the detailed behavior of the particles, or their dynamic behavior, from these measurements. The microscopic technique employed in the present study is ideally suited for the study of suspensions containing solid asphaltene particles in the sub-micrometer size range, which flocculate to form aggregates several micrometers in diameter, and provides information concerning aggregate compactness and fractal properties.

In the present experimental studies, the asphaltene aggregates are formed using the Couette flocculator and the jar tester (four pitched blade-type flocculator). In first set of experiments in Couette flow, photographic technique and image analysis are employed to monitor the dynamic evolution of the aggregates structure at different shear rates in terms of the 2-D fractal dimension. The structure of the asphaltene aggregates at steady state is found to depend on rotational speed, but not on the solvent composition or particle concentration. In the second set of experiments, asphaltene aggregates are formed in a stirred tank under different experimental conditions and transferred to a quiescent glass-settling column having the same solvent mixture. Photographic technique and image analysis are used to determine the aggregate size and settling velocity in the bottom section of the glass column after the aggregates reach the terminal settling velocity. The 2-D and 3-D fractal dimensions of the aggregates are then determined from the slopes of size-projected area and size-settling velocity regression lines.

6.2 Results and Discussion

6.2.1 Determination of Aggregate Fractal dimension in Couette Flocculator

The concept of fractal nature proposed in 1975 by Mandelbrot is useful to describe the ruggedness of flocs. The asphaltene aggregates have rugged, irregular structures and statistical self-similarity, which resemble the shape of cloud and snowflakes (Fig. 6.1).

Table 6.1. The steady-state fractal dimensions as a function of shear rate for asphaltene aggregates produced in a Couette device at toluene-to-heptane solvent ratio of 1:15 and particle concentration of 12.8 mg/L

Equation Number	Fractal Dimension (± Std. Error)	Average Shear Rate, s^{-1}				
		1.2	2.5	3.8	8.4	12.7
6.1	D_1	1.08±0.03	1.05±0.02	1.09±0.03	1.06±0.03	1.06±0.03
6.2	D_2	1.61±0.03	1.80±0.03	1.82±0.04	1.80±0.03	1.90±0.03

Table 6.1 shows the one- and two-dimensional fractal dimensions obtained from the log-log plots (see Figs. 6.2 and 6.3) of aggregate longest dimension versus perimeter and projected area, respectively, based on the analysis of several aggregates, formed in a Couette device and reached steady state at all the employed shear rates. The standard error is applied in determining the slopes from the regression lines. A higher D_2 fractal

dimension with increasing shear indicates that the aggregates became less amorphous and more compact at higher shear rates. However, the one-dimensional fractal dimension did not show any significant dependence on shear rate. Since the one-dimensional fractal dimension increases with the irregularity of a boundary, the fractal nature of the aggregate perimeter was not correlated with changes in the aggregate area. A similar lack of correlation between trends in D_2 and D_1 fractal dimensions has previously been found for synthetic as well as marine snow aggregates (Logan and Kilps, 1995).

If measurement of perimeter (P) of an aggregate is performed with an accuracy defined by the smallest length of the measurement (i.e. resolution), a relationship between the measured perimeter (P) and the projected area (A) of the floc can be expressed by the following equation

$$A \alpha P^{2/D_{\mathrm{pf}}} \tag{6.8}$$

where D_{pf} is the perimeter-based fractal dimension of the floc (Mandelbrot et al., 1984). The value of D_{pf} is a quantitative measure of floc structure that is directly related to the surface fractal dimension, D_{s}, of the floc (Mandelbrot et al., 1984). A surface can be rough in a way such that it can also be characterized by surface fractal dimension (D_{s}). In a 2-D digital image, if a "compass" of opening (t) is used to step around the surface (perimeter) and measure its apparent length $S(t)$, then $S(t) \propto t^{-D_s}$. Using a log-log plot of $S(t)$ vs t, the value of D_{s} can be estimated. Image analysis of floc structure projection is a more direct and rapid measure of floc structure than light scattering and size or sedimentation velocity measurements, and thus has potential for on-line application in the processing industry. The mass fractal dimension, D_{m}, characterizes the fractal nature of an object in a digital image by measuring how the object fills Euclidean space as a function of the size of the region being examined. It is defined as $M \propto R^{D_m}$, where M is the mass of the particle, and R is a linear measure of size. The mass fractal dimension of a floc, D_m, is also a measure of the floc structure and varies form 1 for a line of particles to 3 for a sphere (Mandelbrot, 1989). However, the D_{pf} derived from image analysis is a two-dimensional fractal dimension and is not directly related to D_m (Meakin, 1988).

Equation 6.8 is used to investigate the geometry of asphaltene aggregates. From the measurement of the properties of individual aggregates, it is possible to measure the fractal dimension of a population of aggregates having different sizes. As there are several aggregates in each experiment, the perimeter-based fractal dimension, D_{pf}, of the flocs can be estimated from Eq. (6.8) using a log-log plot of the floc perimeter and projected area. The value of D_{pf} is related to the floc surface morphology since D_{pf} varies between 1 (the projected area of a solid sphere, a circle) and 2 (a line, e.g., a chain of particles). Values of D_{pf} greater than one have been found for synthetic fractals (Mandelbrot, 1983) and a variety of natural objects such as clouds, lakes, and snow patches during melt (Korvin, 1992). The interpretation of $D_{pf} > 1$ is that as the objects become larger, i.e., as A increases, P increases more rapidly than for Euclidean objects so that the boundary becomes more convoluted (De Boer, Stone, and Levesque, 2000). Therefore larger values of D_{pf} represent irregular floc structures.

Fig. 6.4 shows the relation between the projected area (A) of the flocs with their perimeter (P) on logarithmic coordinates. The perimeter based fractal dimension of the flocs at steady state (D_{pfss}) was derived individually for all employed shear rates (i.e. 1.2 – 12.7 s^{-1}) from Fig. 6.4 and are shown together in Fig. 6.5. At higher shear rate, $G = 12.7$ s^{-1}, the flocs were small and the D_{pfss} was smaller (indicating more compact and regular structures), while at comparatively lower shear rates (e.g. 1.2 and 2.5 s^{-1}), they became more porous and irregular (understood from higher D_{pfss} values). At higher shear, the increased amount of splitting or erosion and/or restructuring of the floc result in more compact floc structures at steady state.

Figure 6.6 shows the time evolution of D_{pf} for three different shear rates. The various shear rates (i.e., G) within the Couette device produce a distribution of floc structures as a result of simultaneous shear-induced growth, breakage, and/or restructuring. The D_{pf} values were determined from the log-log plot of flocs perimeter and projected area, obtained from the analysis of the images taken at a specific time. The graph shows that D_{pf} increases from its initial value ($D_{pf} = 1$, assuming spherical "primary" particles when the experiment starts) and reaches a maximum value as the flocs grow and become more porous. When breakage and possibly restructuring begin to dominate, the D_{pf} value decreases until it reaches a steady-state value. Tambo and Watanabe (1979) and Oles (1992) suggested that a decreased floc porosity (as indicated here by the decreasing perimeter-based fractal dimension) results from the production of strong, dense fragments by preferential breakage of the flocs at weak points.

For all cases, D_{pf} values are obtained using regression analysis. Since a whole population of aggregates is used in these calculations, the calculated fractal dimensions represent a statistical average for the population of aggregates. Individual aggregates may have higher or lower fractal dimensions.

The measured steady-state perimeter-based fractal dimensions, D_{pfss}, for different asphaltene particle concentrations and toluene-to-heptane ratios in the solvent mixture are shown in Figs. 6.7 and 6.8 and summarized in Table 6.2. Error bars represent the standard

Table 6.2. The steady-state perimeter-based fractal dimensions (D_{pfss}) of asphaltene aggregates obtained from a Couette device as a function of particle concentration and solvent composition

Average shear rate, s^{-1}	Asphaltene particle concentration, mg/L			Ratio of toluene-to-heptane in the solution		
	4.1	5.3	10.3	1:3	1:7	1:15
2.5	1.12±0.03	1.17±0.03	1.14±0.02	1.12±0.03	1.14±0.02	1.18±0.03

error of the measured values of D_{pfss} during the experiment. The D_{pfss} values were not affected significantly at the lower shear rate of 2.5 s^{-1} by asphaltene particle concentration or toluene-to-heptane ratios in the solvent.

A problem arises when the aggregates of interest are three-dimensional objects, which is usually the case with real systems. The images are two-dimensional projected areas of the actual shape. Consequently, some of the detail of the original shape will be obscured in the projection of the resultant profile. Between 33% and 36% (Rogak and Flagan, 1992; Gray et al., 1985) of the particles will be hidden. Fractal dimensions measured by image analysis techniques are, therefore, intrinsically lower than the actual D values for three-dimensional flocs. The maximum permitted value of fractal dimension for both boundary and scaling methods is 2, since in both cases this corresponds to a curve that fills the plane completely; therefore, any object with a mass fractal dimension $D > 2$ will be underestimated by image analysis techniques. However, Jullien and Thouy (1994) have proposed that for $D < 2$ the values measured from the two-dimensional projected areas concur with the actual value of D, and that the perimeter fractal dimension of the two-dimensional objects is a non-trivial continuously varying function of D. According to Rogak and Flagan (1992), any object with fractal dimension $D > 2$ is underestimated by 10~20% compared to the values obtained using techniques that are sensitive to three-dimensional structure, such as dynamic light scattering (Cai et al., 1993) and settling velocities (Colbeck and Wu, 1994). The comparison of values measured by image analysis with values measured by the above techniques, should, therefore, be used with caution.

6.2.2 Determination of fractal dimension from settling velocity of aggregates

From settling experiments (described in Chapter 5), the 2-D and 3-D fractal dimensions of the aggregates are calculated from the log-log plot of aggregates projected area vs the longest dimension (Fig. 6.9) and aggregates settling velocity vs the longest dimension (Fig. 6.10), based on Eqs. (6.2) and (6.7), respectively. A more accurate 3-D fractal dimension can be obtained by using Eq. (6.5), which was shown in Chapter 6. For asphaltene aggregates formed at different shear rates and particle concentrations, the size of the aggregates varied in a narrow range of 20–200 micron. Table 6.3 exhibits that the

Table 6.3. Fractal dimensions of asphaltene aggregates obtained from settling tests

Variables for asphaltene aggregate formation in the stirred tank (Shear rate; Particle concentration)	2-D Fractal dimension (D_2 ± Std. Error)	3-D Fractal dimension (D_3 ± Std. Error)
36 RPM; 62.5 mg/L Asphaltene	1.57 ± 0.08	1.29 ± 0.16
75 RPM; 62.5 mg/L Asphaltene	1.71 ± 0.10	1.41 ± 0.36
75 RPM; 1000 mg/L Bitumen	1.71 ± 0.05	1.06 ± 0.11
160 RPM; 1000 mg/L Bitumen	1.68 ± 0.05	1.23 ± 0.07

2-D fractal dimensions fall in the range from 1.57–1.71 and the 3-D fractal dimensions fall in the range from 1.06–1.41. The fractal dimensions obtained from size and settling velocity measurement are statistically analyzed. In regression analysis, the precision of parameter estimation using standard error (Box et al., 1978) is applied to identify whether the results are statistically different for the aggregates formed under four different conditions. However, no statistically significant difference is found in fractal dimensions among different groups of asphaltene aggregates studied (Table 6.3). The large standard error in 3-D fractal dimension from experimental data may be caused either by the limitations of the experimental method used or by the real shape distribution of asphaltene aggregates within the same characteristic length. For such a narrow range of smaller size aggregate studied (20-200 μm), a large scatter in the experimental observations between aggregate settling velocity and size is also found in literature (Námer and Ganczarczyk, 1994; Lee et al., 1996; Gorczyca and Ganczarczyk, 1996).

Table 6.4 summarizes 3-D fractal dimension for various aggregates obtained from free-settling experiments of other studies. Inorganic flocs usually exhibit higher fractal dimensions while for the microbial and organic flocs they are smaller. Activated sludge flocs show fractal dimensions ranging from 1.0-2.0. Inorganic flocs have fractal dimensions in a higher range – from 1.59-2.85. Fractal dimensions of asphaltene aggregates are at the lower limit of the range for activated sludge flocs. The lower fractal dimension derived for this work indicates that the asphaltene aggregates possess a highly porous structure. Moreover, the observation that the 3-D fractal dimensions of the three-dimensional aggregate structure are less than 2 (which is the Euclidean dimension of surface) strongly implies that the aggregates have extremely low space-filling capacity.

Table 6.4. Fractal dimensions obtained from free-settling experiments of other studies for inorganic, and microbial aggregates and aggregates formed in organic medium

Type of Aggregate	3-D Fractal Dimension (D_3)	References
	Inorganic Aggregates	
Alum	1.59-1.97	Tambo and Watanabe (1979)[a]
Clay-iron	1.92	Tambo and Watanabe (1979)[a]
Clay-magnesium	1.91	Tambo and Watanabe (1979)[a]
Alum	1.55-1.66	Gorczyca and Ganczarczyk (1992)
	Microbial Aggregates	
Activated sludge	1.0-1.3	Tambo and Watanabe (1979)[b]
Activated sludge	1.44-1.49	Magara et al. (1976)[a]
Activated sludge	1.55-2.0	Li and Ganczarczyk (1989)
Sludge from BF	1.79	Zahid and Ganczarczyk (1990)
Sludge from ASBF	1.85	Park and Ganczarczyk (1994)
Digested sludge	1.63-1.66	Namer and Ganczarczyk (1994)
	Aggregates Formed in Organic Medium	
Asphaltenes	1.06-1.41	this study

[a]Calculated by Li and Ganczarczyk (1989); [b]Calculated by Logan and Wilkinson (1990);

BF = biological filter; ASBF = aerated submerged biological filter.

Theoretically, the solid portion in such a structure is so low that it would not fill completely its own projected area. This conclusion regarding the fractal dimension of the aggregates is in qualitative agreement with the high porosity of the aggregates reported (see Chapter 5).

Because fractal dimension may vary with the aggregates generated under different conditions, it can be used to study the factors that affect the process of aggregation. In this study, it can be observed from Table 6.3 that at the same stirring speed of 75 rpm, asphaltene aggregates formed with extracted and purified asphaltenes produced considerably higher 3-D fractal dimension than that formed with bitumen. It implies that the presence of other compounds (such as – resins, aromatics, and saturates) in bitumen makes the asphaltene aggregates more tenuous and more irregular. Hence, the fractal dimension can link the affecting factor directly to the process of aggregation and the structure of the aggregates. Besides, the fractal nature of the aggregates suggests that the aggregates are filled with gaps of all sizes. It seems possible to quantitatively characterize the gaps in the aggregates by using fractal theory, once the fractal dimension of a sample of aggregates is determined.

6.3 Conclusions

It has been demonstrated that asphaltene aggregates, generated in the flocculation/coagulation process, possess fractal features. Several morphological properties of these aggregates are characterized by fractal dimension. In this study, the asphaltene aggregates are formed using the four-pitch blade-type mixing vessel and the Couette apparatus. It can be noticed that the experimental standard error in the fractal dimensions obtained for aggregates produced in Couette device are considerably smaller. Basically, flows in a mixing vessel are far from homogeneous with very high shear produced near the blade tip and generally low shear elsewhere. Hence a larger experimental standard error is observed in free-settling tests, where aggregates produced from jar tester are used.

The 2-D fractal dimensions, observed in the Couette device, became higher with increasing shear indicating that the aggregates became less amorphous and more compact at higher shear rates. The dynamic evolution of asphaltene aggregate structure was monitored by image analysis of the digitized images. The perimeter-based fractal dimension, D_{pf}, of the flocs was found to initially increase (more open structure) and then decrease slightly (more compact structure) and reach a steady state as a result of shear-induced breakage and/or restructuring. Shear-induced restructuring also narrows the range of D_{pf} values as steady state is attained. The steady-state perimeter-based fractal dimensions, D_{pfss}, of the flocs formed at the lower shear rate of 2.5 s^{-1}, exhibit no significant dependence on asphaltene concentration or solvent composition.

In free-settling test, the size-density fractal dimension (D_3) of the asphaltene aggregates was estimated to be in the range from 1.06–1.41. This value is low and comparable with fractal dimensions for activated sludge flocs. It indicates that the asphaltene aggregates are highly porous and more tenuous. The aggregates have almost linear structure with extremely low space-filling capacity.

From a practical viewpoint, the present study provides quantitative information on the significance of shear rate, particle concentration, and solvent composition on the shape/structure, and consequently density/compactness, of asphaltene aggregates. This knowledge will help to understand the settling behavior of asphaltene aggregates and is essential for proper process design and material handling.

6.4 Nomenclature

A	aggregate projected area (μm^2)
d_a	aggregate projected area diameter (μm)
D	three-dimensional fractal dimension (also used as D_3)
D_1	one-dimensional fractal dimension
D_2	two-dimensional fractal dimension
D_m	mass fractal dimension
D_{pf}	perimeter-based fractal dimension
D_{pfss}	perimeter-based fractal dimension at steady state
D_s	surface fractal dimension of the floc
G	shear rate (s^{-1})
l	the characteristic length scale (shortest / longest / geometric mean / radius of gyration / equivalent radius based on area) of an aggregate
l_a	aggregate longest dimension (μm)
M	Mass of the particle (kg)
N_P	number of primary particles in the aggregate
P	aggregate perimeter (μm)
Re	Reynolds number, $Re = Ud_a / \nu$
U	settling velocity of a permeable aggregate ($\mu m/s$)

Greek

ε	porosity of the aggregates
ν	kinematic viscosity of the fluid (m^2/s)
ρ_a	aggregate density (kg/m^3)
ρ_{eff}	aggregate effective density (kg/m^3)
ρ_l	density of the liquid (kg/m^3)

6.5 References

Bower, C., Washington, C., and Purewal, T. S. (1997). The use of image analysis to characterize aggregates in a shear field. *Colloids and Surf. A Physicochem Aspects*, 127, 105.

Box, G. E. P., Hunter, W. G., and Hunter, J. S. (1978). *Statistics for Experiments: An Introduction to Design, Data Analysis, and model building.* John Wiley and Sons, New York.

Cai, J., Lu, N., and Sorensen, C. M. (1993). Comparison of size and morphology of soot aggregates as determined by light scattering and electron microscope analysis. *Langmuir*, 9, 2861.

Chakraborti, R. K., Atkinson, J. F., and Van Benschoten, J. E. (2000). Characterization of Alum Floc by Image Analysis. *Environ. Sci. Technol.*, 34, 3969.

Colbeck, I., and Wu, Z. F. (1994). Measurement of the fractal dimensions of smoke aggregates. *Journal of Physics. D*, 27, 670.

De Boer, D. H., Stone, M., and Levesque, L. M. J. (2000). Fractal dimensions of individual flocs and floc populations in streams. *Hydrological Processes*, 14, 653.

Gardner, K. H., Theis, T. L., and Young, T. C. (1998). Colloid aggregation: numerical solution and measurements. *Colloids and Surf. A Physicochem Aspects*, 141, 237.

Gorczyca, B., and Ganczarczyk, J. (1996). Image analysis of alum coagulated mineral suspensions. *Environ. Technol.*, 17, 1361.

Gorczyca, B., and Ganczarczyk, J. (1992). Influence of the nature of the turbidity on some properties of alum coagulation flocs. *Paper Presented at the 1992 AWWA Annual Conference*, Vancouver, Canada.

Gray, R. H., Kanapilly, G. M., Cheng, Y. S., and Wolf, R. K. (1985). Image enhancement of aggregate aerosols by stereopsis. *Journal of aerosol science*, 16, 211.

Gregory, J. (1997). The density of particle aggregates. *Water Science Technology*, 36(4), 1-13.

Grijspeerdt, K., and Verstraete, W. (1997). Image analysis to estimate the settleability and concentration of activated sludge, *Wat. Res.*, 31(5), 1126-1134.

Jiang, Q., and Logan, B. E. (1991). Fractal dimensions of aggregates determined from steady-state size distributions. *Environ. Sci. Technol.*, 25(12), 2031.

Johnson, C. P., Li, X., and Logan, B. E. (1996). Settling velocities of fractal aggregates. *Environ. Sci. Technol.*, 30, 1911-1918.

Jullien, R., and Thouy, R. (1994). Numerical investigation of two-dimensional projections of random fractal aggregates. *Physical Review. E.*, 50, 3878.

Kaye, B., Clark, G. G., and Kydar, Y. (1994). Strategies for evaluating boundary fractal dimensions by computer aided image analysis. *Particle & Particle Systems Characterization*, 2, 411.

Korvin, G. (1992). *Fractal models in the earth sciences.* Elsevier, Amsterdam.

Lee, D.J., Chen, G.W., Liao, Y.C., and Hsieh, C.C. (1996). On the free-settling test for estimating activated sludge floc density, *Wat. Res.*, 30, 541–550.

Li, D., and Ganczarczyk, J. (1989). Fractal geometry of particle aggregates generated in water and wastewater treatment processes," *Environ. Sci. Technol.*, 23(11), 1385.

Li, X. Y., and Logan, B. E. (2000). Settling and coagulating behaviour of fractal aggregates. *Wat. Sci. Technol.*, 42(3-4), 253.

Logan, B. E. (1999). *Environmental Transport Processes.* John Wiley and Sons, New York, 466-504.

Logan, B. E., and Kilps, J. R. (1995). Fractal dimensions of aggregates formed in different fluid mechanical environments. *Wat. Res.*, 29(2), 443.

Logan, B. E., and Wilkinson, D. B. (1990). Fractal geometry of marine snow and other biological aggregates. *Limnology and Oceanography*, 35(1), 130.

Lovejoy, S. (1982). Area-perimeter relation for rain and cloud areas. *Science*, 216, 185.

Magara, Y., Nambu, S., and Utosawa, K. (1976). Biochemical and physical properties of an activated sludge on settling characteristics. *Wat. Res.*, 10, 71-77.

Mandelbrot, B. B. (1989). Fractal geometry - what is it, and what does it do. *Proc. Roy. Soc. Lond. A Mat.*, 423, 1864.

Mandelbrot, B. B. (1983). *The fractal geometry of nature.* Freeman, W. H., San Francisco, California.

Mandelbrot, B. B. (1975). Geometry of homogeneous turbulence, with stress on fractal dimension of iso-surfaces of scalars. *Journal of Fluid Mechanics*, 72, 401-416.

Mandelbrot, B. B., Passoja, D. E., and Paullay, A. J. (1984). Fractal character of fracture surfaces of metals. *Nature*, 308, 721-722.

Meakin, P. (1988). Fractal aggregates. *Advances in Colloid and Interf. Sci.*, 28, 249.

Námer, J., and Ganczarczyk, J. J. (1994). Digested sludge particle aggregates. W*ater Poll. Res. J. Canada,* 29(4), 441-455.

Oles, V. (1992). Shear-induced aggregation and breakup of polystyrene latex particles. *J. Colloid Interf. Sci.*, 154, 351.

Park, J. W., and Ganczarczyk, J. J. (1994). Gravity separation of biomass washed-out from an aerated submerged filter. *Environ. Technol.*, 15(10), 945-955.

Robinson, D. J., and Earnshaw, J. C. (1992). Experimental study of colloidal aggregation in two dimensions. I. structural aspects. *Physical Review. A*, 46, 2045.

Rogak, S. N., and Flagan, R. C. (1992). Coagulation of aerosol agglomerates in the transition regime. *J. Colloid Interf. Sci.*, 151, 203.

Selomulya, C., Amal, R., Bushell, G., and Waite, T. D. (2001). Evidence of shear rate dependence on restructuring and breakup of latex aggregates. *J. Colloid Interf. Sci.*, 236, 67–77.

Spicer, P. T., Keller, W., and Pratsinis, S. E. (1996). The effect of impeller type on floc size and structure during shear-induced flocculation. *J. Colloid Interf. Sci.*, 184, 112.

Tambo, N., and Watanabe, Y. (1979). Physical characteristics of flocs: I. the floc density function and aluminum floc. *Wat. Res.*, 13, 409.

Wiesener, M. R. (1992). Kinetics of aggregate formation in rapid mix. *Wat. Res.*, 26, 379–387.

Zahid, W. M., and Ganczarczyk, J. J. (1990). Suspended solids in biological filter effluents. *Wat. Res.*, 24, 215-220.

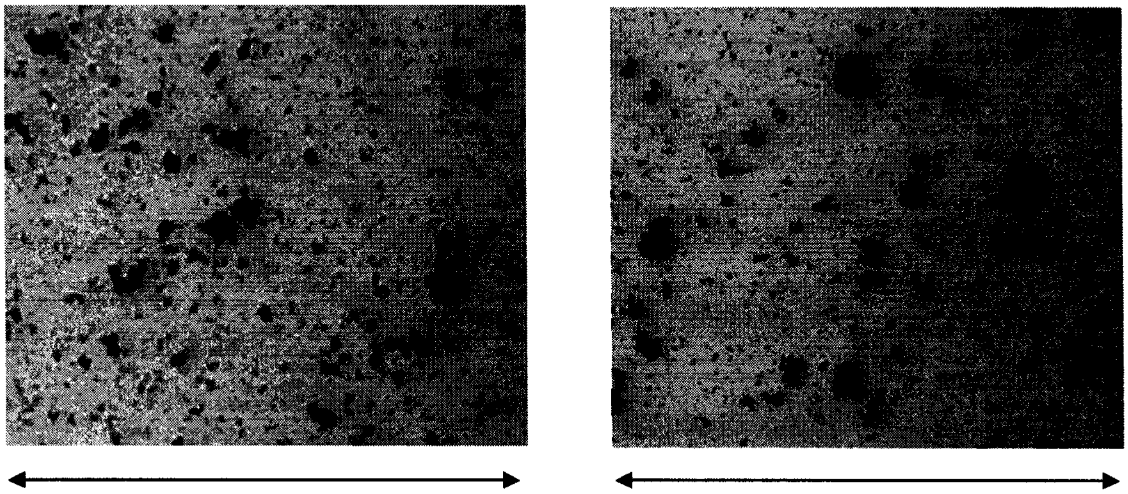

2000 μm
Time = 8 min

6000 μm
Time = 20 min

Figure 6.1. Two photographs of asphaltene aggregates are taken during an experimental run at a shear rate of 1.2 s^{-1}. Though the length scale is different, no distinct difference in shape and structure can be noticed. This implies that the asphaltene aggregates are fractals.

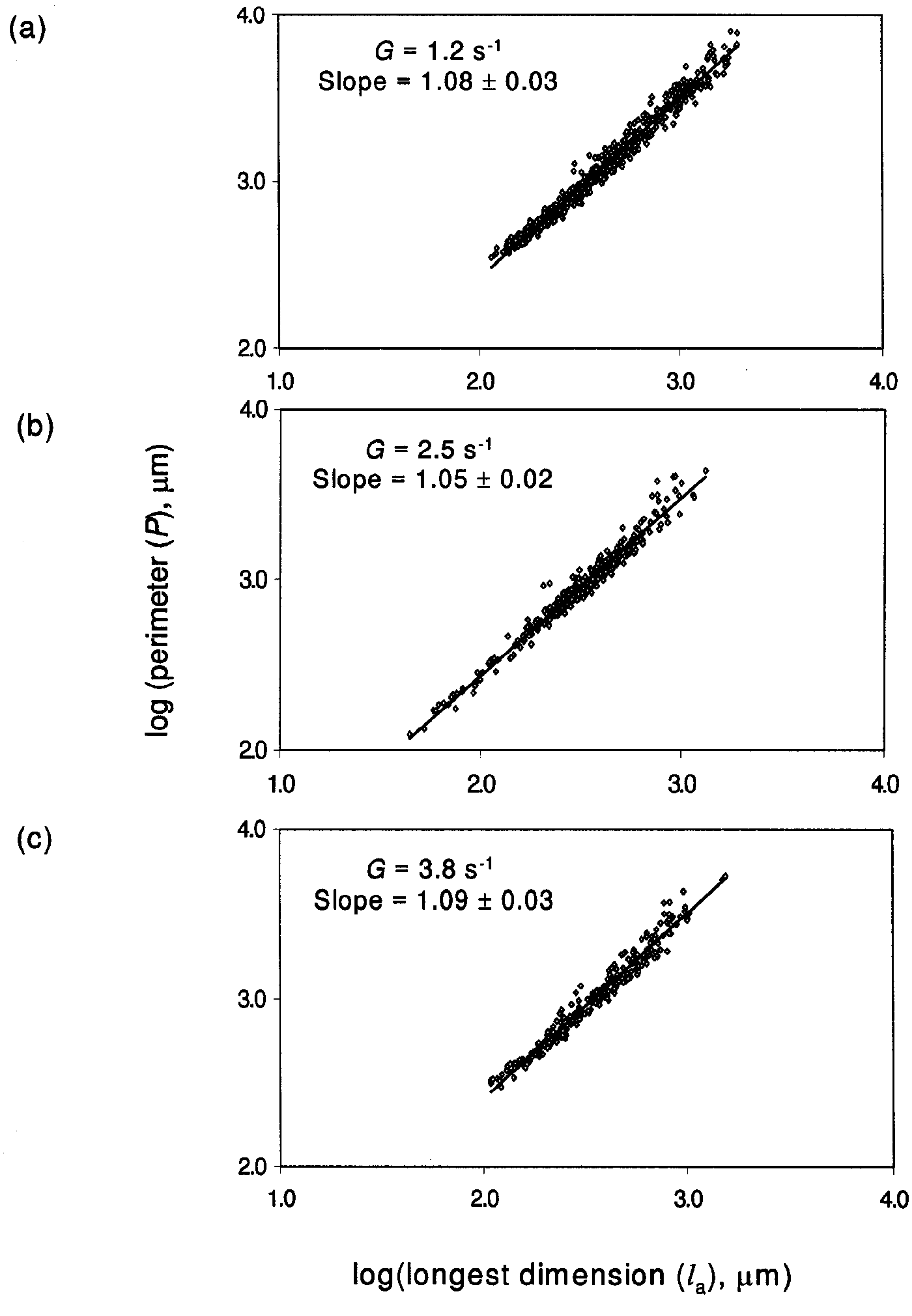

Figure 6.2. Determination of one-dimensional fractal dimension (D_1) for asphaltene aggregates at different shear rates, based on equation 6.1 ($P \alpha l^{D_1}$), from image analysis measurements of aggregate perimeter and longest dimension. The aggregates are formed in Couette device at toluene-to-heptane ratio (T:H) of 1:15 and particle concentration of 12.8 mg/L.
(In Figure 6.2(a), G = 1.2 s^{-1}; in 6.2(b), G = 2.5 s^{-1}; and in 6.2(c), G = 3.8 s^{-1})

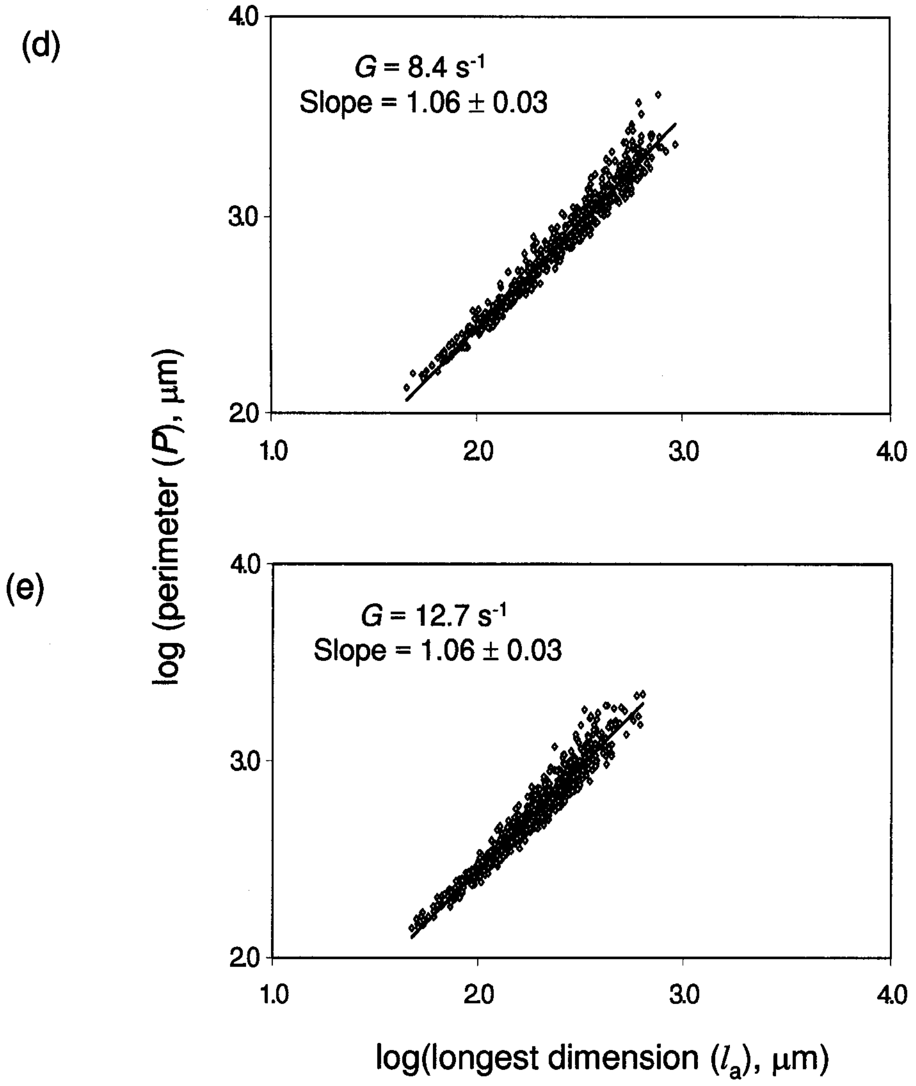

Figure 6.2. Determination of one-dimensional fractal dimension (D_l) for asphaltene aggregates at different shear rates, based on equation 6.1 ($P \,\alpha\, l^{D_l}$), from image analysis measurements of aggregate perimeter and longest dimension. The aggregates are formed in Couette device at toluene-to-heptane ratio (T:H) of 1:15 and particle concentration of 12.8 mg/L.
(In Figure 6.2(d), $G = 8.4$ s^{-1}; in 6.2(e), $G = 12.7$ s^{-1})

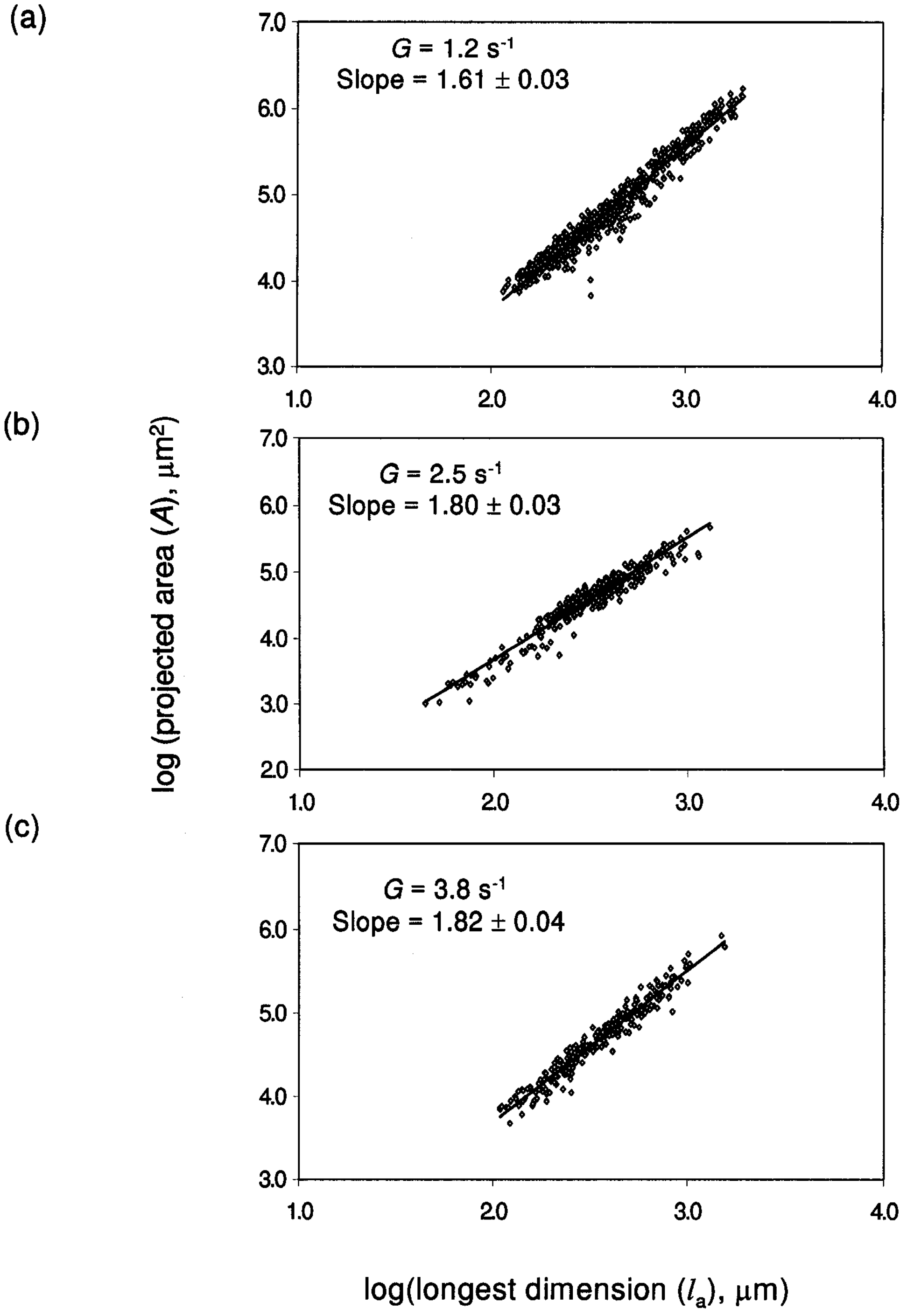

Figure 6.3. Determination of two-dimensional fractal dimension (D_2) for asphaltene aggregates at different shear rates, based on equation 6.2 ($A \alpha l^{D_2}$), from image analysis measurements of aggregate projected area and longest dimension. The aggregates are formed in Couette device at toluene-to-heptane ratio (T:H) of 1:15 and particle concentration of 12.8 mg/L.
(In Figure 6.3(a), $G = 1.2$ s^{-1}; in 6.2(b), $G = 2.5$ s^{-1}; and in 6.2(c), $G = 3.8$ s^{-1})

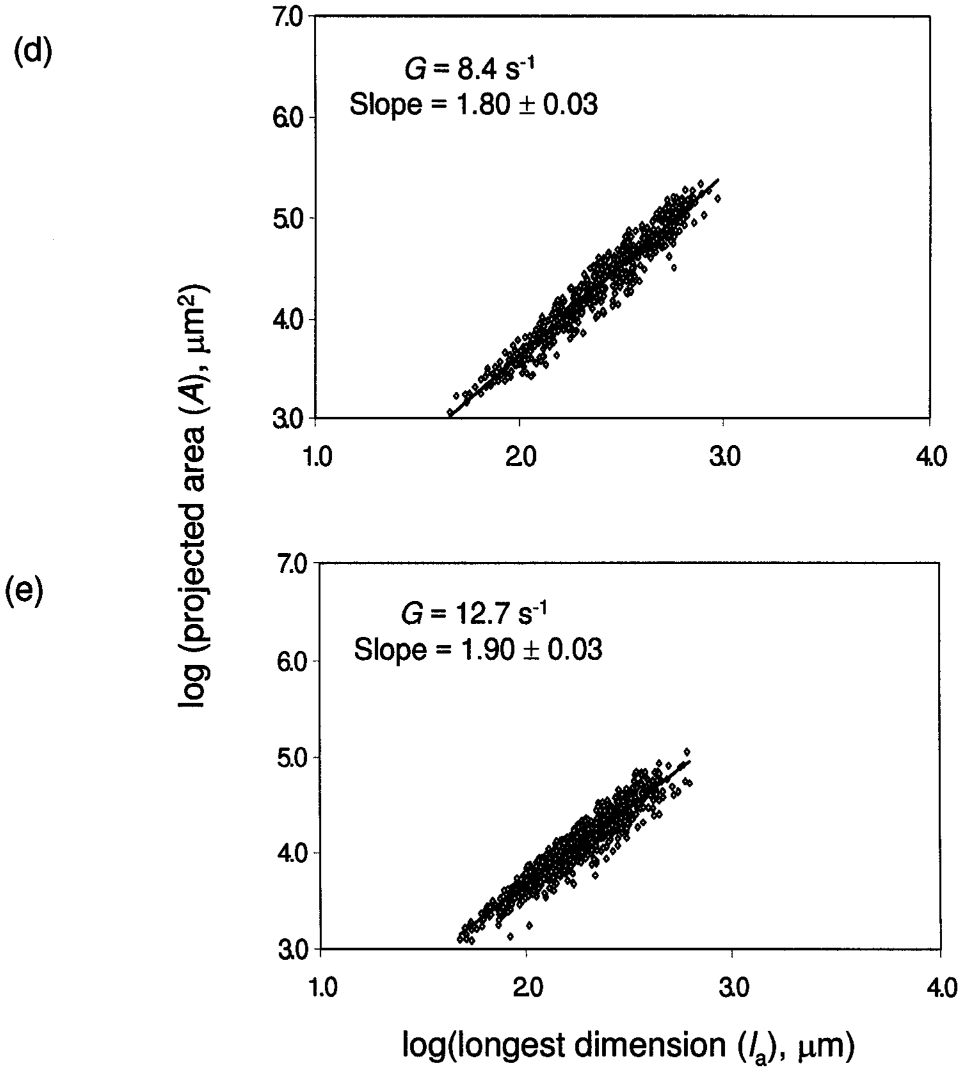

Figure 6.3. Determination of two-dimensional fractal dimension (D_2) for asphaltene aggregates at different shear rates, based on equation 6.2 ($A\, \alpha\, l^{D_2}$), from image analysis measurements of aggregate projected area and longest dimension. The aggregates are formed in Couette device at toluene-to-heptane ratio (T:H) of 1:15 and particle concentration of 12.8 mg/L.
(In Figure 6.3(d), $G = 8.4$ s^{-1}; in 6.2(e), $G = 12.7$ s^{-1})

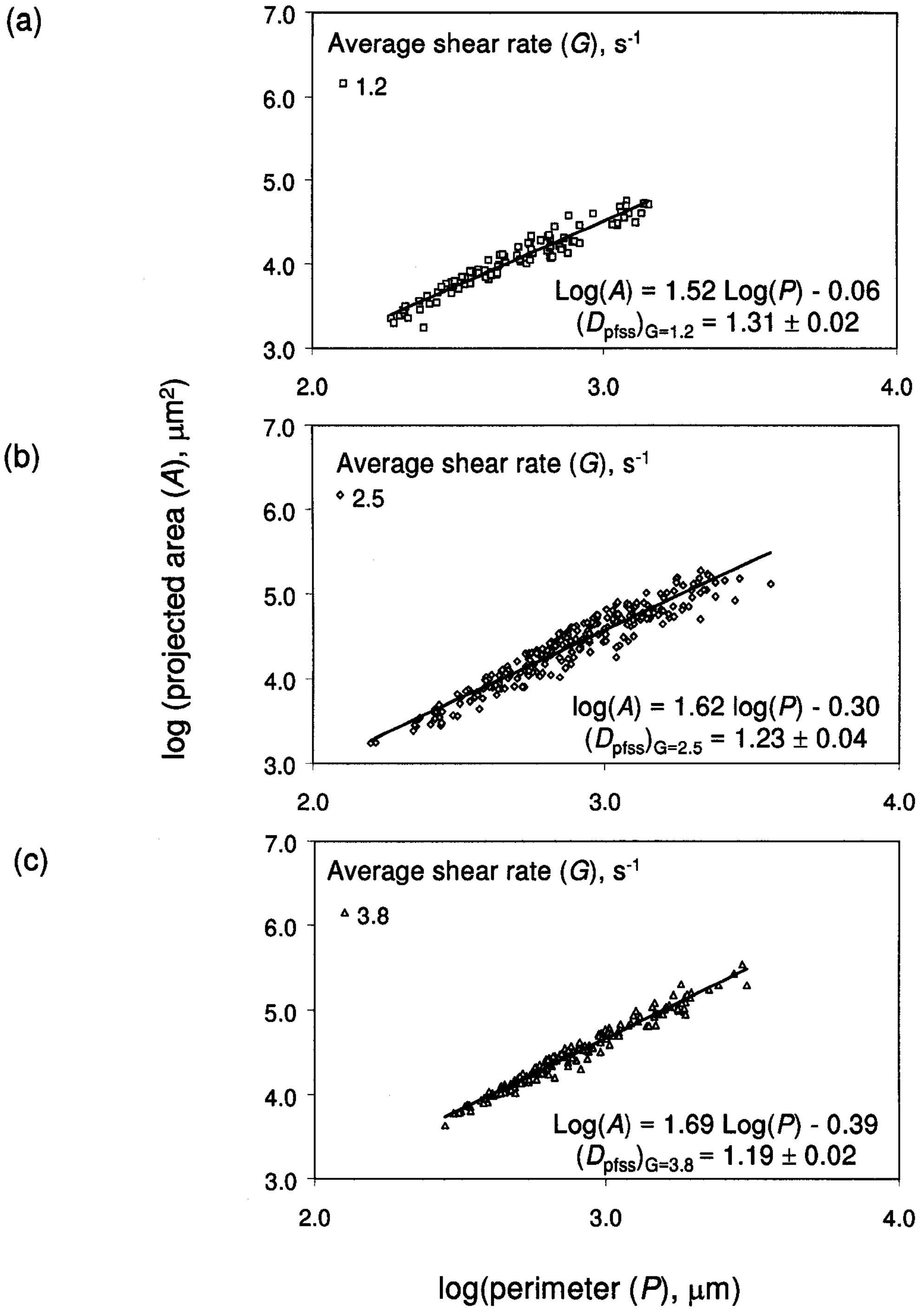

Figure 6.4. Determination of perimeter-based fractal dimension for asphaltene aggregates at steady state (D_{pfss}), based on equation 6.8 ($A\alpha P^{2/D_{pf}}$), from image analysis measurements of aggregate projected area and perimeter. The aggregates are formed in Couette device at toluene-to-heptane ratio (T:H) of 1:15 and particle concentration of 12.8 mg/L.

(In Figure 6.4(a), G = 1.2 s^{-1}; in 6.2(b), G = 2.5 s^{-1}; and in 6.2(c), G = 3.8 s^{-1})

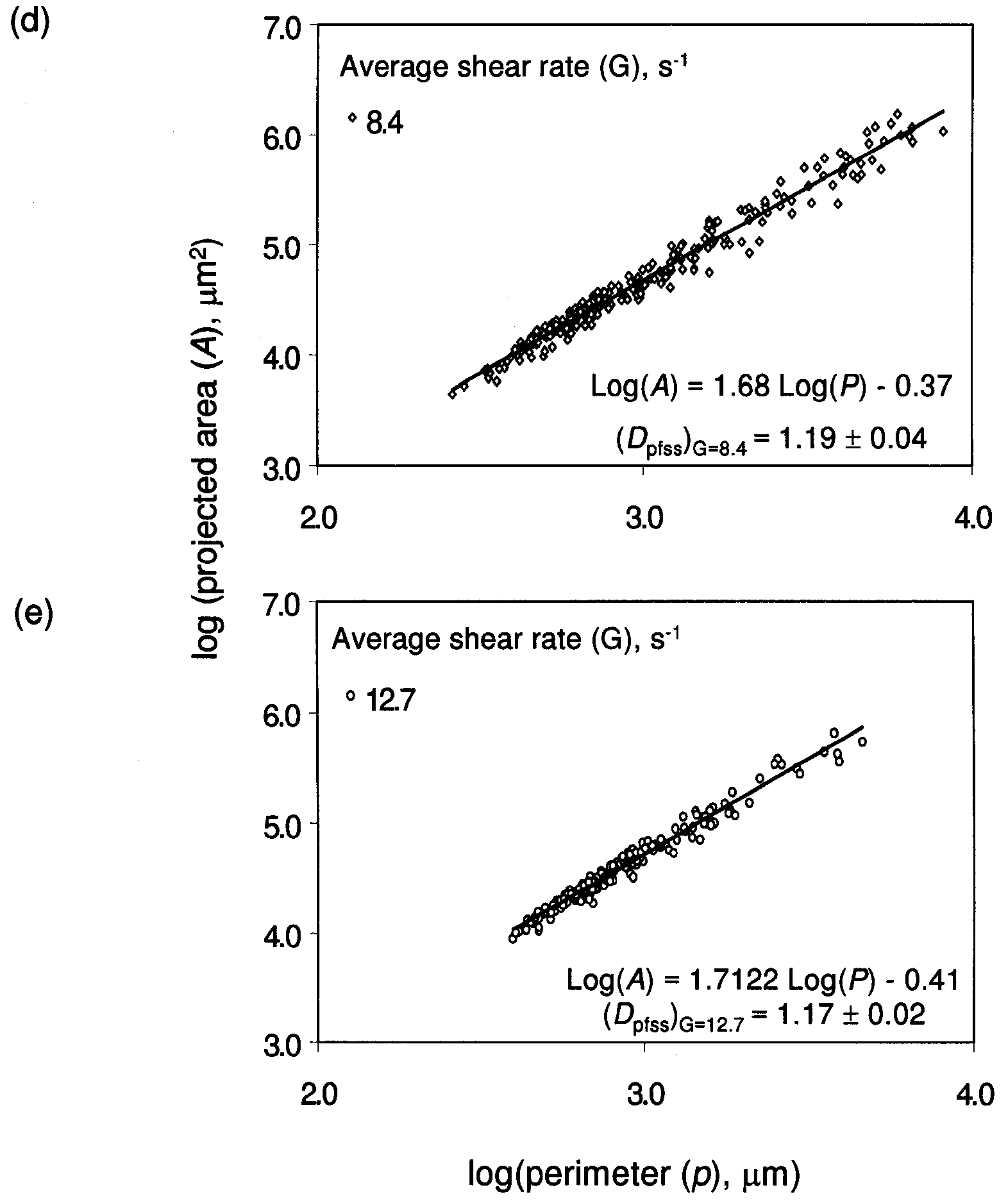

Figure 6.4. Determination of perimeter-based fractal dimension for asphaltene aggregates at steady state (D_{pfss}), based on equation 6.8 ($A\alpha P^{2/D_{pt}}$), from image analysis measurements of aggregate projected area and perimeter. The aggregates are formed in Couette device at toluene-to-heptane ratio (T:H) of 1:15 and particle concentration of 12.8 mg/L.
(In Figure 6.3(d), $G = 8.4\ s^{-1}$; in 6.2(e), $G = 12.7\ s^{-1}$)

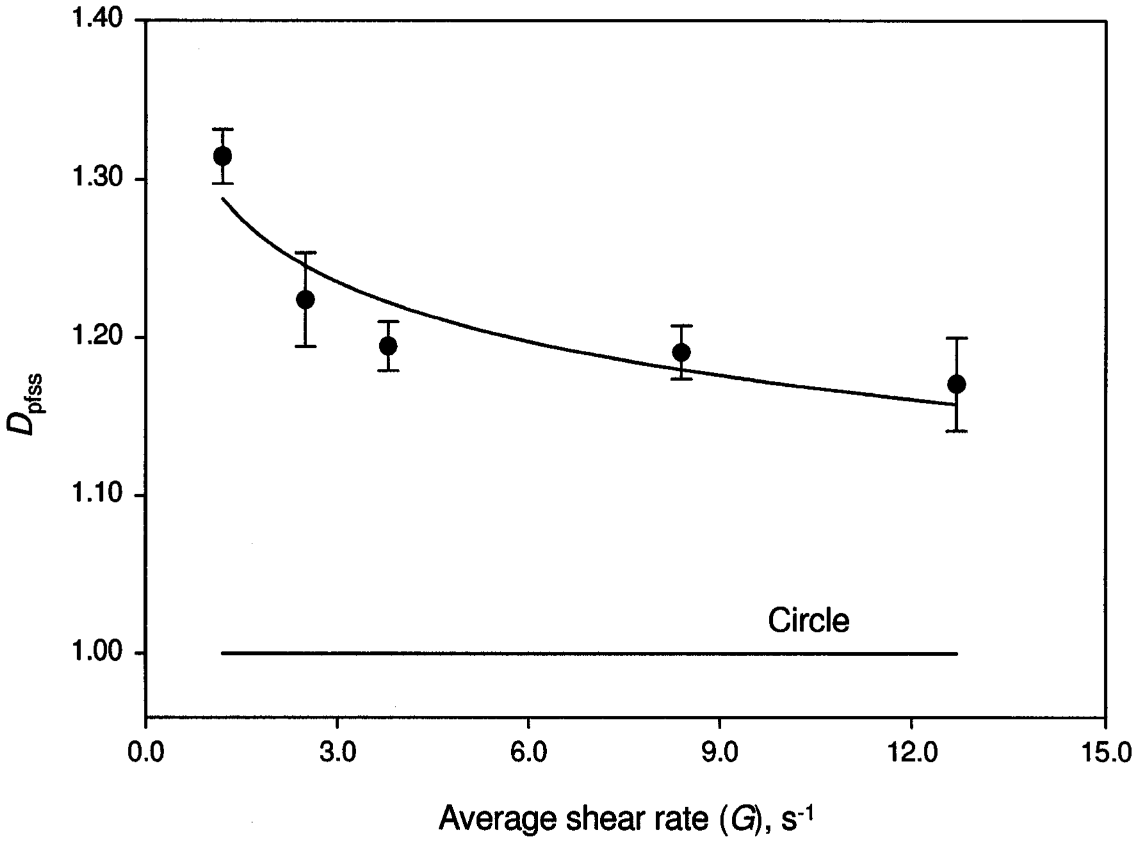

Figure 6.5. Evolution of steady-state perimeter-based fractal dimension (D_{pfss}) for asphaltene aggregates formed in Couette device as a function of shear rate at toluene-to-heptane solvent ratio of 1:15 and particle concentration of 12.8 mg/L. Reducing shear produces more open and irregular aggregate structures at constant particle concentration.

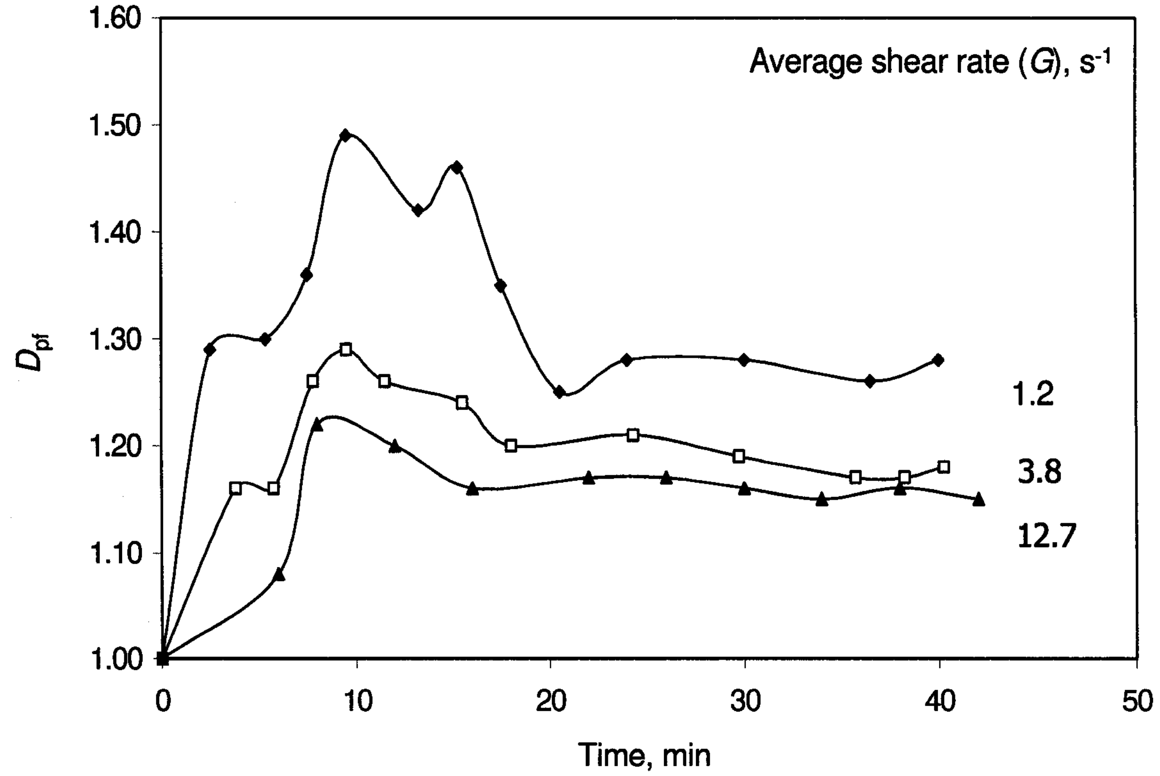

Figure 6.6. Dynamic evolution of the perimeter-based fractal dimension (D_{pf}) for asphaltene aggregates formed in Couette device as a function of shear rate at toluene-to-heptane solvent ratio of 1:15 and asphaltene particle concentration of 12.8 mg/L. After sufficiently long times, D_{pf} approaches an asymptotic, steady state value.

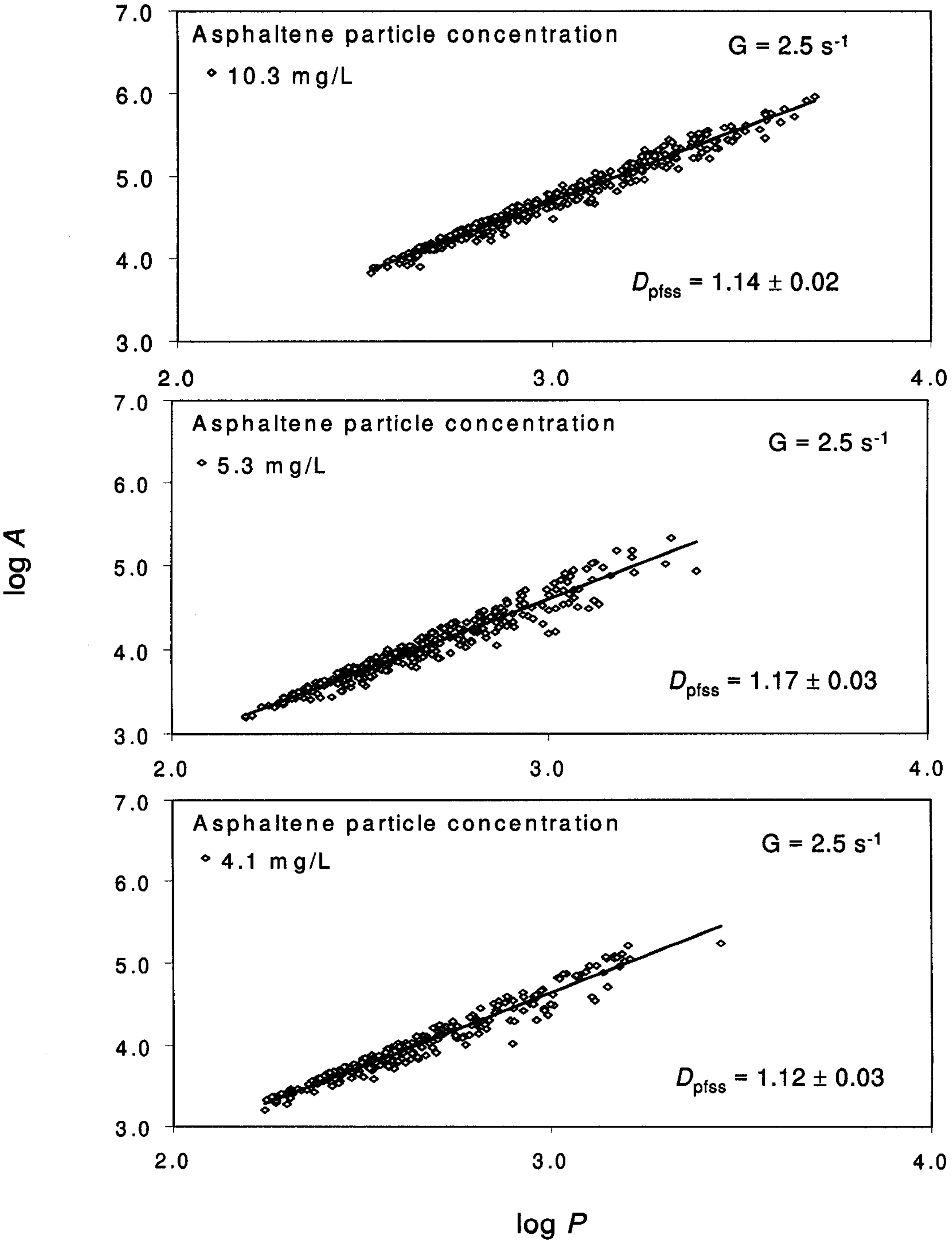

Figure 6.7. Determination of perimeter-based fractal dimension at steady state (D_{pfss}) for different asphaltene particle concentrations at a shear rate of 2.5 s^{-1} and toluene-to-heptane ratio of 1:5 in the solvent mixture from the log-log plot of aggregate projected area vs perimeter. The aggregates are formed in a Couette device.

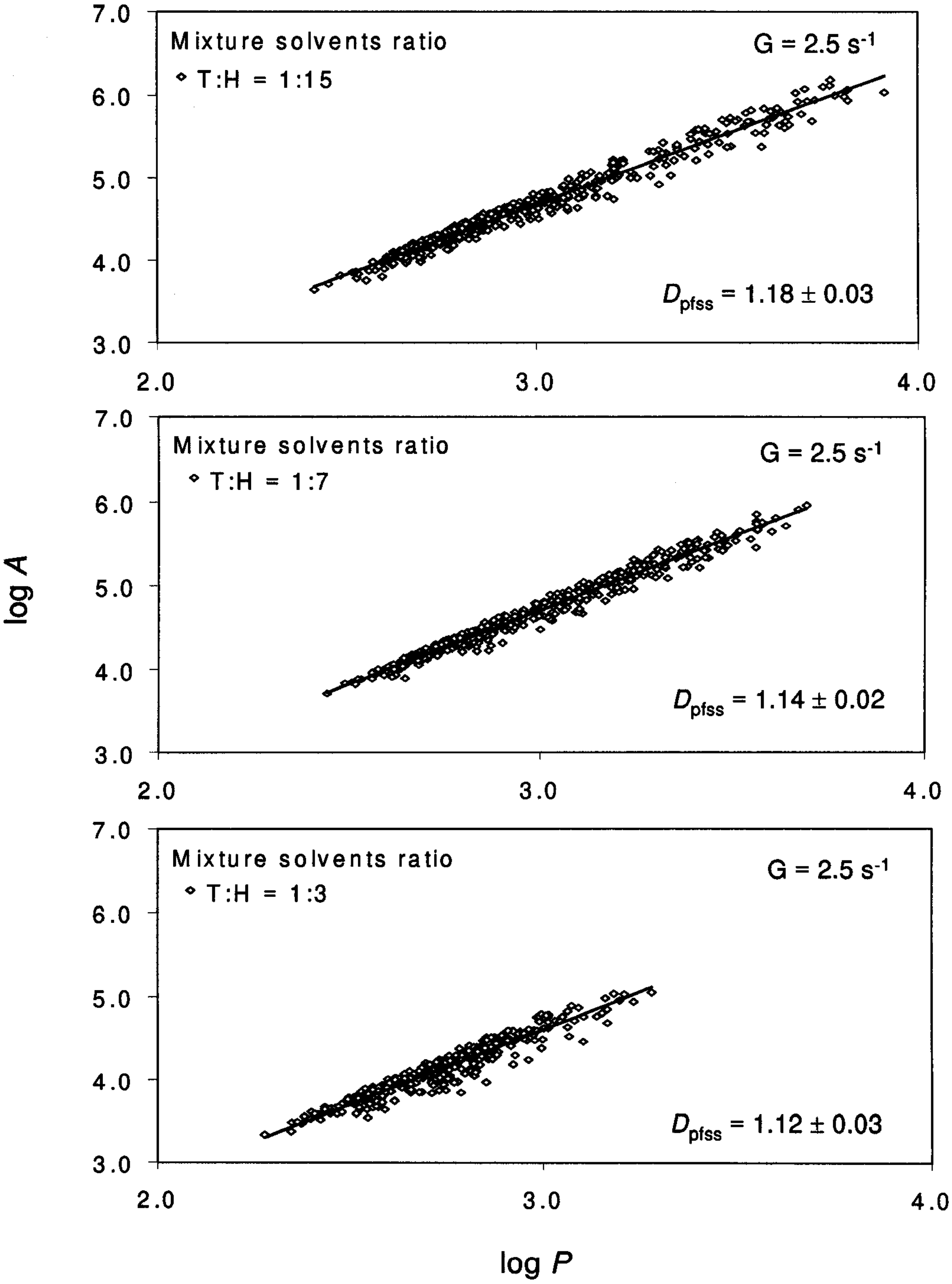

Figure 6.8. Determination of perimeter-based fractal dimension at steady state (D_{pfss}) for different ratios of toluene-to-heptane in solvent mixtures (T:H) at a shear rate of 2.5 s^{-1} from the log-log plot of aggregate projected area vs perimeter. The aggregates are formed in a Couette device.

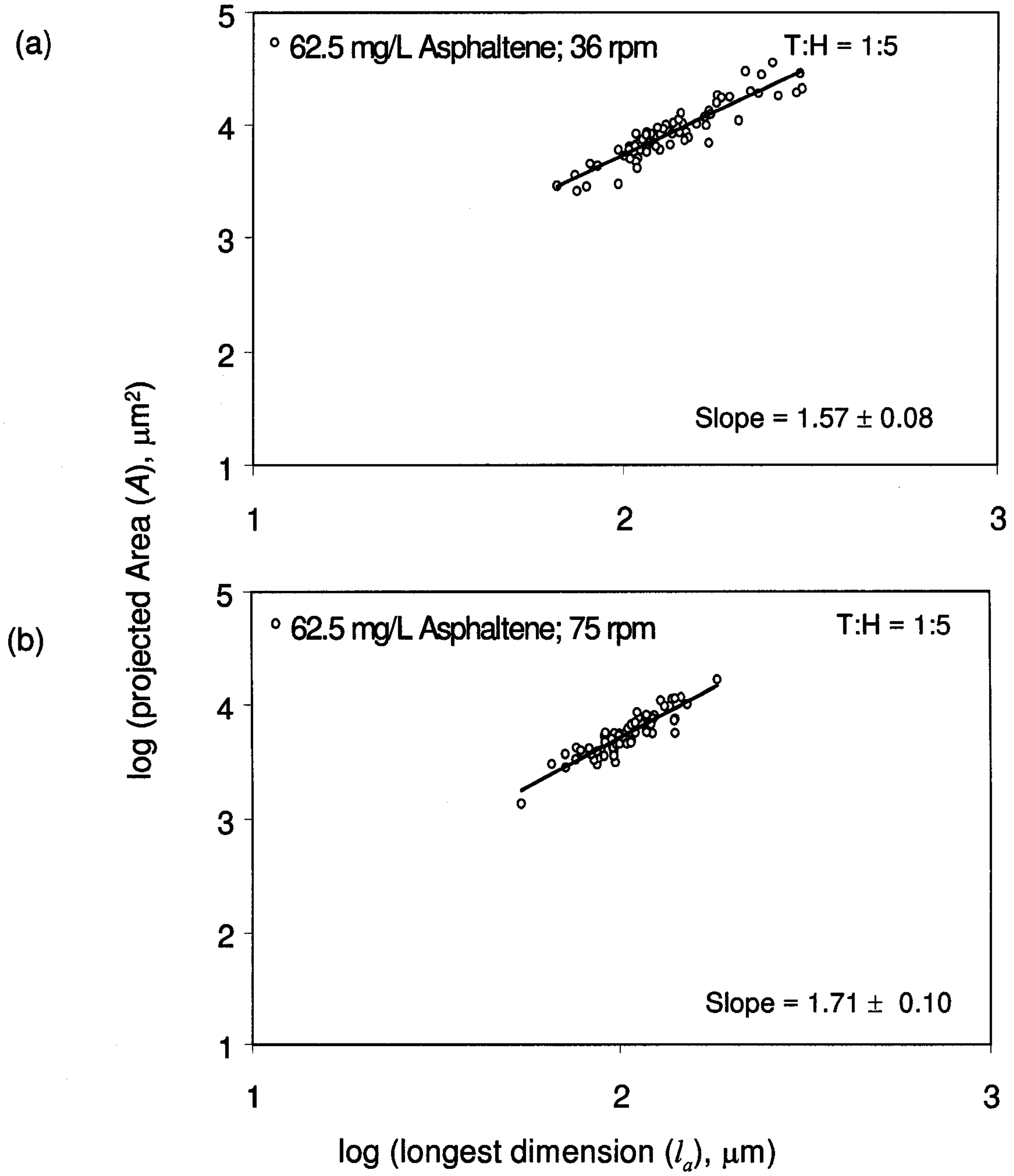

Figure 6.9. Determination of two-dimensional fractal dimension (D_2), based on equation 6.2 ($A \alpha l^{D_2}$), from image analysis measurements of aggregate projected area and longest dimension in settling experiments. The tests were conducted to evaluate the settling velocity of asphaltene aggregates that were formed in a stirred tank with pure asphaltenes at a toluene-to-heptane ratio (T:H) of 1:5 in solvent mixtures and particle concentration of 62.5 mg/L.
(In Fig. 6.9(a), stirring rate = 36 rpm; and in 6.9(b), stirring rate = 75 rpm)

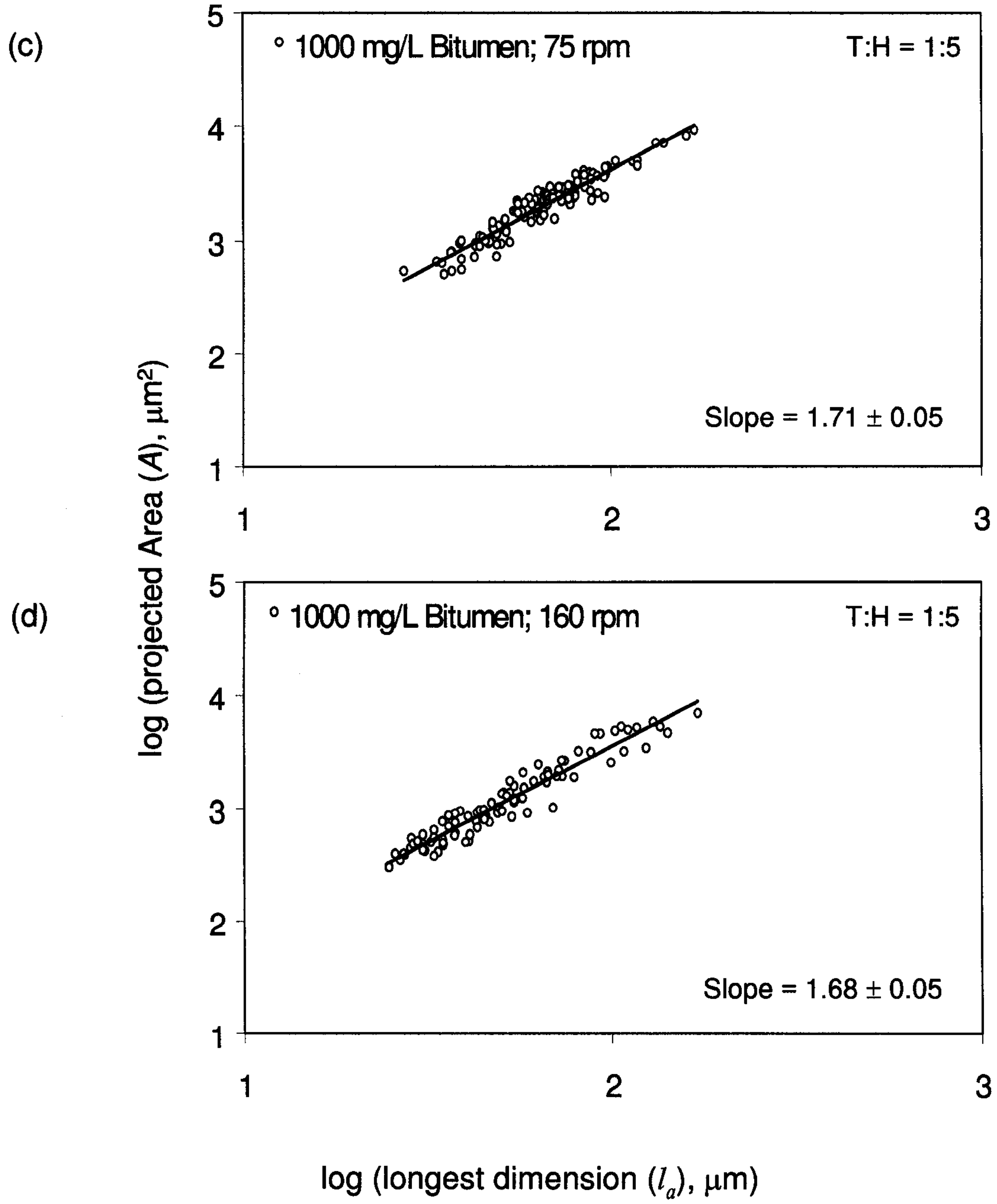

Figure 6.9. Determination of two-dimensional fractal dimension (D_2), based on equation 6.2 ($A \alpha l^{D_2}$), from image analysis measurements of aggregate projected area and longest dimension in settling experiments. The tests were conducted to evaluate the settling velocity of asphaltene aggregates that were formed in a stirred tank with bitumen at a toluene-to-heptane ratio (T:H) of 1:5 and bitumen concentration of 1000 mg/L. (In Fig. 6.9(c), stirring rate = 75 rpm; and in 6.9(d), stirring rate = 160 rpm)

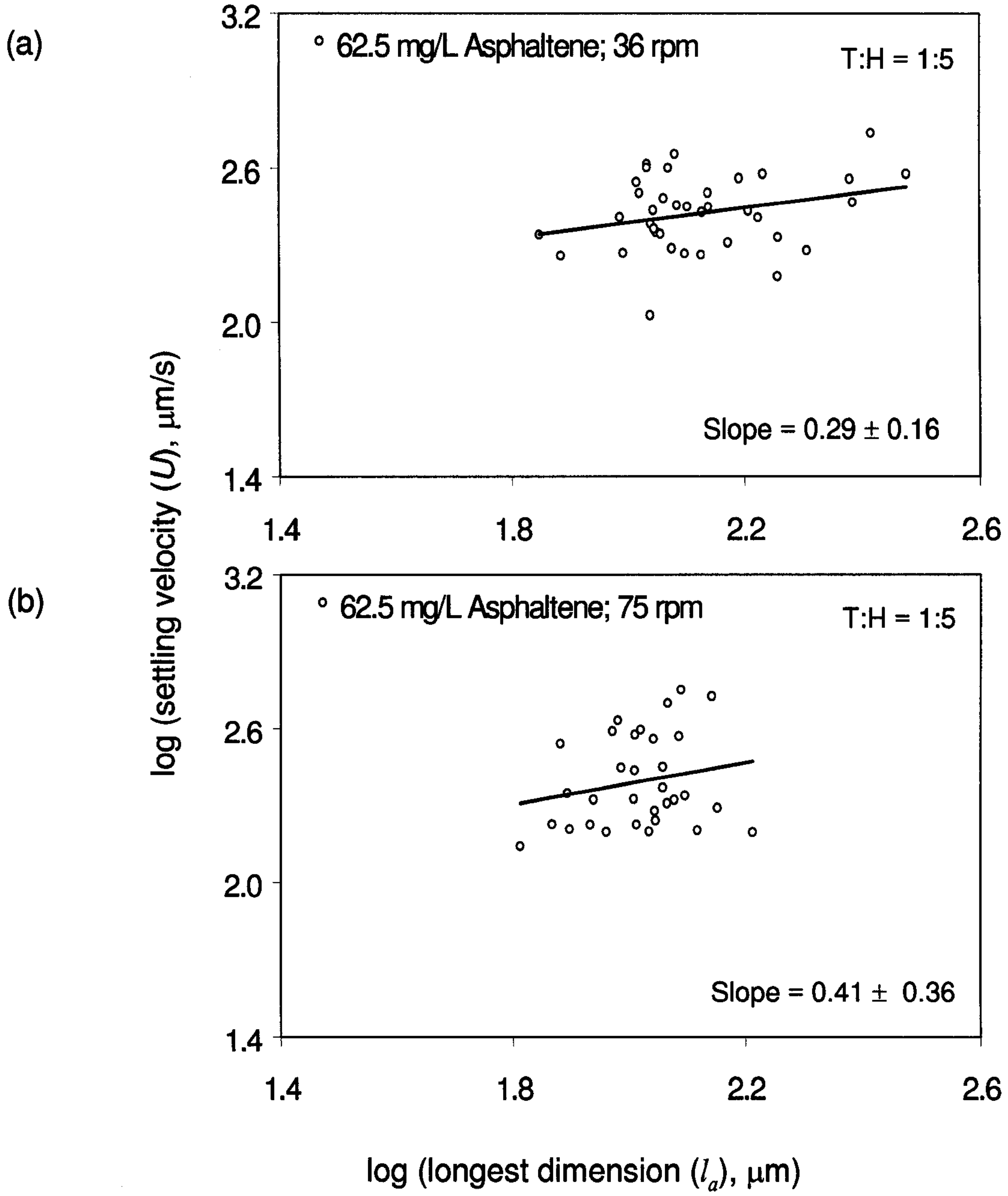

Figure 6.10. Determination of three-dimensional fractal dimension (D_3), based on equation 6.7 ($U \, \alpha \, l^{D_3-1}$), from the slopes of the log-log plot of aggregate settling velocity and longest dimension. The aggregates were formed in a stirred tank with pure asphaltenes at a toluene-to-heptane ratio (T:H) of 1:5 in solvent mixtures and asphaltene particles concentration of 62.5 mg/L.

(In Fig. 6.10(a), stirring rate = 75 rpm; and in 5.7(b), stirring rate = 160 rpm)

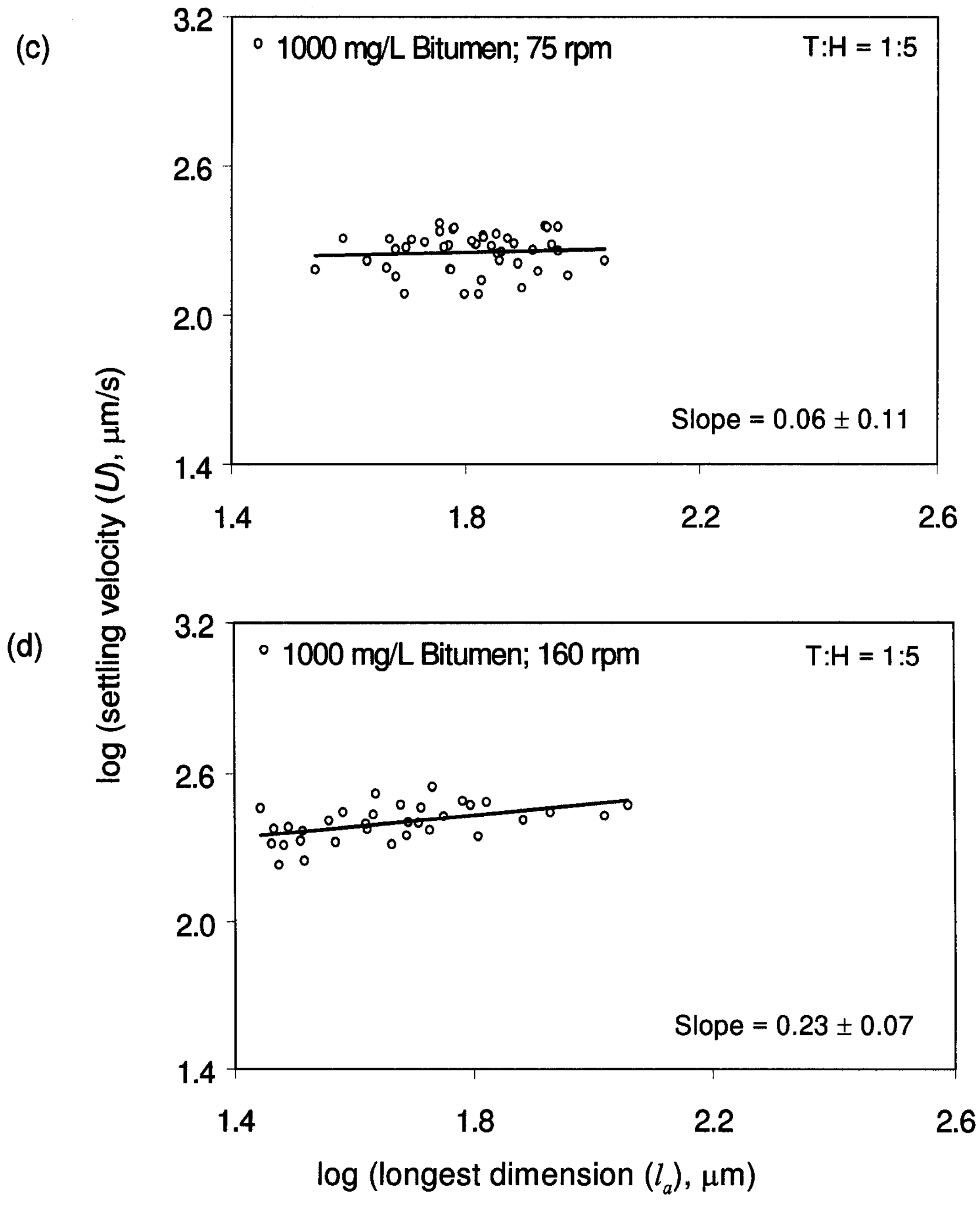

Figure 6.10. Determination of three-dimensional fractal dimension (D_3), based on equation 6.7 ($U \alpha l^{D_3-1}$), from the slopes of the log-log plot of aggregate settling velocity and longest dimension. The aggregates were formed in a stirred tank with bitumen at a toluene-to-heptane ratio (T:H) of 1:5 and bitumen concentration of 1000 mg/L.
(In Fig. 6.10(c), stirring rate = 75 rpm; and in 6.10(d), stirring rate = 160 rpm)

Chapter 7

Conclusions and Recommendations

7.1 Conclusions

The research discussed in this thesis explores different aspects of the aggregation kinetics and the physical behavior of the aggregates. The major contribution of this work is the achievement of a better understanding of asphaltene aggregates based on provided experimental data and theoretical analysis that are new to the field of bitumen froth treatment in the oil sands industry.

The first three chapters of the thesis dealt with the aggregation of extracted asphaltenes in toluene-heptane solvent mixtures as a model system in a Couette geometry. It was shown how the variation in the applied shear rate lead to changes in the system behavior, such as steady-state average aggregate size and the characteristic relaxation time required to achieve the steady state. An increasing shear rate decreased the steady-state size of the aggregates. This is due to the break-up of the aggregates as fluid shear exerts a higher hydrodynamic force on them. Secondly, higher shear corresponded to faster aggregation rates. As the asphaltene particle concentration or the ratio of *n*-heptane to toluene in the solution increased, it exhibited a higher amount of asphaltenes precipitation, faster aggregation rate, and larger maximum and steady-state aggregate size.

The model, based on the population balance, describes and explains the experimental observations quite well. The observations and the model reported are interesting from engineering viewpoint, as they bridge the gap between the fundamentals of the colloid science and the behavior of complex petroleum system.

Inevitably, asphaltenes aggregation in organic solvents is a complex process and it is very difficult to exactly determine the model parameters for such a system. For example, the stability of asphaltenes suspension has a delicate dependency on solvent composition (i.e. toluene to heptane ratio in solvent mixture) or asphaltenes concentration. The aggregates are extremely fragile to handle and it is difficult to find the exact amount of the precipitated asphaltenes. "Primary" particles size were measured and their number concentration were counted from the images captured in the small observation region assuming homogeneous suspension throughout the Couette device. So, an experimental error is involved in determining the initial number concentration and size of "primary" particles from the two-dimensional captured images. This work reviews fundamental research conducted in shear-induced simultaneous aggregation and fragmentation for possible application in recently adopted commercial system of asphaltenes flocculation. Despite these issues it has been demonstrated that population balance equation (PBE) approach provides a useful tool, which is able to render the main features of the system behavior such as growth kinetics, the maximum in the average aggregate size, the final steady state aggregate size, and the dependence of aggregate growth on shear rate, solvent composition, and particle concentration.

On-line monitoring by the photometric dispersion analyzer (PDA) provides instantaneous information on aggregate growth, breakage and reformation mechanisms. Using a bench scale stirred tank, it was found that an increasing stirring speed decreased the steady-state size of the aggregates, which is similar to the observation made in a

Couette flocculator. For a fixed stirring speed, increasing volume fraction of particles as well as increasing ratio of heptane in the solvents mixture greatly enhanced the aggregation rate and increased the steady-state floc size. However, the characteristic relaxation time was found to be small and almost the same within the applied range of shear rates. Whether the aggregation takes place with extracted asphaltenes or with bitumen, it can be inferred from the aggregation kinetics that above a critical concentration of asphaltenes in the toluene-heptane solvent mixtures, the aggregates fragmented after the attainment of maximum size. The breakage is more pronounced when the aggregates are produced from extracted asphaltenes. Restructuring of the flocs could also explain the presence of the maximum size, however, the present population balance equation model did not include terms describing restructuring, and was able to predict the time evolution of the average floc size very well.

A change in the applied stirring speed drives the suspension from one steady state to a new steady state. Once the flocs attained the first steady state, they were fragmented using high stirring speed. After that when the original stirring speed was re-applied, experimentally "*not fully reversible*" behavior was observed. The aggregates did not grow to their previous size as obtained at the original stirring speed. The irreversibility of aggregates during cyclic shear is most likely the result of particle-aggregate bond breakage during fragmentation. Once broken, the resulting fragments attain reduced "stickiness" (which might be due to loss of active sites or change of surface structures) and are not able to form again to their previous extent, thus reducing the efficiency of subsequent aggregate-aggregate collisions. On the other hand, tapered-shear flocculation perfectly exploits floc irreversibility because it tends to form flocs from compact microflocs as opposed to open structures resulting from conventional constant shear flocculation. Hence, the final steady-state floc size obtained at 75 rpm by tapered-shear flocculation (≅ 50 μm) is almost three times smaller than the steady-state size obtained at 75 rpm by constant-shear flocculation (≅ 95 μm). It can be concluded that cyclic- and tapered- shear produces smaller, but more compact aggregates. Also, shear-history plays an important role on achieving the final, steady state aggregate size. In summary, it can be concluded that asphaltenes aggregate growth kinetics and the final aggregate size depend strongly on applied shear, particle concentration, solvent composition and shear history.

Experimental data on the relationship between terminal settling velocities of asphaltene aggregates and their projected area diameters demonstrated that asphaltene aggregates are highly porous, higher shear produces denser and more compact aggregates, and the porosity of the aggregates increases with an increase in their size. The aggregates porosity was found independent of the solid particle concentrations used for their formation.

It was demonstrated that asphaltene aggregates are fractals. In principle, above certain length scale, they do not have any characteristic length scale. Several morphological properties of the aggregates are characterized by fractal dimension. The higher 2-D fractal dimensions observed in Couette apparatus with increasing shear indicate that the aggregates became less amorphous and more compact at higher shears. The dynamic evolution of the perimeter-based fractal dimension (D_{pf}) shows the presence of shear-induced breakage/restructuring during asphaltenes aggregate growth. The 3-D fractal dimension indicates tenuous aggregate structure with extremely low space-filling capacity, which can be inferred from the lower fractal dimension values ($D<2$).

7.2 Recommendations for Further studies

This thesis has applied a number of experimental techniques and various theories to study the physical behavior of asphaltene aggregates. While this contributes to the understanding of asphaltenes flocculation process, it also generates other questions as well as opportunities for further investigation.

As the 3-D fractal dimensions of asphaltene aggregates generated in Couette geometry could not be determined by image analysis, the population balance model was developed on the basis of a constant aggregate porosity. This would lead to a misleading estimate of collision frequency (β_{ij}), particularly for very large aggregates. The collision efficiency (α) for orthokinetic collisions cannot be adequately accounted for without considering hydrodynamic interactions. The reasonable fit of experimental data to model predictions with such simplified assumptions is not rather fortuitous, but happened due to overestimation of α value by neglecting the viscous retardation effect and underestimation of β_{ij} value by not taking into account the fractal nature of the actual flocs. Consequently, the product of α and β_{ij} takes care of the inherent inadequacy of the simplified present model.

In subsequent research studies, the influence of these important operating parameters of the model should be investigated, such as α value can be more realistically determined and fractal theory of collision frequency (β_{ij}) should be incorporated. Instead of binary breakage, other modes of splitting, such as normal distribution of the fragments, or fragmentation due to erosion can be examined. It should be noted that simultaneous solution of fluid dynamical equations and population balance equation allows the description of flocculation processes with higher solid concentrations or in a turbulent flow field for complex systems.

Finally these investigations will result in a tool for the geometrical and fluid dynamical design of the mixing apparatus in the solid-liquid separation process and in the optimization of the flocculation process. The population balance model can be applied to many unit operations, such as, settling vessels, filters and centrifuges with the influence of pressure, inertial and shear forces on the existing flocs. Further on, the mechanisms of flocculation process, which occur when adding chemical additives or polymeric de-emulsifiers to asphaltenes suspension, are of immense practical interest.

The newly commercialized technology for bitumen froth treatment relies on asphaltenes precipitation in terms of forming clusters of precipitated asphaltenes, water droplets and fine solids, thereby, enabling their removal by gravity settling. Since the stable water-in-oil emulsion is a major problem in the oil sands industry, it will be auspicious if the emulsified water droplets can be trapped in the asphaltene precipitate clusters. Hence the effect of water droplets in asphaltenes flocculation process should be examined.

In this study, many simplified assumptions were made in determining the flocs permeability. Further studies are needed for better assumptions, which should be supported by data from direct experimental measurements. This would provide more accurate estimates of the floc permeability under shear flow.

Appendix A

Population Balance Equation: Numerical Code

In chapter 2, numerical procedure is required to simultaneously solve equations 2.13, 2.18, 2.20 – 2.22, 2.24. The kinetics of asphaltene aggregate growth is described by equation 2.14, which is the discretized form of the population balance equation (PBE). The numerical code is written in Matlab (version 5.2) and invokes a shooting method, Runga-Kutta integration for stiff differential equations. Since the PBE is an initial value problem, the initial concentration of "primary" asphaltene particles (N_o) is required. For different experimental conditions, the N_o values are determined from the image analysis of the data and are described below in Tables A, B, and C.

Table A.1. Determination of initial number concentration of asphaltene particles ("primary" particles) for population balance equation model at different shear rates (G = 1.2–12.7 s^{-1}). Image analysis of captured photograph was done for asphaltene particles formed at a toluene-to-heptane ratio (T:H) of 1:15 in solvent mixtures and initial asphaltenes concentration of 62.5 mg/L.

Average shear rate, G (s^{-1})	Lower and upper boundary of bin size, c_i (μm)	Average bin size, d_i (μm)	Average bin volume, V_i (μm^3)	# of particles in the captured image (#)	Total volume of the particles in the image, $V_{particle}$ (μm^3)	Image volume = image area × depth of field (depends on the microscope objective) V_{image} (cm^3)	Particles volume per cm^3 of sample suspension, V_o (= $V_{particle}$ / V_{image}) ($\mu m^3/cm^3$)	Initial number of particle in suspension, $N_{i,o}$ (= V_o / V_i) (# / cm^3)
1.2–12.7	28-39	34	22988	14	328958	0.000477	689639413	30000
	39-51	46	57470	9	493437	0.000477	1034459119	18000
	51-66	60	126430	2	271382	0.000477	568935010.5	4500

Table A.2. Determination of initial number concentration of asphaltene particles (“primary” particles) for population balance equation model for various asphaltenes concentration. Image analysis of captured photograph was done for asphaltene particles formed at G=2.5 s^{-1} and T:H=1:7.

Asphaltene Particles concentration in toluene-heptane mixture (mg/L)	Lower and upper boundary of bin size, c_i (µm)	Average bin size, d_i (µm)	Average bin volume, V_i (µm^3)	# of particles in the captured image (#)	Total volume of the particles in the image, $V_{particle}$ (µm^3)	Image volume = image area × depth of field (depends on the microscope objective) V_{image} (cm^3)	Particles volume per cm^3 of sample suspension, V_o (= $V_{particle}$ / V_{image}) (µm^3/cm^3)	Initial number of particles in suspension, $N_{i,o}$ (= V_o / V_i) (# / cm^3)
10.3	28-39	34	22988	3	74481	0.0018	41378333	1800
	39-51	46	57470	9	506885	0.0018	281602778	4900
	51-66	60	126430	12	1570261	0.0018	872367222	6900
	66-84	76	264360	7	1760638	0.0018	978132222	3700
5.3	28-39	34	22988	5	109872	0.000477	230339623	10020
	39-51	46	57470	9	500729	0.000477	1049746331	18266
	51-66	60	126430	1	162166	0.000477	339970650	2689
4.1	28-39	34	22988	20	463557	0.000477	971817610	42275
	39-51	46	57470	2	143234	0.000477	300280922	5225

Table A.3. Determination of initial number concentration of asphaltene particles ("primary" particles) for population balance equation model for various toluene-to-heptane ratio (T:H) in solvent mixtures. Image analysis of captured photograph was done for asphaltene particles formed at G=2.5 s^{-1}.

Toluene-to-heptane ratio in solvent mixtures (T:H)	Lower and upper boundary of bin size, c_i (µm)	Average bin size, d_i (µm)	Average bin volume, V_i (µm^3)	# of particles in the captured image (#)	Total volume of the particles in the image, $V_{particle}$ (µm^3)	Image volume = image area × depth of field (depends on the microscope objective) V_{image} (cm^3)	Particles volume per cm^3 of sample suspension, V_o (= $V_{particle}$ / V_{image}) (µm^3/cm^3)	Initial number of particles in suspension, $N_{i,o}$ (= V_o / V_i) (# / cm^3)
1:15	28-39	34	22988	14	328958	0.000477	689639413	30000
	39-51	46	57470	9	493437	0.000477	1034459119	18000
	51-66	60	126430	2	271382	0.000477	568935010.5	4500
1:7	28-39	34	22988	3	74481	0.0018	41378333	1800
	39-51	46	57470	9	506885	0.0018	281602778	4900
	51-66	60	126430	12	1570261	0.0018	872367222	6900
	66-84	76	264360	7	1760638	0.0018	978132222	3700
1:3	28-39	34	22988	3	62523	0.0018	34735000	1511
	39-51	46	57470	7	426301	0.0018	236833889	4121
	51-66	60	126430	11	1344052	0.0018	746695556	5906
	66-84	76	264360	6	1503680	0.0018	835377778	3160

```
%%%%%%%%%%%%%%%%%%%%%%%%%%%%%%%%%%%%%%%%%%
Main file for predicting growth of asphaltene aggregates under shear (G = 1.2 s^-1)
%%%%%%%%%%%%%%%%%%%%%%%%%%%%%%%%%%%%%%%%%%

clc
clear

global alpha G b_dash y e x z i_max p k h c_1

alpha = 1; % collision efficiency
G = 1.2; % average shear rate, s-1
b_dash = 0.0000192; % proportionality constant of breakage rate coefficient
y = 0.6048; % power law constant of breakage rate coefficient
e = 0.33; % power law constant of breakage
x = 0.0662; % proportionality constant of porosity
z = 0.9417; % power law constant of porosity
i_max = 31; % number of bins
p = (-x)*G+z; % porosity of the aggregate
k=1-p;
h = pi/k;
c_1 = 28;
u(1) = (h/6)*c_1^3;

for i=2:i_max+1
  u(i)= u(1)*(2^i-1);
  c(i)=(u(i)*(6/pi))^0.33;
end

for i=1:i_max
  V(i)=(u(i)+u(i+1))/2;
  d(i)=(V(i)*(6/pi))^0.33;
end
expt_t = [360 420 480 540 600 690 840 960 1080 1140 1200 1260 1350 1410 1500 1605 1785 1920 2085
          2265 2445 2550 2670]';
expt_d = [40 52 76 95 124 185 257 305 341 372 355 359 366 352 332 303 292 268 260 261 234 228 241]';

t0=550; % Starting time for integration
tf=3200; % End time for integration
delta_t=50; % time interval between two consecutive point
tspan=[t0:delta_t:tf];

r = zeros(i_max-3,1);
n0 = [30000; 18000; 4500; r];

options = odeset('abstol',1e-8);
[t,n]= ode15s('pbe_eqn_G', tspan, n0, options);

A = sum(n');
% n=[p,q]; p = no. of rows (=time span), q = no. of columns (=i_max);
% n'=[q,p];
% A=[1,p]
n_tot(:,1)= A';
% n_tot=[p,1]; total number of particles at any particular time
V_tot(:,1) = n*V';
d_tot(:,1) = ((V_tot(:,1)./n_tot(:,1)).*(6/pi)).^0.3334;
```

```
%U = [0,400,0,3600];
%axis(U);
plot(t,d_tot(:,1),'-r',expt_t,expt_d,'*r');
xlabel('Time, s');
ylabel('Number mean aggregate projected area diameter, micron');
Title('Kinetics of asphaltene aggregates growth under shear');
grid on;
```

%%

Function file for integration of non-linear differential equations

%%

```
function n_prime=pbe_eqn_G (t,n)

global alpha G b_dash y e x z i_max p k h c_1

u(1) = (h/6)*c_1^3;

for i=2:i_max+1
  u(i)= u(1)*2^(i-1);
end

for i=1:i_max
  V(i)=(u(i)+u(i+1))/2;
  d(i)=(V(i)*(6/pi))^0.33;
end

for i=1:i_max
  for j=1:i_max
    beta(i,j) = 10^(-12)*(1/6)*G*(d(i)+d(j))^3;
    tau(i,j)= 0;
  end
end

for i=1:i_max
   S(i)= 10^(-4)*b_dash*(G^y)*V(i)^e;
end

for i=1:i_max-1
  for j=i+1:i_max
    tau(i,j)= (V(j)/V(i));
 end
end

n_prime = zeros(i_max,1);

% higher-order, nonlinear differential equations

for i=1:i_max
 for j=i:i_max
  n_prime(i,1)=n_prime(i,1) - alpha*beta(i,j)*n(j)*n(i) + tau(i,j)*S(j)*n(j);
 end
 n_prime(i,1)=n_prime(i,1) - S(i)*n(i) - tau(i,i)*S(i)*n(i);
```

```
end

n_prime(1,1) = n_prime(1,1) + S(1)*n(1);
n_prime(2,1) = n_prime(2,1) + 0.5*alpha*beta(1,1)*n(1)^2 - 0.5*alpha*beta(2,1)*n(1)*n(2);

for i=3:i_max
 for j=1:i-2
  n_prime(i,1) = n_prime(i,1) + 2^(j-i+1)*alpha*beta(i-1,j)*n(i-1)*n(j) - 2^(j-i)*alpha*beta(i,j)*n(i)*n(j);
 end
 n_prime(i,1) = n_prime(i,1) + 0.5*alpha*beta(i-1,i-1)*n(i-1)^2 - 0.5*alpha*beta(i,i-1)*n(i-1)*n(i);
end
```

%%

Experimental data and model predictions at different shear rates

%%

```
G = 2.5; % average shear rate, s^-1
t0=450;
expt_t = [300 330 390 435 495 600 660 750 840 900 960 1020 1110 1170 1275 1395 1515 1635 1740 1830
          1950 2070 2190 2310 2430 2550 2700]';
expt_d = [43 54 78 95 126 168 198 233 261 286 303 309 324 313 318 301 265 250 222 214 196 191 182
          190 171 178 181]';
% Model prediction of aggregate size distribution after reaching steady-state
d_model = fix(d');
%d_model=average diameter of each bin=[i_max,1]
num_frac_t_2200 = (n(36,:)/n_tot(36,1))';
num_frac_t_3000 = (n(52,:)/n_tot(52,1))';

G = 3.8; % average shear rate, s^-1
t0=300;
expt_t = [210 225 285 345 450 480 555 600 660 750 810 870 960 1050 1140 1212 1320 1440 1542 1680
          1785 1965 2145 2295 2415 2550 2685]';
expt_d = [38 49 70 104 156 167 198 212 230 259 286 268 287 278 292 278 287 265 227 213 198 184 168
          154 157 153 156]';

G = 8.4; % average shear rate, s^-1
t0=100;
expt_t = [150 210 255 315 375 450 540 600 690 810 900 1020 1140 1230 1380 1560 1740 1920 2100 2280
          2460]';
expt_d = [39 75 102 121 142 184 215 198 212 193 205 189 178 148 135 129 124 127 125 125 126]';
% Model prediction of FSDs in terms of relative number frequency (N_i/N_total) at a specific time
d_model = fix(d');
%d_model=average diameter of each bin=[i_max,1]
num_frac_t_100 = (n(1,:)/n_tot(1,1))';
num_frac_t_400 = (n(7,:)/n_tot(7,1))';
% Model prediction of aggregate size distribution after reaching steady-state
num_frac_t_1600 = (n(31,:)/n_tot(31,1))';
num_frac_t_3400 = (n(67,:)/n_tot(67,1))';

G = 12.7; % average shear rate, s^-1
t0=100;
expt_t = [90 150 210 270 320 390 450 510 570 615 675 735 795 855 915 975 1050
          1140 1230 1320 1440 1530 1680 1800 1950 2190 2400]';
expt_d = [47 79 108 123 136 124 137 132 140 137 142 143 134 141 128 133 127 122
```

```
            116 106 109 107 101 107 106 102 101]';
% Model prediction of aggregate size distribution after reaching steady-state
d_model = fix(d');
%d_model=average diameter of each bin=[i_max,1]
num_frac_t_1500 = (n(29,:)/n_tot(29,1))';
num_frac_t_3400 = (n(67,:)/n_tot(67,1))';
```

```
%%%%%%%%%%%%%%%%%%%%%%%%%%%%%%%%%%%%%%%%%%%%%%%%
```

Experimental data and model parameters for predicting growth of the aggregates at G=2.5 s^{-1} and T:H=1:7, for various asphaltenes concentration

```
%%%%%%%%%%%%%%%%%%%%%%%%%%%%%%%%%%%%%%%%%%%%%%%%

Asphaltene particle concentration = 10.3 mg/L
p = 0.65;
c_1 = 28; % initial point of the first bin of average diameter, micron
u(1) = (h/6)*c_1^3; % initial point of the first bin of average volume, micron^3
for i=2:i_max+1
  u(i)= u(1)*(2^i-1);
  c(i)=(u(i)*(6/pi))^0.33;
end
t0=350;
expt_t = [150 210 270 360 420 480 540 600 720 840 960 1080 1200 1380 1500 1620 1740 1860 1980
            2100 2220 2340 2460 2580 2700   2820 3000 3180 3360 3540]';
expt_d = [39 56 74 98 119 132 148 181 214 259 267 286 272 263 282 262 229 225 198 201 197 184 196
            176 163 180 160 182 166 172]';
r = zeros(i_max-4,1);
n0 = [1800;4900;6900;3700; r];
% Model prediction of aggregate size distribution after reaching steady-state
d_model = fix(d');
%d_model=average diameter of each bin=[i_max,1]
num_frac_t_3100 = (n(56,:)/n_tot(56,1))';
num_frac_t_4200 = (n(78,:)/n_tot(78,1))';

Asphaltene particle concentration = 5.3 mg/L
p = 0.42;
c_1 = 28; % initial point of the first bin of average diameter, micron
u(1) = (h/6)*c_1^3; % initial point of the first bin of average volume, micron^3
for i=2:i_max+1
  u(i)= u(1)*2^(i-1);
  c(i)=(u(i)*(6/pi))^0.33;
end
t0=450;
expt_t = [540 660 780 900 1020 1140 1260 1320 1440 1560 1680 1800 1920 2100    2280 2460 2640 2820
            3000 3180 3360 3540]';
expt_d = [40 53 69 81 100 122 134 129 133 128 131 126 119 122 115 118 112 120 114 119 112 117]';
r = zeros(i_max-3,1);
n0 = [10020; 18266; 2689; r];
% Model prediction of aggregate size distribution after reaching steady-state
d_model = fix(d');
%d_model=average diameter of each bin=[i_max,1]
num_frac_t_3600 = (n(64,:)/n_tot(64,1))';
num_frac_t_4200 = (n(76,:)/n_tot(76,1))';
```

Asphaltene particle concentration = 4.1 mg/L

```
p = 0.42;
c_1 = 28; % initial point of the first bin of average diameter, micron
u(1) = (h/6)*c_1^3; % initial point of the first bin of average volume, micron^3
for i=2:i_max+1
  u(i)= u(1)*2^(i-1);
  c(i)=(u(i)*(6/pi))^0.33;
end
t0=900;
expt_t = [960 1050 1200 1380 1560 1680 1830 2040 2160 2220 2340 2430 2520 2610 2700 2790 2910
          3060 3240 3420 3540]';
expt_d = [32 40 50 66 83 99 114 118 123 131 124 129 125 128 124 115 112 109 112 108 111]';
r = zeros(i_max-2,1);
n0 = [42275; 5225; r];
% Model prediction of aggregate size distribution after reaching steady-state
d_model = fix(d');
%d_model=average diameter of each bin=[i_max,1]
num_frac_t_3900 = (n(61,:)/n_tot(61,1))';
num_frac_t_4300 = (n(69,:)/n_tot(69,1))';
```

%%

Experimental data and model parameters for predicting growth of the aggregates at G=2.5 s^{-1} for various toluene-to-heptane ratio (T:H) in solvent mixtures

%%

T:H = 1:15

```
p = 0.76;
c_1 = 28; % initial point of the first bin of average diameter, micron
u(1) = (h/6)*c_1^3; % initial point of the first bin of average volume, micron^3
for i=2:i_max+1
  u(i)= u(1)*(2^i-1);
  c(i)=(u(i)*(6/pi))^0.33;
end
t0=400;
expt_t = [300 330 390 435 495 600 660 750 840 900 960 1020 1110 1170 1275 1395 1515 1635 1740 1830
          1950 2070 2190 2310 2430 2550 2700]';
expt_d = [43 54 78 95 126 168 198 233 261 286 303 309 324 313 318 301 265 250 222 214 196 191 182
          190 171 178 181]';
r = zeros(i_max-3,1);
n0 = [30000; 18000; 4500; r];
% Model prediction of aggregate size distribution after reaching steady-state
d_model = fix(d');
%d_model=average diameter of each bin=[i_max,1]
num_frac_t_2600 = (n(45,:)/n_tot(45,1))';
num_frac_t_3600 = (n(65,:)/n_tot(65,1))';
```

T:H = 1:7

```
p = 0.65;
c(1) = 28; % initial point of the first bin of average diameter, micron
u(1) = (h/6)*c(1)^3; % initial point of the first bin of average volume, micron^3
for i=2:i_max+1
  u(i)= u(1)*(2^i-1);
  c(i)=(u(i)*(6/pi))^0.33;
```

```
end
t0=350;
expt_t = [150 210 270 360 420 480 540 600 720 840 960 1080 1200 1380 1500 1620 1740 1860 1980
          2100 2220 2340 2460 2580 2700   2820 3000 3180 3360 3540]';
expt_d = [39 56 74 98 119 132 148 181 214 259 267 286 272 263 282 262 229 225 198 201 197 184 196
          176 163 180 160 182 166 172]';
r = zeros(i_max-4,1);
n0 = [1800; 4900; 6900; 3700; r];
% Model prediction of aggregate size distribution after reaching steady-state
d_model = fix(d');
%d_model=average diameter of each bin=[i_max,1]
num_frac_t_2600 = (n(46,:)/n_tot(46,1))';
num_frac_t_3600 = (n(66,:)/n_tot(66,1))';

T:H = 1:3
p = 0.50;
c(1) = 28; % initial point of the first bin of average diameter, micron
u(1) = (h/6)*c(1)^3; % initial point of the first bin of average volume, micron^3
for i=2:i_max+1
  u(i)= u(1)*2^(i-1);
  c(i)=(u(i)*(6/pi))^0.33;
end
t0=1100;
expt_t = [900 1140 1320 1500 1680 1920 2100 2280 2460 2640 2820 3000 3240 3540]';
expt_d = [41 61 77 109 134 155 197 182 194 177 154 135 119 126]';
r = zeros(i_max-4,1);
n0 = [1511; 4121; 5906; 3160; r];
% Model prediction of aggregate size distribution after reaching steady-state
d_model = fix(d');
%d_model=average diameter of each bin=[i_max,1]
num_frac_t_3500 = (n(49,:)/n_tot(49,1))';
num_frac_t_3900 = (n(57,:)/n_tot(57,1))';
```

Appendix B

Aggregate Porosity Determination: Computer Code

In chapter 5, numerical procedure is required to simultaneously solve equations 5.9, 5.10, 5.25, and 5.18 for a known size of primary particle (d_p). From settling experiments, the porosity of asphaltene aggregates is determined using equation 5.24, which is the alternate form of the aggregate settling model. The numerical code is written in Matlab (version 5.2) and invokes a root finding technique, Newton's method for non-linear equations.

```
%%%%%%%%%%%%%%%%%%%%%%%%%%%%%%%%%%%%%%%%%%%%%%%%
Main file to determine porosity from settling experiment, where asphaltene aggregates
are formed at stirring speed = 36 rpm, and asphaltene particle concentration = 62.5 mg/L
%%%%%%%%%%%%%%%%%%%%%%%%%%%%%%%%%%%%%%%%%%%%%%%%

clc
clear

global mu_l rho_l rho_p d_p g d_agg Vs_expt

h = 24; % creeping flow, Re<<1
mu_l = 0.00045; % viscosity of the tolune-heptane solvent mixtures, Pa.s
rho_l = 714.8; % density of the tolune-heptane solvent mixtures, kg/m^3
rho_p = 1200; % density of asphaltene primary particle, kg/m^3
g = 9.81; % gravitational acceleration, m/s^2

% aggregate projected area diameter (di_agg), m
di_agg = [9.345E-05  9.809E-05  9.300E-05  1.235E-04  1.509E-04  8.282E-05  1.107E-04
          8.185E-05  1.726E-04  9.129E-05  8.498E-05  1.108E-04  1.159E-04  1.018E-04
          2.010E-04  1.279E-04  1.553E-04  1.093E-04  1.062E-04  1.109E-04  1.022E-04
          9.026E-05  9.868E-05  5.861E-05  6.350E-05  7.409E-05  1.074E-04  9.199E-05
          9.752E-05  8.328E-05  7.285E-05  8.420E-05  1.771E-04  1.280E-04  1.564E-04
          9.300E-05  9.104E-05]';

% Terminal settling velocity of the aggregates (Vsi_expt), m/s
Vsi_expt = [2.436E-04   1.946E-04  2.254E-04  2.570E-04  2.153E-04  1.066E-04  1.836E-04
            1.868E-04   1.915E-04  2.219E-04  2.743E-04  2.821E-04  1.515E-04  2.048E-04
            2.947E-04   2.730E-04  3.630E-04  1.860E-04  2.865E-04  2.830E-04  3.052E-04
            3.536E-04   3.650E-04  2.199E-04  1.823E-04  2.325E-04  3.203E-04  4.135E-04
            4.000E-04   4.013E-04  2.576E-04  3.201E-04  3.799E-04  3.792E-04  5.483E-04
            2.695E-04   4.522E-04]';
```

```
% p = initial guess for aggregate porosity as determined using Stokes' law
p = [0.948   0.958   0.950   0.970   0.983   0.971   0.973   0.949   0.988   0.949   0.929
     0.958   0.980   0.962   0.984   0.970   0.967   0.972   0.954   0.959   0.948   0.921
     0.921   0.882   0.917   0.911   0.948   0.913   0.923   0.883   0.907   0.916   0.973
     0.951   0.949   0.936   0.892]';

for i=1:37
  d_agg=di_agg(i);
  Vs_expt=Vsi_expt(i);
  z(i)=fsolve('permeable_brinkman', p(i));
end

for i=1:37
  Re(i)=di_agg(i)*Vsi_expt(i)*rho_l/mu_l;
  Cd(i)=h/Re(i);
  k(i)=((d_p^2)/12)*(3+4/(1-z(i))-3*sqrt(8/(1-z(i))-3));
  beta(i)=di_agg(i)/(2*sqrt(k(i)));
  omega(i)=2*beta(i)^2*(1-(tanh(beta(i)))/beta(i))/(2*beta(i)^2+3*(1-(tanh(beta(i)))/beta(i)));
end
```

```
%%%%%%%%%%%%%%%%%%%%%%%%%%%%%%%%%%%%%%%%%%%%%%%%
```

Function file for solving non-linear equations

```
%%%%%%%%%%%%%%%%%%%%%%%%%%%%%%%%%%%%%%%%%%%%%%%%

function y = permeable_brinkman (p)

global mu_l rho_l rho_p d_p g d_agg Vs_expt

% Initialization of the variables
h = 24; % creeping flow, Re<<1
mu_l = 0.00045; % viscosity of the tolune-heptane solvent mixtures, Pa.s
rho_l = 714.8; % density of the tolune-heptane solvent mixtures, kg/m^3
rho_p = 1200; % density of asphaltene primary particle, kg/m^3
g = 9.81; % gravitational acceleration, m/s^2

% Initialization of the parameter
d_p=0.0000001; % "primary" particle size of asphaltenes, m
%d_p=0.000001; % "primary" particle size of asphaltenes, m
%d_p=0.000005; % "primary" particle size of asphaltenes, m

Re=d_agg*Vs_expt*rho_l/mu_l;
Cd=h/Re;
k=((d_p^2)/12)*(3+4/(1-p)-3*sqrt(8/(1-p)-3));
beta=d_agg/(2*sqrt(k));
omega=2*beta^2*(1-(tanh(beta))/beta)/(2*beta^2+3*(1-(tanh(beta))/beta));
y = (Vs_expt^2*3*rho_l*omega*Cd)-(4*g*(1-p)*(rho_p-rho_l)*d_agg);
% end subprogram permeable_brinkman (p)
```

```
%%%%%%%%%%%%%%%%%%%%%%%%%%%%%%%%%%%%%%%%%%%%%%%%%%%%%%%%%
Aggregate settling velocity–size data for different experimental conditions
%%%%%%%%%%%%%%%%%%%%%%%%%%%%%%%%%%%%%%%%%%%%%%%%%%%%%%%%%
```

Stirring speed = 75 rpm; Asphaltene particle concentration = 62.5 mg/L

```
% aggregate projected area diameter (di_agg), m
di_agg = [9.188E-05 1.067E-04  8.603E-05  8.110E-05  9.933E-05  8.096E-05  9.085E-05
          8.087E-05 9.852E-05  7.341E-05  8.168E-05  8.672E-05  6.756E-05  6.252E-05
          7.413E-05 5.350E-05  9.609E-05  9.148E-05  1.171E-04  8.103E-05  6.647E-05
          7.036E-05 6.758E-05  6.994E-05  7.114E-05  9.506E-05  1.072E-04  8.784E-05
          1.149E-04 7.580E-05  1.336E-04  7.488E-05]';

% Terminal settling velocity of the aggregates (Vsi_expt), m/s
Vsi_expt = [5.646E-04  5.330E-04  3.940E-04  4.300E-04  3.715E-04  2.102E-04  2.024E-04
            1.677E-04  2.085E-04  2.329E-04  2.725E-04  2.814E-04  1.677E-04  2.217E-04
            2.797E-04  1.384E-04  5.013E-04  3.629E-04  1.945E-04  1.574E-04  3.478E-04
            3.765E-04  3.888E-04  1.609E-04  1.681E-04  1.740E-04  2.165E-04  1.892E-04
            1.592E-04  2.093E-04  1.566E-04  1.572E-04]';

% p = initial guess for aggregate porosity as determined using Stokes' law
p = [0.874  0.899  0.901  0.880  0.930  0.938  0.953  0.951  0.961  0.904  0.925
     0.931  0.931  0.891  0.904  0.905  0.902  0.919  0.974  0.954  0.861  0.851
     0.832  0.940  0.940  0.964  0.966  0.955  0.978  0.933  0.984  0.944]';
```

Stirring speed = 75 rpm; Bitumen concentration = 1000.0 mg/L

```
% aggregate projected area diameter (di_agg), m
di_agg = [7.929E-05 5.043E-05  4.729E-05  5.853E-05  5.085E-05  6.512E-05  4.248E-05
          4.943E-05 4.945E-05  4.439E-05  6.554E-05  6.416E-05  3.829E-05  3.659E-05
          2.714E-05 5.547E-05  3.888E-05  6.272E-05  5.723E-05  6.479E-05  7.187E-05
          5.564E-05 6.953E-05  3.319E-05  5.808E-05  3.694E-05  3.312E-05  5.593E-05
          5.824E-05 5.911E-05  5.650E-05  3.544E-05  4.835E-05  4.713E-05  5.192E-05
          4.784E-05 3.824E-05  5.628E-05  5.645E-05  5.118E-05  5.312E-05  4.793E-05
          5.845E-05 5.342E-05  4.383E-05]';

% Terminal settling velocity of the aggregates (Vsi_expt), m/s
Vsi_expt = [1.656E-04  2.135E-04  2.103E-04  2.063E-04  2.234E-04  2.292E-04  2.185E-04
            2.256E-04  2.348E-04  1.976E-04  2.045E-04  1.508E-04  1.880E-04  1.434E-04
            1.531E-04  1.383E-04  1.555E-04  1.616E-04  1.942E-04  2.273E-04  2.275E-04
            1.937E-04  1.821E-04  1.657E-04  1.836E-04  2.026E-04  1.848E-04  1.948E-04
            1.289E-04  1.773E-04  1.449E-04  2.045E-04  1.537E-04  1.916E-04  1.218E-04
            1.997E-04  2.034E-04  1.903E-04  1.926E-04  1.886E-04  1.661E-04  1.531E-04
            1.808E-04  1.218E-04  1.221E-04]';

% p = initial guess for aggregate porosity as determined using Stokes' law
p = [0.946  0.840  0.810  0.880  0.833  0.895  0.765  0.829  0.821  0.810  0.873
     0.889  0.649  0.704  0.426  0.876  0.710  0.882  0.833  0.857  0.885  0.836
     0.894  0.624  0.825  0.605  0.532  0.835  0.881  0.845  0.827  0.568  0.820
     0.758  0.873  0.732  0.584  0.820  0.792  0.799  0.813  0.805  0.845  0.881
     0.822]';
```

Stirring speed = 160 rpm; Bitumen concentration = 1000.0 mg/L

```
% aggregate projected area diameter (di_agg), m
di_agg = [5.408E-05  8.079E-05  5.089E-05  2.873E-05  4.954E-05  2.635E-05  3.513E-05
          2.332E-05  3.231E-05  2.609E-05  2.784E-05  2.239E-05  2.463E-05  4.797E-05
          3.976E-05  2.504E-05  3.700E-05  3.329E-05  3.446E-05  3.278E-05  4.477E-05
          4.064E-05  3.458E-05  3.507E-05  5.789E-05  2.867E-05  4.558E-05  6.404E-05
          8.090E-05  2.548E-05  2.759E-05  2.503E-05  2.638E-05]';

% Terminal settling velocity of the aggregates (Vsi_expt), m/s
Vsi_expt = [3.097E-04  2.695E-04  3.063E-04  2.384E-04  2.595E-04  2.431E-04  2.229E-04
            2.138E-04  2.070E-04  2.110E-04  2.055E-04  1.774E-04  1.710E-04  2.368E-04
            2.246E-04  2.082E-04  2.543E-04  2.736E-04  2.795E-04  3.323E-04  2.689E-04
            3.535E-04  2.911E-04  2.990E-04  2.981E-04  2.900E-04  2.528E-04  2.781E-04
            2.978E-04  2.390E-04  2.503E-04  2.344E-04  2.582E-04]';

% p = initial guess for aggregate porosity as determined using Stokes' law
p = [0.808  0.914  0.750  0.349  0.733  0.222  0.479  0.041  0.519  0.229  0.355
     0.122  0.293  0.786  0.695  0.292  0.651  0,531  0.572  0.416  0.748  0.597
     0.514  0.535  0.814  0.343  0.762  0.849  0.896  0.348  0.333  0.279  0.300]';
```